GRAN SASSO SCIENCE INSTITUTE

DOCTORAL THESIS

Probing the physics of γ-ray bursts through high-energy and multi-messenger observations

Author:
Samuele RONCHINI

Supervisors:
Prof. Marica BRANCHESI
Dr. Gor OGANESYAN

PhD Program in Astroparticle Physics, XXXIV Cycle

Abstract

γ-ray bursts (GRBs) are among the most enigmatic and energetic phenomena of the Universe. After decades of theoretical studies and observational results, they still puzzle the astronomical community. Powered by a compact central engine, either a black hole or a neutron star, these objects are able to launch ultra-relativistic jets whose interaction with the surrounding medium leads to an electromagnetic emission visible from radio wavelengths up to very high-energy gamma rays. Besides being unique tools to probe relativistic astrophysics through multi-band observations, the detection of a γ-ray flash in coincidence with the binary neutron star merger GW170817 showed the groundbreaking potential of GRBs as multi-messenger sources, which are able to unveil properties of relativistic jets, nucleosynthesis of heavy elements, to evaluate the expansion rate of the Universe and set constraints on fundamental physics. However, despite the remarkable advances achieved in the last years, many open questions remain to be addressed, such as the origin of prompt emission, the composition and geometrical structure of relativistic jets, the nature of the emitting particles, the connection between the central engine and the afterglow physics, the acceleration mechanisms or the jet launching process.

This thesis is devoted to understand the physics governing GRBs using γ/X-ray observations and to evaluate the perspectives opened by gravitational-wave observations. Exploiting the wealth of data provided in almost twenty years of activity of the Neil Gehrels *Swift* Telescope, I investigated the spectral and temporal properties of GRB X-ray light curves. In particular, I analysed the transition phase between the prompt and the afterglow emission, which typically shows a steep flux decay phase, and I discovered a new relation between X-ray flux and spectral index. This relation challenges the common interpretation of the steep decay phase and requires the presence of specific radiative and cooling processes of the emitting particles. This study enabled a refined understanding of the prompt emission physics probing the jet nature, dynamics, structure and composition after the bulk of γ-ray radiation is released.

In order to investigate the late time activity of the central engine, I also focused my analysis on the plateau phase of GRBs, whose origin is a long-standing open issue. After having defined a complete sample of GRBs with an X-ray plateau, a combined optical/X-ray time resolved spectral analysis of the plateau sample has been performed to probe the emission mechanism and discuss the main consequences for the currently available physical scenarios, which interpret the plateau as due to the presence of a central

magnetar activity or the high latitude emission from a structured jet.

The modelling developed to describe the GRB high-energy emission has then been used to evaluate the perspectives of multi-messenger astronomy with the next generation of gravitational-wave detectors, such as Einstein Telescope (ET) and γ/X-ray mission concepts, such as THESEUS. My thesis work provides a theoretical setup able to robustly simulate the statistical and observational properties of a population of short GRBs in the gravitational and electromagnetic domain. The versatility of our approach allowed us to apply this method for diverse purposes, such as evaluate the number of binary neutron star merger observed with an associated GRB for different ET configurations or the number of GRBs detectable by future high-energy mission concepts assuming different observational strategies. Synergies between the next GW detectors and high-energy satellites are a unique opportunity to detect, localise and characterise the electromagnetic counterpart of binary neutron star merger up to cosmological distances and shed light on GRB physics.

Acknowledgements

The first thanks go to my mentors, Marica and Gor, who have accompanied me with constant passion and dedication in the realization of this project. I thank Marica for the profound and genuine humanity shown on every occasion, for the rare foresight that distinguishes her and that has allowed me to explore new horizons and take advantage of unique opportunities. I thank her for teaching me that research is made up of patience, waiting, attempts, humility and sincere respect for others, but also of spirit of initiative and the courage to dare.
I thank Gor, who followed me by making his time and his expertise available to guide me through the labyrinths of this discipline. I thank him for teaching me to take research as something that really goes beyond a job, a passion or a challenge. I have always admired the lightness and ease that distinguish him in transforming problems and adversities into chances for growth and maturation, both inside and outside the academic world.
I thank all the gravitation group, for the collaborative spirit and the demonstrated support. I thank Jan and Marica for making this group grow so quickly in number and variety, for giving a common direction to our efforts. I thank the staff of the Gran Sasso Science Institute, who have made this institute competitive and a point of reference at an international level.
Finally, my most heartfelt thanks go to my parents, who never hesitated to support my steps, choices or challenges. I thank them for every advice, for their support in the most critical moments and the enthusiasm demonstrated for every success.

Il primo ringraziamento va ai miei mentori, Marica e Gor, che con assidua passione e dedizione mi hanno accompagnato nella realizzazione di questo progetto. Ringrazio Marica per la profonda e genuina umanità dimostrata in ogni occasione, per la rara lungimiranza che la contraddistingue e che mi ha permesso di esplorare nuovi orizzonti e di sfruttare opportunità uniche. La ringrazio per avermi insegnato che la ricerca è fatta di pazienza, di attesa, di tentativi, di umiltà e di sincero rispetto per il prossimo, ma anche di spirito di intraprendenza e del coraggio di osare.
Ringrazio Gor, che mi ha seguito mettendo a disposizione il suo tempo e la sua competenza, per guidarmi nei labirinti di questa disciplina. Lo ringrazio per avermi insegnato a considerare la ricerca come qualcosa che va al di là di un lavoro, di una passione o di una sfida. Ho sempre ammirato la leggerezza e disinvoltura che lo contraddistinguono nel trasformare i problemi e le avversità in spunti di crescita e maturazione, sia all'interno, sia al di fuori del mondo accademico.
Ringrazio tutto il gruppo di gravitazione, per lo spirito collaborativo e il supporto dimostrato. Ringrazio Jan e Marica per aver fatto sì che questo gruppo crescesse così velocemente in numero e varietà, per aver dato una direzione comune ai nostri sforzi. Ringrazio il personale del Gran Sasso Science Institute, che ha reso competitivo e un punto di riferimento questo istituto a livello internazionale.
Infine, il mio ringraziamento più sentito va ai miei genitori, che non hanno mai esitato a supportare ogni mio passo, scelta o sfida. Li ringrazio per ogni consiglio, per il sostegno nei momenti più critici e l'entusiamo per ogni successo.

Contents

List of Abbreviations

CBM	**C**ompact **B**inary **M**erger
BH	**B**lack **H**ole
BNS	**B**inary **N**eutron **S**tar
CE	**C**osmic **E**xplorer
EM	**E**lectro**m**agnetic
ET	**E**instein **T**elescope
GRB	**G**amma - **R**ay **B**urst
GW	**G**ravitational **W**ave
HLE	**H**igh **L**atitude **E**mission
NS	**N**eutron **S**tar
SD	**S**teep **D**ecay
SFR	**S**tar **F**ormation **R**ate
SNR	**S**ignal-to-**N**oise **R**atio

Chapter 1

Introduction

γ-ray bursts are explosive transient events, associated with either the collapse of a massive star, or the merger of two compact objects. The initial erratic gamma-ray emission, known as prompt phase, is followed by a multi-wavelength emission, the afterglow, which can last up to several days. The origin of these two emission phases is related to the radiation released by an ultra-relativistic collimated outflow launched by a central engine, which can be either a black hole or a neutron star. The use of a network of astronomical observatories which operate in different bands of the electromagnetic (EM) spectrum is essential to fully characterise the panchromatic emission of GRBs. The field of GRBs rapidly evolved in the last years, with a major revolution given by the advent of the Neil Gehrels *Swift* Telescope (Gehrels, 2004). In the next chapter we will go through the main discoveries achieved thanks to the unique operational strategy of Swift, which gave relevant insights about the properties of the afterglow emission, the physics of relativistic jets and the nature of the GRB engine.
As it will be shown in chapter 3, the X-ray light curve of the GRB afterglow contains a wealth of information regarding the jet physics, its dynamical evolution during the interaction with the interstellar medium, its angular structure, as well as the dominating radiative processes. *Swift* showed that the X-ray light curves are characterised by the presence of multiple features. They show an initial rapid steep decline followed by a shallower phase. The former is known as *steep decay* (Tagliaferri, 2005; Nousek, 2006; O'Brien, 2006) and it is connected with the final stages of prompt emission, the latter is associated with the decelerating phase of the jet. A considerable fraction of GRBs shows a flat emission phase of the X-ray light curve, known as *plateau* (Zhang, 2006).
The geometrical structure of the relativistic jet is a crucial ingredient to understand and interpret the multi-band emission of GRBs. As it will be

extensively discussed in section 3.3, theoretical arguments and observational evidences point toward a jet structure which deviate from the simple uniform top-hat structure (see Salafia and Ghirlanda, 2022 and references therein). We will show how this impacts the appearance of the X-ray light curve, especially regarding the transition between the steep decay and the plateau phase. In the specific, the temporal and spectral analysis of these phases are particularly interesting to understand if there exist a universal jet structure and how it is related to the nature of the central engine and to the observational properties of the GRB. A deep investigation of the jet structure has a key role for GRB population studies and for the estimation of the detectability of these events as a function of the viewing angle.
The first part of my thesis is dedicated to the analysis of the steep decay phase, the investigation of its origin and the connection with prompt and afterglow physics. The standard and most accepted interpretation of the steep decay is related to the emission at large angles of the jet. This effect is known as *High Latitude Emission* (HLE) (Fenimore et al., 1996; Kumar and Panaitescu, 2000; Liang, 2006) and successfully explains the temporal decline of steep decay, though a detailed study of the spectral evolution expected in this scenario and a direct comparison with data have not been performed so far. In addition to HLE, other physical effects can shape the temporal and spectral evolution of the steep decay (Zhang et al., 2007), including the cooling and radiative efficiency of particles. Within this context, my work aims at studying the X-ray steep decay through a systematic time-resolved spectral analysis of Swift data, which reveals a common relation between X-ray flux and spectral index. The origin of this relation will be deeply studied, in order to infer physical information about the emission at large angles from the jet surface, the final phases of the prompt emission, the radiative evolution and the nature of the emitting particles, as well as possible effects induced by the jet structure. The work on the steep decay will be presented in chapter 4.
A similar approach is adopted to investigate the origin of the X-ray plateau, based on a time resolved X-ray spectral analysis, with the advantage of adding also the information coming from the inclusion of optical data. The interpretation of the X-ray plateau requires a modification of the standard scenario where an ultra-relativistic jet gradually decelerates in the interstellar medium. One possible scenario, among the most accepted, involves the presence of a long-lasting activity of the central engine, in the form of late time accretion on a black hole or the spin down energy from a rapidly rotating magnetised neutron star (Dai and Lu, 1998b; Zhang and Mészáros,

2001a; Troja et al., 2007; Rowlinson et al., 2010; Rowlinson et al., 2013; Metzger et al., 2011; Bucciantini et al., 2012). The energy released by the central engine can either refresh the shock or produce itself a wind of particles, inducing a flattening of the X-ray light curve. Alternatively, the jet structure can produce a plateau in the X-ray light curve (Oganesyan, 2020; Ascenzi et al., 2020a; Beniamini et al., 2020a; Beniamini et al., 2020c; Beniamini et al., 2022). Therefore, in order to discern which is the most favoured scenario, my work exploits a multi-band analysis of the temporal and spectral properties of the plateau. In particular, we investigate whether a single emission site is compatible with the broad band emission during and after the plateau, in the assumption that synchrotron radiation is the dominant radiative process. The analysis and results of this work will be presented in chapter 5.
The steep decay and plateau phases enclose important information about the X-ray emission during the afterglow of GRBs, also in connection with the prompt emission properties, the nature of the central engine and the jet structure and dynamics. A complete and exhaustive view of the X-ray afterglow phenomenology is essential to probe the physics acting in GRBs and also to evaluate the detectability perspectives by future instruments and thus to identify the best instrumental requirements to maximise the scientific return of each GRB observation.

The first detection of gravitational waves (GWs) in coincidence with a GRB represented another outstanding turning point for this field (Abbott et al., 2017c; Abbott et al., 2017d; Abbott et al., 2017b; Goldstein et al., 2017a; Savchenko et al., 2017). With GW170817 a new astronomical era started, opening remarkable possibilities to study more in detail the connection between compact binary mergers (CMBs) and short GRBs (Metzger, 2019; Branchesi et al., 2020; Nakar, 2020; Burns, 2020). In chapter 2, after an historical background on GRB observations, we will retrace all the observational campaign that followed the detection of GW170817 and the groundbreaking influence it had for the field of GRBs, demonstrating the relevance of multi-messenger astrophysics. The observation of the kilonova IR/optical/UV emission associated with GW170817 demonstrated that CBMs are ideal sites for the nucleosynthesis of heavy elements (Pian et al., 2017a; Smartt et al., 2017; Watson et al., 2019; Perego et al., 2022). Recent detections with both space-based telescopes and Cherenkov telescopes showed that GRBs are also strong GeV and TeV emitters (see Miceli and Nava 2022 for a review), thus potential sources of ultra-high energy cosmic rays and neutrinos. The observational results of the last decades

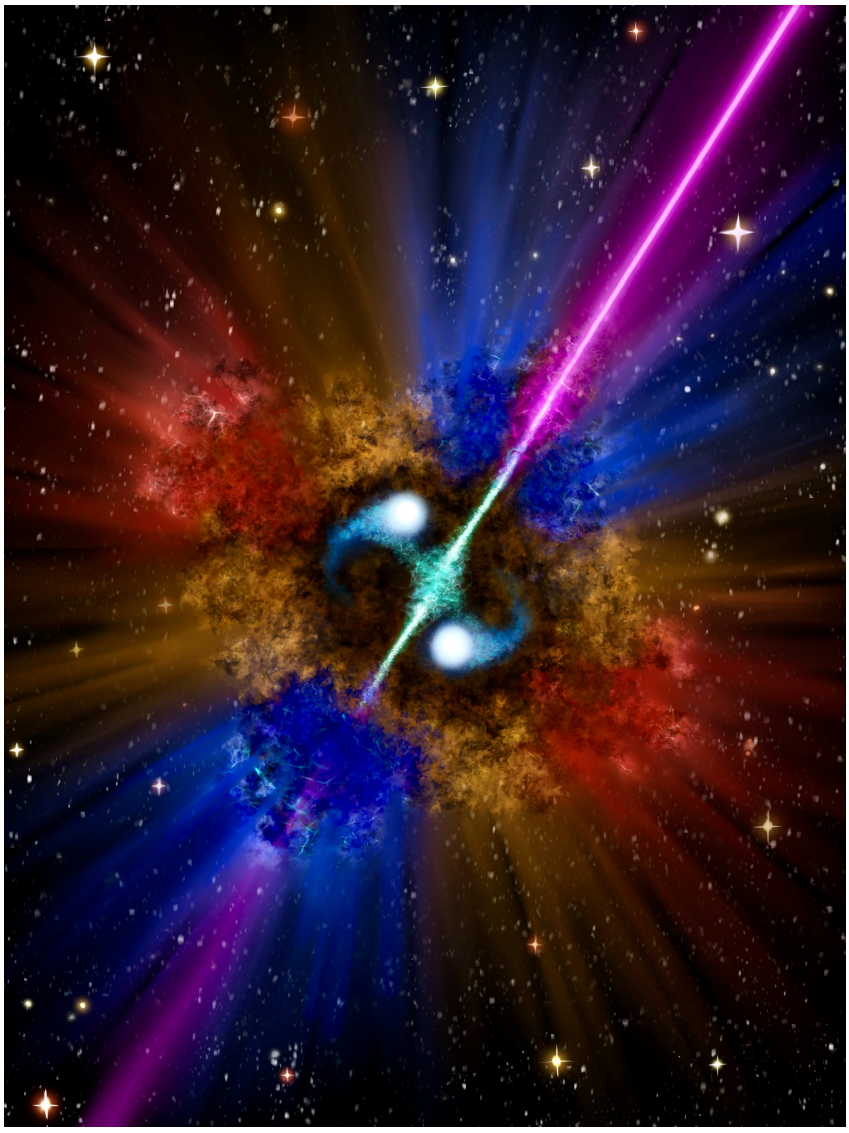

FIGURE 1.1: Artistic representation of a γ-ray burst originated by the merger of two neutron stars. The relativistic jet is illustrated in purple, while the blue and red clouds are the merger ejecta which give rise to the kilonova emission.

demonstrated that GRBs are ideal multi-messenger factories and astrophysical laboratories for performing studies in the fields of general relativity, stellar evolution, relativistic astrophysics, plasma physics, nuclear physics and cosmology.
This thesis aims at evaluating the prospects to investigate the GRB physics through multi-messenger observations by future detectors. In particular,

my thesis is dedicated to develop the multi-messenger science case of the Einstein Telescope (ET) (Punturo et al., 2010), an ambitious project of third generation gravitational-wave detector, planned to be operative from the second half of 2030s. ET is designed to be a detector with a triangular shape, built underground to minimise the impact of seismic noise and optimised to work both at low and high frequencies. Its unprecedented sensitivity (around one order of magnitude of improvement with respect to current GW detectors) will allows us to detect $\sim 10^5$ CMBs per year (Maggiore et al., 2020), accessing regions of the Universe not explored yet. Chapter 6 will describe the synergy between ET and high energy (X-ray and gamma) satellites. We will present a theoretical machinery for the prediction of both the EM and GW signals, able to estimate the detection efficiency of several combination of instruments and to predict rates of joint GW/GRB detections in the ET era.
Several types of high-energy EM signals from CBMs will be taken into account, including standard prompt and afterglow emission, effects related the jet structure and the viewing angle, as well as to shock breakout emission. We will test the potentiality of future mission concepts, identify the best combination of instruments and respective characteristics, in order to maximise their efficiency in the multi-messenger context. Among all the missions taken into account, we will investigate wide field γ-ray and X-ray instruments, such as those onboard of the THESEUS mission. In particular we will test its performances for the study of the X-ray steep decay and plateau and respective spectral evolution, investigation of the effects induced by the jet structure, as well as the crucial part that will be played in the multi-messenger field.
We will conclude discussing how different design configurations of the Einstein Telescope will perform in terms of joint GW/GRB detection, with particular emphasis to multi-messenger aspects and cosmological studies.
A summary of the thesis work will be provided in chapter 7.

Chapter 2

Multi-messenger observations of GRBs

In this chapter we present the main observational studies that brought to our current knowledge of GRBs, from their discovery, passing through the confirmation of their extragalactic origin, the new insights by the Swift mission and the revolution represented by the multi-messenger detection of GW170817. We review the major advances achieved in this field, highlighting which questions are still unresolved.

2.1 Pre-Swift era

GRBs were serendipitously discovered in the late '60s by satellites dedicated to the search of γ-ray radiation emitted in nuclear explosions. Since the localisation capability of the first γ-ray instruments was limited, it was impossible to associate the GRB with other known sources and, more important, no distance estimation was available. Therefore two schools of thinking competed for years, one supporting the cosmological origin of GRBs, the other claiming a Galactic origin. With the advent of the BATSE instrument (Meegan et al., 1992; Band et al., 1993) we had the first systematic census of the GRB population and the evidence that these sources are homogeneously distributed in the sky, indicating no preference in the arrival direction. Moreover, a bimodal distribution of the duration of the burst started to appear, indicating the possible existence of two distinct classes (Kouveliotou et al., 1993). A first class, called *short*-GRBs, with a duration less than 2 seconds and with a harder spectrum and a second class, called *long*-GRBs, with a duration larger than two seconds and softer spectrum.
In the hypothesis of a Galactic origin, GRBs could be associated to high-energy emission from galactic compact objects, such as magnetar outbursts or sporadic accretion episodes on stellar mass black holes. Hence, GRBs should be clustered across the Galactic plane. Even if the evidence of

isotropy was going in favour of the cosmological origin, there were scenarios claiming that GRBs are located in the immediate neighbourhood of the Solar System and therefore still compatible with an isotropic distribution (e.g., Belli 1997).
In order to solve this controversy, a direct measurement of the source distance was necessary. The turning point was represented by the advent of Beppo-SAX (Boella et al., 1997), a mission equipped with a wide field X-ray camera able to pinpoint the GRB with arcmin precision and to follow-up with a second small field of view (FOV) X-ray telescope. With the discovery of GRB 970228 (Costa et al., 1997), Beppo-SAX provided the sky position with a precision sufficient to point ground-based telescopes which were able to detect the first optical counterpart of a GRB (van Paradijs et al., 1997; Bloom et al., 2001). Subsequently, with GRB 970508 (Bloom et al., 1998; Galama et al., 1998), the first radio counterpart was discovered and, more important, the analysis of the optical spectrum revealed the presence of an absorption line pointing to a redshift z=0.835. With this discovery, the extra-galactic origin of GRBs was definitively accepted (Paczynski, 1986). Moreover, these observations demonstrated that GRBs are able to produce after the initial γ-ray flash (known as *prompt* emission) a broad multi-band emission called *afterglow* phase, marking the beginning of the multi-wavelength era of GRBs.

Association of long GRBs with Supernova explosions

One of the most plausible scenarios initially proposed for the origin of GRBs was based on the idea that these cosmic events are connected with the final stages of the collapse of massive stars (Woosley, 1993). The first tentative association between a long GRB and a supernova came with GRB 980425 (Kulkarni et al., 1998), where the sky region of the GRB overlapped with the position of SN1998bw. The supernova contribution appears as a bump superimposed to the declining trend of the GRB optical afterglow. An even more robust evidence of GRB/supernova association arrived with GRB 030329 and SN 2003dh, located at z=0.167 (Hjorth et al., 2003; Stanek et al., 2003).
With accumulating evidences of association between GRBs and SNae, it became clear that typically long GRBs are connected with Type Ic SNae, a specific class characterised by the lack of silicon, helium and hydrogen lines. The absence of hydrogen suggests the presence of strong stellar winds able to sweep away the outer layers of the stellar envelopes. Strong winds are usually due to high metallicity of the stellar material and this feature is

typical of Wolf-Rayet (WR) stars. Though, only a limited fraction of Type Ic SNae have an associated long GRB, indicating that only under special conditions a GRB occurs and/or that GRB emission is highly collimated and hence detectable only if the collimation axis is close to the line of sight.
After the first years of observations of GRB afterglows and associated host galaxies, it appeared evident that these events are preferably located in low-luminosity star forming galaxies (Fruchter et al., 2006). This points toward an evolution of GRBs connected to the star formation history, compatible with the collapsar origin. Alternatively, a young and star-forming host galaxy is compatible as well with a scenario interpreting the GRBs as flares from newly-born highly magnetised neutron stars.
Nowadays two methods are used to confirm the association between GRBs and SNae, one photometric and the other spectroscopic. The photometric method consists in the identification of a bump in the optical light curve of the GRB, occurring few days/weeks after the burst, characterised by a thermal spectral shape instead of the typical non-thermal nature of the GRB afterglow. More robust is the spectroscopic identification, which directly relies on the detection of typical spectral features of SNae.

2.2 The *Swift* Era

At the end of the '90s, hundreds of GRBs had been discovered and localised. Though, the process of detection of the multi-wavelength afterglow and consequent redshift determination needed hours from the GRB trigger. Therefore there was an intermediate temporal window (from the burst to the first few hours) where the GRB emission was unknown and the scientific community deemed necessary a new mission concept able to detect, precisely localise and follow-up the GRB emission within a short amount of time. Hence the idea to launch the Neil Gehrels *Swift* Telescope (*Swift*) on 2004 (Gehrels, 2004). The telescope mounts three instrument: 1) Burst Alert Telescope (BAT), a hard X-ray coded-mask detector sensitive in the energy range 15-350 keV and with a FOV of 1.6 sr, 2) X-Ray Telescope (XRT), a small FOV focusing X-ray telescope sensitive in the soft X-ray band 0.2-10 keV, 3) Ultra-Violet/Optical Telescope (UVOT), an optical/UV telescope sensitive in the range 170-650 nm and able to reach a limiting magnitude of $\sim$23.
This unique combination of instruments enables us to trigger the GRB with BAT, slew XRT in $\lesssim$100 s and finally collect optical data with UVOT, everything with an automatised on-board procedure. Simultaneously to the GRB detection, a low-latency alert is spread in the astronomical community

with the position of the source, giving the possibility to promptly activate the follow-up with ground-based telescopes. The outstanding role of *Swift* resides also in its unprecedented capability of providing a precise localisation of the burst, thanks to an angular resolution of 20 arcmin for BAT and 2.4 arcsec for XRT.
The operation of *Swift* revolutionised the observation of GRBs, allowing us to systematically characterise the afterglow emission, since the early stages. Deviations from the standard power-law temporal decay of the X-ray light curve appeared and new features were discovered, such as X-ray flares and X-ray plateaus (Chincarini et al., 2010; O'Brien, 2006; Zhang et al., 2006a).
In particular, *Swift* had a fundamental role for the study of short GRBs, whose afterglow was too faint and too short-living to be detected in pre-*Swift* era. The afterglow emission of several short GRBs has been detected but in no case a SNa association was found (but see the case of GRB 200826A, Zhang et al. 2021). The host galaxies of short GRBs are late-type (spiral/irregular) and usually gas poor, with minor star formation rate with respect to long GRB hosts (Berger, 2009; Fong et al., 2013; Berger, 2014; Fong et al., 2022; Nugent et al., 2022). Moreover, measuring the offset of GRBs from the centre of the host galaxy, the short ones are on average located farther away with respect to the long ones. With the years, the collection of these hints corroborated the hypothesis that short GRBs cannot be originated by stellar explosions (Berger, 2014).
Along with *Swift* and Beppo-SAX, the mission HETE2 had a relevant role for the study of GRBs, including the discovery of the first bright supernova associated to the long GRB 030329 (Stanek et al., 2003; Vanderspek et al., 2004), or the first optical afterglow associated with the short GRB 050709 (Fox et al., 2005).
One of the most favoured progenitors of short GRBs are compact binary mergers (CBMs), as originally proposed by Eichler et al., 1989. Compared to star collapse, a smaller amount of mass is expected to be accreted around the stellar object and on a shorter time scale. This is in agreement with the shorter duration and lower energetics observed for short GRBs. Moreover, during the evolutionary path of the binary stellar system, both the companions have to go through an explosion, and a natal kick usually tends to displace the binary system from the birth place (Beniamini et al., 2016). Given the time delay between the star formation and the merger, the binary system has enough time to migrate from the galactic disk towards the outskirts of the galaxy. This would explain the large galaxy off-set usually measured for short GRBs. In addition to a high-energy emission, CBMs

produce a variety of mildly relativistic, quasi-isotropic ejecta. These outflows are neutron-rich and the radioactive decay of heavy elements power a short, fastly decaying UV/optical/IR emission, known as *kilonova* (Li and Paczyński, 1998). There are few cases where the kilonova emission/short-GRB association has been claimed (Berger et al., 2013; Tanvir et al., 2013; Yang et al., 2015; Jin et al., 2016), but the only with the event GW170817 we had the first smoking gun that CBMs can be the progenitor of short GRBs and kilonova emission (see section 2.3.1).
Moreover, increasing the sample of GRBs, the standard dichotomy short-hard/long-soft started to reveal contamination between the two classes, pointing towards a more complex scenario which indicates that duration and spectral properties are possibly not enough to identify unequivocally the GRB progenitor. Beyond the short/long classification, also new classes have been identified, such as ultra-long GRBs, X-ray outbursts or γ-ray flashes associated to tidal disruption events around super-massive black holes.
New insights about the broad-band spectral properties of GRBs came with the launch on 2008 of the *Fermi* satellite, a γ-ray telescope with two instruments onboard: 1) the Gamma-ray Burst Monitor (GBM, Meegan et al. 2009a) observing in the band 8 keV-40 MeV, 2) the Large Area Telescope (LAT, Atwood et al. 2009), operating in the band 20 MeV-300 GeV. Before the launch of *Fermi*, the γ-ray spectrum of GRBs was well fitted with mainly three empirical shapes: a single power law, a broken power law with a smooth connection in correspondence of the break (better known as *Band* function), or a power law plus a high-energy cutoff. Such components suggest a non-thermal origin of the prompt emission. The observations of *Fermi* revealed more complex features, such as quasi-thermal components superimposed to the standard non-thermal emission (Ryde and Pe'er, 2009; Ghirlanda et al., 2007). After the first years of operation, *Fermi* discovered that few % of GRBs have an emission in the GeV band ($\gtrsim$ 100 MeV) (Miceli and Nava, 2022). The GeV emission typically appears when the *prompt* emission is over and it lasts more than the GRB duration itself, suggesting that the emission site should be distinct with respect to the *prompt* emission one. On the other hand, the fast variability observed in the *Fermi*-LAT light curves suggests that the GeV emission can occur in the same emission site of the prompt emission observed in the MeV energy range (Ajello et al., 2019). Another great leap forward came with the detection of Very High-Energy (VHE) emission of GRBs with Imaging Atmospheric Cherenkov Telescopes (IATCs) (Aharonian et al., 1997; Aleksić et al., 2016a; Aleksić et al., 2016b). Cherenkov telescopes are sensitive to photons in the

energy range between ∼100 GeV up to ∼ 100 TeV, whose detection is not within the reach of γ-ray space telescopes, due to the limited volume of the detectors. The detection of VHE emission from GRBs came only in the last years due to technical difficulties related to IATCs, such as the limited field of view and the strong absorption by extra-galactic background light (Domínguez et al., 2011). This implies that only GRBs located in the nearby Universe have a detectable VHE emission. Moreover the duty cycle of these instruments is affected by atmospheric conditions, absence of Moon light and position of the source with respect to the horizon. Therefore, even if Cherenkov telescopes can potentially slew to the GRB sky position in few tens of seconds, these limitations may delay the actual beginning of the observations. At the time of writing, 6 GRBs have been detected in VHE, of which one short and 5 long (among them, 2 have a detection significance $3.5 < \sigma < 5$, while 4 have $\sigma > 5$) (MAGIC Collaboration et al., 2019; H. E. S. S. Collaboration et al., 2021; Abdalla et al., 2019; Acciari et al., 2021; Miceli and Nava, 2022). The VHE emission has been detected during the afterglow phase, between ∼100 s and ∼ 10^5 s and the luminosity at TeV energies is comparable with the X-ray luminosity, indicating an underlying process, possibly SSC from the forward shock, that produces a similar amount of energy in the two bands.
After ∼50 yr from their discovery, we are able to investigate the nature of these transients across an energy band of almost twenty orders of magnitudes in frequency, from radio band to VHE. A wide network of instruments is necessary to perform an efficient study of these sources, starting from wide-field X-ray and γ-ray instruments for the detection of the early emission, going to facilities able to promptly follow-up and characterise the full multi-wavelength emission.

2.3 The gravitational wave era

Binary systems of black holes (BHs) and neutron stars (NS) are GW emitters during the inspiral and merger phases[1]. The emission is detectable by current GW detectors LIGO (LIGO Scientific Collaboration et al., 2015),

[1] A detectable GW signal can be also produced during the collapse of a star, though the strength is so weak that it is within the reach of current detectors only if the explosion occurs inside our Galaxy or slightly farther away. GW emission from a stellar collapse is expected only if the explosion is asymmetric (e.g., Bartos et al. 2013), and/or the collapse remnant is a rapidly rotating neutron star, which deviates from the spherical symmetry (e.g., Corsi and Mészáros 2009)

Virgo (Acernese et al., 2015) and KAGRA (Aso et al., 2013) observing in the Hz-KHz band. In 2015 LIGO/Handford and LIGO/Livingstone started their first observing run and they detected the first GW from a binary BH coalescence on September 14th 2015 (Abbott et al., 2016), opening a new window on the Universe. Subsequently, the Virgo interferometer joined the network in 2017, with KAGRA starting observations in 2020. At the moment of the writing, after three observing runs, the network of interferometers collected 90 detections of CBMs (The LIGO Scientific Collaboration et al., 2021a), including 86 BH mergers, two BH-NS mergers and two NS-NS mergers (BNS).
The total number of detections is dominated by BBHs because the intensity of the GW signal scales with the total mass, and hence more massive systems can be detected up to larger distances. For the third observing run the detector ranges were, in the case of BNS mergers, $100 - 140$ Mpc for LIGO, $40 - 50$ Mpc for Virgo and < 1 Mpc for Kagra. A substantial improvement is expected for the next observing run (see Sec. 2.4).
While for BH-BH mergers no electromagnetic (EM) counterpart is expected (except for some exotic scenarios), binary mergers involving at least one NS can likely produce an EM emission which can be detected in all wavelengths (see next section for further details). Depending on the relativistic motion (mildly or ultra-relativistic) and radiative efficiency of the outflow, the EM signal associated to these sources can be detected up to cosmological distances. The search and the identification of the EM counterpart relies on the observations of a network of space-based and ground-based instruments. The success of the EM observational campaign strongly depends on a variety of factors, such as the uncertainty of the GW sky area, the capability of EM observatories to monitor large regions of the sky, the lifetime and brightness of the EM emission, as well as the ability to identify and remove transient contaminants. This last depends on the properties of the merging system, including the mass and spin of the components, the nature of the remnant, the amount of ejected mass, and the inclination of the orbital plane. Among the four GW detections which include at least one NS, three had no identification of the EM counterpart (mainly due to large uncertainties on the GW sky error box and properties of the system), while GW170817 represents so far the only firm association of a BNS merger with an EM transient. In the next section we present the wealth of information derived for this event, emphasising the deep consequences for our understanding of these phenomena. An exhaustive review of the scientific progress following GW170817 in terms of our knowledge about EM transients associated to GW sources can be found in Metzger, 2019, Branchesi

et al., 2020, Nakar, 2020, and Burns, 2020.

2.3.1 The revolution of GW170817

The most relevant event for the multi-messenger astrophysics is GW170817, the merger of two NS and the only event so far followed by the detection of the electromagnetic (EM) counterparts (Abbott et al., 2017c; Abbott et al., 2017b; Abbott et al., 2017d). The extensive effort carried out by the astronomical community allowed us to obtain a broad view of the EM signals produced by BNS mergers. The γ-ray flash detected by Fermi and Integral, together with all the follow-up observations from radio to X-ray, allowed us to infer fundamental information about the nature of the outflows produced during BNS mergers. For the first time, we had the confirmation that BNS mergers are able to produce short γ-ray bursts. The observation of the UV/optical/infrared emission $\sim$ 10 hours after the merger led to the conclusion that a kilonova accompanied the BNS merger (Coulter et al., 2017). The spectroscopic analysis confirmed that these events are ideal candidates for the nucleosynthesis of heavy elements through r-processes (Pian et al., 2017a; Smartt et al., 2017). The multi-wavelength analysis of the afterglow light curve and the measurement of the apparent super-luminal motion of the radio emission brought to the conclusion that in this event a relativistic, collimated and structured jet was launched (Hallinan et al., 2017; Troja et al., 2017; Ghirlanda et al., 2019a; Mooley et al., 2018b). Moreover the jet was observed off-axis, with an inclination angle of $15 - 30^{\circ}$ (e.g., Lazzati et al. 2018a; Lamb et al. 2019; Mooley et al. 2022), justifying the sub-luminous nature of the associated γ-ray burst.
In the following sections we retrace the steps, the observational results and the wealth of information that came with the multi-messenger detection of GW170817. All these insights will be the starting point to provide an exhaustive panoramic about the EM signals expected from CBMs. We will discuss the current strategies adopted for the EM follow-up of GW events, in order to understand how they can be improved for future detections.

Conclusions from the GW analysis

From the GW analysis of the chirp signal, it was inferred that the two NS have masses $m_1 \in (1.36, 2.26) M_{\odot}$ and $m_2 \in (0.86, 1.36) M_{\odot}$, for a total mass $2.82^{+0.47}_{-0.09} M_{\odot}$. These values slightly change with different priors on the NS spins. The inferred luminosity distance is $D_L = 40^{+8}_{-14}$ Mpc and the orbital plane axis was oriented at an angle $\theta_{JN} < 56^{\circ}$ with respect to the

BOX 2.1: REMNANTS OF BNS MERGERS

Depending on the final mass, the internal differential rotation and magnetic field structure, as well as on the EoS, several merger remnants are expected:

- A *stable* NS, whose collapse is prevented by the pressure induced by nuclear interactions alone. The maximum allowed mass (defined as M_{TOV}) is uniquely determined by the EoS.
- If $M > M_{TOV}$, a *supra-massive* meta-stable NS is formed, supported by internal rotation and hence by centrifugal forces. If the NS is also magnetised, the rotational energy is converted into spin-down luminosity, inducing a slowing-down process. As soon as the NS spin in no more large enough to support gravity, the NS collapses into a BH.
- A *hyper-massive* NS is formed if neither the nuclear pressure or the centrifugal forces are enough to contrast the gravity pull. Still, an additional support can be given by internal friction induced by differential rotation of the NS, where also the internal magnetic field can play a crucial role. Though, such configuration has a very limited life-time ($\sim 10 - 10^2$ of ms), beyond which the NS collapses in a BH.
- If the final mass is so high that none of the mechanisms reported above are enough to support gravity, the two merging NS directly collapse into a BH.

line of sight (Abbott et al., 2017c). The deviations of the late-inspiral signal from the two-points approximation allowed us to derive the properties of NS tidal deformability, directly connected to the equation of state (EoS). Though, no conclusive information can be extracted from GW data regarding the nature of the merger remnant. Indeed, the remnant depends not only on the final mass (see box 2.1). Even if we have no definitive answer about the merger remnant, further hints come from the modelling of the kilonova emission, whose luminosity depends on the ejected mass. Indicatively, a prompt collapse into a BH would produce a limited ejected mass, in contrast with the observed kilonova brightness. Therefore, the kilonova brightness suggests a long-lived NS as remnant (Li et al., 2018; Yu et al., 2018)

The GW analysis also provided a quite precise location of the source, with an uncertainty of ~ 30 deg^2. This information was promptly circulated in the astronomical community and exploited for the search of EM counterpart, as well as for the identification of the host galaxy.

Joint GW/γ-ray detection

Around 1.7 s after the merger *Fermi* (Goldstein et al., 2017a) and *Integral* (Savchenko et al., 2017) detected a short (2.0 ± 0.5 s) γ-ray flash, GRB170817A. The associated sky error region of *Fermi* is very wide (~ 1100 deg^2, 90% level of confidence) and compatible with the GW error region. The duration and the spectral properties of this GRB are compatible with the typical values of the class of short GRBs. On the other hand, the total isotropic energy of $(3.1 \pm 0.7) \times 10^{46}$ erg makes this event the dimmest GRB ever observed. A straightforward explanation is that GRB170817A has the standard energetics of short GRB population, but the jet is observed off-axis and therefore the photons are de-beamed, making the GRB subluminous. Another possibility is that the γ-ray flash is not produced by standard dissipation of the relativistic jet, but rather by the emission from a cocoon produced by the pressure of the jet on the surrounding material (e.g., Gottlieb et al. 2018a). Hence the origin of the γ-ray flash observed in coincidence with GW170817 is still debated. Though, arguments related to the compactness of a relativistic jet observed off-axis challenge the scenario in which γ-ray photons can escape a structured jet from a large inclination angle, giving more plausibility to the cocoon origin (Matsumoto et al., 2019). Independently of the origin of the γ-ray flash, however, further observations of the afterglow emission confirmed the existence of a relativistic jet, as shown later in the text. This fact highlights that, in absence of an EM follow up and extended multi-wavelength observations, we would have not been able to confirm that BNS mergers can produce relativistic jets and hence to confirm the BNS/short GRB association.
Thanks to the GW-GRB association and the small temporal delay between the two signals, tight constraints can be derived regarding the propagation of GWs and the validity of GR. In the specific, considering a plausible range of values for the time delay and the distance associated to the γ-ray flash, we can constrain: i) the difference between the GW speed and the speed of light, ii) the violation of Lorentz invariance and iii) the validity of the equivalence principle (Abbott et al., 2017b).

The search of the host galaxy and the detection of the kilonova emission

Roughly 5 hr after the merger, the LIGO/Virgo collaboration circulated the GW localisation, which was located in the southern hemisphere, and ground based telescopes started the search for the counterpart as soon as the sky region was visible above the horizon. Two search strategies where

BOX 2.2: GWS AS STANDARD SIRENS

With the simultaneous knowledge of the host galaxy redshift and the luminosity distance provided by GWs it is possible to perform cosmological studies (Schutz, 1986). Indeed, the luminosity distance depends on redshift only through cosmological parameters. For close-by events, such as GW170817, the tighter constraints can be derived for the Hubble constant. The work of Chen et al., 2018 shows that with $\sim$ 10 yr of observations of GWs from CBMs with LIGO/Virgo detectors, the Hubble constant can be constrained down to a precision of few %.

adopted: i) for wide-field telescopes, the entire GW sky region was surveyed, through multiple tiling ii) for small-FOV robotic telescopes a targeted search was adopted. In the latter case, the observations are restricted only to the galaxies contained in the GW uncertainty volume, following a prioritisation based on the parameters of the galaxy (such as luminosity, mass and type). After $\sim$10 hr, an optical transient was identified in the galaxy NGC 4993, located at a distance of 40 Mpc, compatible with the uncertainty given by GWs (Hjorth et al., 2017). The identification of the host galaxy provides the exact redshift of the source, giving the possibility to exploit BNS mergers as standard sirens (Chen et al., 2018) and perform cosmological studies (see box 2.2).

At the beginning, early data showed a featureless spectrum peaking in the UV band, whose shape was consistent with a single black body component. At this stage, it was not possible to exclude that the transient was associated to the early phase of a SNa explosion. Though, later observations showed a rapid decline of the light curve and a fast transition to a spectrum whose peak was progressively transiting towards the IR band. Moreover, high-resolution spectra showed the appearance of broad and complex absorption lines, not compatible with any SNa spectrum (Villar et al., 2017). The photometric and spectroscopic characterisation of this transient were the smoking gun which confirmed that the UV/Optical/IR emission was powered by the radio-active decay of heavy elements synthetised in the neutron-rich outflows launched after the BNS merger. In such conditions, a specific process, called rapid neutron capture, efficiently synthetizes heavy elements (Li and Paczyński, 1998; Metzger, 2019). In the case of GW170817, despite the difficulty in identifying the single elements, due to the high velocities of the ejected material and the many atomic levels of heavy elements, a first attempt brought to the identification of spectral lines associated to the recombination of Cs and Te (Smartt et al., 2017). A following more solid result came with the identification of Sr, confirming that the BNS mergers are ideal factories for r-processes (Watson et al., 2019). Such

BOX 2.3: TYPES OF EJECTA FROM CBMS

- **Dynamical ejecta**
  During the very last phases of the inspiral, the NS is strongly deformed by tidal forces and part of the star is ejected along the orbital plane, becoming gravitationally unbounded (Radice et al., 2018). The amount of ejected mass ($\sim 10^{-4} - 10^{-2} M_\odot$) and the velocity ($\sim$ 0.1c) depend on the EoS of the NS; for NS-BH mergers also the mass ratio and the BH spin play a major role because it determines the innermost stable circular orbit. Typical values of $Y_e < 0.2$ make this type of ejecta an ideal place for r-process nucleosynthesis.
  In case of BNS merger, at the moment of the contact between the two surfaces, a shock-induced ejecta is produce perpendicularly to the orbital plane (Sekiguchi et al., 2016). The temperature is higher compared to tidal ejecta, giving a higher abundance of electrons ($Y_e > 0.3$). Therefore no formation of heavy elements is expected and the low opacity corresponds to a bluer emission.
- **Disk-wind ejecta**
  The material that remains bound to the remnant circularizes and forms an accretion disk, which produces a large amount of neutrinos and it is possibly magnetised. The high neutrino density induces an over-pressure in the disk, which is inflated. If the neutrino flux is large enough, the exerted pressure generates vertical winds from the disk (Dessart et al., 2009). The neutron density in these outflows is suppressed by inverse beta decay, therefore the disk-winds contribute mainly to the blue component of the kilonova.
- **Viscous ejecta**
  Additional heating of the disk can be produced by viscous effects, mediated also by magnetic fields (Fernández and Metzger, 2013). A large fraction of the disk can be ejected (up to $10^{-2} M_\odot$), but at small velocity and with a large range of Y_e.

For an extensive review, see Metzger, 2019.

a result was also theoretically confirmed by Perego et al., 2022. The specific efficiency of nucleosynthesis processes mainly depends on the electron abundance Y_e (defined as the neutron-to-proton ratio), and the lower Y_e the more efficient is the process. For high values of Y_e ($Y_e \gtrsim 0.25$), the nucleosynthesis is poorly efficient and the outflows is Lanthanides-poor. A higher abundance of Lanthanides, in turn, increases the opacity of the medium, influencing therefore the peak time and the peak luminosity of the light curve. A summary of the several components of CBM ejecta and associated neutron abundance is reported in Box 2.3. Thanks to the accurate modelling of the kilonova light curve, as well as of the spectral features, it was possible to converge to the following conclusions:

- The initial UV/blue featureless emission was dominated by a Lanthanides-free outflow, moving at high speed ($v \sim 0.3$ c) and with

a mass of $\sim 0.03 M_\odot$ (Nicholl et al., 2017). Due to the reduced opacity, this component peaks around 1-2 days after the merger.

- The following emergence of the IR emission, appeared few days after the merger and lasted $\sim$ 10 days, is associated to a Lanthanides-rich outflow. The complexity of the spectral features points toward a variety of multiple outflows, with low-medium values of Y_e. Pian et al., 2017b identify two main components, one faster ($v \sim 0.2$ c) associated to the dynamical ejecta and one slower ($v \sim 0.05$ c) associated to disk-winds. The total ejected mass is estimated to be in the range $\sim 0.03 - 0.05 M_\odot$.

- Considering the total ejected mass, the abundance of Lanthanides synthetised and the estimated local rate of these events, it is possible to conclude that the abundance of heavy elements in the Solar System can be attributed to BNS mergers.

The origin of the afterglow emission

In the following days, after the detection of the kilonova, the observational campaign continued and the source was first detected 9 days after in X-rays by *Chandra* (Troja et al., 2017) and 16 days after in radio by JVLA (Hallinan et al., 2017). The observations continued in the next months and the source was detectable in optical by HST (Lyman et al., 2018), and in X-rays by XMM-Newton (D'Avanzo et al., 2018) and *Chandra* (Haggard et al., 2017). This multi-band emission was compatible with a single power law spectrum, indicating a non-thermal origin. After the first detection, the flux started to increase, following a quite shallow power law $F_\nu \propto t^{0.8}$, until $\sim$160 days after the merger the light curve reached its peak and started to decline as $t^{-2.2}$. Such behaviour cannot be interpreted in the scenario of a forward shock from a top-hat jet. Two main solutions were proposed for the interpretation of the afterglow: i) an ultra-relativistic collimated structured jet (Lazzati et al., 2018a; D'Avanzo et al., 2018) ii) a more isotropic and less energetic outflow produced by the interaction of an unsuccessful jet which drills trough the post-merger ejecta (Mooley et al., 2018a). In the latter case the shallow increase of the light curve would be explained with a stratification of the outflow, namely the ejected material is composed by several layers, each expanding at different velocity.
The final answer came with the measurement of the centroid motion (Mooley et al., 2018c) and the size evolution (Ghirlanda et al., 2019b) of the radio image through VLBI observations, which are in agreement only with the

obs. run	LIGO	Virgo	Kagra	LIGO/India
O4	160-190 Mpc	90-120 Mpc	25-130 Mpc	-
O5	330 Mpc	150-260 Mpc	$>$ 130 Mpc	330 Mpc

TABLE 2.1: Detection ranges in the next observing runs of the GW detectors, from Abbott et al., 2020a.

structured jet scenario. Several works tried to fit the multi-band afterglow light curve adopting a structured jet, finding that both Gaussian and power law profiles are consistent with the data (Lazzati et al., 2018a; Hajela et al., 2019; Wu and MacFadyen, 2019a; Resmi et al., 2018; Ryan et al., 2020a; Troja et al., 2019; Lamb et al., 2019; Hotokezaka et al., 2019; Nakar and Piran, 2021; Makhathini et al., 2021; Mooley et al., 2022). Independently on the assumed structure profile, works that model only the afterglow light curve prefer a quite larger value of viewing angle ($\theta_v \sim 20 - 35$ deg) compared to the values derived in works that also exploit the information of the centroid motion of the radio image ($\theta_v \sim 14 - 28$ deg). Moreover, precise astrometric measurement with the Hubble Space Telescope (Mooley et al., 2022) allowed to shrink the uncertainty on the viewing angle, giving $\theta_v \in [19 - 25]$ deg. At the moment of writing, the X-ray emission is still being monitored. A recent study (Hajela et al., 2022) claims a re-brightening of the X-ray light curve, not compatible with the standard decelerating blast wave (but see also Troja et al. 2022). One option could be the emergence of the afterglow emission associated to the kilonova ejecta. Further observations are required to confirm this scenario.

2.4 GW counterparts of merger-driven GRBs: prospects for near and far future

After the first three observing runs, two other phases of operations (O4 and O5) are planned by the LIGO/Virgo/KAGRA (LVK) collaboration, starting in 2023 and $\sim$mid 2026, respectively, with a substantial upgrade of the detector sensitivities. Later in this decade also an additional interferometer, LIGO-India, is expected to join (Bailes et al., 2021). The final target detection ranges for BNS mergers are shown in Tab. 2.1, which would correspond in the following rates for O4: 10^{+52}_{-10} BNS/yr and 1^{+91}_{-1} NS-BH/yr, with a median sky localisation of 33^{+5}_{-5} deg^2 and 50^{+8}_{-8} deg^2, respectively (Abbott et al., 2020b; Petrov et al., 2022).

Since so far almost all short GRBs (apart GRB 170817A) have been detected at $z > 0.1$ ($\sim$ 400 Mpc), the expected rate of joint GW/GRB detections in O4 is rather low. This is mostly due to the high level of beaming of short GRBs. An accurate estimate of the rate of joint GW/GRB detection has to take into account the uncertainty of the local rate of BNS mergers, the typical properties of the jet structure of short GRBs, as well as a reliable model which is able to reproduce the statistical observational properties of the short GRBs detected so far. The work of Patricelli et al., 2022 presents an exhaustive overview for the detection of γ-ray and X-ray signals from BNS observed in O4, considering a variety of high-energy satellites, such as Swift, Fermi, Integral and SVOM. Among all the telescopes, Fermi results the most efficient, thanks to the wide FOV, giving a number of joint GW/γ-ray detections in the range $[< 1 - 6]$/yr, where the main source of uncertainty is related first to the assumptions on the local BNS rate, and secondly to the assumptions on the jet structure. Notice that in this work the rates estimation is done assuming that all BNS give a successful jet. Comparable rates are derived by other works (Saleem et al., 2018b; Saleem et al., 2018a; Song et al., 2019; Saleem, 2020; Howell et al., 2019; Colombo et al., 2022). These expectations can further improve considering targeted sub-threshold searches (Goldstein et al., 2019), which consist in exploiting the GW information (sky area and merger time) to search for γ-ray signals that in the online search do not reach the detection threshold.
Apart from the detection of the γ-ray, the EM counterpart can be searched considering other energy bands. Regarding the detection of the X-ray emission from BNS mergers, two possibilities are available:

1. Swift-like operation: the short GRB is first detected in γ-rays by BAT and it is localised with arcmin precision. Subsequently XRT can slew in that direction. Once the source is localised with XRT, also other space based X-ray telescopes, such as XMM-Newton or Chandra, can point in the same direction.

2. No γ-ray emission is detected. In this case the GW sky error region is exploited to start a galaxy-targeted search (Evans et al., 2016; Singer et al., 2016; Klingler et al., 2019; Page et al., 2020). This strategy is based on a priority-based schedule for the observation of the galaxies contained in the GW uncertainty volume. The priority is chosen assigning to each galaxy a probability of hosting a BNS merger, where the probability may depend on the luminosity, dimension, age or morphological class of the galaxy (Artale et al., 2020). While this strategy is efficient to optimise the search of the EM counterpart, on the other

hand it is reliable only for the local Universe (below ~ 100 Mpc) where the galaxy catalogues are complete.

Another promising way to identify the EM counterpart of CBMs is the search of the UV/Optical/IR transient, associated to the kilonova emission (Mochkovitch et al., 2021; Frostig et al., 2022). The search consists in comparing images taken at different epochs with archival data, in order to discover new transients. The main challenge consists in covering in a short amount of time the entire GW sky map, since in the first hours the strong colour evolution of the kilonova allows us to distinguish it from other contaminants, such as supernova explosions. Therefore, to maximise the detection efficiency, it is preferable to catch the optical emission at the moment of its peak ($\sim$1-2 days for the blue/UV component, $\sim$ one week for the red component). A first strategy consists in exploiting wide field telescopes able to cover and tile with few exposures the GW sky map. A tiling prioritisation is necessary to maximise the probability of detecting the EM counterpart (Ghosh et al., 2016; Coughlin and Stubbs, 2016; Salafia et al., 2017). A second strategy is based on galaxy targeted search, as mentioned in the case of small FOV X-ray telescopes. While the X-ray emission from CMBs is collimated and the detection probability strongly depends on the viewing angle, the associated kilonova is more isotropic and the dependence on the viewing angle much more mild. Though, there are two main drawbacks:

1. the kilonova emission, even if more isotropic, is intrinsically fainter compared to emission at higher energies. This means that, given the typical kilonova luminosity, the detectability range of distance is limited to few hundreds of Mpc (e.g. Andreoni et al. 2022).

2. The identification of a kilonova is affected by the presence of numerous contaminants, namely artefacts and astrophysical transients that could have similar temporal and spectral properties. Large GW sky areas can potentially contain a wealth of contaminants which need to be discarded with an efficient classification strategy.

During O4, wide-FOV facilities will have a crucial role in the search of the UV/Optical/IR counterpart, such as ZTF (Anand, 2021), Pan-STARRS (Smartt, 2016) and DECam (Soares-Santos et al., 2017). Moreover, during the fifth GW observing run, 05, planned for 2025, the Vera Rubin Observatory (VRO) (Ivezic, 2008) is expected to be operative and join the effort for the search of GW optical counterparts. With its unprecedented sensitivity VRO will be able to deeply probe the entire volume accessible to GW instruments in O5.

Third generation GW detectors

The advent of third-generation (3G) GW observatories, such as the Einstein Telescope (ET) (Punturo et al. 2010) and Cosmic Explorer (CE) (Abbott et al. 2017a), will be a substantial leap forward for the detection of GW sources at cosmological distances. ET is an underground observatory, designed as three low and three high frequency interferometers nested in a triangular shape forming three 10 km arms. CE, instead, is an L-shaped surface interferometer 40 km in length. The exquisite improvement of sensitivity of about one order or magnitude with respect to current detectors, as well as the widening of the frequency band, will correspond to a unique scientific return. In the specific, 3G detectors will give us the possibility to:

1. systematically probe the coalescence of compact binaries, with a deep impact on multi-messenger astrophysics. The ET and CE are expected to detect $\sim 10^5$ BNS per year, reaching redshifts well above the star formation peak (Maggiore et al. 2020, Evans et al. 2021a); for optimally located and oriented systems, ET will be able to detect BNS up to $z \sim 5$, while CE will do so up to $z \sim 10$. For comparison, the current GW detectors are expected to reach $z \sim 0.2$, even considering new upgrades planned for the fifth run of observations in 2025 (Abbott et al. 2020a).

2. Accurately reconstruct the merger rate of binary systems up to high redshifts. This enables us to disentangle between different channels of formation, as well as to reduce the systematic uncertainties on the prescriptions of population synthesis models.

3. Investigate the population of primordial BHs, whose existence is still widely debated. Their detection would shed new light on the nature of dark matter, with deep consequences on cosmological models. In the hypothesis of a population $\sim 10^6$ primordial BHs located at $z > 10$, ET will be able to recover $\sim 10^3$ detections during one year of observation.

4. Probe the physics of curved space-time in the vicinity of the event horizon, thanks to the high SNR signals in correspondence of the ringdown of BH mergers. This translates not only in testing the validity of general relativity to an unprecedented level of precision, but also to have access to exotic phenomena, such as GW echoes.

5. Extract information about nuclear physics and equation of state (EoS) of NS. From the precise estimation of the NS tidal deformability, we

can derive tight constraints on the mass-radius relation, possibly excluding all the EoS which do not satisfy such relation.

6. Perform precision cosmology, with the use of both bright and dark sirens. This includes the measurement of the Hubble constant, probe of the dark energy equation of state and modified gravity propagation across cosmological distances.

The ET, in particular, is very promising for multi-messenger purposes. It will be capable of detecting BNSs well before the merger, following their inspiral not only for minutes but also for several hours in the case of close-by events. This enables us to use the Earth rotation to determine the sky localisation even when ET is operating as a single detector (Chan et al., 2018; Grimm and Harms, 2020; Nitz and Dal Canton, 2021; Li et al., 2022). These authors found that a fraction of a few percents of BNS detected by ET will have a sky localisation uncertainty $\Delta\Omega < 100$ deg^2. This fraction increases to a few tens of percents when ET is operating in network with CE. Considering a network of three 3G detectors located in Europe, USA, and Australia a few tens of percents of detected BNS will be localised within 10 deg^2 and almost the totality within 100 deg^2 (Li et al. 2022, Borhanian and Sathyaprakash 2022, Mills et al. 2018). A detailed study of performance metrics of several configurations of network including CE, ET, and the second generation detectors and their upgrade, are given in Borhanian and Sathyaprakash 2022; Ronchini et al. 2022a; Iacovelli et al. 2022. Another proposed GW observatory to be mentioned is the Neutron star Extreme Matter Observatory (NEMO, Ackley et al., 2020), a 4-km detector whose sensitivity at high frequencies will be relevant for the investigation of neutron star physics and for multimessenger purposes (Sarin and Lasky, 2022). To maximise the scientific return of the next generation GW detectors in the multi-messenger context it is of paramount importance to evaluate the expected rate of joint detections, to identify the necessary instrumental requirements and optimal observation strategy. This was largely explored in my thesis work and will be described in Chapter 6.

Chapter 3

Prompt and afterglow emission modelling

In this chapter we review the basic processes associated with the dissipation of the internal energy of the GRB relativistic jets as well as their interaction with the circum-burst medium. Particular attention is dedicated to the role played by the jet structure, both for prompt and afterglow emission, as well as in the context of GRB luminosity function and population studies.

3.1 Prompt emission of $\gamma-$ray bursts

The prompt phase of GRBs is defined as high-energy emission (keV-MeV range), whose duration is characterised by the quantity t_{90}, defined in such a way that

$$\Phi_{90} = \int_{t_0}^{t_{90}} F_d dt = 90\% \Phi_{tot},$$

where F_d is the flux measured by the detector and Φ_{tot} is the total energy fluence of the GRB. Given this definition, it is clear that the duration of the GRB is not an intrinsic and absolute quantity, but it depends on the sensitivity and the energy band of the instrument. The light curve is highly irregular and it is composed by the superposition of several pulses. The shape of single pulses is usually well fitted by a fast-rise followed by an exponential decay (Norris et al., 1996). A faction of GRBs (3-20%) presents an additional emission before the initial trigger, known as *precursor* (Koshut et al., 1995; Lyutikov and Usov, 2000; Hu et al., 2014). A proxy of the total energy released during the prompt emission is called the *isotropic* energy $E_{\rm iso}$ and it is defined as

$$E_{\rm iso} = \frac{4\pi D_L^2 k \Phi}{1+z},$$

where k is the k-correction to account for redshift of the energy spectrum and the fluence Φ is typically taken in the rest frame energy range $1 - 10^4$ keV, in order to give a bolometric estimate of the energy released. The typical values are in the range $[10^{49} - 10^{55}]$ erg, with a median value $\sim 10^{52}$ erg for long GRBs (Ghirlanda and Salvaterra, 2022) and $\sim 10^{51}$ erg for the short ones (Ghirlanda et al., 2016a). The adjective isotropic is used to specify that this energy estimate is done under the assumption that the source emits isotropically. If instead the emission is beamed in a cone with a solid angle aperture $\Delta\Omega$, then the true energy released is $E_{\rm iso} \times \Delta\Omega/4\pi$.
When the prompt emission light curve is analysed in different energy bands, the width w of the pulses results to be wider at lower frequencies, following a behaviour like

$$w(E) \propto E^{-s}, s > 0.$$

with typical values of s in the range $[0.3 - 0.4]$ (Norris et al., 2005). Moreover, softer photons arrive later to the observer, causing a spectral lag which is more evident in long GRBs, but not significant in the short ones (Norris and Bonnell, 2006). The spectral lag, instead, does not hold for GeV emission (e.g., Abdo et al. 2009), which usually appears later, possibly indicating a different origin with respect to the keV-MeV emission. The energy dependence of the pulse width together with the evidence of spectral lag can be interpreted as due to a peaked spectrum whose peak energy evolves in time towards lower values.
When the energy band of the instrument is wide enough, the spectrum is well fitted by the *Band* function (Band et al., 1993):

$$N(E) = \begin{cases} AE^{\alpha} \exp\left(-\frac{E}{E_0}\right), & E < (\alpha - \beta)E_0 \\ A\left[(\alpha - \beta)E_0\right]^{\alpha-\beta} \exp(\beta - \alpha)E^{\beta}, & E \geq (\alpha - \beta)E_0 \end{cases}$$

and the peak energy is $E_p = (2 + \alpha)E_0$. The values of the low- and high-energy photon indices are $\alpha \sim -1$ and $\beta \sim -2$ (Preece et al., 2000). Though, when multiple energy bands are considered (from optical to MeV), the overall spectrum shows significant deviations from the Band function and the addition of an additional spectral break is required (Oganesyan, 2017; Oganesyan, 2018; Oganesyan, 2019; Ravasio, 2018; Ravasio, 2019). These recent studies confirm that the presence of an additional break corroborated the validity of synchrotron as dominant process in the prompt emission (see also Burgess 2020).
The energetic and spectral properties of GRB emission are characterised by

the following empirical correlations:

- *Amati relation*: $\hat{E}_p \propto E_{iso}^{p_a}$ (Amati et al., 2002)
- *Yonetoku relation*: $\hat{E}_p \propto L_{p,iso}^{p_y}$ (Yonetoku et al., 2004)
- *Ghirlanda relation*: $\hat{E}_p \propto E_{\gamma}^{p_g}$ (Ghirlanda et al., 2004)

where $\hat{E}_p = (1+z)E_p$ is the rest frame peak energy, $L_{p,iso}$ is the isotropic peak luminosity, and $E_\gamma = E_{\rm iso} \times \Delta\Omega/4\pi$ is the beaming corrected isotropic energy. The typical values are $p_a \sim 1$, $p_y \sim 0.5$ and $p_g \sim 0.7$. The Ghirlanda relation can be defined only for a limited sample of GRBs where an estimate of the beaming angle is available and results be to less scattered than the Amati relation. Both long and short classes follow these correlations, but the short ones are shifted to higher values of peak energy.

3.1.1 The theoretical foundations

The current standard interpretation of prompt emission invokes the presence of a ultra-relativistic collimated outflow which moves towards the observer and dissipates its internal energy in the form of γ-ray radiation. One of the strongest arguments supporting the relativistic motion is the compactness problem. Since we observe photons above the pair production threshold, the emission region should be optically transparent. In the hypothesis of a non relativistic motion, the dimension of the emission site is $R \sim c\delta t$, with δt the temporal variability. The resulting pair production opacity would be

$$\tau_{\gamma\gamma} \sim \sigma_T n R \gg 1,$$

where the photon density n can be derived from the typical GRB energetics. Therefore no radiation should escape from the source, unless it moves at relativistic speeds. In this case two combining effects can solve the compactness problem:

- the pair production threshold is decreased by a factor Γ^2, since $\epsilon_1\epsilon_2 > m_e c^2$ holds in the comoving frame,
- the dimension of the emitting region as well is reduced by a factor Γ^2 in the observer frame,

where Γ is the bulk Lorentz factor of the outflow. In order to accelerate matter to relativistic speed, a central powerful engine is required. Given

the small temporal variability, stellar compact objects are usually invoked, in particular BH and NS. In the case of a BH, the gravitational energy of the accreting material is converted to kinetic energy of the outflow (Blandford and Znajek, 1977). The presence of a magnetic field tangled with the accretion disk allows the extraction of rotational energy from the BH, which is spent to accelerate the relativistic jet. For a NS as central engine, similarly, a strong magnetic field could play a major role in powering and collimating the jet, even if the required conditions are still under debate (e.g. see Ciolfi 2020 for an exhaustive review). Depending on the initial physical conditions at the moment of the jet launching, the plasma can be either weakly or highly magnetised. In the former case the outflow is matter dominated, in the second it is Poynting-flux dominated. The magnetisation is defined as

$$\sigma = \frac{B_0^2}{4\pi\eta\rho c^2},$$

where B_0 is the initial magnetic field strength, η the energy per baryon and ρ the matter density. In the limit of $\sigma \ll 1$, the outflow follows the evolution of the so called *fireball* scenario. The concept of fireball was initially introduced by Goodman, 1986 and Paczynski, 1986, where only a mixture of $e^{\pm}$ pairs and photons was considered, without any baryon loading. The baryon load was subsequently introduced by Shemi and Piran, 1990. At the beginning the fireball is confined into a region of dimension R_0 and due to the initial high temperature the radiation pressure dominates the expansion of the gas. Only later the fireball becomes optically thin to pair annihilation and photons can leave. The expected spectrum is therefore purely thermal, which is not consistent with observational evidences. If a rather small baryon load is included in the initial state of the fireball, part of the thermal energy is converted to the bulk kinetic energy. As soon as the radiation energy density is sub-dominant with respect to the matter density, the fireball enters the *coasting* phase, expanding with a constant bulk Lorentz factor Γ. In order to explain the non-thermal nature of the GRB prompt spectra, a physical process is necessary to convert the kinetic energy of the jet into internal energy of the paricles. The presence of relativistic shocks and/or regions of magnetic reconnections are viable mechanism to energize particles. One of the most widely accepted scenario invokes the launching of multiples shells of material from the central engine, which is expected in the case of a central engine with erratic activity. For instance, in the case of a highly-accreting BH, the outflow episodes would reflect the rate of accretion, which is expected to be non stationary and highly variable. The

variable ejection mass rate is translated in the observed high variability of the $\gamma-$ray emission. If the ejected shells move with different speeds, the faster one will catch the slower one, producing a shock region where particles can be accelerated. This scenario is known as *internal shock model* (Rees and Meszaros, 1994). After the two shells merge, a single resulting shell will move with a final speed such that the conditions of energy and momentum conservations are satisfied. Calling m_1, m_2 and Γ_1, Γ_2 the mass and the Lorentz factor of the two shells, the energy conversion efficiency (i.e. $E_{final}/(E_1+E_2)$) is:

$$\eta_{IS} = 1 - \frac{m_1 + m_2}{\sqrt{m_1^2 + m_2^2 + m_1 m_2 \left(\frac{\Gamma_2}{\Gamma_1} + \frac{\Gamma_1}{\Gamma_2}\right)}}.$$

For equal mass shells the efficiency reaches its maximum, but usually it cannot be larger than $\sim 1 - 10\%$.
In the presence of relativistic shocks, particles are expected to be accelerated, under the effect of mechanisms such as diffuse shock acceleration. Alternatively, in jet dominated by magnetic energy, the magnetic field structure can assume particular configurations that can favour the phenomenon of magnetic reconnection and acceleration of plasmoids. The acceleration mechanism modifies the energy distribution of particles, which initially corresponds to a Maxwellian, through the formation of a high-energy tail, usually close to a power law, i.e. in the form:

$$N(E) = \frac{dN}{dE} \propto E^{-p}.$$

The most updated particle-in-cell simulations of relativistic shocks predict an average value of $p \sim 2.2$ (Sironi et al., 2015). Thanks to its radiative efficiency, one of the most plausible radiative processes through which particles can cool is the synchrotron emission. The synchrotron losses tend to modify the particle energy distribution and hence the overall spectral shape changes in time. More in the specific, we can define an energy $\gamma_c(t)$ which corresponds to the energy of the particle which loses most of its energy during an interval of time t. Knowing the synchrotron power, we have:

$$\gamma_c(t) \simeq \frac{6\pi m_e c}{\sigma_T B^2 t}$$

in the limit of $\gamma_c \gg 1$ and valid in the assumption of a time independent magnetic field. This means that, for a fixed time t, all the particles with energy $\gamma > \gamma_c$ have lost all their initial energy. In order to understand how the particle distribution evolves in time due to energy losses, we have to solve the continuity equation, which reads as:

$$\frac{\partial N}{\partial t} = -\frac{\partial}{\partial \gamma}[\dot{\gamma} N] + Q(\gamma, t),$$

where N is the particle density and Q is the injection rate,[1] which corresponds to:

$$Q(\gamma, t) \propto \gamma^{-p}, \quad \gamma_m < \gamma < \gamma_M, \quad 0 < t < \delta t$$

If the duration of injection δt is much smaller than all the other time scales of the system, then the resulting synchrotron spectral shape can be derived in two regimes:

- *slow cooling:* $\gamma_c(t) > \gamma_m$

$$F_\nu \propto \begin{cases} \nu^{-1/2}, & \nu_c < \nu < \nu_m \\ \nu^{-p/2}, & \nu_c < \nu_m < \nu \end{cases} \tag{3.1}$$

- *fast cooling:* $\gamma_c(t) < \gamma_m$

$$F_\nu \propto \begin{cases} \nu^{-(p-1)/2}, & \nu_m < \nu < \nu_c \\ \nu^{-p/2}, & \nu_m < \nu_c < \nu \end{cases} \tag{3.2}$$

where ν_m and ν_c are the frequencies corresponding to the energies γ_m and γ_c, respectively (for a given γ, the corresponding synchrotron frequency is $\nu(\gamma) = \frac{3}{4\pi}\gamma^2 \frac{qB}{mc}$, with q the charge of the particle). In both regimes, $F_\nu \propto \nu^{1/3}$ for $\nu < \min(\nu_m, \nu_c)$, which is the typical low-energy slope for synchrotron spectrum from a single particle. The spectral shape reported above is valid in the limit of a randomly oriented magnetic field and for an isotropic motion of particles in the comoving frame. Modifications to this standard picture are expected if the magnetic field is dominated by small scale perturbations, as in the case of magnetic reconnections (e.g., Goto and Asano 2022).

[1] The diffusion term is neglected, since in GRB outflows diffusion is expected to occur on time scales much larger than cooling time scales. In addition, the term associated to losses due to escape from the system is neglected.

As mentioned before, recent works revealed that a single broken power law is not sufficient to fit the multi-band emission during the prompt phase. An additional spectral break is necessary and the overall spectral shape is consistent with a single synchrotron emission in a marginal fast cooling regime. This means that the particles responsible for the prompt emission are not able to cool efficiently. Though, considering the typical values of GRB luminosity, dissipation radius and magnetic field, electrons are expected to cool on a time scale much smaller than the dynamical time scale of the jet (Ghisellini et al., 2000). Therefore a synchrotron radiation in fast cooling regime would be expected, against the observational evidence. There are several solutions that have been proposed to solve this inconsistency, such as reheating processes (Asano et al., 2009), decaying magnetic field (Uhm and Zhang, 2014), or hadronic scenarios (Asano and Mészáros, 2012; Murase et al., 2012). Moreover, recently Ghisellini, 2020 proposed that the fast cooling issue can be attenuated assuming that synchrotron emission from protons, instead of electrons, dominates the prompt emission. Being more massive, protons cool more slowly compared to electrons, in agreement with the observational evidence of a synchrotron spectrum in marginal fast cooling regime (see also Daigne et al. 2011; Beniamini et al. 2018).
As exhaustively summarised by Panaitescu and Vestrand, 2022, the low-energy spectrum of GRB prompt emission can deviate from the standard picture reported in eq. 3.1 and 3.2 introducing a temporal evolution of the particle injection and the magnetic field decay. In the case of particles accelerated by a relativistic shock, the injection time scale is realistically not negligible and it is given by life-time of the shock plus and the time needed by the particle to cross the shock front multiple times. Moreover, if the magnetic field is originated by turbulence and/or stream instabilities in the downstream shock region, its intensity is expected to decrease in time as the shock expands and the downstream region enlarges. From eq. 3.1 and 3.2, the hardest low-energy spectral index is $\beta_{LE} = \min(-1/2, -(p-1)/2)$. If we define t_B the typical variation timescale for the magnetic field and t_{rad} the cooling time scale, then we have:

- for $t_B \gg t_{rad}$ and for dominant adiabatic cooling,

$$\beta_{LE} = \begin{cases} 1/3, & y < 5/9 \\ 3/4(1-y), & 5/9 < y < 2 \\ -3/4, & y > 2 \end{cases},$$

  where the injection rate scales with time as t^{-y}

- for $t_B \in (1, 10) t_{rad}$, $\beta_{LE} \in [-1/2, 1/3]$ if synchrotron is the dominant cooling process, $\beta_{LE} \in [-3/4, 1/3]$ if adiabatic cooling is dominant. The specific value of β_{LE} depends on the injection rate.

In all the cases, the largest spectral index is $\beta_{LE} = 1/3$ and an observed value harder than this limit would be in contrast with this framework.

3.2 Afterglow emission

After the jet dissipates part of its internal energy during the prompt emission phase, most of the energy is still in the bulk motion. As the outflow expands in the circum-burst medium a forward shock forms, which starts to significantly decelerate as soon as its mass is comparable to the swept-up mass (Mészáros and Rees, 1997; Rhoads, 1999). Simultaneously to the formation of the forward shock, also a reverse shock starts to cross the jet, increasing its internal energy. Particles are accelerated in the downstream region and are expected to cool and radiate mainly through synchrotron emission. Depending of the relative ratio between the magnetic field density and the photon density, also cooling through inverse Compton can play a relevant role. The combined action of particle cooling and jet deceleration produce a long-lasting multi-band emission known as *afterglow* phase. In order to derive the expected radiative output from the external shock, including the spectral and the temporal properties, the knowledge of the jet dynamics is necessary.

3.2.1 Dynamics of the blast wave and related multi-wavelength emission

From first principles, the jet dynamical evolution can be derived imposing energy conservation, namely in the approximation that only a negligible fraction of the kinetic energy of the jet is radiated away (Mészáros and Rees, 1997; Sari et al., 1998b). Under this assumption and considering a generic circum-burst medium whose density radial profile goes as $n \propto r^{-k}$, the temporal evolution of the bulk Lorentz factor and the shock radius is:

$$\Gamma \propto t^{\frac{k-3}{8-2k}}, \quad r \propto t^{\frac{1}{4-k}}.$$

The analogous temporal evolution can be derived in case of highly-radiative blast wave imposing momentum conservation, instead of energy

conservation. These simple scaling relations can be further extended including possible energy injection into the blast wave, due to late-time activity of the central engine (Zhang and Mészáros, 2001b). Considering an injection luminosity

$$L_{inj}(t) \sim t^{-q},$$

for $q > 1$ the injected energy is asymptotically constant in time, giving negligible contribution to the blast wave evolution, while for $q < 1$ the injected energy increases with time as

$$E_{inj} \propto \int L_{inj}(t)dt \sim t^{1-q}.$$

As soon as the injected energy is comparable to the blast wave energy, the asymptotic temporal evolution is given by:

$$\Gamma \propto t^{\frac{k-q-2}{8-2k}}, \quad r \propto t^{\frac{2-q}{4-k}}.$$

The original discovery of the blast-wave evolution is due to the self-similar solution provided by Blandford and McKee, 1976. A more detailed solution is given by Nava et al., 2013, where terms related to radiative losses and adiabatic losses are taken into account. The inclusion of all these ingredients leads to a set of coupled differential equations in the form:

$$\begin{cases} \frac{d\Gamma}{dr} = f(\Gamma, \rho, U) \\ \\ \frac{dU}{dr} = g(\Gamma, \rho, U) \end{cases},$$

where U is the total internal energy, ρ is the ISM density and r is the radial coordinate. Once the initial conditions are set up, the temporal evolution of $\Gamma(t)$ is univocally determined. One information which needs to be specified is the contribution due to radiative losses, which impact the evolution of the internal energy. This term depends on the microphysical properties of the forward shock, which can be summarized by two terms:

- ϵ_e which is the fraction of energy of the blast wave that goes into non-thermal electrons
- ϵ_b which is the fraction of energy of the blast wave that goes into the magnetic field energy density

The interplay of these two factors determines the temporal evolution of the particle energy distribution and hence the evolution of the total internal energy, as well.
The blast wave dynamics determines the observational properties of the afterglow emission, which is given by the dominant radiative process. In the standard scenario, synchrotron emission is the leading process for afterglow and its spectral and temporal evolution can be derived knowing the evolution of the characteristic frequencies ν_m and ν_c, as well as the flux density at $\nu^* = \min(\nu_m, \nu_c)$. The basic scaling relations are given by:

$$\nu_m \propto \Gamma \gamma_m^2 B,$$
$$\nu_c \propto \Gamma \gamma_c^2 B,$$
$$F_{\nu,\max} \propto N_{\rm tot} P_{\nu,\max},$$

where $N_{\rm tot}$ is the total number of emitting particles and $P_{\nu,\max}$ is the synchrotron power emitted by a particle with $\gamma = \min(\gamma_m, \gamma_c)$. Therefore, once the dynamics of the jet and the evolution of magnetic field are known, the synchrotron emission can be derived.
So far, the treatment adopted considers the blast wave isotropic but it remains valid also in the case of a collimated outflow, provided that the beaming factor $1/\Gamma(t) < \theta_j$, where θ_j is the aperture angle of the jet cone (Rhoads, 1999). Instead, as soon as $1/\Gamma(t_b) = \theta_j$ the observed flux is affected by the non-isotropy of the blast wave. The observational effect is the appearance of a jet break at the time t_b. Since this is a purely geometric effect, the jet break is achromatic, namely occurs at the same time independently on the observed energy band. The evidence of jet breaks in afterglow light curve is one of the smoking guns to prove that GRB outflows are highly collimated.
The final appearance of afterglow emission can deviate from what described so far if further effects are included, such as:

1. the contribution from equal arrival time surfaces (Huang et al., 2007). Such effect is not negligible if the emitting region is not much smaller than the emission radius. In this case, different fluid elements located at different polar angles and emitting at different times (in the source frame) contribute simultaneously to the total flux received by the observer at given time.

2. the inclination between the line of sight and the symmetry axis of the jet. Indicatively, the larger the inclination angle, the fainter the afterglow emission and the later the peak time of the light curve.

3. the jet structure. In the Blandford-McKee self-similar solution no dependence on the polar angle is included and therefore the shock surface is approximated as a spherical shell. As explained later, deviations from the spherical approximation are expected, introducing a dependence of the bulk motion on the angle (Rossi et al., 2002a). Moreover the jet structure can introduce also an angular dependence of the microphysical shock parameters, such as the acceleration and/or radiation efficiency.

3.2.2 X-ray afterglow light curve: open issues in interpreting steep decay, flares and plateau

The transition between the end of the prompt emission and the onset of the afterglow is often characterised by a steep decline of the light curve, well observed in the X-ray band (Tagliaferri, 2005; Nousek, 2006; O'Brien et al., 2006; Zhang et al., 2006b; Zhang et al., 2007). The discovery of this feature was possible thanks to the fast re-pointing capabilities of *Swift*-XRT. However, since the prompt emission, depending on the GRB duration, can stop well before the beginning of the XRT observation, the steep decay can be missed. The temporal decline is well fitted by a single power law, with a temporal slope $\alpha > 3$. Such a steep decline cannot be reconciled with an external shock origin, since it would require an unphysically fast deceleration of the fireball. Moreover, since the steep decay is smoothly connected to the end of the last prompt emission pulse, this phase is interpreted as the *X-ray tail* of the prompt emission. Therefore its origin is attributed to an internal jet dissipation, rather than related to the external shock. The rapid decline can be either due to the high-latitude emission (HLE) effect, related to the geometrical curvature of jet (Kumar and Panaitescu, 2000), or to an intrinsic decaying activity of the central engine (Barniol Duran and Kumar, 2009; Fan and Wei, 2005).
The X-ray tail of the prompt emission is also usually characterised by a continuous spectral softening (Zhang et al., 2007). Though, its origins is still under discussion, since it could be due to a pure HLE effect or a combination of HLE plus an intrinsic spectral evolution in the jet comoving frame, related to the cooling of the particles after the end of prompt emission. Therefore, a systematic study of the relation between the flux decay and the spectral evolution is necessary to shed light on the late phases of the prompt emission, the origin of dissipation and cooling processes, as well as

the nature of the emitting particles. Part of this thesis work has been dedicated to this investigation (see Chapter 4).
The standard blast wave deceleration produces a smooth decline of the X-ray light curve, though very often the X-ray light curve presents sudden peaks also known as *X-ray flares* (Chincarini et al., 2007; Burrows et al., 2005; Chincarini et al., 2010). Most of them happen $10^2 - 10^3$ s after the trigger and the emitted energy is few % of the total prompt emission fluence. They are much softer than usual prompt emission pulses and they are characterised by a hard-to-soft spectral evolution. Due to their rapid rise and fall, their origin cannot be related to the external shock, while it is commonly thought that they are connected to the late time accretion episodes on the central engine.
Finally, another intriguing feature of the X-ray light curve is the presence of a shallow decay phase, which can last $\sim 10^2 - 10^4$ s, or even more in some extreme cases. The temporal decay slope is $\alpha \lesssim 0.7$. When $\alpha \sim 0$ this phase is better known as *X-ray plateau* (Zhang et al., 2007). When compared to the expected temporal slopes from standard blast wave deceleration, the plateau cannot be explained within this scenario, unless an energy injection is assumed[2]. In this last case, the temporal evolution of the light curve should be achromatic, namely independent on the observed band. Though, a large fraction of plateaus shows a chromatic behaviour when both X-ray and optical data are taken into account, posing a challenge to energy injection models. Additionally, there are few cases of shallow X-ray phases followed by a very steep ($\alpha \gg 2$) temporal decline. Since the angular time scale $t_a \sim R/2c\Gamma^2$ represents the minimum time scale over which the light curve can substantially vary, such steep declines have to be attributed to an internal origin, for instance due to the internal dissipation in a wind powered by a magnetar spin down. In this case the plateau is defined *internal*.
As explained in detail in Sec. 3.3.1, alternative models can explain the plateau phase as a direct consequence of the jet structure. The origin could be either connected to the prompt emission from a structured jet (Oganesyan, 2020; Ascenzi et al., 2020b) or by the afterglow emission from a structured jet viewed slightly off-axis (Beniamini et al., 2020a). Therefore, the origin of the plateau phase is still matter of discussion. A detailed investigation of its origin can give information about the connection with the central engine and its late-time activity. My thesis work was in part devoted to understand the origin of the plateau phase of GRBs. Details are

[2]Notice that the forward shock can still produce a plateau phase in the case of a wind medium and low values of Γ

given in Chapter 5.

3.3 The jet structure

As mentioned in the previous sections, a series of compelling evidences, both observational and theoretical, show that the GRB outflow should be ultra-relativistic and highly collimated. As a zero-order approximation, the jet geometry is close to a bi-conical outflow with an aperture angle θ_c, known also as *top-hat* jet. The value of θ_c can be inferred by the observation of the jet-break in the afterglow light curve, but its identification is usually not straightforward. Hence, only for a limited number of cases, the jet aperture can be reliably estimated. On average long GRBs show larger θ_c than short GRBs (Frail et al., 2001; Fong et al., 2015a). The knowledge of θ_c is also fundamental to estimate the true energy content E_j of the jet, which is related to the isotropic energy as follows:

$$E_j = (1 - \cos(\theta_c))E_{\rm iso}.$$

More in general, the jet can deviate from a simple top-hat approximation, with a structure described by a more complex function which specifies the angular energy distribution:

$$\frac{dE}{d\Omega} = \mathcal{E}(\theta, \phi),$$

where θ and ϕ are the polar and azimuth angles, respectively (Rossi et al., 2002a; Kumar and Granot, 2003; Lazzati and Begelman, 2005) . Due to typical cylindrical symmetry of the processes responsible for the jet launch, the dependency on ϕ is neglected (though, see Lamb et al. 2022a). In turn, the energy angular structure is translated in a dynamical structure (i.e. $\Gamma \rightarrow \Gamma(\theta)$) and in a geometrical structure (i.e. $R \rightarrow R(\theta)$), which depend also on time. With this definition the total jet energy is:

$$E_j = \int \mathcal{E}(\theta) d\Omega.$$

A structured jet can be always characterised by:

- a jet core ($\theta < \theta_c$), where the jet is indistinguishable from a spherical, uniformly expanding outflow;

- an off-core component ($\theta > \theta_c$), also knows as *jet wings*. Two commonly adopted profiles are the Gaussian ($\mathcal{E}(\theta) \propto \exp\{[-\theta^2]\}$) and the power law profile ($\mathcal{E}(\theta) \propto \theta^{-k}$).

This is translated in:

$$\mathcal{E}(\theta) = \begin{cases} \sim \mathcal{E}_0, & \theta < \theta_c \\ \sim \mathcal{E}_0 \cdot f_\varepsilon(\theta), & \theta > \theta_c \end{cases}$$

and similarly for Γ:

$$\Gamma(\theta) = \begin{cases} \sim \Gamma_0, & \theta < \theta_c \\ \sim \Gamma_0 \cdot f_\Gamma(\theta), & \theta > \theta_c \end{cases},$$

where $f_\varepsilon(\theta)$ not necessarily has the same functional behavior of $f_\Gamma(\theta)$.

The origin of the jet structure is attributed to a combination of the specific launching mechanism, the collimation process and the interaction between the jet and the circum-burst medium (see Salafia and Ghirlanda, 2022 for a comprehensive review). These processes occur at different spatial and temporal scales, and it is still under debate which is the dominant one for the final determination of the structure. Once the jet is launched, it propagates through a dense, possibly baryon-polluted, environment. For collapsar-driven GRBs, this medium is represented by the outer layers of the star envelope, while for merger-driven GRBs by the merger ejecta. In both cases, as soon as the jet meets the dense medium a first shock is formed, but radiation still cannot escape due to high opacity, if the shock occurs below the photospheric radius. During the jet propagation, transverse pressure waves propagates towards the external sides of the jet head, inflating them and creating a self-sustained cylindrical cocoon which helps the jet to keep the collimation. Therefore, even if originally the jet is launched with an aperture angle θ_a, it is re-collimated thanks to the cocoon pressure, which transforms a conical outflow into a more cylindrical motion.
The jet keeps propagating and if it is not successful in drilling through the envelope/ejecta, no EM emission can escape and the jet is defined *chocked*. If instead it is energetic enough, it reaches the outer layers of the envelope/ejecta. Due to the abrupt decrease of density, the jet has no more material that slows down its propagation and undergoes to a rapid expansion. This transition phase is known as *jet breakout* or *shock breakout* (SBO), during which the jet becomes transparent and radiation is released (Nakar and Piran, 2017a). In the case of merger-driven GRBs, the success of the jet in breaking out depends also on the time delay between the merger and

the jet launch, possibly due to the time needed for the remnant to collapse into a BH. The larger the delay, the longer the time the ejecta have to expand and decrease in density, facilitating the propagation of the jet. On the other hand, neutrino-driven winds produced after the merger can significantly pollute the ejecta, disfavouring the jet propagation (Nativi et al., 2022; Just et al., 2016). The contribution of these winds is more severe for long-lasting hyper-massive NS (Murguia-Berthier et al., 2014). Therefore the final success of the jet is given by a trade-off between a not too high baryon-pollution, which does not obstacles its forward propagation, and a quite large density which ensures a self-sustained confinement and hence collimation. Indeed, in the case of NS-BH mergers, where the dynamical ejecta are mostly confined along the orbital plane, the collimation can be hardly achieved, unless neutrino- and magnetic-driven winds are powerful enough (Nagakura et al., 2014).

EM signatures from the cocoon

As explained by Nakar and Piran, 2017a, the jet breakout produces two cocoon components: 1) a shocked jet which expands sideways and 2) a shocked envelope/ejecta at wider angles. Similar energies are deposited in both components, but the shocked jet is more diluted, hence a higher energy/baryon would lead to a faster expansion. The shocked jet is expected to produce a photospheric emission similar to a baryon-loaded fireball, but less energetic and collimated with respect to the jet head. The expected emission peaks in the γ-rays/X-rays, few seconds after the breakout. In few hundreds seconds, the spectral peak moves from X-rays to UV. If the inner cocoon component is also highly relativistic, an associated afterglow emission can arise, whose brightness is a factor $\sim 10^{-2}$ dimmer than the forward shock emission from the jet head. The shocked envelope/ejecta, as well, is characterised by a quasi-thermal emission peaking when it reaches the transparency radius, but the expansion is sub-relativistic. In case of merger ejecta, the cocoon energy reflects the energy content of the jet, which is typically less energetic than the jet in collapsar-driven GRBs. Though, in CBMs a further source of energy coming from the radioactive decay of heavy elements can heat up the cocoon material, influencing the overall dynamical and radiative evolution (Gottlieb et al., 2018d).
Thanks to the quasi-isotropic nature, the cocoon emission represents a likely candidate EM emission from GRBs whose jet is observed off-axis. If too off-axis, the γ-ray flash from the jet could be undetectable and only

the late time afterglow emission would arise, defined in this case *orphan afterglow* (Nakar et al., 2002). Though, due to the limited Doppler boosting, both cocoon breakout and orphan afterglows could be detected only in the closer universe. Cocoon emission is also expected for chocked jets, which are possibly connected to low-luminosity GRBs.
Cocoon shock breakout is also a viable explanation for the γ-ray flash observed in GRB 170817A. Indeed, even if it was confirmed for this event the presence of an ultra-relativistic jet, it is still unclear which process originated the initial γ-ray flash. Applying the compactness argument (Kasen et al., 2017; Gottlieb et al., 2018b; Matsumoto et al., 2019), the observation of a γ-ray flash requires an outflows which moves at a velocity which is at least mildly relativistic. As demonstrated by Gottlieb et al., 2018b by the use also of numerical simulations, the duration, luminosity, spectral peak and hard-to-soft spectral evolution of GRB 170817 are perfectly compatible with a cocoon shock breakout. Right after the breakout the emission is confined to a very thin layer, therefore the emitted energy is a tiny fraction of the total internal energy of the cocoon. This is in agreement with the subluminous nature of GRB170817. At this stage the spectrum is non-thermal and as soon as the cocoon evolves in the cooling phase, thermal equilibrium is reached and the spectrum is close to a single temperature black body. During the cooling phase, the cocoon energy decreases mainly due to adiabatic losses, which is translated into a gradual hard-to-soft spectral transition (Nakar and Sari, 2012).
Thanks to its properties, the shock breakout associated to the jet cocoon is a potential EM counterpart of CBMs in the high-energy domain. It is worth to notice that, depending on the details of the jet propagation and the post-merger ejecta, the delay between the GW detection and the detection of the γ-ray/X-ray emission from the cocoon may vary from fraction of seconds up to several seconds, being the delay dependent also on the viewing angle. Moreover, an additional delay can be introduced if the remnant is meta-stable NS and the jet is launched only when the BH is formed. All these factors have to be taken into account when, in the future, we will need to establish the significance of the association between a GW event and an EM signal separated in time by a non-negligible amount.

Resulting structure from jet-cocoon interaction

The specific shape of the final jet structure depends on several factors, including the initial conditions at the jet launch, the density profile of the stellar enevelope/merger ejecta, microphysical parameters such as the jet

magnetisation. The jet-cocoon interaction, in particular, has a major role in determining the overall structure and relativistic hydrodynamical simulations are necessary to fully describe this phase. The jet-cocoon interface (Gottlieb et al., 2021) is subject to hydrodynamical instabilities, such as the Rayleigh-Taylor and the Kelvin-Helmotz instabilities, which tend to mix the two components. Such a mix is less severe in merger-driven GRBs, implying a steep off-core structure and most of the jet energy stored in the central core (Gottlieb et al., 2021); though, if the jet is magnetised, even weakly, the jet-cocoon mixing is suppressed and less steep structure profiles are found (Gottlieb et al., 2020).
The most recent 3D hydrodynamical and magneto-hydrodynamical simulations show that both for collapsars (Gottlieb et al., 2022a; Urrutia et al., 2022) and binary mergers (Nathanail et al., 2021; Gottlieb et al., 2022b; Lamb et al., 2022a) the emerging jet has a narrow central core (few degrees) characterised by a constant Lorentz factor, surrounded by steep wings (with a typical profile slope $k \gtrsim 3$, where $\mathcal{E}(\theta) \propto \theta^{-k}$). Urrutia et al., 2022 shows that the jet structure at its birth is preserved if the jet life time (duration of the ejection activity of the central engine) is longer than the breakout time. In the opposite case, the jet looses memory of the initial structure, unless it propagates in a very low-density medium. Jets launched after merger events are strongly affected by anisotropies and inhomogenities of the surrounding ejecta. In this regard, Pavan et al., 2021 (and Pavan et al., 2022 including also the role of magnetic field) investigated the jet propagation and the final 3D jet structure considering a realistic environment directly derived by simulations of BNS mergers. These simulations show that the final jet coming out from BNS merger could be tilted with respect to the normal to the orbital plane and also deviating from the usual assumed cylindrical symmetry. Additionally, Gottlieb et al., 2022a showed that initial instabilities in the accretion disk can induce to a jet wobbling, namely a jet with an axis precession. The interplay of all these processes make the prediction of the jet structure challenging and it is not yet well established whether all the GRBs can share a common jet structure, or the final outcome strongly depends on the progenitor, on the initial condition or the properties of the circum-burst medium.

The jet structure and the impact on prompt emission observables

In the top-hat limit, each patch of the jet moves with the same Lorentz factor Γ. For an on-axis observer, the received radiation comes from a fraction of the jet contained in a solid angle with aperture $1/\Gamma$. Moreover, due to

jet uniformity, any observable does not depend on the viewing angle θ_v, provided that $\theta_v < \theta_j - 1/\Gamma$, where θ_j is the semi-aperture angle of the jet. In the case of a structured jet, instead, radiation departing at an angle θ_v from the jet axis is less beamed and less Doppler boosted. Therefore for an off-axis observer, the presence of a jet structure has the following consequences:

1. The isotropic energy (as well as the isotropic luminosity) depends on the viewing angle. Following the approach of Salafia et al., 2015a, each part of the jet subtended to the solid angle $d\Omega$ contributes to the total energy as
$$\frac{\mathrm{d}E_{\mathrm{iso}}}{\mathrm{d}\Omega} = \frac{\mathcal{D}^3\left(\theta, \phi, \theta_{\mathrm{v}}\right)}{\Gamma(\theta)} \frac{\mathrm{d}E}{\mathrm{d}\Omega}(\theta),$$
where $\mathcal{D} = [\Gamma(1 - \beta\cos\alpha)]^{-1}$ is the Doppler factor and α the angle between the velocity vector of the jet patch and the line of sight. $\frac{\mathrm{d}E}{\mathrm{d}\Omega}(\theta)$ is the energy angular distribution and it implicitly takes into account that a fraction η_γ of the jet energy is converted into radiation. In principle also η_γ could be angle-dependent.

2. the overall prompt emission spectrum is the result of an integration of the comoving emissivity along the jet surface. As a first approximation, the emission from an off-axis observer is dominated by the region of the jet along the line of sight, which has a $\Gamma(\theta = \theta_v) < \Gamma(\theta = 0)$. Therefore the spectrum is shifted at lower energies with respect to an on-axis observer.

3. the shape of the prompt light curve has a less steep decay for off-axis observers, hence possibly increasing the duration of the burst. This would imply that a GRB could have a duration $t_{90} < 2$ s if viewed on-axis, but it could be classified as faint long GRB if observed enough off-axis.

If E_{iso} and peak energy decrease for off-axis observers, it is legitimate to think that the jet structure is somehow connected with the $E_p - E_{\mathrm{iso}}$ correlation, also known as Amati relation. This is indeed shown by Salafia et al., 2015a for long GRBs, where the Amati relation is reproduced assuming a quasi-universal Gaussian structure. In this scenario, the scatter of the Amati relation is compatible with a narrow dispersion of the structure parameters $(\mathcal{E}_0, \Gamma_0, \theta_c)$. This model also predicts a population of sub-luminous GRBs in the bottom left corner of the Amati relation, whose weakness is not intrinsic, but related to viewing angle effects. In addition, the typical spectral

peak of this population would be shifted towards soft X-rays and therefore their prompt emission would be undetectable by currently operating γ-ray telescopes. Future wide field X-ray monitors, such as THESEUS (Amati et al., 2021), Gamow (White et al., 2021), or Einstein Probe (Yuan et al., 2018), would be ideal to detect this kind of objects.
Similarly, a quasi-universal jet structure can reproduce the $E_p - E_{\rm iso}$ correlation for short GRBs (Salafia et al., 2019a), though the case of GRB 170817A is slightly in tension with this scenario. This inconsistency can be attenuated assuming that, in addition to a dynamical and energetic structure, there is an angular dependence of microphysical parameters related to the conversion efficiency η_γ, mentioned above. In the specific, the jet wings, being less energetic, could be less efficient in accelerating particles and/or magnetic fields could be less intense. This would imply also different cooling regimes as a function of the angular distance, hence leading to an angular-dependent comoving spectral shape (Ioka and Nakamura, 2019).

3.3.1 Afterglow and high latitude emission from a structured jet

Once the jet breaks out, it continues its expansion in a much more diluted medium. As before, a cocoon is inflated on the lateral sides of the jet, but now, in absence of a counter-balancing pressure, it freely expands. The mutual interaction between the jet-cocoon system and the circum-burst medium strongly defines the final structure of the jet. During the free expansion, or *coasting phase*, the jet releases its internal energy, through internal shocks or magnetic reconnections. Independently on the dissipation mechanism, the jet structure influences the appearance of the prompt emission light curve, through the effect of high-latitude emission (HLE).
HLE is a direct consequence of the curved geometry of the jet emitting surface. In the simple case of a top-hat jet aligned along the line of sight, photons departed from a region at $\vartheta > 0$ arrive later with respect to photons emitted at $\vartheta = 0$ at the same time in the source frame. This implies that, even if the prompt emission instantaneously stops at the same time in the source frame, a tail appears in the observer frame light curves. The temporal decay is expected to be rather steep, i.e. $F(t) \propto t^{-(2+\beta)}$, assuming that the spectrum follows $F_\nu \sim \nu^{-\beta}$. Such prompt-tail, since high-latitude photons are less boosted, peaks in the X-rays. In the case of a structured jet (Oganesyan, 2020) observed on-axis, the contribution from off-core wings induces a deviation from a simple steep decline, introducing a flattening of

the light curve which starts as soon as the observer receives photons from $\vartheta > \vartheta_c$. Therefore the beginning and duration of the shallow decay depends on the jet geometrical and dynamical properties (e.g. radius, Γ, θ_c). Depending on the specific structure, the temporal decay slope can also reach values close to zero, in which case the light curve would show a plateau phase. X-ray plateaus are often observed in both long and short GRB light curves, whose origin is still under debate. The presence of a structure in the jet would easily explain this feature. When observed off-axis (Ascenzi et al., 2020c), the prompt HLE from a structured jet is fainter, the initial decay is less steep and tends to disappear for $\vartheta_v \gg \vartheta_c$, while the spectrum peaks at lower energies ($\sim$ X-rays) at the moment of the light curve peak. Since the HLE from a structure jet can last[3] even $10^4 - 10^5$ s, it can overlap with the standard afterglow emission from the forward shock.
The afterglow emission from a structured jet has been investigated by several works, through analytical, semi-analytical and numerical approaches (Rossi et al., 2002b; Granot and Kumar, 2003; Kumar and Granot, 2003; Lamb and Kobayashi, 2017a; Beniamini et al., 2020b; Lamb et al., 2021; Beniamini et al., 2022). For an observer located at a viewing angle θ_v, the regions of the jet which mainly contribute to the observed flux are those for which the beaming cone intersects the line of sight. This corresponds to impose that

$$|\theta - \theta_v| < \theta_b(\theta), \tag{3.3}$$

where $\theta_b(\theta)$ is the semi-aperture angle of the beaming cone. In the simple approximation of a uniform jet moving at ultra-relativistic velocity, $\theta_b \sim 1/\Gamma$ and therefore the observed emission is totally dominated by jet region along the line of sight. In the case of a structured jet, the condition 3.3 could be satisfied for multiple ranges of θ.
After internal dissipation, the jet structure is expected to be maintained, if each portion follows an independent Blandford-McKee expansion. Only once sound waves cross transversely the jet, lateral expansion occurs and angular anisotropies start to be levelled out (Granot and Piran, 2012).

[3] the total duration of the HLE corresponds to $t(\vartheta_{\rm max}) - t(\vartheta = 0)$, where $t(\vartheta)$ is the time at which the observer receives photons from an angular distance ϑ. The maximum angle $\vartheta_{\rm max}$ from which we can receive radiation depends on the condition $\tau(\vartheta) < 1$, where τ is the opacity of the patch of the jet at angle ϑ (e.g, Matsumoto et al. 2019.)

3.4 Cosmic evolution and luminosity function of GRBs

In order to describe the statistical properties of GRBs as a population, the knowledge of the intrinsic energy and redshift distribution is necessary. The GRB cosmic rate density function is usually defined as:

$$\dot{\rho}(z) = \frac{dN}{dt_s dV_c},$$

namely as the number of sources per unit time (measured in the source frame) and unit of comoving volume. This corresponds to the *intrinsic* rate density of GRBs, while the *observed* one would correspond to:

$$\dot{\rho}_{\rm obs}(z) = \frac{\epsilon_{\rm det}(z)}{1+z}\frac{dN}{dt_s dV_c}, \tag{3.4}$$

where $\epsilon_{\rm det}$ is the detection efficiency of a given instrument and it depends on the luminosity distribution of the GRB population. This last is described by the luminosity function

$$\Phi(L,z) = \frac{dN}{dL}.$$

Using this definition, the luminosity should correspond to the bolometric luminosity measured at the peak of the light curve. Usually the peak flux in the rest-frame band E=(1-10^4) keV is a good proxy to derive the bolometric luminosity. Since GRBs are distributed at cosmological distances, also the k-correction[4] needs to be taken into account. The luminosity is then related to the observed flux $F_{\rm obs}$ as:

$$L = 4\pi k(z) D_L^2(z) F_{\rm obs},$$

where k is the k-correction and D_L the luminosity distance.
The functions $\rho(z)$ and $\Phi(L,z)$ define the statistical properties of the GRB population and its evolution across the cosmic history. The luminosity

[4]the k-correction transforms the observed flux in the energy band of the instrument into the source-frame flux measured in the same energy band. Hence, the k-correction needs the knowledge of the broad-band spectrum of the source

function is usually modeled as a broken power law:

$$\Phi\left(L,z\right) \propto \begin{cases} L^{-a_1} & \text{if } L \leqslant L_{\rm b} \\ L^{-a_2} & \text{if } L > L_{\rm b} \end{cases},$$

where L_b is the characteristic break luminosity. Since the luminosity function is a probability distribution, the normalisation is chosen in such a way that $\int \Phi(L,z)dL = 1$. Therefore the only three free parameters are a_1, a_2 and L_b, which in principle can evolve in redshift.
The cosmic rate density is strongly related to the GRB progenitor:

- For collapsar-driven GRBs, the rate is directly correlated to the star formation rate (SFR), since the delay between the formation and death of massive stars is negligible ($\sim$ Myr). Moreover several studies (Graham and Fruchter, 2013; Vergani et al., 2015; Palmerio et al., 2019) show that long GRBs prefer sub-solar metallicity environments, corroborating the scenario according to which a lower metallicity enhances the rotation of WR-stars and hence the efficiency of the jet launching mechanism. Due to the role of metallicity, GRBs do not follow directly the SFR $\dot{\rho}_*(z)$ and this behavior can be synthetised introducing a weighting function $\xi(z)$, such that:

  $$\dot{\rho}(z) = \dot{\rho}_*(z)\xi(z). \tag{3.5}$$

  The function $\xi(z)$ implicitly contains also the information about the fraction of collapsars which are able to launch a jet.

- For merger-driven GRBs, the delay between star formation and the merger is typically non negligible. The most adopted approach consists in defining a typical delay τ between the star formation time T_* and the merger time $T_{\rm merger}$:

  $$T_{\rm merger} = T_* + \tau.$$

  Usually, a probability function is associated to τ, which is in the form:

  $$P(\tau) = \begin{cases} 0 & \tau < \tau_0 \\ \propto \tau^{-n}, & \tau > \tau_0 \end{cases},$$

with $\tau_0 \sim 10$ Myr and $n \sim 1$. Hence, the compact binary merger (CBM) rate would be connected to the SFR as:

$$\dot{\rho}_{CBM}(z) = \int_0^\infty \lambda(t(z)+\tau)\dot{\rho}_*(t(z)+\tau)P(\tau)d\tau, \tag{3.6}$$

where $\lambda(z)$ is the fraction of stars that give a binary coalescence. The redshift dependence in λ is introduced since both stellar metallicity and initial mass function can play a major role in determining which fraction of stars gives a binary merger. Additionally, the metallicity can also influence the typical delay τ, since a higher metallicity accelerates the orbital shrinking, in the so called common envelope phase (e.g., Mapelli and Giacobbo, 2018). This implies that also $P(\tau)$ has an implicit dependence on redshift. See Appendix A.1 for a detailed derivation of formula 3.6. Finally the short GRB rate is a fraction of $\dot{\rho}_{CBM}(z)$, corresponding to those mergers that successfully launch a jet.

Once the GRB cosmic rate and luminosity function are defined, the actual observed rate (in units of detections per unit time) would be given by (e.g., Pescalli et al., 2016):

$$N(>S) = A_{\rm det}\int_0^{z(L_{\rm max},S)} \frac{\dot{\rho}(z)}{(1+z)}\frac{{\rm d}V_c}{{\rm d}z}\int_{L_{\rm lim}(S,z)}^{L_{\rm max}} \Phi(L,z)\,{\rm d}L\,{\rm d}z, \tag{3.7}$$

where S is the limiting flux (namely the detection threshold of the instrument), $L_{\rm lim} = 4\pi k(z) D_L^2(z) S$, $\frac{{\rm d}V_c}{{\rm d}z}$ is the differential comoving volume and $z\,(L_{\rm max}, S)$ is the largest reachable redshift, given S and the largest GRB luminosity $L_{\rm max}$. The overall constant $A_{\rm det}$ depends on the field of view and the duty cycle of the instrument[5] and can be written as $A_{\rm det} = \epsilon_{DC}\epsilon_{\Delta\Omega}$. The corresponding observed rate per unit volume can be computed as:

$$\frac{dN(>S)}{dV_c} = \dot{\rho}_{\rm det}(z) = \varepsilon_{DC}\varepsilon_{\triangle\Omega}\frac{\dot{\rho}(z)}{1+z}\int_{L_{\rm min}\,(z)}^{L_{\rm max}} \Phi(L)dL.$$

Comparing this with eq. 3.4, the detection efficiency function would correspond to:

$$\epsilon_{\rm det}(z) = \varepsilon_{DC}\varepsilon_{\triangle\Omega}\int_{L_{\rm min}\,(z)}^{L_{\rm max}} \Phi(L)dL.$$

[5]the duty factor is defined as the fraction of the time during which the instrument is fully operative at 100% of its capabilities

Implicitly eq. 3.7 contains also the information about the viewing angle. In the rough approximation of a uniform jet with a semi-aperture angle θ_j, the GRB could be detected up to a maximum viewing angle $\theta_{\rm max} \gtrsim \theta_j$. Therefore $L = 0$ if the line of sight is outside the solid angle defined by $\theta_v \in [0, \theta_{\rm max}]$ and $\phi \in [0, 2\pi]$. Using conditional probability, $\Phi(L)$ can be expanded as:

$$\Phi(L) = \int_0^{\pi/2} P_L(L \mid \vartheta) P_\vartheta(\vartheta) d\vartheta,$$

where $P_L(L \mid \vartheta)$ is the probability of observing a luminosity L, given a viewing angle ϑ, and $P_\vartheta(\vartheta)$ is the probability distribution of θ. For a top-hat jet:

$$P_L(L \mid \vartheta) = \begin{cases} \delta(L=0) & , \vartheta > \vartheta_{\rm max} \\ \varphi(L) & , \vartheta < \vartheta_{\rm max} \end{cases},$$

where with $\varphi(L)$ we indicate the *intrinsic* [6] luminosity function, which is angle independent and can be thought as the probability that a GRB jet produce a luminosity in the interval $[L, L + \Delta L]$. Therefore we would have:

$$\Phi(L) = (1 - \cos\theta_{\rm max})\, \varphi(L) + \cos\theta_{\rm max}\, \delta(L = 0).$$

Since $L_{\rm min}(z) > 0$, we can write:

$$\varepsilon_{\rm det}(z) = \varepsilon_{DC} \varepsilon_{\Delta\Omega} (1 - \cos\theta_{\rm max}) \int_{L_{\rm min}(z)}^{L_{\rm max}} \varphi(L) dL.$$

This treatment can be extended to the case where $\theta_{\rm max}$ is not the same for all the GRBs, but has some probability distribution with a mean value $\langle \theta_{\rm max} \rangle$, which in principle can evolve with z. In this case, an average detection efficiency can be defined as:

$$\langle \varepsilon_{\rm det} \rangle (z) = \varepsilon_{DC} \varepsilon_{\Delta\Omega} [1 - \cos(\langle \theta_{\rm max} \rangle (z))] \int_{L_{\rm min}(z)}^{L_{\rm max}} \varphi(L) dL.$$

Defining the average beaming factor $\epsilon_b(z) = [1 - \cos(\langle \theta_{\rm max} \rangle (z))]$, eq. 3.7 can be written in terms of the intrinsic luminosity function $\varphi(L)$:

$$N(>S) = \varepsilon_{DC} \varepsilon_{\Delta\Omega} \int_0^{z(L_{\rm max}, S)} \varepsilon_b(z) \frac{\dot\rho(z)}{(1+z)} \frac{{\rm d}V_c}{{\rm d}z} \int_{L_{\rm lim}(S,z)}^{L_{\rm max}} \varphi(L, z)\, {\rm d}L\, {\rm d}z.$$

[6] Alternatively, $\varphi(L)$ can be interpreted as the luminosity function per unit solid angle. Indeed, since $P_\vartheta(\vartheta) d\vartheta = d\mu$, where $\mu = \cos(\vartheta)$, we have $2\pi \frac{d\Phi}{d\Omega} = \varphi(L)$, for $\vartheta < \vartheta_{\rm max}$.

In sec. 3.4 we will show how this approach can be extended relaxing the assumption of a top-hat jet and working in the more realistic scenario of a structured jet.
As evident from the last equation, both the cosmic rate and luminosity function of GRBs cannot be derived directly from observational data. The most adopted method consists in assuming a parametric representation for these two functions and finding the best set of parameters that reproduce the observables. One of the most delicate points in this approach is the completeness of the GRB samples, since an incomplete sample can lead to biased estimation of the population properties. The incompleteness is mostly related to the following points:

1. Instrumental effects. The detection probability decreases as the peak flux of the source is close to the detection threshold, being determined also on the specific trigger algorithm. This bias can be avoided considering a higher cut of the detection threshold.

2. Redshift determination. In order to perform population studies only GRBs with measured redshift can be taken into account. Though, the redshift determination depends on several factors, including the brightness of the optical emission (which can be strongly absorbed by the host galaxy) or the distance of the source.

Population models have the aim of reproducing the average properties of GRBs, including the peak flux, duration, fluence, time-integrated spectral properties, observed redshift distribution. Moreover, further information can be exploited, such as the empirical $E_p - E_{\rm iso}$ correlation (e.g., Ghirlanda and Salvaterra 2022).
For long GRBs, population studies converge to a luminosity function with $a_1 \sim 1$, $a_2 \sim 2.2$ and $\log_{10}(L_b/(\mathrm{erg/s})) \sim 52$ (Wanderman and Piran, 2010; Salvaterra et al., 2012; Ghirlanda and Salvaterra, 2022). Past studies (e.g., Palmerio and Daigne 2021) concluded that it is not possible to distinguish between a pure density evolution and a pure luminosity evolution. In a pure density evolution scenario, the luminosity function does not depend on redshift, while in a pure luminosity evolution scenario, the GRB cosmic rate is a fixed fraction of the SFR (i.e., in eq. 3.5 $\xi(z) = \text{const}$). On the other hand, Ghirlanda and Salvaterra, 2022 showed that a mixed scenario is strongly favoured. In the specific they find a GRB cosmic rate which has the same redshift dependence of SFR rate, but peaking at higher z ($\sim 2-3$), and a luminosity function which mildly evolves with $L_b \propto (1+z)^{0.6}$.
More uncertainties, instead, affect the luminosity function of short GRBs,

mainly due to fact that they are less numerous than long ones and this can enhance the issue of sample incompleteness. For instance, Ghirlanda et al., 2016a find a luminosity function with $a_1 \sim 0.5$, $a_2 \sim 3.4$ and $L_b \sim 3 \times 10^{52}$ erg s^{-1}, while Wanderman and Piran, 2015 find a similar high-luminosity slope, but a much steeper low-luminosity slope $a_1 \sim 2$. This has strong impact on the predicted average luminosity, with $\langle L \rangle \sim 1.5 \times 10^{52}$ erg s^{-1} in the first study, $\langle L \rangle \sim 4.5 \times 10^{50}$ erg s^{-1} in the second one. Moreover, significant differences are found regarding the redshift distribution, with the second work finding a cosmic rate much more suppressed at $z \gtrsim 1$. Such discrepancies can be ascribed to different working assumptions, such as the adopted cut of the peak flux, internal correlation between physical parameters, samples from different instruments. The concepts and relations described in this section will be used extensively in chapter 6.2, where we need to define a detailed modelling of the short GRB population in terms of energetic properties and redshift distribution.

The GRB luminosity function as a result of jet structure

A direct consequence of the jet structure is that GRBs observed off-axis appear less luminous. Therefore for an isotropic distribution of the jet axis with respect to the line of sight, a luminosity distribution can be derived. In the simple approximation of a universal jet structure $S(\vartheta)$ and a common energy reservoir for all the GRBs, the inferred isotropic luminosity can be written as a unique function of the viewing angle:

$$L = L_0 S(\vartheta).$$

Following the derivation detailed in Appendix A.2, we have:

$$\Phi(L) = \sin\vartheta(L) \cdot \frac{1}{dL/d\vartheta}\Big|_{\vartheta(L)}.$$

In the specific case of Gaussian and power law profiles (Rossi et al., 2002b; Zhang and Mészáros, 2002):

$$\Phi(L) \propto \begin{cases} L^{-1} & , \quad S(\vartheta) \propto e^{-(\vartheta/\vartheta_c)^2} \\ L^{-1-2/k} & , \quad S(\vartheta) \propto (\vartheta/\vartheta_c)^{-k} \end{cases},$$

valid in the limit $\vartheta \sim \vartheta_c$, i.e. $L \sim L_0$, while $\Phi(L)$ tends to shallower slopes for $L \ll L_0$. Though, as pointed out by Salafia and Ghirlanda, 2022, for $L \ll L_0$ the source is observed very off-axis and therefore the observational

properties, such as duration and spectral peak, can substantially deviate from the ones of an on-axis GRB, possibly inducing a mis-classification of the source. The derivation can be extended in the case of quasi-universal jet structure, introducing a small scatter in L_0 (see Appendix A.2).
Several investigations have been carried out to test if a quasi-universal jet structure can account for the luminosity function inferred from population studies. Regarding long GRBs, Pescalli et al., 2015 concluded that a top-hat geometry with a universal jet aperture angle is excluded, since it would predict a flat low-luminosity distribution. On the other hand, both the following scenarios are compatible with data: 1) A top-hat jet with a constant energy reservoir $\vartheta_j^2 E_{\rm iso}$; 2) a universal structured jet, with a jet core energy following a log-normal distribution centred around 6×10^{52} erg and a $\vartheta_c \sim 5^\circ$. In particular, in the structured jet case, the agreement is found for power law profiles, provided that $k > 4$. Also in the case of short GRBs, a quasi-universal jet structure is able to reproduce the luminosity function (Salafia et al., 2020a), but too shallow profiles ($k < 2$) are excluded because they would overestimate the local rate of short GRB inferred from the detection of GW170817.

Chapter 4

The origin of the X-ray steep decay

The final phases of prompt emission are usually characterised by a steep decline visible in X-rays. In order to understand the X-ray steep decay phase in connection with the nature of the GRB prompt emission I performed a systematic analysis of the temporal and spectral properties during this phase. This chapter describes in details this analysis for a sample of GRBs and reports the discovery of a unique relation between the X-ray photon index and the flux. This relation is incompatible with the long standing scenario which invokes the delayed arrival of photons from high-latitude parts of the jet. Comparing different scenarios we found that the adiabatic cooling of the emitting particles is the most plausible explanation for the discovered relation, suggesting a proton-synchrotron origin of the GRB emission. This work has been published in Ronchini et al., 2021. I conclude the chapter by evaluating the future prospects of observations of the X-ray steep decay by instruments such as the mission concept THESEUS and the importance of this emission phase in the multi-messenger context.

In order to model and interpret the temporal and spectral evolution observed during the steep decay it is necessary to consider the geometry of the jet surface. If the emitting region is curved, photons that depart simultaneously in the source frame arrive at different times to the observer. The delayed arrival of photons departing from the external regions of the jet is known as High Latitude Emission (HLE) (Fenimore et al., 1996; Kumar and Panaitescu, 2000; Liang et al., 2006). In the standard picture of HLE, since the emitting surface of the jet is curved, an on-axis observer first receives photons from the line of sight and later photons from higher latitudes which are less Doppler boosted. This combination of effects produces at the same time a steep flux decline and a spectral softening. Therefore, it has been considered the most accepted scenario for the interpretation of the X-ray steep decay. Since the X-ray steep decay is tightly connected to the final phases of prompt emission, we will refer to it also as *X-ray tail*.
Under the assumption of a single power-law spectrum ($F_\nu \propto \nu^{-\beta}$), the HLE predicts that the flux decays as $F_\nu(t) \propto \nu^{-\beta} t^{-(\beta+2)}$. On the other hand, if the spectrum is curved, the HLE can also lead to the transition of the spectral peak across the observing band (Lin, 2017), causing a spectral evolution, as often observed in the soft X-rays (Zhang et al., 2007; Mangano and Sbarufatti, 2011). Generally, if the intrinsic spectral shape does not change in time, the flux density in a given band would be:

$$F_\nu(t) = F_p(t) S_\nu(\nu/\nu_p(t)),$$

where $F_p(t)$ is the spectral normalisation, S_ν the time independent spectral shape and $\nu_p(t)$ the spectral peak. The work of Zhang et al., 2007 systematically analyses and models the spectral evolution during the steep decay of 44 GRBs. A good agreement with data is found adopting a phenomenological model which parametrizes the peak flux and the spectral peak as $F_p(t) \propto t^{-\alpha_1}$ and $\nu_p(t) \propto t^{-\alpha_2}$. In the case of HLE, $\nu_p(t) \propto t^{-1}$ and $F_p(t) \propto t^{-2} \propto \nu_p^2$, while in this work the best fit is found for a quite wide range of $\alpha_1 \sim 0.5 - 4$, whose distribution is peaked around 2, while $\alpha_2 \sim 1.5$. Therefore, even if HLE could explain some of the analysed cases, it is not clear if it is the dominant process at the basis of the spectral evolution. Few other works tried to test the validity of HLE performing a simultaneous fit of the temporal and spectral evolution of the X-ray steep decay (e,g., Qin 2008; Zhang et al. 2009). Therefore, a systematic analysis of this feature for a complete sample of GRBs is mandatory to ultimately verify the validity of the HLE model.

Simultaneously to the flux density, the local spectral slope can be measured in a narrow band centred around ν, corresponding to $\beta(t) = \frac{\partial \log F_\nu(t)}{\partial \log \nu}$. Therefore for each time t the flux density and the spectral slope can be related to each other, eliminating the dependence on time. Moreover, if the flux is normalised to the flux at the moment of the steep decay peak, the spectral slope-flux relation has the advantage of being 1) time independent and 2) redshift independent. Therefore, if a universal process at the origin of the steep decay exists such that a unique $F_p(\nu_p)$ relation holds, then the observed spectral slope-flux relation should be unique[1]. The aim of my work detailed in this chapter is indeed to test whether such a unique relation exits and to investigate its physical origin.

4.1 Sample selection and data analysis

In order to investigate the spectral evolution during the steep decay phase, we select a sample of GRBs from the archive of the *Swift*/XRT telescope. We restrict our study to a sample of GRBs whose brightest pulse in the Burst Alert Telescope (BAT, $15 - 350$ keV) corresponds to the XRT peak preceding the X-ray tail (see as example the Fig. 4.1a). The steep decay is selected imposing that the light curve is well approximated by a power law, $F \propto t^{-\alpha}$ with $\alpha > 3$. Such criterion allows us to exclude a decay coming from a forward shock (Paczynski and Rhoads, 1993; Mészáros and Rees, 1997; Sari et al., 1998a). In order to determine the presence of a steep decay (SD), we analyze the light curve of the integrated flux in the XRT $E = 0.3 - 10$ keV band.
From the Swift catalogue (Evans, 2009) as of the end of 2019, we selected all GRBs with an XRT peak flux $F_{\rm p}^{\rm XRT} > 10^{-8}$ erg cm^{-2}s^{-1}. We selected the brightest pulses in order to have a good enough spectral quality as to perform a time resolved spectral analysis. The peak flux is computed taking the maximum of $F(t_i)$, where $F(t_i)$ are the points of the light curve at each time t_i. Among these GRBs, we selected our *sample 1* according to the following criteria:

1. The XRT light curve shows at least one SD segment that is clean, i.e. without secondary peaks or relevant fluctuations.

[1]This statement is valid only if the observed spectral slope at the peak of the steep decay is common for all the analysed cases.

2. If we call F_1 and F_2 the fluxes at the beginning and at the end of the SD, respectively, we require that $\frac{F_1}{F_2} > 10$. This requirement is necessary to have a sufficient number of temporal bins inside the SD segment and therefore a well sampled spectral evolution.

3. The beginning of the SD phase corresponds to a peak in the XRT light curve, such that we have a reliable reference for the initial time. We stress that the identification of the SD starting time in XRT is limited by the observational window of the instrument. This means that, if the XRT light curve starts directly with a SD phase, with no evidence of a peak, the initial reference time is possibly located before and its value cannot be directly derived.

4. The XRT peak before the SD has a counterpart in BAT, whose peak is the brightest since the trigger time. This requirement is necessary to ensure that XRT is looking at a prompt emission episode, whose typical peak energy is above 100 keV. In a quantitative way, we define two times, $t_{\rm p}$ and $t_{90}^{\rm stop}$, where the first indicates the beginning of the peak that generates the SD, while the second is the end time of T_{90} (Lien, 2016), with respect to the trigger time. We require $t_{90}^{\rm stop} > t_{\rm p}$ in order to have an overlap between the last prompt pulses (monitored by BAT) and the XRT peak that precedes the SD phase. Namely, such requirement ensures that a considerable fraction of the energy released by the burst goes into the pulse that generates the X-ray tail.

It is possible that more than one peak is present in the XRT light curve, each with a following SD. In this case we consider only the SD after the brightest peak. If two peaks have a similar flux, we consider the SD with the larger value of $\frac{F_1}{F_2}$.
We define then a second sample of GRBs (*sample 2*) that satisfy the first two points listed before, but have a SD at the beginning of the XRT light curve, namely no initial peak preceding the SD is present. In addition, we require that a BAT pulse precedes the XRT SD and is the brightest since the trigger time. The BAT pulse enables us to constrain the starting time of the SD. The selection criteria limit the size of our sample, but they are unavoidable to perform a well targeted analysis of X-ray tails and to achieve robust conclusions about their origin. The first sample consists of 8 GRBs, as well as the second sample, for a total of 16 GRBs considered in our analysis.

4.1.1 Time resolved spectral analysis

For each GRB we divided the XRT light curve in several time bins, which are chosen according to the following criteria:

1. Each bin contains only data in Windowed Timing (WT) mode or in Photon Counting (PC) mode, since mixed WT+PC data cannot be analysed as a single spectrum.

2. Each bin contains a total number of counts $N_{\rm bin}$ in the $E = 0.3 - 10$ keV band larger than a certain threshold N_0, which is chosen case by case according to the brightness of the source (see below). The definition of the time bins is obtained by an iterative process, i.e. starting from the first point of the light curve we keep including subsequent points until
$$N_{\rm bin} = \sum_{t_n=t_i}^{t_f} N(t_n) > N_0, \tag{4.1}$$
where $N(t_n)$ are the counts associated to each point of the light curve, while t_i and t_f define the starting and ending time of the bin. Then the process is repeated for the next bins, until t_f is equal to the XRT ending time. Due to the large range of count rates covered during a typical XRT light curve, the choice of only one value for N_0 would create an assembly of short bins at the beginning and too long bins toward the end. Therefore we use one value of N_0 for bins in WT mode ($N_0^{\rm WT}$) and a smaller value of N_0 for bins in PC mode ($N_0^{\rm PC}$). In our sample, the SD is usually observed in WT mode, therefore we adjust $N_0^{\rm WT}$ in order to have at least 4-5 bins inside the SD. A typical value of $N_0^{\rm WT}$ is around 1500-3000, while $N_0^{\rm PC}$ is around 500-1000. Using these values, we verified that the relative errors of photon index and normalization resulting from spectral analysis are below $\sim 30\%$.

3. For each couple (N_i, N_j) of points inside the bin, the following relation must hold:
$$\frac{\left|N_i - N_j\right|}{\sqrt{\sigma_i^2 + \sigma_j^2}} < 5, \tag{4.2}$$
where σ_i and σ_j are the associated errors. Such requirement avoids large flux variations within the bin itself.

4. The duration of the bin is larger than 5 seconds, in order to avoid pileup in the automatically produced XRT spectra.

It is possible that condition 3 is satisfied only for a duration of the bin $T_{\rm bin} < T_0$, while condition 2 is satisfied for $T_{\rm bin} > T_0^*$, but $T_0^* > T_0$, meaning that they cannot be satisfied at the same time. In this case, we give priority to condition 3, provided that $N_{\rm bin}$ is not much smaller than N_0. Due to the iterative process that defines the duration of the bins, it is possible that the last points in WT and PC mode are grouped in a single bin with a too small $N_{\rm bin}$, giving a too noisy spectrum. Therefore, they are excluded from the spectral analysis.
The spectrum of each bin is obtained using the automatic online tool provided by Swift for spectral analysis. Each spectrum is analyzed using XSPEC (Arnaud, 1996), version 12.10.1, and the Python interface PyXspec. We discard all photons with energy $E < 0.5$ keV and $E > 10$ keV. The spectra are modeled with an absorbed power law and for the absorption we adopted the Tuebingen-Boulder model (Wilms et al., 2000). If the GRB redshift is known, we use two distinct absorbers, one Galactic (Kalberla et al., 2005) and one relative to the host galaxy (the XSPEC syntax is tbabs*ztbabs*po). The column density $N_{\rm H}$ of the second absorber is estimated through the spectral analysis, as explained below. On the other hand, if the GRB redshift is unknown, we model the absorption as a single component located at redshift z=0 (the XSPEC syntax is tbabs*po) and also in this case the value of $N_{\rm H}$ is derived from spectral analysis.
For the estimation of the host $N_{\rm H}$ we consider only the late part of the XRT light curve following the SD phase. At late time with respect to the trigger we do not expect strong spectral evolution, as verified in several works in the literature (Butler and Kocevski, 2007; Mu, 2016). Therefore, for each GRB, the spectrum of each bin after the SD is fitted adopting the same $N_{\rm H}$ which is left free during the fit. Normalization and photon index are also left free, but they have different values for each spectrum. We call $N_{\rm H}^{\rm late}$ the value of $N_{\rm H}$ obtained with this procedure. In principle the burst can affect the ionization state of the surrounding medium, but we assume that such effects are negligible and $N_{\rm H}$ does not change dramatically across the duration of the burst (Perna and Lazzati, 2002). Hence we analyzed separately all the spectra of the SD using a unique value of $N_{\rm H} = N_{\rm H}^{\rm late}$, which is fixed during the fit. Normalization and photon index, instead, are left free.
An alternative method for the derivation of $N_{\rm H}$ is the fitting of all the spectra simultaneously imposing a unique value of $N_{\rm H}$ that is left free. On the other hand, since $N_{\rm H}$ and photon index are correlated, an intrinsic spectral evolution can induce an incorrect estimation of $N_{\rm H}$. For the same reason we do not fit the spectra adopting a free $N_{\rm H}$, since we would obtain an evolution of photon index strongly affected by the degeneracy with $N_{\rm H}$. In this

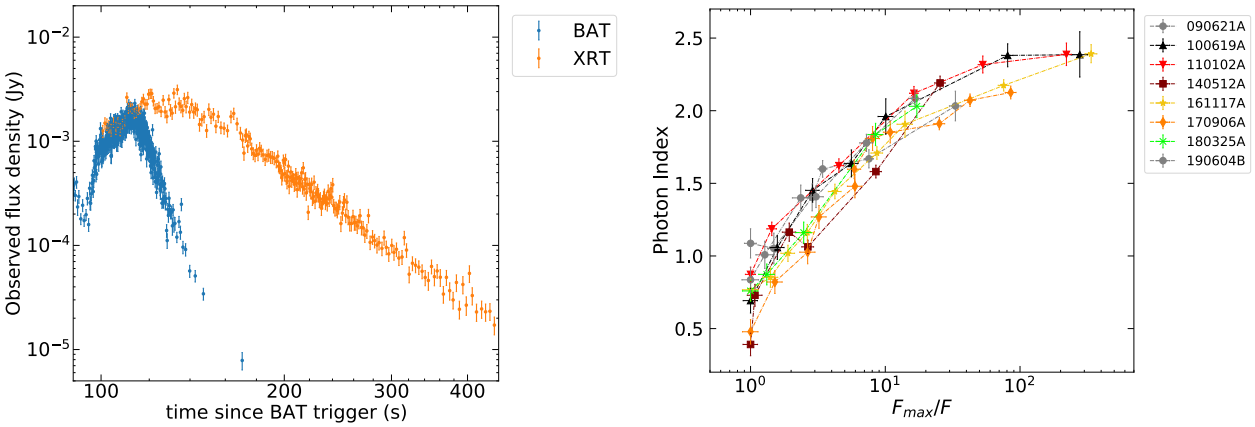

(a) (b)

FIGURE 4.1: The steep decay phase and the correspondent spectral evolution for *sample 1*. Panel (a) shows an example of a light curve of an X-ray tail selected from our sample, taken from the GRB 161117A. We show on the same plot the XRT (orange) and the BAT (blue) flux density at 1 keV and 50 keV, respectively. In panel (b) we report the spectral evolution of the X-ray tail for all the GRBs in the first sample (shown with different colors). The photon index α is represented as a function of the reciprocal of the normalized flux $F_{\rm max}/F$.

regard, we tested how our results about spectral evolution depend on the choice of $N_{\rm H}$. On average we found that the fits of the SD spectra remain good (stat/dof $\lesssim 1$) for a variation of $N_{\rm H}$ of about 50%. As a consequence, the photon index derived by the fit would change at most of 30%. Therefore the error bars reported in all the plots are possibly mildly under-estimated, but even considering a systematic error that corresponds to $\sim$ 30% of the value itself would not undermine the solidity of the results.

4.1.2 The $\alpha - F$ relation

For each temporal bin, we extract the $0.5 - 10$ keV un-absorbed flux F and the photon index α. We represent the spectral evolution during the steep decay plotting α as a function of the flux F, normalized to the peak value of the X-ray tail. Hereafter refer to it as the $\alpha - F$ relation. This normalization to the peak value of the X-ray tail makes the result independent of the intrinsic brightness of the pulse and of the distance of the GRB. In the case of *sample 2*, the peak flux at the beginning of the steep decay is extracted as follows. We consider the peak time $T_{\rm p}^{\rm BAT}$ of the BAT pulse that precedes the SD. In the assumption that the SD starts at $T_{\rm p}^{\rm BAT}$, we can derive $F_{\rm max}$

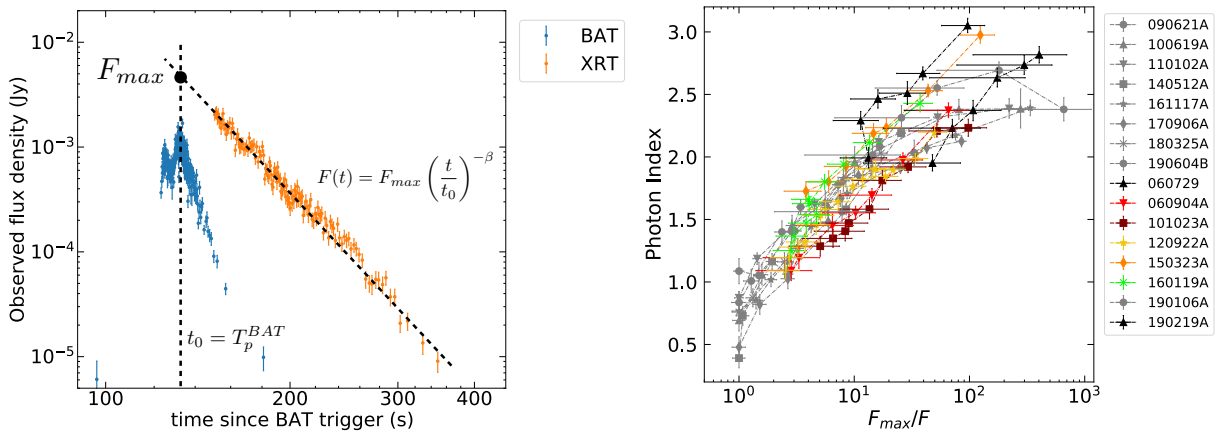

(a) (b)

FIGURE 4.2: The steep decay phase and the correspondent spectral evolution for the extended sample (*sample 1+sample 2*). Panel (a) shows an example of a light curve of an X-ray tail selected for our extended sample, taken from GRB 150323A. We report on the same plot the XRT (orange) and the BAT (blue) flux density at 1 keV and 50 keV, respectively. The peak flux $F_{\rm max}$ is estimated extrapolating the X-ray tail back to the BAT peak. Panel (b) shows the spectral evolution of the extended sample of GRBs

using the following procedure. We consider the $0.5-10$ keV flux $F(t_i)$ for each bin time t_i in the SD, derived from spectral analysis. Then we fit these points with a power law

$$F(t_i) = F_{\rm max}\left(\frac{t_i}{t_0}\right)^{-s}, \tag{4.3}$$

with $s > 0$ and imposing that $t_0 = T_{\rm p}^{\rm BAT}$. Finally we derive the best fit value of $F_{\rm max}$ with the associated 1σ error. The error of $F_{\rm max}$ has a contribution coming from the error associated to s and another associated to t_0, as well as from the assumption of a power law as fitting function. The value of $T_{\rm p}^{\rm BAT}$ is obtained fitting the BAT pulse with a Gaussian profile. Since usually the BAT pulse can have multiple sub-peaks and taking also into account possible lags between XRT and BAT peaks, we adopt a conservative error associated to $T_{\rm p}^{\rm BAT}$ equal to 5 seconds. We find that both *sample 1* and *sample 2* follow a unique $\alpha - F$ relation, as shown in Fig. 4.1b and 4.2. This is consistent with a systematic softening of the spectrum. For *sample 1* (*sample 2*) the photon index evolves from a value of $\alpha \sim 0.5-1$ $(1-1.5)$ at the peak of the XRT pulse to $\alpha \sim 2-2.5$ $(2.5-3)$ at the end of the tail emission, while

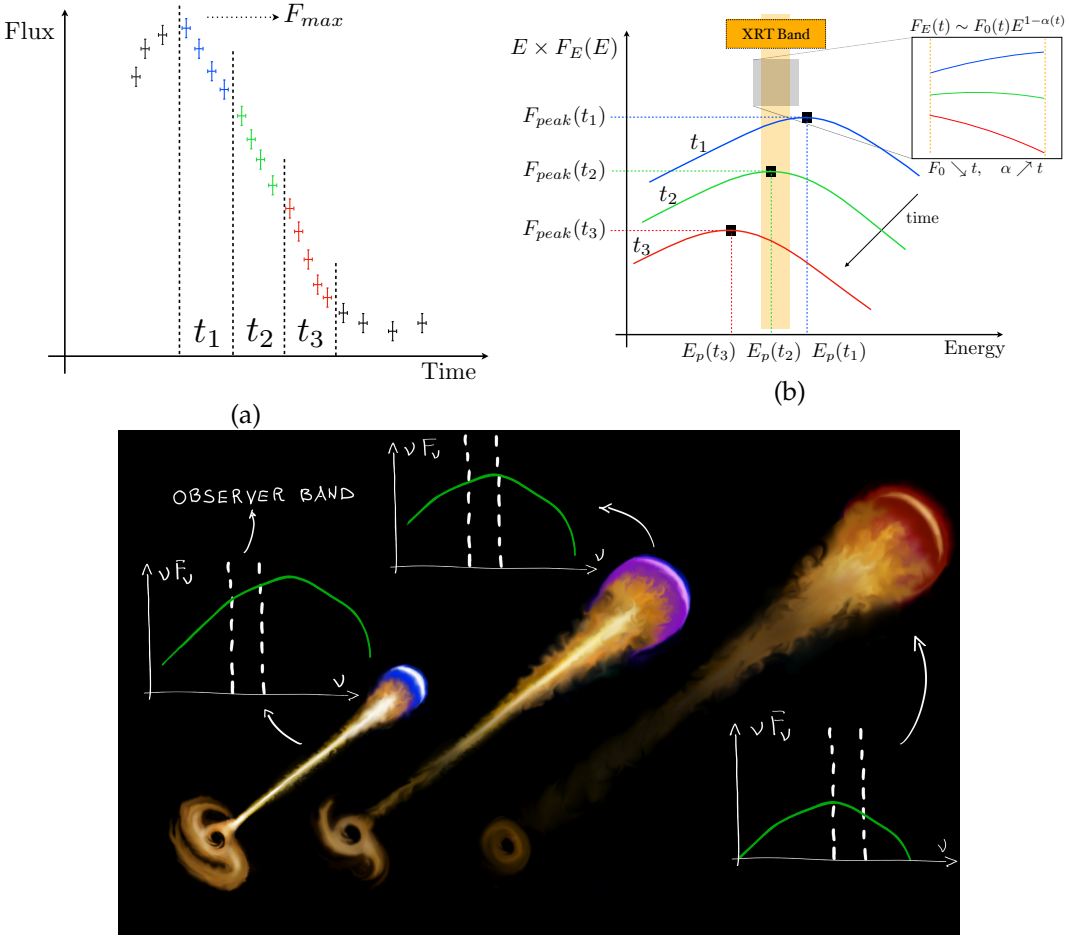

FIGURE 4.3: Illustration of the spectral evolution caused by a shift of the spectrum towards lower energies. The transition of the spectral peak through the XRT band explains the observed spectral softening. The spectra in panel (b) coloured in blue, green and red correspond to the three temporal bins shown in panel (a) with the same colours. The inset in panel (b) shows how the local spectral slope evolves as observed in the XRT band. Since in the panel (b) we plot the flux density, the local slope in the XRT band is given by $1 - \alpha$, where α is the photon index. Both the x and y axes in panels (a) and (b) have arbitrary units. Panel (c) is an artistic illustration of the correspondence between the jet expansion and the spectral evolution.

the flux drops by two orders of magnitude. The initial and final photon indexes are consistent with the typical low- and high-energy values found from the analysis of the prompt emission spectrum of GRBs, namely ~ 1

and $\sim$ 2.3 (Frontera, 2000; Kaneko, 2006; Nava et al., 2011), respectively. The $\alpha - F$ relation can be interpreted as being due to a spectral evolution in which the spectral shape does not vary in time, but the whole spectrum is gradually shifted towards lower energies while becoming progressively dimmer (see Fig. 4.3). The consistent spectral evolution discovered in our analysis is a clear indication of a common physical mechanism responsible for the tail emission of GRBs and the corresponding spectral softening.

4.2 Theoretical interpretation

In this section we the verify the validity of the HLE interpretation, exploring several hypothesis and extensions of the model. The common assumption at the basis of the HLE scenario is that particles are able to cool on a time scale much shorter than the dynamical time scale. We then extend this interpretation, testing what happens in the opposite regime, namely when particles inefficiently radiate and the dominating cooling process is driven by the adiabatic expansion of the jet.

4.2.1 High latitude emission scenario

We first compare our results with the expectations from the standard HLE, which is the widely adopted model for interpreting the X-ray tails of GRBs. As already described, when the emission from a curved surface is switched off, an observer receives photons from increasing latitudes with respect to the line of sight. The higher the latitude, the lower the Doppler factor, resulting in a shift towards lower energies of the spectrum in the observer frame.

HLE from an instantaneous pulse

We assume that an infinitesimal duration pulse of radiation is emitted on the surface of a spherical shell, at radius R_0 from the center of the burst. Such treatment implicitly assumes particles that cool on timescales much smaller than the dynamical timescales. Therefore, all the X-ray tail emission is dominated by photons departed simultaneously from the last emitting surface. The jet has an aperture angle ϑ_j and it expands with a bulk Lorentz factor Γ. We assume also that the comoving spectrum is the same on the whole jet surface. The temporal evolution of the observed flux density is

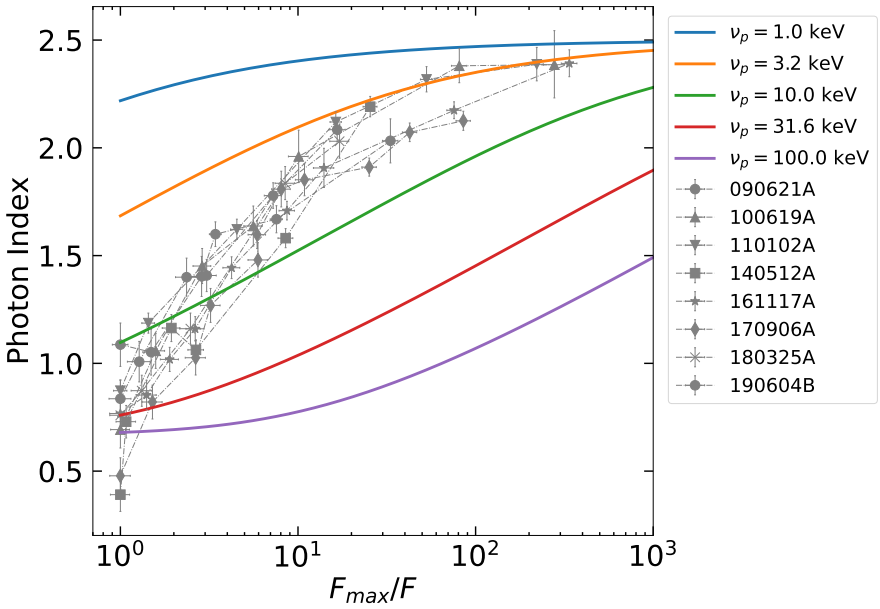

FIGURE 4.4: Spectral evolution expected for HLE from an infinitesimal duration pulse. The comoving spectrum is assumed to be a SBPL. The several colors indicate the observed peak frequency at the beginning of the decay. The error bars represent 1σ uncertainties, calculated via spectral fitting in XSPEC. In the legend we report the name of each GRB.

given by Oganesyan, 2020:

$$F_\nu(t_{\rm obs}) \propto S_{\nu'}(\nu/\mathcal{D}(\vartheta))\mathcal{D}^2(\vartheta)\cos(\vartheta), \tag{4.4}$$

with $S_{\nu'}(\nu/\mathcal{D}(\vartheta))$ the comoving spectral shape, $\mathcal{D}(\vartheta)$ the Doppler factor and ϑ the angle measured from the line of sight, which is assumed to coincide with the jet symmetry axis. The observer time $t_{\rm obs}$ is related to the angle ϑ through this formula:

$$t_{\rm obs}(\vartheta) = t_{\rm em}(1 - \beta\cos\vartheta), \tag{4.5}$$

where $t_{\rm em}$ is the emission time. Eq. (4.4) is valid for $\vartheta < \vartheta_j$, while for $\vartheta > \vartheta_j$ the emission drops to zero. This implies that for $t_{\rm obs} > t_{\rm em}(1 - \beta\cos\vartheta_j)$ the flux drops to zero. At each time $t_{\rm obs}(\vartheta)$ the observer receives a spectrum that is Doppler shifted by a factor $\mathcal{D}(\vartheta)$ with respect to the comoving spectrum. If the comoving spectrum is curved, i.e. if $\frac{d^2}{d\nu'^2}S_{\nu'} \neq 0$, then also

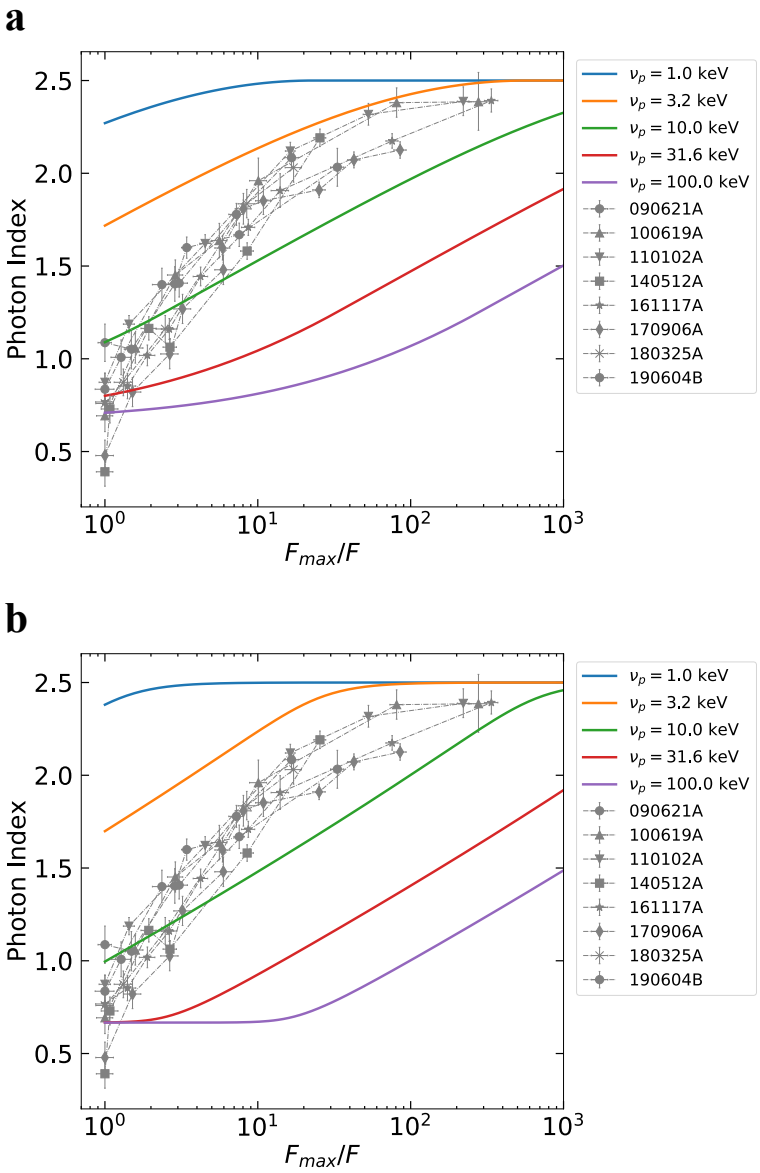

FIGURE 4.5: Spectral evolution expected for HLE from a infinitesimal duration pulse, for alternative spectral shapes. In **a** we adopt a Band function, while in **b** we adopt a SBPL with sharpness parameter $n = 4$. The error bars represent 1σ uncertainties, calculated via spectral fitting in XSPEC. In the legend we report the name of each GRB.

the photon index is a function of time (Lin, 2017). The shape of the resulting curve $\alpha - F$ is determined only by the spectral shape and the comoving

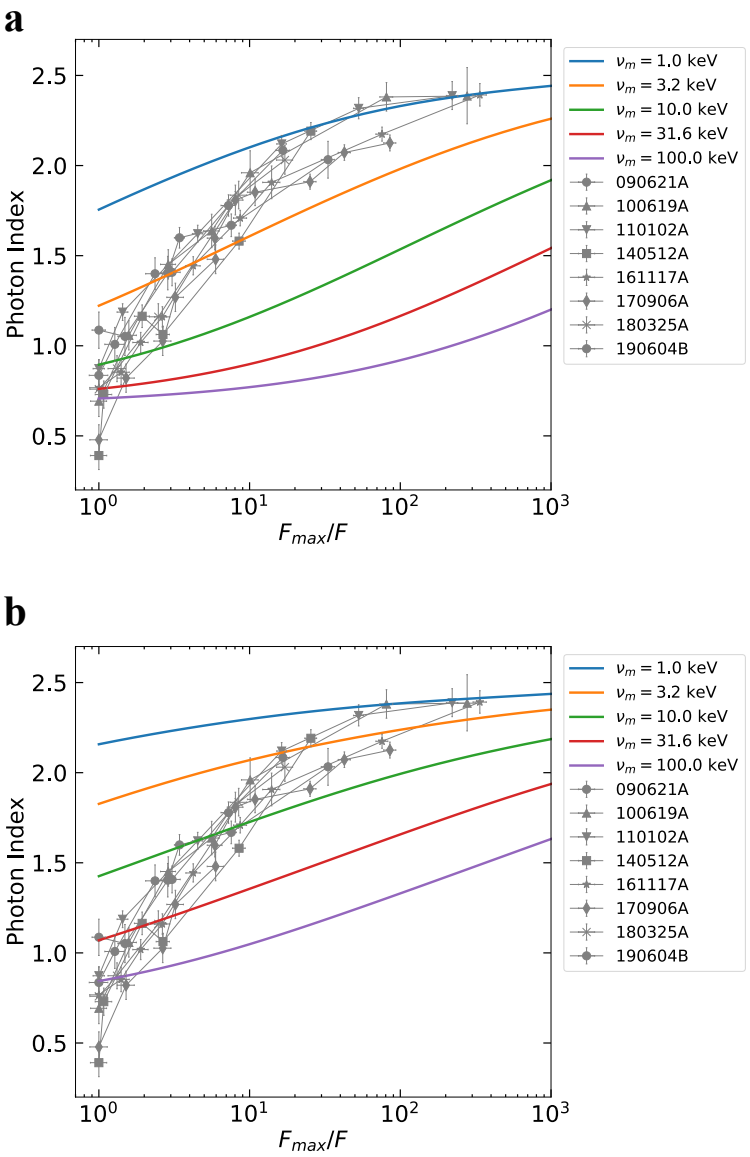

FIGURE 4.6: Spectral evolution expected for HLE from a infinitesimal duration pulse, assuming a synchrotron spectrum as spectral shape. In **a** we adopt $\nu_m/\nu_c = 1$, while in **b** $\nu_m/\nu_c = 10$. The several colors indicate the observed peak frequency at the beginning of the decay. In **b** the spectral evolution appears slightly steeper with respect to the case $\nu_m/\nu_c = 1$ because for $\nu_c < \nu < \nu_m$ the spectrum goes like $F_\nu \sim \nu^{-p/2}$. The error bars represent 1σ uncertainties, calculated via spectral fitting in XSPEC. In the legend we report the name of each GRB.

peak frequency $\nu'_{\rm p}$, while it is independent on the emission radius R_0 and the bulk Lorentz factor Γ.
We notice that the observed photon index goes from $0.5-1.0$ up to $2.0-2.5$, consistent with the slopes of a synchrotron spectrum before and after the peak frequency. Indeed for a population of particles with an injected energy distribution $N(\gamma) \propto \gamma^{-p}$ that has not completely cooled, the expected shape of the spectrum is $F_\nu \sim \nu^{1/3}$ ($\alpha = 2/3$) for $\nu < \nu_c$ and $F_\nu \sim \nu^{-p/2}$ ($\alpha = p/2+1$) for $\nu > \nu_{\rm m} \gtrsim \nu_{\rm c}$. At each arrival time we compute the flux and the photon index in the XRT band using eq. (4.4). In particular, the XRT flux is given by

$$F_{0.5-10\,\rm keV}(t_{\rm obs}) = \int_{0.5\,\rm keV/\mathit{h}}^{10\,\rm keV/\mathit{h}} F_\nu(t_{\rm obs}) d\nu, \tag{4.6}$$

where h is Planck's constant, while the photon index is computed as (Genet and Granot, 2009; Lin, 2017)

$$\alpha(t_{\rm obs}) = 1 - \frac{\log\left[F_{\nu=10\,\rm keV/\mathit{h}}(t_{\rm obs})/F_{\nu=0.5\,\rm keV/\mathit{h}}(t_{\rm obs})\right]}{\log\left(10\,\rm keV/0.5\,keV\right)}. \tag{4.7}$$

This method for the evaluation of photon index is valid in the limit of a spectrum that can be always approximated with a power law as it passes through the XRT band, which is the case for typical prompt emission spectra.
In the specific we test the HLE adopting the following spectral shapes:

1. Smoothly broken lower law (SBPL). It well approximates the synchrotron spectrum below and above the peak frequency. The adopted spectral shape is

$$S_\nu^{(n)}\left(\frac{\nu}{\nu_0}\right) \propto \left[\left(\frac{\nu}{\nu_0}\right)^{n\alpha_{\rm s}} + \left(\frac{\nu}{\nu_0}\right)^{n\beta_{\rm s}}\right]^{-1/n}, \tag{4.8}$$

with $\alpha_{\rm s} = -1/3$ and $\beta_{\rm s} = 1.5$. Larger values of n correspond to sharper spectral peaks. The $\alpha - F$ relation for $n = 1$ ($n = 4$) is shown in Fig. 4.4 (Fig. 4.5b). For $n = 4$, the shape of the curves becomes flatter at the beginning and at the end of the decay, but with no substantial steepening of the intermediate part. This is attributable to HLE that imposes an evolution of the observed peak frequency like $t_{\rm obs}^{-1}$. Thus, while the initial and final values of photon index are dictated by the spectral shape, the steepness of the transition from the

initial to the final value is governed by HLE and is independent on the spectral shape.

2. Band function (Band, 1993):

$$B(\epsilon) = \begin{cases} \epsilon^{1+\alpha_s} e^{-\epsilon} & \epsilon < \alpha_s - \beta_s \\ (\alpha_s - \beta_s)^{\alpha_s - \beta_s} e^{-\alpha_s + \beta_s} \epsilon^{1+\beta_s} & \epsilon > \alpha_s - \beta_s \end{cases}, \tag{4.9}$$

where $\epsilon = \nu/\nu_0$. In this case the peak of the energy spectrum is at $\nu_p = (2 + \alpha_s)\nu_0$. The resulting spectral evolution is very similar to the case of SBPL, as visible in Fig. 4.5a.

3. Synchrotron spectrum emitted by a population of particles with an initial energy distribution $N(\gamma) \propto \gamma^{-p}$. Synchrotron is considered the dominant radiative process in prompt emission of GRBs (Rees and Meszaros, 1994; Zhang, 2020). In the fast cooling regime, the particle distribution becomes

$$N(\gamma) \propto \begin{cases} \gamma^{-2} & \gamma_c < \gamma < \gamma_m \\ \gamma^{-(p+1)} & \gamma > \gamma_m \end{cases}. \tag{4.10}$$

The only three parameters that define the shape of the synchrotron spectrum are $\nu_m \propto \gamma_m^2$, $\nu_c \propto \gamma_c^2$ and p. For the computation of the spectrum we use ("Rybicki, G. B. & Lightman, A. P. Riadiative Processes in Astrophysics. Wiley-Interscience Publication (1979)." n.d.):

$$F_\nu \propto \int_{\gamma_c}^{\infty} P(\nu, \gamma) N(\gamma) d\gamma, \tag{4.11}$$

with

$$P(\nu, \gamma) \propto B \left[\left(\frac{\nu}{\nu_{ch}} \right) \int_{\frac{\nu}{\nu_{ch}}}^{\infty} K_{5/3}(x) dx \right], \quad \nu_{ch} \propto \gamma^2 B, \tag{4.12}$$

where B is the magnetic field and $K_{5/3}(x)$ is the modified Bessel function of order 5/3. A value of $\nu_m/\nu_c \sim 1$ is expected in the marginally fast cooling regime (Kumar and McMahon, 2008; Beniamini and Piran, 2013; Beniamini et al., 2018), which is favoured by broad-band observations of GRB prompt spectra (Oganesyan, 2017; Oganesyan, 2018; Oganesyan, 2019; Ravasio, 2018; Ravasio, 2019; Burgess, 2020).

The resulting spectral evolution for values of $\nu_m/\nu_c = 1$ and $\nu_m/\nu_c = 10$ is reported in Fig. 4.6.

We finally test how the $\alpha - F$ relation changes if we assume a structured jet with an angle-dependent comoving spectrum. In particular, we consider a spectral peak energy that is nearly constant inside an angle ϑ_c (measured with respect to the line of sight) and starts to decrease outside it. Regardless of the choice of the specific law for the angular dependence (e.g. Gaussian or power law), the HLE can reproduce the $\alpha - F$ relation only if all the analyzed GRBs have a fine-tuned value of $\vartheta_c < 1^\circ$. Such a small value of ϑ_c, on the other hand, would imply a very short steep decay, in contradiction with observations.
In conclusion, regardless of the choice of the peak energy, the bulk Lorentz factor or the radius of the emitting surface, the HLE predicts an $\alpha - F$ relation whose rise is shallower than the observed one.

HLE from finite duration pulse

If we relax the assumption of infinitesimal duration of the pulse (in the jet comoving frame), we can assume that the jet continuously emits until it switches off at a radius R_0 (Genet and Granot, 2009). For the computation of the flux as a function of time we therefore integrate the comoving intensity along the equal-arrival-time surfaces (EATS) (e.g., Fenimore et al. 1996; Dermer 2004; Genet and Granot 2009; Salafia et al. 2016. Photons emitted at different times along the EATS arrive simultaneously to the observer. Knowing that $t_{obs}(\vartheta) = t_{em}(1 - \beta\cos\vartheta)$ and imposing that $t_{obs}(\vartheta, R) = \text{const}$, the polar equation which describes the EATS is given by:

$$R(\vartheta, t_{obs}) = \frac{\beta c t_{obs}}{1 - \beta\cos\vartheta}, \tag{4.13}$$

where we have expressed the emission time as $t_{em} = R/\beta c$, in the assumption of constant expansion velocity. From the above equation, we see that our assumption that the emission switches off when the radius crosses R_0 translates to a ϑ-dependent switching off in the observer frame. At any time $t_{obs} > (1 - \beta)R_0/\beta c$the observer receives the photons emitted along a surface given by the intersection of the EATS and the jet cone, defined by $R < R_0$, $\vartheta < \vartheta_j$ and $0 < \phi < 2\pi$, where ϕ is the azimuth angle. The resulting surface extends from a minimum angle $\vartheta_{min}(t_{obs})$ out to $\vartheta = \vartheta_j$,

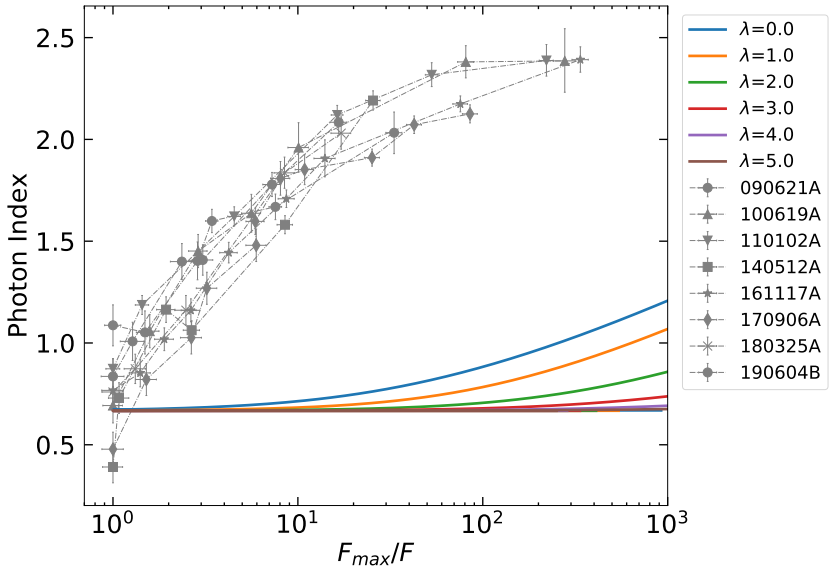

FIGURE 4.7: Spectral evolution in case of HLE from a finite-duration pulse. The adopted parameters are $R_{\rm in} = 3 \times 10^{15}$ cm, $R_{\rm off} = 9 \times 10^{15}$ cm, $\Gamma_0 = 100$ and $\nu_p = 100$ keV. The adopted spectral shape is a SBPL. The value of λ specifies the evolution of the magnetic field. The error bars represent 1σ uncertainties, calculated via spectral fitting in XSPEC. In the legend we report the name of each GRB.

where the former is given by

$$\vartheta_{\rm min}(t_{\rm obs}) = \arccos\left(\frac{1}{\beta} - \frac{ct_{\rm obs}}{R_0}\right). \tag{4.14}$$

The flux density is given by

$$F_\nu(t_{\rm obs}) = \int_{\rm EATS} I_\nu(\vartheta_{\rm obs}) \cos(\vartheta_{\rm obs})\, d\Omega_{\rm obs}, \tag{4.15}$$

where I_ν is the specific intensity and $d\Omega_{\rm obs}$ is the solid angle in the observer frame. Transforming to the comoving frame we have $I_\nu(\nu) = \mathcal{D}^3 I'_{\nu'}(\nu/\mathcal{D})$. We decompose the comoving intensity as

$$I'_{\nu'} = I'_{\nu'_p} \cdot S_{\nu'}, \tag{4.16}$$

where $I'_{\nu'_p}$ is the comoving intensity at the peak frequency ν'_p and $S_{\nu'}$ is the comoving spectral shape, normalized so that $S_{\nu'}(\nu'_p) = 1$. In general,

$I'_{\nu'_p} \propto N_{\rm tot}/R^2$, where $N_{\rm tot}$ is the number of emitting particles. If the emission process is synchrotron, $I'_{\nu'_p}$ is also proportional to B, the magnetic field as measured by an observer comoving with the jet, which is assumed to evolve as $B = B_0(R/R_0)^{-\lambda}$, with $\lambda \geq 0$ is a free parameter. If we assume $N_{\rm tot}$ to be constant in time, then $I'_{\nu'_p} \propto R^{-2}$ and, since $d\Omega_{\rm obs} \propto R^2 \sin\vartheta$, the final form of the integral is

$$F_\nu(t_{\rm obs}) \propto \int_{\vartheta_{\rm min}(t_{\rm obs})}^{\vartheta_j} S_{\nu'}(\nu/\mathcal{D}(\vartheta)) \left(\frac{R(\vartheta, t_{\rm obs})}{R_0}\right)^{-\lambda} \mathcal{D}^3(\vartheta) \sin\vartheta \cos\vartheta d\vartheta. \tag{4.17}$$

The $\alpha - F$ relation for several values of λ is plotted in Fig. 4.7. The contributions from regions $R < R_0$ are sub-dominant with respect to the emission coming from the last emitting surface at $R = R_0$, resulting in a spectral evolution still incompatible with the observations.

HLE from jet with time-dependent bulk Lorentz factor

An interesting alternative is the HLE emission from an accelerating region (Uhm and Zhang, 2015; Uhm and Zhang, 2016b; Uhm and Zhang, 2016a; Uhm et al., 2018) taking place in some Poynting flux dissipation scenarios (Zhang and Yan, 2011). For our treatment we consider that the emission starts at $R = R_{\rm in}$ and finishes at $R = R_{\rm off}$. We assume also that Γ evolves as a power law with the radius, namely

$$\Gamma(R) = \Gamma_0 \left(\frac{R}{R_{\rm in}}\right)^k, \tag{4.18}$$

with $k > 0$ if the shell accelerates or $k < 0$ if the shell decelerates. We consider the emission of a photon at radius $R_{\rm em}$ and an angle $\vartheta = \vartheta_{\rm em}$, then we define $\Delta t_{\rm em}$ the time necessary to expand from $R_{\rm in}$ to $R_{\rm em}$. During the same interval of time, a photon emitted at radius $R_{\rm in}$ and an angle $\vartheta = 0$ travels a distance $c\Delta t_{\rm em}$. Therefore the delay between these two photons is $\Delta t_{\rm obs} = (R_{\rm in} + c\Delta t_{\rm em} - R_{\rm em}\cos\vartheta)/c$. From eq. (4.18) we can write

$$\frac{1}{\sqrt{1 - \frac{1}{c^2}\left(\frac{dR}{dt}\right)^2}} = \Gamma_0 \left(\frac{R}{R_{\rm in}}\right)^k, \tag{4.19}$$

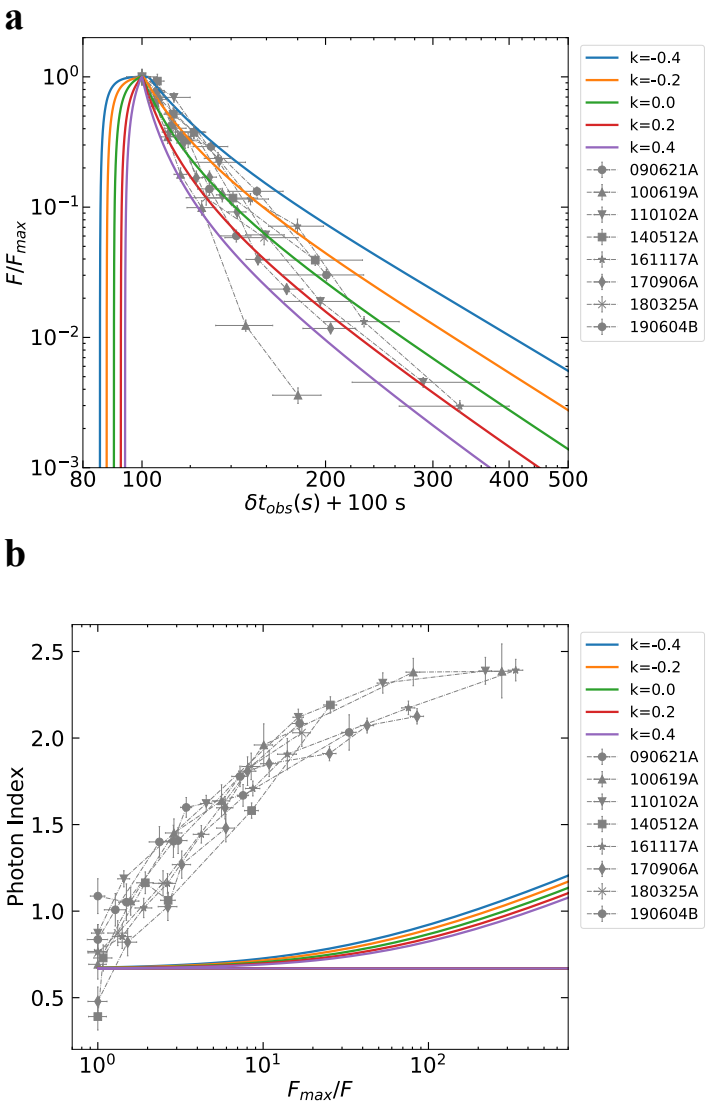

FIGURE 4.8: Temporal (a) and spectral (b) evolution for HLE from a finite-duration pulse, in case of not constant Γ. The magnetic field does not evolve with radius, i.e $\lambda = 0$. The adopted parameters are $R_{\rm in} = 3 \times 10^{15}$ cm, $R_{\rm off} = 9 \times 10^{15}$ cm, $\Gamma_0 = 100$ and $\nu_p = 100$ keV. The value of k specifies the evolution of Γ. The adopted spectral shape is a SBPL. The peak of each curve is shifted at 100 s. In **a** the vertical error bars represent 1σ uncertainties, calculated via spectral fitting in XSPEC, while horizontal error bars represent the width of the time bin. In **b** the error bars represent 1σ uncertainties, calculated via spectral fitting in XSPEC. In the legend we report the name of each GRB.

from which we derive

$$\frac{dR}{\sqrt{1-\frac{1}{\Gamma_0^2}\left(\frac{R}{R_{\rm in}}\right)^{-2k}}} = c\,dt. \tag{4.20}$$

In the limit of $\Gamma_0 \gg \left(\frac{R}{R_{\rm in}}\right)^{-k}$, we can write

$$\int_{R_{\rm in}}^{R_{\rm em}} \left[1+\frac{1}{2\Gamma_0^2}\left(\frac{R}{R_{\rm in}}\right)^{-2k}\right] dR \simeq c\Delta t_{\rm em}. \tag{4.21}$$

Thus, the delay time is

$$\Delta t_{\rm obs} = \frac{R_{\rm em}}{c}(1-\cos\theta) + \frac{1}{2c}\int_{R_{\rm in}}^{R_{\rm em}} \frac{1}{\Gamma^2} dR. \tag{4.22}$$

Given an arrival time $\Delta t_{\rm obs}$, this equation allow us to associate a radius $R_{\rm em}$ to each angle $\vartheta_{\rm em}$ through the following expression:

$$\cos\vartheta_{\rm em} = 1 - \frac{c\Delta t_{\rm obs}}{R_{\rm em}} + \frac{R_{\rm in}}{2R_{\rm em}}\frac{1}{\Gamma_0^2}\frac{1}{1-2k}\left[\left(\frac{R_{\rm em}}{R_{\rm in}}\right)^{1-2k} - 1\right]. \tag{4.23}$$

Inverting this equation, we obtain the polar equation $R_{\rm em}(\vartheta_{\rm em}, \Delta t_{\rm obs})$ which defines the EATS, namely all the photons emitted from this locus of points arrive to the observer with a time delay $\Delta t_{\rm obs}$ with respect to the first photon coming from $R = R_{\rm in}$ and $\vartheta = 0$. The computation of the flux as a function of time is again done using eq. (4.17), with the only difference that now β and Γ, which appear in the Doppler factor $\mathcal{D}(\vartheta)$, depend on $R(\vartheta)$.
The light curve and the spectral evolution for values of k in the range $-0.4 \leq k \leq 0.4$ are shown in Fig. 4.8. Even though it can explain the temporal slopes observed in the X-ray tails, also this scenario fails in reproducing the $\alpha - F$ relation.

HLE with alternative scenarios

In this section we explore other possible models of prompt emission which can drive the evolution during the X-ray tails. We first consider an anisotropic emission from the jet core, made of mini-jets (Narayan and Kumar, 2009; Barniol Duran et al., 2016; Geng et al., 2017) with angular sizes

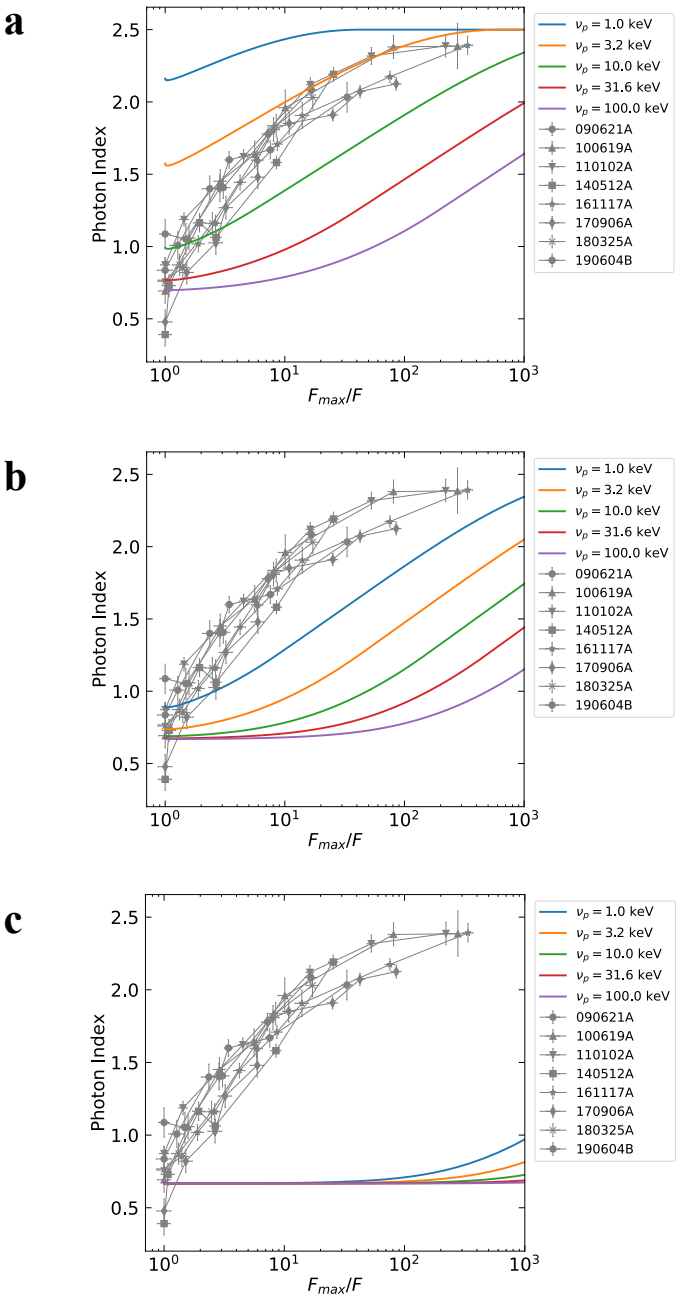

FIGURE 4.9: Predicted $\alpha - F$ relation in case of mini-jets model. We show the evolution for $n = 2$ (**a**), $n = 5$ (**b**) and $n = 10$ (**c**). The error bars represent 1σ uncertainties, calculated via spectral fitting in XSPEC. In the legend we report the name of each GRB.

$< 1/\Gamma$. In order to model such anisotropy we adopt an angular distribution of the emission in the form $P(\theta') \propto (\sin\theta')^n$, where n is the degree of anisotropy and θ' is the angle between the direction of the emitted photons and the local radial direction, as measured in the comoving frame. We evaluate the resulting HLE flux received by the observer as

$$F_\nu \propto P(\theta')\mathcal{D}^2(\theta)S\left(\frac{\nu}{P(\theta')\mathcal{D}(\theta)\nu_c'}\right), \tag{4.24}$$

where the dependence on time is implicit in θ. The resulting $\alpha - F$ relation for $n = 2$, $n = 5$ and $n = 10$ is shown in Fig. 4.9. The figure demonstrates that the larger the value of n, the more the predicted curves move away from the data. Since for $n = 0$ we are in the limit of standard HLE, which is already disfavoured by our study, we conclude that also mini-jets are not able to successfully reproduce the α - F relation.
Within the HLE scenario, only models which assume a dissipation occurring above the jet photosphere, such as in internal shocks (Rees and Meszaros, 1994) or in magnetic reconnection scenarios (Drenkhahn and Spruit, 2002; Lyutikov and Blandford, 2003), are able to reproduce the typical duration of X-ray tails ($\sim$ 100 s). Photospheric models (Pe'er, 2008), where dissipation occurs at radii $R_{\rm ph} \sim 10^{12}$ cm (Piran, 1999), give smaller times scales of $\sim 10^{-2}$ s, incompatible with observations. Only a common declining activity of the central engine (Hascoët et al., 2012; Kumar et al., 2008) and a fine-tuned intrinsic spectral softening (Beloborodov, 2011) would be required to account for the $\alpha - F$ relation.
In slow heating/reacceleration scenarios (Asano and Terasawa, 2009), as soon as the shock crosses the shell, particle acceleration is halted along with the generation of magnetic field (as both rely on the presence of shock-generated turbulence), leading to an abrupt switch-off of the emission. This leads again to HLE being the dominant effect in determining the tail flux and spectral evolution, which is clearly disfavoured by our analysis. A slower decay of the magnetic field after the shock crossing (Asano and Terasawa, 2015), along with a decaying particle acceleration, could be compatible with our results, but we still need adiabatic cooling (which is anyway unavoidable) to play the leading role in the spectral evolution, as discussed in the next section. We therefore conclude that, while the slow-heating scenario is not *per se* rejected by our results, it cannot be invoked as the main mechanism behind the α - F relation.

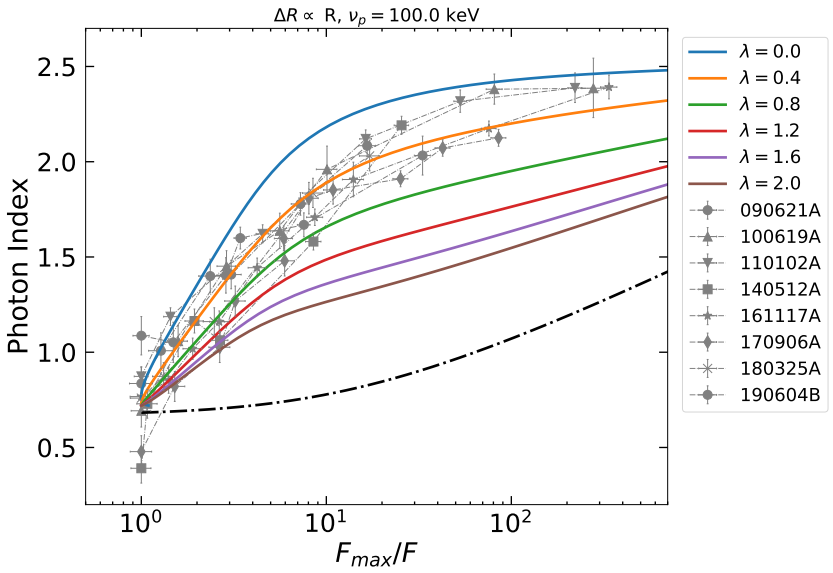

FIGURE 4.10: $\alpha - F$ plot in case of adiabatic cooling, but with the shell thickness $\Delta R \propto R$, instead of $\Delta R = \text{const}$. The theoretical curves are computed taking also into account the effect of HLE. The value of λ specifies the evolution of the magnetic field. We adopt a SBPL as spectral shape with $\alpha_s = -1/3$ and $\beta_s = 1.5$, an initial observed peak frequency of 100 keV. The dot-dashed line is the evolution expected in case of HLE without adiabatic cooling, assuming the same spectral shape and initial observed peak frequency. The error bars represent 1σ uncertainties, calculated via spectral fitting in XSPEC. In the legend we report the name of each GRB.

4.2.2 Adiabatic cooling

Since the standard HLE from efficiently cooled particles and its modified versions, as well as alternative scenarios, are not able to robustly interpret the observed $\alpha - F$ relation, we consider a mechanism based on an intrinsic evolution of the comoving spectrum. The most natural process is the adiabatic cooling of the emitting particles (Barniol Duran and Kumar, 2009). Here we assume conservation of the entropy of the emitting system $\langle\gamma\rangle^3 V'$ throughout its dynamical evolution, where $\langle\gamma\rangle$ is the average random Lorentz factor of the emitting particles and $V' \propto R^2 \Delta R'$ the comoving volume (Meszaros and Rees, 1993). We consider both thick and thin emitting regions, i.e. a comoving thickness of the emitting shell $\Delta R' = \text{const}$ or $\Delta R' \propto R$, respectively. We assume a power law radial decay of the magnetic field $B = B_0 (R/R_0)^{-\lambda}$, with $\lambda > 0$, and synchrotron radiation as the dominant emission mechanism. Here R_0 is the radius at which adiabatic

cooling starts to dominate the evolution of the emitting particles. We compute the observed emission taking also into account the effect of HLE by integrating the comoving intensity along the equal arrival time surfaces In this section we derive the effect of adiabatic cooling of the emitting particles (Panaitescu, 2019) on the light curve and the spectral evolution of X-ray tails. We assume that the emission is dominated by a single species of particles that can be treated as a relativistic gas in adiabatic expansion. We assume also that there is no interaction with other species of particles. If the particles are embedded in a region of comoving volume V', an adiabatic expansion satisfies the equation

$$\langle\gamma\rangle^3 V' = \text{const}, \tag{4.25}$$

where $\langle\gamma\rangle$ is the average Lorentz factor of the emitting particles in the comoving frame. The last equation is valid in the limit in which the adiabatic cooling timescale is smaller than the cooling time of other radiative processes, such as synchrotron or inverse Compton. Namely, particles radiate only a negligible fraction of their internal energy during the expansion of the system. Regarding the radial dependence of the volume V', we distinguish two cases:

- thick shell, with a comoving width $\Delta R'$ that does not evolve with time, hence $V' \propto R^2 \Delta R' \propto R^2$
- thin shell, with a comoving width $\Delta R'$ that evolves linearly with R, hence $V' \propto R^2 \Delta R' \propto R^3$

We assume that the dominant radiative process is synchrotron. The evolution of the spectrum in the observer frame is therefore fully determined once we know how the spectrum normalization F_{ν_p} and the peak frequency ν_p evolve in time. These two quantities, under the assumption of constant total number of emitting particles and constant bulk Lorentz factor Γ, take the following form:

$$F_{\nu_p} \propto B, \quad \nu_p \propto \langle\gamma\rangle^2 B, \tag{4.26}$$

where B is the magnetic field (assumed tangled) as measured by a comoving observer. As described in the main text, we adopt the following parametrization for the magnetic field:

$$B = B_0 \left(\frac{R}{R_0}\right)^{-\lambda}, \tag{4.27}$$

where $\lambda \geq 0$, under the reasonable assumption that magnetic field has to decrease or at most remain constant during the expansion. The value of R_0 corresponds to the radius where particles are injected, namely when adiabatic cooling starts to dominate. We use the integration along the Equal Arrival Time Surfaces (EATS) to compute the evolution of flux, as done for HLE from finite-duration pulse, with the only difference that in this case the emission never switches off. The final form of the integral is

$$F_\nu(t_{\rm obs}) \propto \int_0^{\vartheta_j} S_{\nu'}(\nu/\mathcal{D}(\vartheta)) \left(\frac{R(\vartheta, t_{\rm obs})}{R_0}\right)^{-\lambda} \mathcal{D}^3(\vartheta) \sin\vartheta \cos\vartheta d\vartheta, \quad (4.28)$$

where the factor $(R/R_0)^{-\lambda}$ comes from $I'_{\nu'_{\rm p}} \propto B$, while $\nu'_{\rm p}$ evolves in time according to eq. (4.31).

In this scenario, contrary to HLE alone, the emission from the jet is not switched off suddenly, but the drop in flux and the spectral evolution are produced by a gradual fading and softening of the source, driven by adiabatic cooling of particles. The resulting spectral evolution and light curves for the *sample 1* are shown in Fig. 4.11.

Adiabatic cooling produces a much faster softening of α as a function of the flux decay, with respect to HLE alone, in agreement with the data. Assuming a different evolution of the shell thickness, the behavior of the curves changes only marginally (see Fig. 4.10). For large values of λ the evolution of α flattens in the late part of the decay (see Fig. 4.11a), indicating that the spectral evolution becomes dominated by the emission at larger angles, rather than by adiabatic cooling in the jet core. Adiabatic cooling can also well reproduce the light curve of X-ray tails (Fig. 4.11b). For comparison, in the same plot we show the light curve given by pure HLE, adopting the same value of R_0 and Γ.

Moreover we find that GRBs from *sample 2* follow the overall $\alpha - F$ relation (Fig. 4.2b), confirming that a common physical process is governing the spectral evolution of X-ray tails. Also in this case adiabatic cooling is capable of reproducing the data (Fig. 4.12a), provided that we assume a slightly softer high energy intrinsic spectrum ($\alpha \sim 3$ instead of $\alpha \sim 2.5$). Alternatively, the introduction of an exponential cutoff in the spectral shape at $\nu = \nu_{\rm c} \sim \nu_{\rm m}$ can also reproduce the data (see Fig. 4.12b), where $\nu_{\rm c}$ and $\nu_{\rm m}$ are the synchrotron characteristic frequencies. The cutoff is formed by a combined action of adiabatic cooling and mild synchrotron cooling.

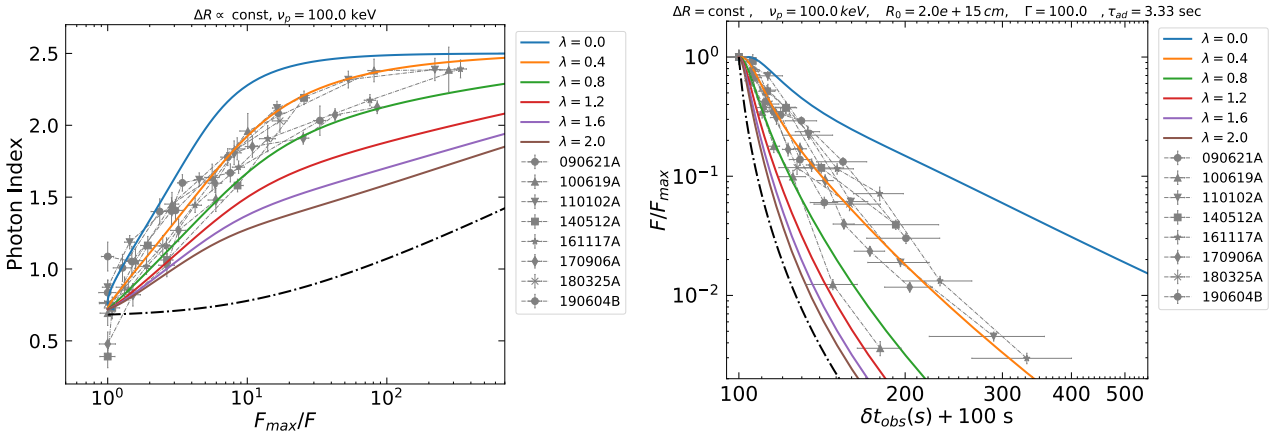

(a) (b)

FIGURE 4.11: Spectral and temporal evolution in case of adiabatic cooling. Panel (a) shows the $\alpha - F$ relation expected in the case of adiabatic cooling (solid lines). The theoretical curves are computed taking also into account the effect of HLE. The value of λ specifies the evolution of the magnetic field. We adopt a SBPL as spectral shape with $\alpha_s = -1/3$ and $\beta_s = 1.5$, an initial observed peak frequency of 100 keV and a thickness of the expanding shell that is constant in time. The dot-dashed line is the evolution expected in case of HLE without adiabatic cooling, assuming the same spectral shape and initial observed peak frequency. Panel (b) shows the temporal evolution of normalized flux expected in case of adiabatic cooling. $\delta t_{obs} + 100$ s is the time measured from the peak of the decay shifted at 100 s. We adopt the same parameters as in panel (a), assuming $R_0 = 2 \times 10^{15}$ cm and $\Gamma = 100$. The dot-dashed line is the corresponding HLE model without accounting for adiabatic cooling. $\tau_{ad} = R_0/2c\Gamma^2$ indicates the timescale of adiabatic cooling, which is the same of HLE.

A different prescription for adiabatic cooling has been suggested in the literature (Barniol Duran and Kumar, 2009), in which the particle's momentum gets dynamically oriented transverse to the direction of the local magnetic field. In this case, HLE is the dominant contributor to the X-ray tail emission, which is again incompatible with the observed $\alpha - F$ relation.

HLE vs adiabatic cooling: model comparison using Monte Carlo Markov Chain

In order to fully explore the parameter space of the HLE and adiabatic cooling models, we performed a MCMC simulation, using the emcee algorithm (Foreman-Mackey, 2013). The setup of our analysis is described

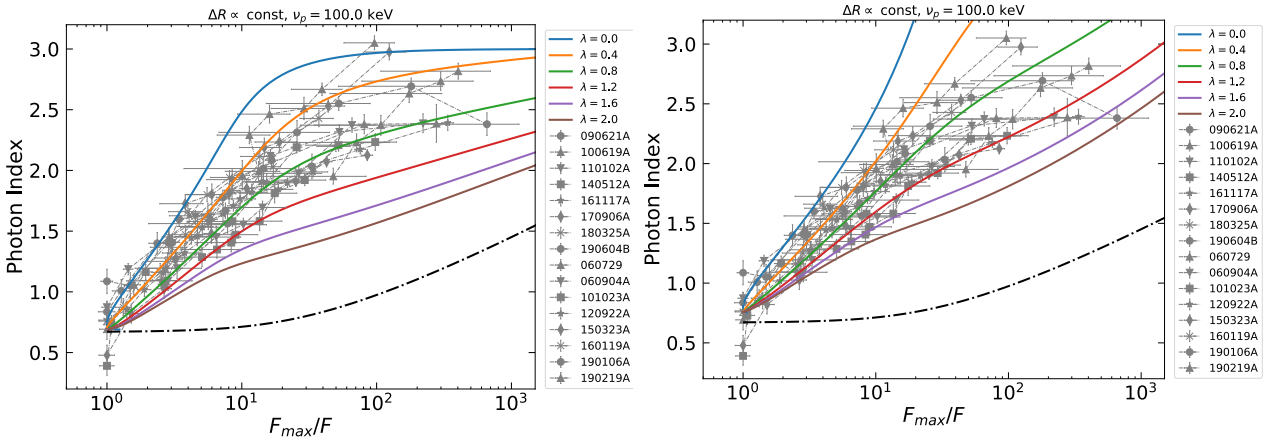

(a) (b)

FIGURE 4.12: Spectral evolution expected in case of adiabatic cooling (solid lines) superimposed to the extended sample (*sample 1+sample 2*). In panel (a) the theoretical curves are computed considering adiabatic cooling and inefficient synchrotron cooling, taking also into account the effect of HLE. The value of λ specifies the evolution of the magnetic field. We adopt a SBPL as spectral shape with $\alpha_s = -1/3$ and $\beta_s = 2.0$, an initial observed peak frequency of 100 keV and a thickness of the expanding shell that is constant in time. Panel (b) shows the spectral evolution expected in case of combined adiabatic cooling and mild synchrotron cooling. The adopted spectral shape is a SBPL plus an exponential cutoff. The initial peak frequency is 100 keV. The theoretical curves are computed taking also into account the effect of HLE. In both panels, the dot-dashed line is the evolution expected considering only HLE, assuming the same spectral shape and initial observed peak frequency.

in the following points:

1. The model contains as free parameters E_p, λ and $\tau_{ad} = R/2c\Gamma^2$, which are the peak energy at the beginning of the steep decay, the decay index of the magnetic field, and the adiabatic time scale. The inclusion of Γ as free parameter returns a flat posterior distribution, indicating that the model is insensitive to it. Therefore we performed the analysis fixing $\Gamma = 100$.

2. The MCMC in performed jointly for flux and photon index evolution. The adopted likelihood is:

$$\log(\mathcal{L}) = -\frac{1}{2}\sum_n \left[\frac{(\phi_n - \bar{\phi}(t_n))^2}{s^2_{\phi,n}} + \ln\left(2\pi s^2_{\phi,n}\right) \right] - \frac{1}{2}\sum_n \left[\frac{(\alpha_n - \bar{\alpha}(t_n))^2}{s^2_{\alpha,n}} + \ln\left(2\pi s^2_{\alpha,n}\right) \right], \tag{4.29}$$

where $\phi = F/F_{\max}$, α is the photon index and with $\bar{\phi}$, $\bar{\alpha}$ we indicate the value predicted by the model at each time t_n. Moreover,

$$s^2_{\phi,n} = \sigma^2_{\phi,n} + f_\phi \cdot \bar{\phi}(t_n), \quad s^2_{\alpha,n} = \sigma^2_{\alpha,n} + f_\alpha \cdot \bar{\alpha}(t_n), \tag{4.30}$$

where σ_ϕ and σ_α are the errors, while f_ϕ and f_α are introduced to take into account possible underestimation of the errors. Since keeping $f_\alpha \neq 0$ leads to a posterior distribution of f_α peaked around $\sim 10^{-7}$, the parameter estimation was performed fixing $f_\alpha = 0$. Instead, we keep $f_\phi \neq 0$ taking into account that the error on the flux resulting from the fitting of time-averaged spectrum may not represent the true flux error over the time bin.

3. The MCMC runs until the number of steps exceeds 100 times the autocorrelation time (its maximum) and the averaged autocorrelation time (over 100 steps) becomes constant within 1% accuracy. The burn-in is chosen as twice of autocorrelation time.

An example of corner plot obtained via MCMC is shown in Fig. 4.15. In Fig. 4.13 and 4.14, we show for each burst the observed temporal evolution of photon index and normalized flux in comparison with the curves produced with 500 random draws from the posterior sample set of the MCMC.

We performed an analogous MCMC analysis adopting the model of HLE from an instantaneous emission. However, the algorithm is unable to converge, demonstrating that the model cannot successfully match with the observations. The only way to obtain converged chains by this model is to admit extreme and unrealistic values of f_ϕ, of the order $10^4 - 10^8$. The only exception is GRB 090621, which can be fitted by HLE alone. This is the only case where it is meaningful to compute the Bayes factor between HLE and AC, which results to be ~ 200. Thus we prove that the adiabatic cooling model is strongly preferred for all the analyzed cases.

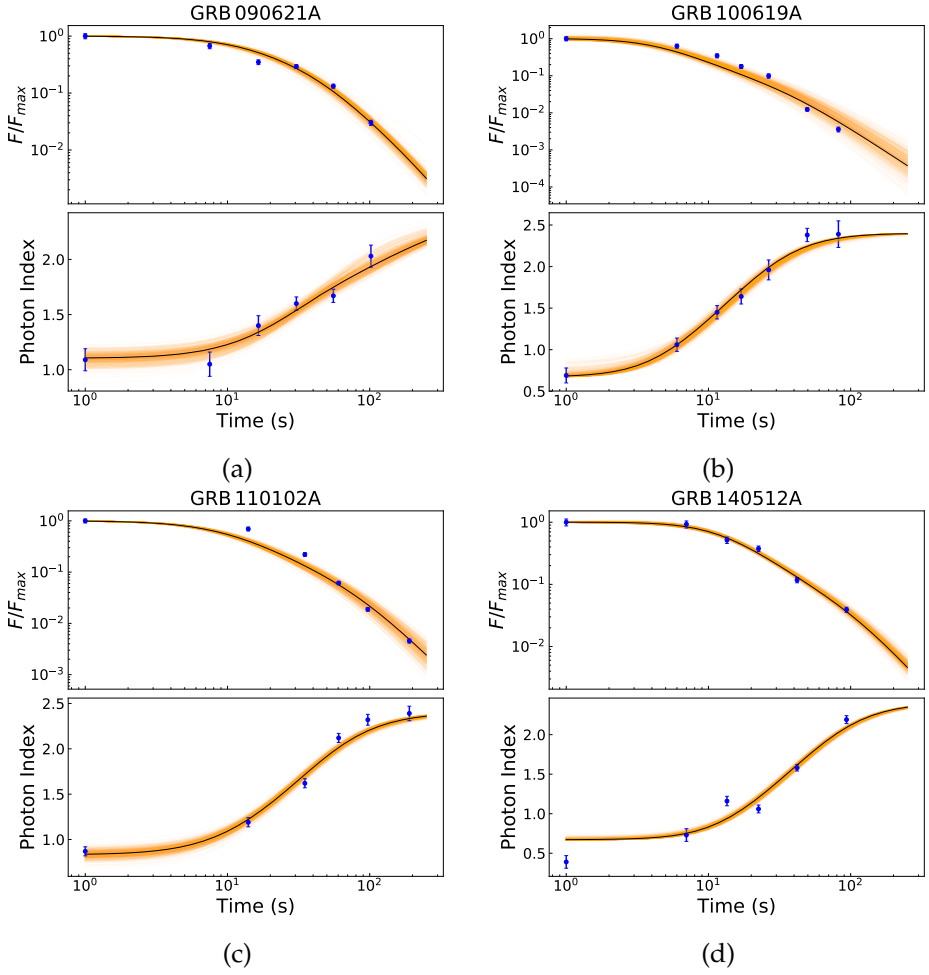

FIGURE 4.13: Joint temporal evolution of normalized flux and photon index. For each GRB we compare the data (blue points) with the best fit curve of the adiabatic cooling model (black line). The orange lines are curves produced extracting randomly the model parameters from the posterior distribution obtained from the MCMC.

The model comparison (adiabatic cooling + HLE against HLE-only) is also done assuming different spectral shapes: SBPL, Band and synchrotron. The spectral parameters are the same as those adopted before. For synchrotron, we use $\nu_c = \nu_m$ (the case $\nu_c \neq \nu_m$ does not improve the goodness of fit). In order to compare the goodness of fit of the two models, we used the Akaike Information Criterion (AIC), which is defined as $\mathrm{AIC} = 2k - 2\ln(\mathcal{L})$, where k in the number of parameters of the model, and $\mathcal{L}$ is the best fit likelihood, that is, $2\ln(\mathcal{L}) = -\chi^2$. In Tab. 4.1 we show

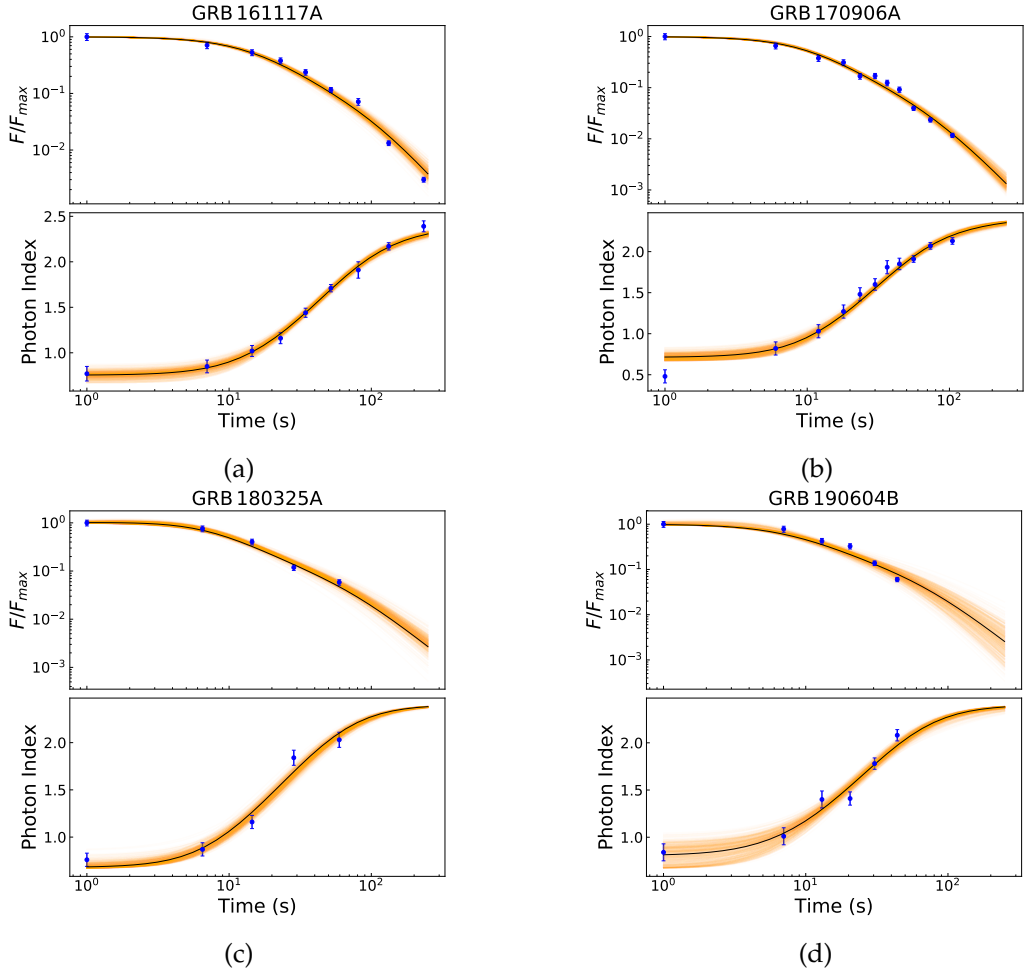

FIGURE 4.14: Continuation of Fig. 4.13.

the value of $\Delta_{\rm AIC} = {\rm AIC_{HLE}} - {\rm AIC_{AC}}$ for each spectral shape. For all cases, the adiabatic cooling is significantly favoured with respect to HLE.

Best fit parameters of the adiabatic cooling model and relative interpretation

The best fit parameters of the adiabatic cooling model are summarized in Tab. 4.2. The uncertainties are reported based on the 16th, 50th, and 84th percentiles of the samples in the marginalized distributions (1σ level of confidence). We obtain a value of λ in the range $0.4 - 0.7$ (except for 090621A which prefers $\lambda \sim 2$). On average, these values of λ are smaller than those expected in an emitting region with a transverse magnetic field ($\lambda = 1$ or

GRB	$(\Delta_{AIC})\|_{SBPL}$	$(\Delta_{AIC})\|_{Band}$	$(\Delta_{AIC})\|_{Sync}$
090621A	8	6	9
100619A	69	66	67
110102A	145	141	145
140512A	193	190	43
161117A	132	124	133
170906A	148	135	145
180325A	80	76	91
190604B	61	59	65

TABLE 4.1: Comparison of best fit statistics between Adiabatic Cooling (AC) and HLE, adopting a SBPL, a Band function or a synchrotron spectrum, using the Akaike Information Criterion (AIC). The large values of $(\Delta_{AIC})|_{spectrum} = (AIC_{HLE} - AIC_{AC})|_{spectrum}$ indicate that, regardless of the assumed spectral shape, the HLE from efficiently cooled particles is strongly disfavoured with respect to the adiabatic cooling model.

GRB	E_{peak} (keV)	λ	τ_{ad}(s)
090621A	18^{+3}_{-2}	$2.11^{+0.56}_{-0.54}$	$24.4^{+4.7}_{-3.0}$
100619A	> 129	$0.47^{+0.11}_{-0.07}$	$0.3^{+1.0}_{-0.2}$
110102A	46^{+15}_{-9}	$0.61^{+0.10}_{-0.10}$	$5.8^{+1.9}_{-1.1}$
140512A	> 323	$0.48^{+0.04}_{-0.03}$	$0.9^{+0.9}_{-0.4}$
161117A	80^{+55}_{-21}	$0.69^{+0.10}_{-0.10}$	$6.2^{+2.0}_{-2.3}$
170906A	135^{+204}_{-53}	$0.66^{+0.10}_{-0.09}$	$3.0^{+1.6}_{-1.5}$
180325A	> 122	$0.39^{+0.06}_{-0.05}$	$0.8^{+1.3}_{-0.5}$
190604B	54^{+227}_{-20}	$0.45^{+0.25}_{-0.15}$	$3.5^{+2.6}_{-2.8}$

TABLE 4.2: Results of the parameter estimation via MCMC, adopting the adiabatic cooling model. The confidence intervals and the lower limits represent the 16th, 50th, and 84th percentiles of the samples in the marginalized distributions (i.e. 1σ level of confidence).

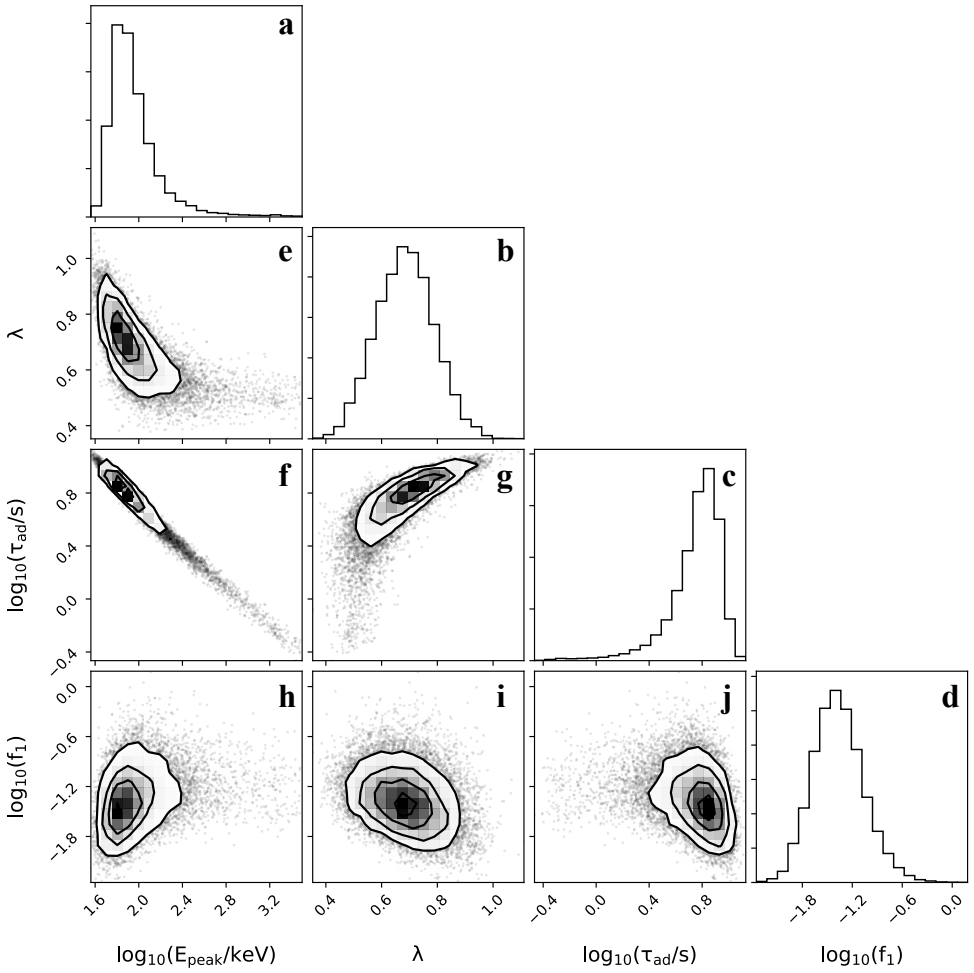

FIGURE 4.15: An example of corner plot from the MCMC (GRB 161117A). $E_{\rm peak}$ is the peak energy at the beginning of the steep decay, λ is the decaying index of magnetic field (adimensional parameter), $\tau_{\rm ad}$ is the adiabatic timescale, f_1 is a parameter used in the definition of the likelihood (see the methods section in the main text for further details). The panels **a-d** show the 1D posterior probability distribution of each parameter; since the y axis is a measure of probability density, it has an arbitrary scale. The panels **e-j** show the 2D posterior distribution for each couple of parameters and the contour lines represent the confidence regions at 0.5σ, 1σ, 1.5σ and 2σ level of confidence (if only 3 contours are visible, this means that the inner one, corresponding to 0.5σ, is so small that it is reduced to a point and is not shown).

$\lambda = 2$ for a thick or a thin shell, respectively) or magnetic field in pressure equilibrium with the emitting particles ($\lambda = 4/3$ or $\lambda = 2$ for a thick or a thin shell, respectively, Mészáros and Rees 1999).
The typical timescale of adiabatic cooling $\tau_{\rm ad} = R_0/2c\Gamma^2$, i.e. the observed time interval during which the radius doubles, is equal to the HLE timescale (Fenimore et al., 1996; Sari and Piran, 1997) and radically affects the slope of X-ray tails. Therefore, the comparison between the model and the observed light curves allows us to constrain the size R_0 of the emitting region as in HLE (Lyutikov, 2006; Lazzati and Begelman, 2006). We find values in the range $0.3\,{\rm s} \lesssim \tau_{\rm ad} \lesssim 24\,{\rm s}$. These values are quite larger than the typical duration of GRB pulses (<1 sec, Walker et al. 2000), which can be due to the following reason. For the spectral analysis to be feasible, we had to choose only tails that are long enough (to be divided down into a sufficient number of temporal bins). Moreover, the prompt emission is usually interpreted as a superposition of several emission episodes: the steep decay observed in XRT is likely dominated by the tails with the slowest decay timescales. Since, in our model, the decay timescale is $\tau_{\rm ad} = R/2c\Gamma^2$, this could indicate that the emission radius of the pulses that dominate the tail is systematically larger than that of pulses that dominate the prompt emission. If this is the case, a lower magnetic field is also expected, which goes well along with the long radiative timescale and slow (or marginally fast) cooling regime, in agreement with our results. For the range of $\tau_{\rm ad}$ obtained from the analysis, the corresponding range for the emission radius is $1.8 \times 10^{14}(\Gamma/100)^2\,{\rm cm} \lesssim R_0 \lesssim 1.4 \times 10^{16}(\Gamma/100)^2\,{\rm cm}$.
Even if HLE and adiabatic cooling have the same timescale ($\tau_{\rm ad} = R/2c\Gamma^2$), the relevance of one process with respect to the other is determined by the decay of the magnetic field, which governs the drop of the spectrum normalization. The expected value of λ can be derived in several scenarios, according to the process that rules the magnetic field evolution. In case of conservation of magnetic flux, the perpendicular and parallel component of B evolve as $B_\perp \sim 1/(\Delta R' \cdot r)$ and $B_{//} \sim r^{-2}$, where r is the transverse radial dimension of the jet in a cylindrical reference system (r, ϕ, z). If the jet is conical then $r \propto R$, leading to $B \sim R^{-1}$ ($\lambda = 1$) for $\Delta R' = {\rm const}$ and $B \sim R^{-2}$ ($\lambda = 2$) for $\Delta R' \propto R$. Another possibility predicts equipartition between magnetic energy density and particle energy density, giving $B^2 \sim \langle\gamma\rangle / V \sim V^{-4/3}$, where in the last step we used eq. (4.31). In this case $B \sim R^{-4/3}$ ($\lambda = 4/3$) for $\Delta R' = {\rm const}$ and $B \sim R^{-2}$ ($\lambda = 2$) for $\Delta R' \propto R$. All these predicted values of λ are larger than the range found from our analysis. Such tension can be solved, for instance, if the shell thickness decreases as the jet expands, or if the jet is not conical (e.g. paraboloidal, with

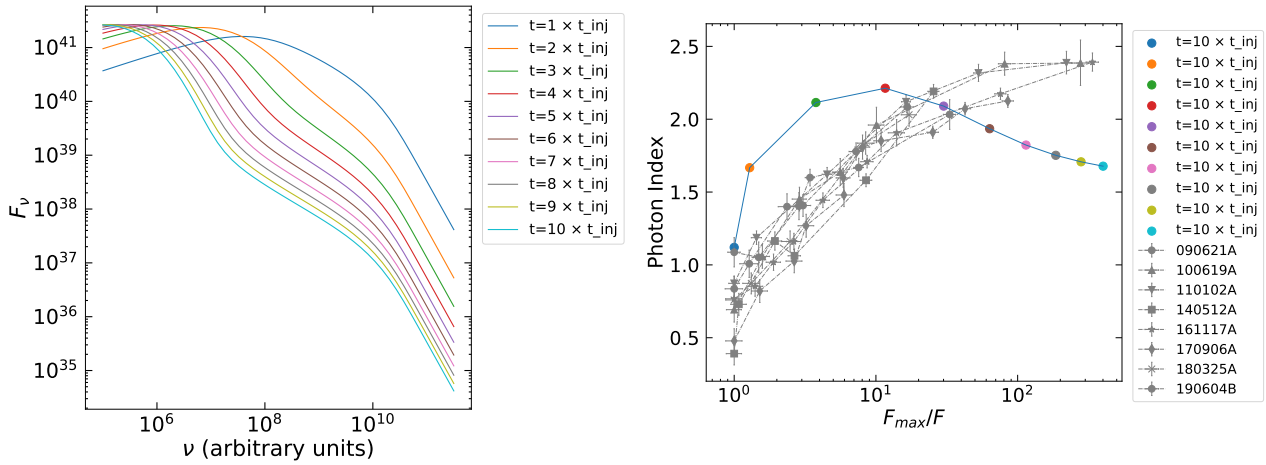

(a) (b)

FIGURE 4.16: Spectral evolution of the synchrotron spectral shape for a decaying particle injection. Panel (a) shows how the spectral shape evolves, adopting a decaying index for the injection rate $y = 3$ and a constant magnetic field. The time goes from $t = t_{\rm inj}$ (blue line) up to $t = 10 \times t_{\rm inj}$ (cyan line), with steps of $t_{\rm inj}$. In panel (b) the blue line shows the corresponding $\alpha - F$ relation imposing that the observing band is below the initial spectral peak, which ensures that the initial photon index is $\sim 2/3$. With different coloured points we indicate the evolution in the $\alpha - F$ plane as a function of time, from $t = t_{\rm inj}$ (blue point) up to $t = 10 \times t_{\rm inj}$ (cyan point), with steps of $t_{\rm inj}$.

$r \propto \sqrt{R}$).

4.2.3 Impact of temporal evolution of the comoving spectral shape on the $\alpha - F$ relation

In the derivation of spectral evolution from adiabatic cooling, we implicitly assumed that we are in the early post-prompt phase, namely where no more particles are injected/accelerated and the particle distribution only evolves according to the cooling processes. If adiabatic cooling is dominant, the energy of all particles evolve at the same way, according to the following equation:

$$\gamma^3 V' = \text{const}, \tag{4.31}$$

where γ is the Lorentz factor of the particle and V' is the comoving volume. Therefore the shape of the particle distribution, and hence of the spectrum, does not change in time, but is only rigidly shifted at lower energies.

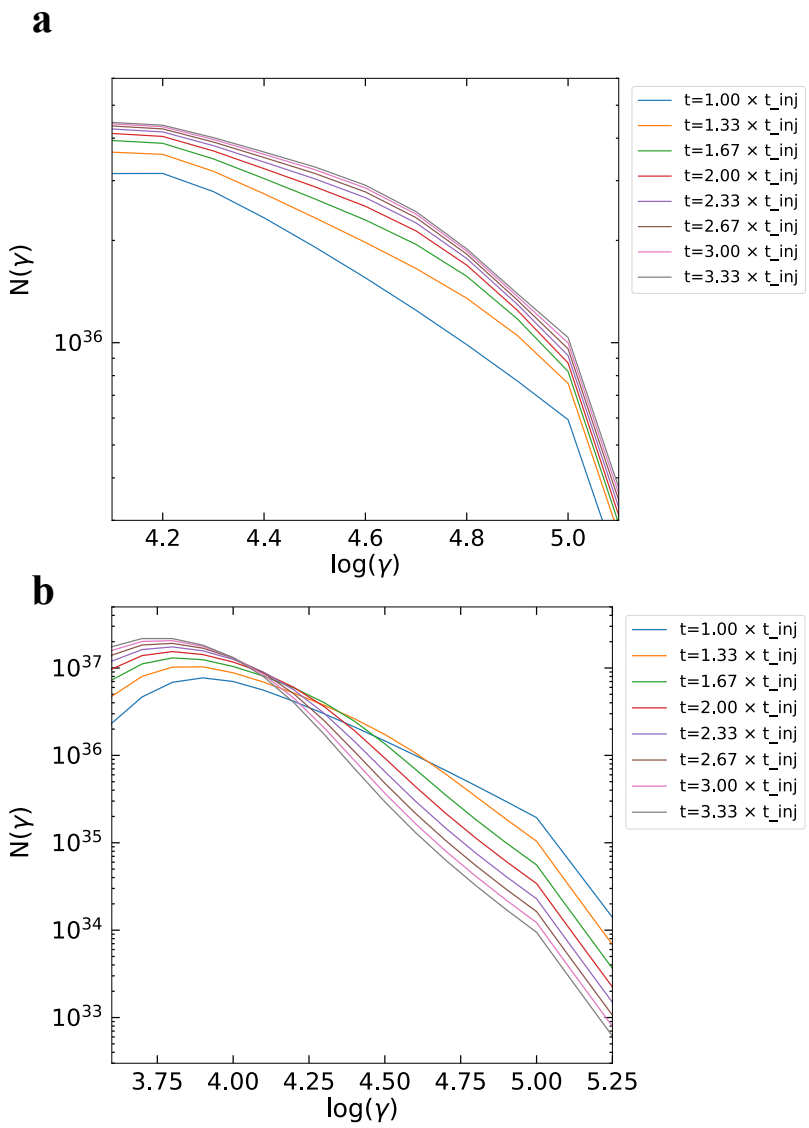

FIGURE 4.17: Temporal evolution of the particle distribution for a decay of both $\dot{N}_{\rm inj}$ and magnetic field. The adopted parameters are $y = 2$ and $\lambda = 2$ for **a**, $y = 4$ and $\lambda = 1$ for **b**. The evolution is followed from $t = t_{\rm inj}$ (blue line), which is the standard γ^{-2} cooling branch of the distribution) up to $t = 3.33 \times t_{\rm inj}$ (grey line), with steps of $\sim 4/3\, t_{\rm inj}$.

If adiabatic and radiative cooling are competing on comparable timescales, in the post-prompt phase an exponential cutoff appears above the cooling energy γ_c. If also the magnetic field decays, the adiabatic cooling tends to

dominate with time and also the cutoff energy would eventually evolve according to eq. 4.31, going again in the limit of rigidly shifted spectrum.
The assumption of rigidly shifted spectrum might not hold if the particle injection gradually decreases in time, instead of ceasing abruptly. The temporal evolution of particle distribution in case of decreasing injection of particles is studied solving numerically the cooling equation

$$\frac{\partial N}{\partial t} = \dot{N}_{\rm inj} - \frac{\partial}{\partial \gamma}(N\dot{\gamma}), \tag{4.32}$$

where $N(\gamma) = dN_{\rm e}/d\gamma$ ($N_{\rm e}$ being the number of emitting particles). The resulting evolution of the synchrotron spectrum is shown in Fig. 4.16a, where we assumed an injection term of the form $\dot{N}_{\rm inj} \propto (t/t_{\rm inj})^{-y}$, with $y > 0$, and a constant magnetic field. Imposing that, at the beginning, the F_ν peak is just above the observing band, the resulting spectral evolution would be an initial softening followed by a hardening, as shown in Fig. 4.16b. In the case of a decay of both the magnetic field and $\dot{N}_{\rm inj}$, the corresponding effects on the spectral shape tend to compensate each other (Panaitescu, 2019), giving a bare modification of the spectral shape or even a hardening (see Fig. 4.17). In conclusion, intrinsic modifications of the spectral shape can hardly give an agreement with data comparable to the case of a rigidly shifting spectrum.

4.3 Conclusions

The $\alpha - F$ relation, found in our analysis, requires a mechanism that produces the X-ray tails of GRBs with a unique law of flux decay and spectral softening. Although other scenarios cannot be ruled out, we find that adiabatic cooling of the emitting particles, together with a slowly decaying magnetic field, is the most plausible scenario able to robustly reproduce this relation. Our results suggest an efficient coupling between a slowly decaying magnetic field and the emitting particles. Our findings are generally in agreement with moderately fast and slow cooling regimes of the synchrotron radiation, which is able to reproduce the overall GRB spectral features (Zhang, 2020). In the adiabatic cooling scenario, most of the internal energy is not radiated away before the system substantially expands. If electrons are responsible for the emission, an extremely small magnetic field would be required (Kumar and McMahon, 2008; Beniamini and Piran, 2013; Beniamini et al., 2018), which is unrealistic for this kind

of outflows. Protons radiating through synchrotron emission can solve this problem (Ghisellini, 2020). Due to their larger mass, they radiate less efficiently than electrons, explaining why adiabatic cooling dominates the spectral evolution.
In conclusion, our results indicate that adiabatic cooling can play a crucial role for the collective evolution of the radiating particles in GRB outflows and consequently for the determination of spectral and temporal properties of prompt emission episodes. The coupling between particles and magnetic field ensures the intrinsic nature and hence the universality of this process, whose effects are independent of the global properties of the system, such as the luminosity of the GRB or the geometry of the jet. The full work presented in this chapter has been published in Ronchini et al., 2021.

4.3.1 Impact of this study on the detectability of GRBs in the multi-messenger context

The investigation of the prompt emission characteristic features is crucial if we need to evaluate the detectability of GRBs with future high-energy instruments. This, in turn, has deep impact on the prediction of future multi-messenger detection of GRBs. In this regard, the role of the X-ray steep decay could be relevant for the following reasons:

1. The prompt tail is clearly visible in the X-rays and it is characterised by a gradual transition of the spectral peak towards lower energies. This means that X-ray missions are ideal to continuously monitor the full transition from the prompt to the afterglows phases. Depending on the emission radius, Lorentz factor, jet structure and dominating cooling processes, the typical duration of prompt tails can be comparable or even larger than the duration of the prompt emission itself. This implies that, taking into account the expected improvement of future X-ray detectors, thanks to the relatively long duration of the steep decay we will be able to perform detailed temporally-resolved spectral analysis, as described in this chapter.

2. Currently, a considerable fraction of X-ray steep decays is missed due to observational limitations. One of these is the amount of time δt_{slew} needed by Swift to point XRT in the GRB direction. This means that, if the prompt tail starts at a time t_0 after the trigger and lasts $\sim \delta t$, the steep decay is missed if $\delta t_{slew} > t_0 + \delta t$. This is commonly expected for short GRBs, where usually $t_0 \ll \delta t_{slew}$. In the future, sensitive

wide-field X-ray monitors such as THESEUS, or Einstein Probe, will have the chance to monitor the X-ray light curve from the trigger time, allowing us to follow in detail the temporal and spectral evolution of the steep decay. As shown in Sec. 4.4.1, the results of this chapter have been exploited to perform a detailed assessment of the potentialities of THESEUS for the investigation of the prompt emission and X-ray steep decay (Ghirlanda et al., 2021).

3. In relation to the previous point about the detectability of short GRBs, a precious help can come from 3G GW detectors. Indeed, as it will be thoroughly discussed in Chapter 6, the access at lower frequencies and the high signal-to-noise ratio by 3G detectors will make it possible to detect the GW signal before the merger and circulate early warning alerts containing information about the sky location of the source. This will enable us to point high-energy satellites toward the source direction to catch the very first phases of the prompt emission. This, in turn, would give the possibility to monitor the X-ray steep decay also for short GRBs, possibly revealing helpful information about the nature of the prompt emission

4. As shown in Ascenzi et al., 2020a, if the GRB is observed off-axis, the prompt emission is fainter, but with a tail which has a less steep decline. This means the possibility to monitor the prompt-to-afterglow transition for a longer time. In addition, longer exposure times would decrease the minimum detectable flux. The detection and characterisation of off-axis prompt tails will give the chance to investigate the jet structure and, in turn, its role for the multi-messenger detection of GRBs.

4.4 Future prospects

4.4.1 The X-ray steep decay observed with THESEUS

As we mentioned before, one of the main current limitations of Swift is that the soft X-ray emission ($\sim 1 - 10$ keV) cannot be monitored from the very first instants after the GRB trigger. This represents an obstacle for a systematic and complete analysis of the X-ray steep decay. Future missions, such as THESEUS, will overcome this problem, thanks to the presence of a wide field instrument, SXI, sensible in the soft X-rays.
I evaluated the potential of THESEUS/SXI regarding the investigation of

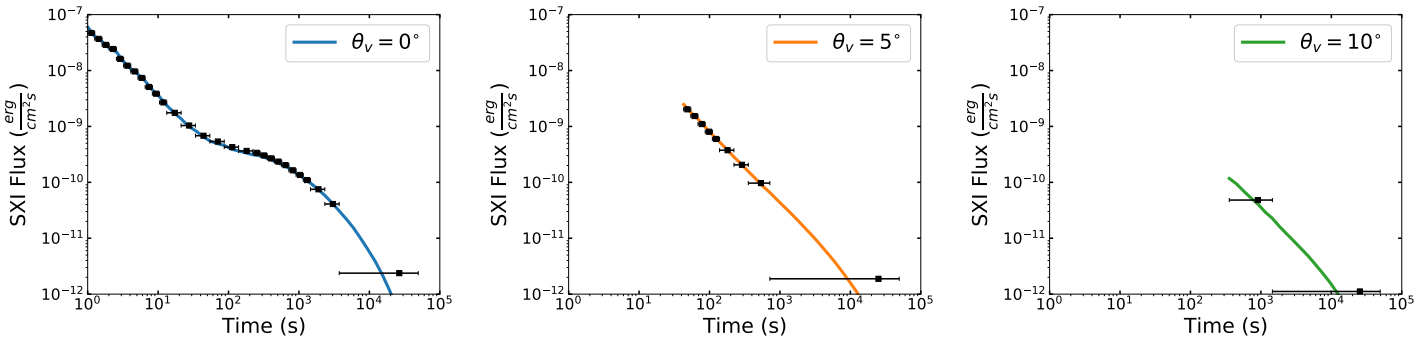

(a) (b) (c)

FIGURE 4.18: Temporal sampling of THESEUS-SXI of the HLE from a structured jet, at different viewing angles. The source is located at $z = 0.5$. Figure adapted from Ghirlanda et al., 2021.

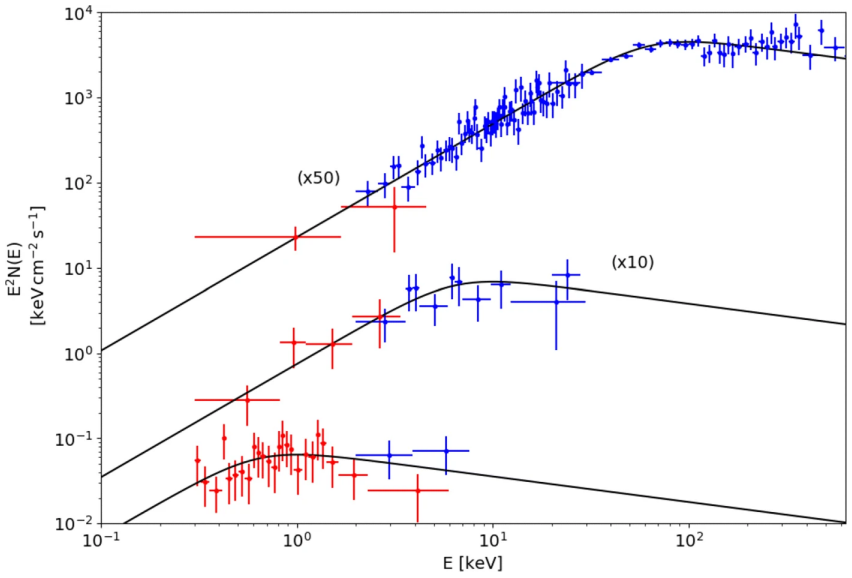

FIGURE 4.19: Simulated reconstruction of the spectral evolution during and after the steep decay, using both XGIS and SXI.

the steep decay, testing its capacity both for the temporal sampling and for the monitoring of the spectral evolution. In order to model the early X-ray light curve, we assume that the emission is dominated by the HLE from a structured jet. Moreover, we introduce for simplicity an empirical evolution of the spectrum, where the peak energy decays as t^{-1}, while the

Time $[s]$	$\alpha_{\rm Input}$	$\beta_{\rm Input}$	$E_{\rm p,\,Input}$ [keV]	α	β	$E_{\rm p}$ [keV]
10	-0.67	-2.3	100	-0.74 ± 0.04	-2.27 ± 0.08	120^{+10}_{-8}
100	-0.67	-2.3	10	$-0.72^{+0.27}_{-0.25}$	< -2.20	$7.8^{+3.5}_{-1.6}$
1000	-0.67	-2.3	1	$-1.12^{+0.50}_{-0.28}$	< -2.3	$1.87^{+0.58}_{-0.47}$

TABLE 4.3: Comparison between injected and recovered parameters by SXI+XGIS, for the analysis of the spectral evolution during and after the steep decay.

spectral shape remains unchanged[2]. The assumed structure is:

$$\Gamma(\vartheta) = (\Gamma_0 - 1)\,\frac{1}{1 + (\vartheta/\vartheta_c)^s} + 1$$
$$\epsilon(\vartheta) = \frac{1}{1 + (\vartheta/\vartheta_c)^s},$$

where $\Gamma(\vartheta)$ and $\epsilon(\vartheta)$ are the structures of the bulk Lorentz factor and the emissivity, respectively, with $\vartheta_c = 2^\circ, \Gamma_0 = 200$ and $s = 2.5$. We also assumed an emission radius $R_0 = 5 \times 10^{15}$ cm and a prompt luminosity $L_{iso} = 10^{52}$ erg/s. The normalisation of the light curve is chosen in such a way that the peak luminosity in the soft X-rays is $L_X = 10^{-3} L_{iso}$. The light curve is computed at different viewing angles, $\vartheta_c = 0^\circ$, $\vartheta_c = 5^\circ$ and $\vartheta_c = 10^\circ$. The details to produce the angle-dependent light curve for a structured jet are reported in Appendix B.1. The distance of the GRB is fixed at $z = 0.5$. The temporal sampling is obtained knowing the SXI sensitivity as a function of the exposure time. The results, shown in Fig. 4.18, demonstrate that THESEUS is able not only to monitor in detail the soft X-ray emission from the GRB trigger, including the steep decay, but also to detect the HLE up to a viewing angle $\sim$ few θ_c. First, this has a relevant impact for the investigation of the jet structure and its role for the appearance of the X-ray light curve. A systematic monitoring from the GRB trigger for an extended sample of GRBs can allow us to test whether a universal jet structure is a viable scenario. Second, the possibility to detect also off-axis events is a major advantage for the study of sub-luminous GRB, orphan GRBs, to perform more accurate population studies and improve our knowledge of

[2] As we saw in this chapter, HLE alone could be not enough to model the X-ray steep decay and its spectral evolution. Though, we work in the rough approximation that HLE dominates the flux and spectral evolution, since this simplification has a marginal effect on the determination of the THESEUS performances.

the GRB luminosity function.
THESEUS has also the right requirements to analyse in detail the spectral evolution from the initial stages of the prompt emission up to the late time afterglow, thanks to the wide spectral coverage offered by the combination of SXI+XGIS. In order to test the instrumental performances in this regard, we test how the spectral parameters would be recovered considering three temporal bins in the light curve of Fig. 4.18(a), at 10 s, 100 s, and 1000 s, roughly corresponding to the beginning of the steep decay, the transition from steep decay to plateau and the end of plateau, respectively. The spectrum is assumed to be a SBPL and the injected parameters are $\alpha = -0.67$, $\beta = -2.3$ and an initial peak energy $E_p = 100$ keV. The simulated spectra are reported in Fig. 4.19, while the comparison between injected and recovered parameters is shown in Tab. 4.3.
These results show how missions like THESEUS will allow us to repeat more in detail and in a systematic way the analysis presented in this chapter. The wide spectral coverage of XGIS+SXI is essential to monitor the spectral evolution in the prompt phase, during its tail and in the transition to the afterglow phase, with the possibility of discerning between available physical scenarios. The wide field of both XGIS and SXI is also crucial to monitor the very early stages of the soft/hard X-ray emission of short GRBs, whose steep decay phase is still very poorly investigated, due to the limitations of current instruments. Moreover, the so called *extended emission* of short GRBs can be studied more in detail, whose origin is still unclear (Ciolfi et al., 2021). The analysis and the results for the THESEUS performances presented in this section have been reported in Ghirlanda et al., 2021, where the authors show a comprehensive estimation of the impact and potentiality of THESEUS for the open question of the GRB physics.
Similarly to THESEUS, also the space mission SVOM is expected to have comparable performances in the analysis of the spectral evolution during the early phases of the GRB emission. This is possible thanks to the ECLAIRs coded mask telescope, whose sensitive band extends down to 4 keV, giving the possibility to monitor the full prompt emission tail, even when the spectral peak migrates towards the soft X-rays.

Chapter 5

The origin of the X-ray plateau

In this chapter we focus our attention on the X-ray plateau, another phase of the afterglow light curve whose origin and interpretation are still debated. The standard emission from a decelerating forward shock can hardly explain such a flat temporal behaviour and alternative scenarios have to be taken into account. Here we report a detailed statistical study of a sample of GRBs with an X-ray plateau, exploring the connection between different observables. This study is then followed by a combined optical/X-ray spectral and temporal analysis during the plateau phase. The observational results are discussed in terms of emission process, and comparing several physical scenarios, including the energy injection from a spinning down magnetar and the high latitude emission from a structured jet. The work and results presented in this chapter are summarised in Ronchini et al., 2022b, currently submitted for publication.

The X-ray plateau was first discovered thanks to the new capabilities of Swift. The unique level of detail of the Swift-XRT light curves allowed us to verify that in a large fraction of GRBs[1] the X-ray light curve deviates from a standard power law decline expected in the case of emission from an external shock decelerating in the ISM. One possible scenario which can explain a plateau phase in X-ray light curves assumes the injection of additional energy into the forward shock, due to late time activity of the central engine. This last can be connected either to late-time fall-back material on a BH or to the spin-down radiation from a fast rotating magnetar (Dai and Lu, 1998b; Zhang and Mészáros, 2001b; Dall'Osso et al., 2011; Metzger et al., 2011; Bucciantini et al., 2012). In such scenarios we do not see directly the emission of the central engine, but rather the emission from the external shock which is re-energised by the central engine activity.
A weak point against the validity of the energy injection scenarios is the evidence of chromatic behaviours of the X-ray and optical light curves (e.g., Panaitescu et al. 2006). Indeed, for those GRBs that do not show a spectral transition across the end time of the plateau, the post-plateau phase should not be related to the evolution of the spectrum, but rather to an overall decay of the bolometric flux. This would imply that both X-ray and optical light curves should have a common trend, which is not usually observed (e.g. Li et al. 2012; Li et al. 2015). Chromaticity is observed in several forms: 1) both X-ray and optical light curves show a shallow-to-normal decay, but with different break times, 2) the optical does not show at all a temporal break, 3) the optical light curve presents a completely different morphology, consisting in single or multiple bumps that overlap to the normal power law decay. While the first two cases can still be interpreted in the energy injection scenario assuming a spectral break between optical and X-rays, the third evidence can be hardly contemplated by energy injection scenarios.
Another evidence which weakens the validity of the energy injection scenario is the presence in several GRBs of an X-ray plateau followed by a very steep decline (temporal slope $> 2 - 3$). Such sudden drop of the light curve is incompatible with an external shock origin, since this would require an un-physically small angular time scale, much smaller than the dynamical time scale $R/2c\Gamma^2$. Hence, since the origin is plausibly connected to an internal dissipation process (i.e., below the external shock radius), a plateau followed by a steep decline is also known as *internal plateau*. Evidences of

[1]The exact fraction can change study by study, due to the quite strong dependence on the selection criteria used to define the plateau sample. The differences may consist in the specific functions used to fit the X-ray light curve, the requirement about the plateau temporal slope, the availability of redshift or further cuts based on the data quality.

internal plateaus are available both for long (Troja et al., 2007; Lyons et al., 2010) and short (Rowlinson et al., 2010; Rowlinson et al., 2013) GRBs.
One possible solution, for both the evidence of chromaticity and internal plateaus, may be the interpretation of the X-ray plateau as direct signature of a wind powered by a spinning-down magnetar. Contrary to the energy injection scenario, in this case the X-ray emission is directly coming from the wind and the radiation is not reprocessed by the external shock. The evolution and EM signature of a magnetar wind has been investigated both in the case of a collapsar scenario (Metzger et al., 2014) and a BNS merger scenario (Metzger and Piro, 2014; Ciolfi and Kalinani, 2020). In both cases, the magnetar spin-down generates a wind of e^-/e^+ pairs followed by an EM cascade, which ionises the circum-burst medium. Such radiation is initially trapped and tends to thermalise, until the medium expands enough to become optically thin. In this case the expected EM transient would appear hours/days after the magnetar formation and it would peak in the optical/UV with a quasi-thermal spectrum. If instead the e^-/e^+ pairs are bright enough, the associated EM cascade can fully ionise the circum-burst medium. This prevents the fully thermalisation of the spectrum and an earlier non-thermal X-ray transient is expected, whose luminosity reflects the spin-down evolution of the magnetar. In this scenario the sudden transition between the plateau phase and a very steep decline is identified as the collapse of the meta-stable NS into a BH. Though, notice that also the magnetar scenario as GRB central engine has some caveats and criticisms, as pointed out by Beniamini et al., 2017.
If the magnetar wind is a distinct component with respect to the external shock, then it is natural to expect that the two components are dominant at different times and we could observe the transition from one emission site to the other. This is what has been claimed by Hou et al., 2021, which find several light curves following this behaviour:

$$F_X \propto \begin{cases} t^{-\alpha_1} & t < \tau \\ t^{-\alpha_2}, & \tau < t < t_c \\ t^{-q}, & t > t_c \end{cases},$$

where the first two segments with $\alpha_1 \sim 0$, $\alpha_2 \sim 2$ represent the plateau and post-plateau decay, while for $t > t_c$ the forward shock emission starts to dominate. Generally, in the magnetar scenario, a value of $\alpha_2 \sim 2$ indicates that the light curve follows the spin-down luminosity which decays as t^{-2} as soon as $t > \tau_{SD}$, while a value $\alpha_2 \gg 2$ points toward a direct collapse into a BH at $t_{coll} \sim \tau$.

The X-ray plateau is also characterised by an empirical relation (Dainotti et al., 2010), which relates the plateau luminosity L_p with its duration t_p. The general agreement, almost independent on the sample selection criteria, is that $L_p \propto t_p^{-1}$, even if, due to the large intrinsic scatter, this relation is far from being universal. Such a correlation would have a direct interpretation in the framework of the magnetar scenario. Indeed the plateau luminosity is a direct proxy of the initial spin down power, while the end of the plateau occurs at a time which is around the spin down time scale τ_{SD} (Dainotti et al., 2016; Dainotti and Del Vecchio, 2017; Stratta et al., 2018). Therefore a relation $L_p t_p \sim$ const would indicate a quasi-common initial rotational energy of the magnetar ($E_{rot} \sim L_{SD}(t = 0) * \tau_{SD}$).
Nevertheless, regarding the plausibility of the magnetar origin of the X-ray plateau, there are two main caveats that have to be taken into account:

1. All the GRBs showing an X-ray plateau should have a NS as progenitor which is stable against collapse for at least $\sim 10^3 - 10^4$ s. Since a large fraction of long GRBs shows a plateau, this would imply that the probability that the final remnant of a massive star collapse is a NS, instead of a BH, is quite high.

2. The magnetar should be able to launch a relativistic and collimated outflow. This, based on current state-of-the-art simulation, it is not clear yet, neither for merger-driven or collapsar driven GRBs (Ciolfi, 2020).

3. It is not clear whether the magnetic and rotational energy stored in the magnetar are enough to power the prompt emission of all the GRBs with evidence of an X-ray plateau.

Another effect which can explain the presence of plateaus in X-ray light curves is the jet structure, both related to prompt emission (Oganesyan et al., 2020a; Ascenzi et al., 2020c) and to afterglow emission from jets viewed slightly off-axis (Beniamini et al., 2020a; Beniamini et al., 2020c; Beniamini et al., 2022). Currently, both observations and numerical simulations indicate that the structure of the jet can significantly deviate from the top-hat approximation and this can have relevant consequences on the appearance of the light curve, at all wavelenghts. In the approach of Oganesyan et al., 2020b (extended to an off-axis observer in Ascenzi et al. 2020c), the photons emitted during the prompt emission at large angles with respect to the jet core arrive to the observer at late times and less Doppler boosted. In the approximation of an instantaneous prompt emission and in the limit of an

on-axis observer, there is a bi-univocal relation between the arrival time t_{obs} of the photon and θ, where θ is the polar angle between the jet axis and the patch of the shock front from which the photon departed. Namely, the flux observed at time t_{obs} corresponds to the contribution from a jet ring at a polar angle $\theta(t_{obs})$.
Generally, the HLE from a structured jet produces an X-ray light curve characterised by steep-shallow-steep profile. The duration and steepness of the intermediate shallower segment depends on the structure profile, as well as on the radius and Lorentz factor of the jet core. Therefore the appearance of an X-ray plateau lasting $10^2 - 10^4$ s can be compatible with this scenario. Moreover, as soon as we start to receive the photons from the external edges of the jet wings, the light curve suddenly drops, due to a combined action of the suppressed Doppler factor and local emissivity, as well as to the plausible substantial increase of the optical depth. This phenomenology is in agreement with the evidence of the internal plateau.
As shown in Appendix B.2, the observational properties of the plateau, such as duration and luminosity, can be related to the jet structure properties. In the specific, it turns out that the plateau duration scales as $t_p \propto R\theta_c^m$, with R and θ_c the radius and the aperture of the jet core ($0.5 \lesssim m \lesssim 1$), while the luminosity scales as $L_p \propto \lambda L_{peak}/(\theta_c\Gamma)^2$, where L_{peak} is the peak luminosity of the prompt emission, λ is the fraction of prompt energy which is released in X-rays and Γ the core Lorentz factor. As shown by Dainotti et al. (2017), there exists a quite tight correlation between $L_p - t_p - L_{peak}$, in the form

$$L_p \propto \frac{L_{peak}^{0.7}}{t_p},$$

which is satisfied for a jet structure if:

$$\theta_c^{2-m} \sim \Delta\Omega^{1-m/2} \propto \frac{R}{\Gamma^2}\epsilon L_{peak}^{0.3},$$

where $\Delta\Omega$ is the solid angle subtended by the jet core in the limit of small θ_c. Namely, the empirical relation $L_p - t_p - L_{peak}$, if interpreted in the scenario of prompt HLE form a structured jet, implies that the jet aperture scales with the angular time scale $R/2c\Gamma^2$. In the specific, for a fixed value of Γ a jet which dissipates its internal energy at a larger radius has also a larger aperture angle. This is in agreement with numerical simulations, which show that, as soon as the jet successfully breaks out the envelope/ejecta, it has no more pressure from the sides to keep the collimation. Hence, considering also the lateral expansion of the cocoon, a jet which is initially highly

collimated is expected to increase its aperture angle as it propagates. The duration and luminosity of the X-ray plateau would therefore depend on the radius at which the release of the prompt emission occurs.
All the mentioned properties of the HLE from a structured jet make this scenario a viable alternative for the interpretation of the X-ray plateau. Though, given that both the HLE and the magnetar model can potentially explain the temporal properties of the X-ray plateau, there is no definitive answer about which one is more promising. For this reason, I analysed a complete sample of data aiming at understanding the emission process during the plateau phase and adding information to discern the best scenarios. Hence, in this chapter, after presenting the statistical properties of the plateau sample in Section 5.1, we perform in Section 5.2 a systematic analysis of the spectral properties of the plateau, combining both X-ray and optical data. We conclude in Section 5.3 discussing the results and the relative impact. This work is described in Ronchini et al., 2022b and is currently under review in A&A.

5.1 The sample of GRBs with an X-ray plateau

In this section we build the sample of all the GRBs with an X-ray plateau. We consider all the GRBs detected with Swift in about 14 years (from 2005 up to end 2019) with an X-ray afterglow. In order to identify GRBs with evidence of a plateau feature in their afterglow, we use the publicly available Swift XRT Repository[2] (Evans et al., 2007; Evans et al., 2009) and the provided data analysis tools to fit multiple power laws along the light curve of each GRB. We select all the GRBs that present in the X-ray light curve at least one segment with a temporal slope $-0.8 \leq \alpha \leq 0.8$ within errors. With these selection criteria, the sample consists of 424 GRBs. If we need to derive the source-frame information, such as luminosity and plateau duration, we have to restrict our selection to GRBs with known redshift, reducing the sample size to 155 elements. In this selection we considered only the GRBs with known prompt duration (1313 in total).

5.1.1 Statistical properties of the plateau sample

The statistical properties of the sample of GRBs with plateau, including the GRB duration and the presence of redshift, are summarised in Tab. 5.1. We

[2] https://www.swift.ac.uk/xrt_live_cat/

P/T	Z/T	$\frac{P\cap Z}{Z}$	$\frac{P\cap Z}{P}$	$\frac{P\cap Z}{T}$	S/T	$\frac{S\cap Z}{Z}$	$\frac{S\cap P}{P}$	$\frac{S\cap P\cap Z}{P\cap Z}$
32.3%	24.9%	47.4%	36.5%	11.8%	9%	4.3%	3.3%	2.6%

(a)

$\frac{S\cap Z}{S}$	$\frac{S\cap P}{S}$	$\frac{S\cap P\cap Z}{S\cap Z}$	$\frac{S\cap P\cap Z}{S\cap P}$
11.9%	11.8%	60.4%	61.0%

(b)

$\frac{L\cap Z}{L}$	$\frac{L\cap P}{L}$	$\frac{L\cap P\cap Z}{L\cap Z}$	$\frac{L\cap P\cap Z}{L\cap P}$
26.2%	34.3%	48.2%	36.8%

(c)

TABLE 5.1: Summary of the statistical properties of the plateau sample. With each letter we indicate the set. The intersection between two sets A and B is $A \cap B$. The meaning of the letters is: T=full sample, P=GRBs with X-ray plateau, Z=GRBs with measured redshift, S=short GRBs, L=long GRBs.

notice that $\sim$ 32% of all GRBs presents an X-ray plateau, while $\sim$ 12% have both an X-ray plateau and a measured redshift.
Looking at Tab. 5.1(b) and (c), the fraction of GRBs with plateau is $\sim$ 12% ($\sim$ 34%) for short (long) GRBs. This first evidence shows that the plateau is observed more often in long GRBs. Though, this may be a mix of an intrinsic property (i.e., a plateau phase occurs more frequently in long GRBs) and an observational bias. If, for instance, the occurrence of plateau in short and long GRBs is intrinsically the same, but the short GRB plateaus have a shorter duration, in this last case the plateau could be missed either because the light curve is not well sampled, or Swift-XRT starts the monitoring after the end of the plateau phase.
Additionally, restricting our considerations to GRBs with known redshift, the percentages change substantially. Indeed, among the GRBs with measured redshift, the fraction of those with a plateau increases to $\sim$ 47%. This

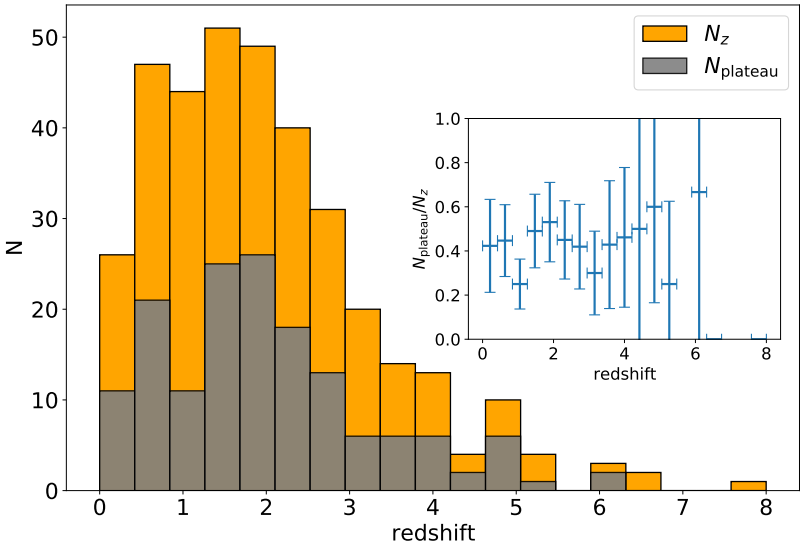

FIGURE 5.1: Comparison between the redshift distribution of all the GRBs, $N_z(z)$, and the GRBs with an X-ray plateau, $N_{\rm plateau}(z)$. The inset shows the redshift distribution of the ratio $N_{\rm plateau}/N_z$. The error bars are computed assuming Poisson fluctuations of the counts in each redshift bin.

evidence can have several possible explanations:

1. If the optical light curve follows the X-ray one, a longer optical emission implies more integrated flux and hence better spectral resolution. This last helps in the identification of the spectral lines and hence for the determination of the redshift.

2. The optical afterglow of GRBs with an X-ray plateau is intrinsically brighter than the ones without plateau and therefore it is more probable to determine the redshift.

3. The identification of the plateau phase may depend on redshift. This is highly plausible, since GRBs at larger redshift have a lower X-ray flux, implying that either the afterglow is no more detectable as it drops below the instrument sensitivity, or it is barely detectable but the light curve is not well sampled and the plateau is not statistically evident.

The redshift distribution of the GRBs with plateau is shown in Fig. 5.1, with a comparison with the full GRB redshift distribution. The inset indicates

that, considering the sample of GRBs with redshift, the fraction of those with plateau does not change significantly with z.
The effect on redshift selection is even more evident when we look at the sub-samples of short and long GRBs with measured redshift. Indeed the fraction of short (long) GRBs with plateau is $\sim$ 12% ($\sim$ 34%), and this fraction increases to $\sim$ 60% ($\sim$ 48%) if we consider only the ones with redshift. Notice that, without considering the redshift availability, the fraction of short GRBs with plateau is much lower than the one reported in Rowlinson et al., 2013, which finds that in a sample of 44 short GRBs around half of them have an X-ray light curve compatible with a magnetar spin-down emission. Though, this does not imply the evidence of an X-ray plateau, because in many cases the light curve has temporal gaps such that the presence of a flat power law segment for the light curve fit is not statistically required. Namely, even if potentially the magnetar model, which presents a flat X-ray phase, is compatible with $\sim$ half of the X-ray light curves of short GRBs, the fraction which statistically requires the presence of a plateau could be much lower.

5.1.2 Luminosity-duration correlation in X-ray plateaus

For each GRB, we compute the X-ray plateau luminosity as the average luminosity in the plateau temporal range. All the information about the sample are summarised in Tab. 5.2, 5.3 and 5.4. As well known and deeply investigated in previous studies (Dainotti et al., 2010), the plateau luminosity L_p and duration t_p show an anti-correlation, which is shown in Fig. 5.2. The plateau energy defined as $E_{\rm plateau} = L_p t_p$ spans $\sim$six orders of magnitude and it is clustered around $10^{50} - 10^{52}$ erg. Once the luminosity and duration are interpolated with a relation in the form:

$$L_p = L^* \left(\frac{t_p}{t^*}\right)^n, \tag{5.1}$$

we find a best fit for $n = -1.15 \pm 0.02$, fully consistent with previous studies. The $L_p - t_p$ relation has a Pearson correlation coefficient $C_p = -0.71$ (p-value$= 4 \times 10^{-25}$). The vertical scatter of this relation is 1.58 dex (1σ level of confidence). The vertical scatter is computed considering the 16^{th} and 84^{th} percentile of the distribution of $L_p/L_{p,pre}$, where $L_{p,pre}$ is the luminosity predicted by the best fit relation 5.1.
In Fig. 5.3 we show the same $L_p - t_p$ relation adding the dependence on the duration of the GRB. For the duration, we adopt the t_{90} measured by

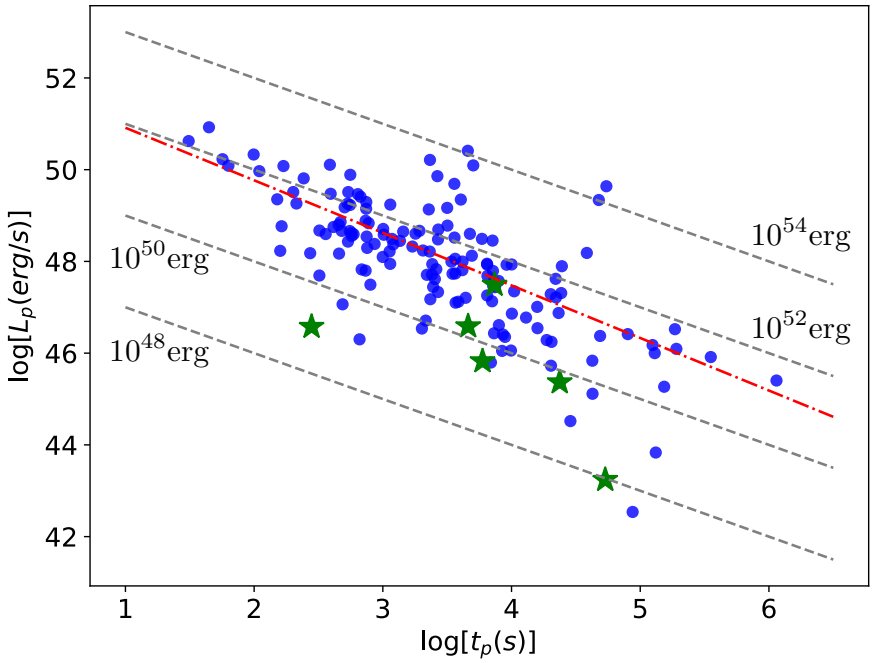

(a)

FIGURE 5.2: The relation between luminosity and duration of the X-ray plateau. The plateau duration is in source frame. The grey dashed lines are at constant plateau energy $E_p = L_p t_p$. The red dashed line is the best fit interpolation with a relation $L_p \propto t^n$. The green stars indicate short GRBs. For visibility reasons, error bars are not reported. Usual errors associated to the estimation of the lumninosity are $\sim 10\%$.

the Swift-BAT instrument. Fig. 5.3(a) indicates that longer GRBs prefer to lay along lines corresponding to larger $E_{\rm plateau}$. This evidence is even more clear in Fig. 5.3(b), where we distinguish three GRB classes, based on the t_{90}: $t_{90} < 2$s, $2 < t_{90} < 10$s and $t_{90} > 10$s. This is a first indication that the properties of the plateau phase are connected to the prompt phase.
In order to further test if the typical prompt duration of GRBs with an X-ray plateau is significantly different from the one of the full GRB sample, we compare the t_{90} and the isotropic energy distribution in Fig. 5.4. The histogram is normalised such that

$$\sum N_i \Delta_i = 1,$$

where N_i and Δ_i are the height and width of the bins. The panel (a) indicates that:

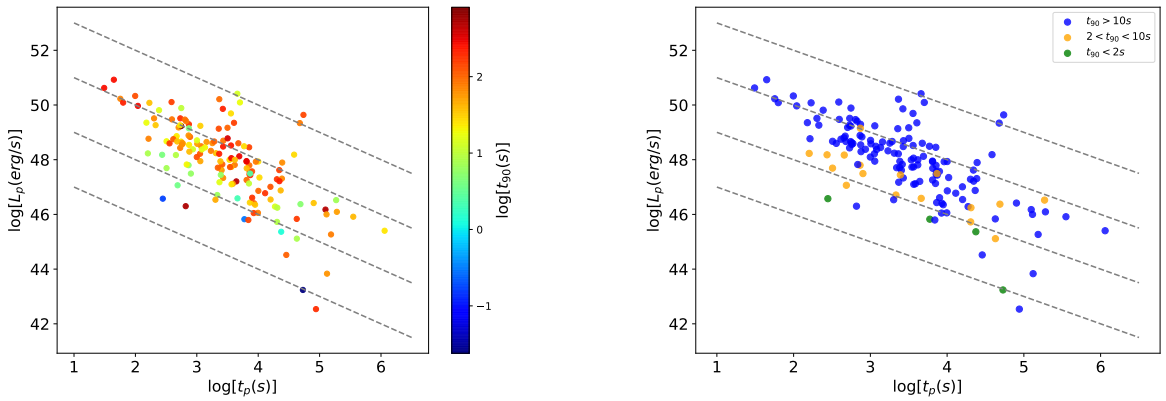

(a) (b)

FIGURE 5.3: The panel (a) reports the $L_p - t_p$ relation with a colour bar indicating the prompt phase duration t_{90}. In panel (b) we distinguish three classes: $t_{90} < 2$s, $2 < t_{90} < 10$s and $t_{90} > 10$s. The dashed lines have the same meaning of Fig. 5.2.

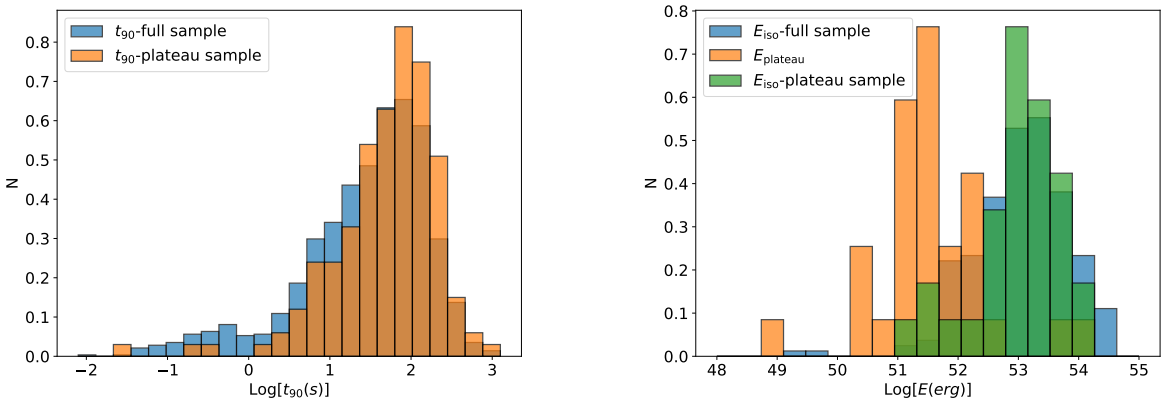

(a) (b)

FIGURE 5.4: Panel (a): normalised histogram of the t_{90} for the GRBs with plateau (orange) and the full sample of GRBs (blue). Panel (b): histogram of the plateau energy (orange) and the prompt isotropic energy (green), compared with the prompt isotropic energy of the full GRB sample (blue).

1. the t_{90} distribution of the GRBs with X-ray plateau shows a preference towards larger t_{90}, with respect to the full GRB sample;

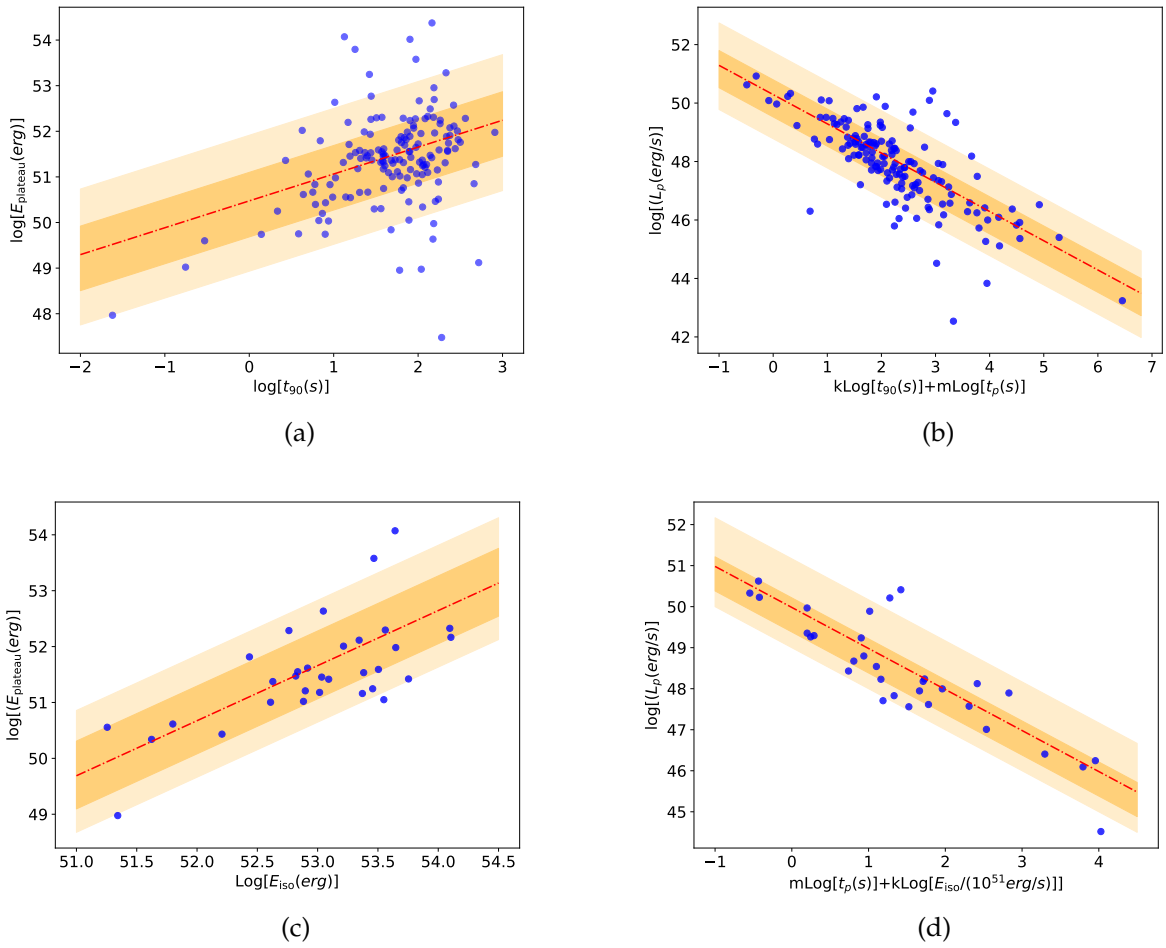

FIGURE 5.5: Panel (a): relation between the plateau energy and the t_{90}. Panel (b): $L_p - t_p - t_{90}$ relation. Panel (c): relation between the plateau energy and the isotropic prompt energy. Panel (d): $L_p - t_p - E_{\rm iso}$ relation. In panels (b) and (d) the values of k and m are found minimising the vertical scatter of L_p. In all the panels the red dot-dashed line is the best fit with a power law relation, while the light and dark shaded regions represent the 1σ and 2σ vertical scatter, respectively.

2. the ratio short/long GRBs is much smaller in the plateau sample, as already shown in Tab. 5.1.

The lack of short GRBs with X-ray plateau, as mentioned in the previous section, may be a combination of an intrinsic properties and observational

GRB	z	s_1	t_i (s)	t_f (s)	s_2	$F_{0.3-10\,\mathrm{keV}}$ (erg cm $^{-2}$ s^{-1})	$L_{0.3-10\,\mathrm{keV}}$ (erg s^{-1})
050315	1.95	0.68	5321	168000	1.6	$(4.25 \pm 0.97) \times 10^{-12}$	$(1.20 \pm 0.27) \times 10^{47}$
050319	3.24	0.53	235	30200	1.4	$(2.93 \pm 0.62) \times 10^{-11}$	$(2.84 \pm 0.60) \times 10^{48}$
050401	2.90	0.58	133	4456	1.4	$(2.33 \pm 0.41) \times 10^{-10}$	$(1.73 \pm 0.31) \times 10^{49}$
050416A	0.65	0.60	85	3556	0.9	$(2.76 \pm 0.59) \times 10^{-11}$	$(5.12 \pm 1.09) \times 10^{46}$
050505	4.27	0.33	2833	7585	1.2	$(2.38 \pm 0.54) \times 10^{-11}$	$(4.46 \pm 1.00) \times 10^{48}$
050509B	0.23	0.39	62	65763	-	$(1.08 \pm 0.31) \times 10^{-13}$	$(1.73 \pm 0.49) \times 10^{43}$
050730	3.97	-0.03	246	1927	1.0	$(8.10 \pm 1.23) \times 10^{-10}$	$(1.28 \pm 0.19) \times 10^{50}$
050802	1.71	0.73	606	9246	1.8	$(4.86 \pm 1.08) \times 10^{-11}$	$(9.89 \pm 2.20) \times 10^{47}$
050803	4.30	-0.16	364	14300	2.1	$(2.60 \pm 0.58) \times 10^{-11}$	$(4.95 \pm 1.10) \times 10^{48}$
050822	1.43	0.36	598	17500	1.0	$(2.23 \pm 0.48) \times 10^{-11}$	$(2.92 \pm 0.63) \times 10^{47}$
050824	0.83	0.66	6092	2095361	-	$(7.48 \pm 1.84) \times 10^{-13}$	$(2.53 \pm 0.62) \times 10^{45}$
050904	6.29	0.49	1099	5420	1.8	$(4.23 \pm 0.94) \times 10^{-11}$	$(1.97 \pm 0.44) \times 10^{49}$
050922B	4.90	0.21	2137	130000	1.5	$(1.61 \pm 0.41) \times 10^{-12}$	$(4.17 \pm 1.05) \times 10^{47}$
051109A	2.35	0.56	199	6870	1.2	$(3.89 \pm 0.84) \times 10^{-11}$	$(1.73 \pm 0.37) \times 10^{48}$
051221A	0.55	0.48	1610	36700	1.4	$(1.88 \pm 0.45) \times 10^{-12}$	$(2.32 \pm 0.56) \times 10^{45}$
060115	3.53	0.66	656	36000	1.4	$(3.14 \pm 0.73) \times 10^{-12}$	$(3.74 \pm 0.87) \times 10^{47}$
060124	2.30	0.26	112	15100	1.1	$(6.12 \pm 0.79) \times 10^{-09}$	$(2.58 \pm 0.33) \times 10^{50}$
060204B	2.34	0.68	207	7603	1.5	$(3.10 \pm 0.49) \times 10^{-10}$	$(1.36 \pm 0.21) \times 10^{49}$
060218	0.03	-0.33	159	2570	5.3	$(2.07 \pm 0.29) \times 10^{-09}$	$(4.33 \pm 0.61) \times 10^{45}$
060306	1.55	0.57	187	6471	1.1	$(2.58 \pm 0.57) \times 10^{-11}$	$(4.12 \pm 0.92) \times 10^{47}$
060502A	1.51	0.58	252	26300	1.1	$(1.49 \pm 0.33) \times 10^{-11}$	$(2.23 \pm 0.49) \times 10^{47}$
060510B	4.90	0.19	127	263	5.6	$(3.24 \pm 0.43) \times 10^{-09}$	$(8.40 \pm 1.13) \times 10^{50}$
060526	3.21	0.37	518	20700	1.7	$(1.40 \pm 0.31) \times 10^{-11}$	$(1.33 \pm 0.29) \times 10^{48}$
060604	2.68	0.50	724	23800	1.2	$(2.95 \pm 0.72) \times 10^{-12}$	$(1.81 \pm 0.44) \times 10^{47}$
060605	3.80	0.44	189	5662	1.2	$(2.18 \pm 0.48) \times 10^{-11}$	$(3.09 \pm 0.68) \times 10^{48}$
060607A	3.08	0.49	394	12900	3.5	$(1.72 \pm 0.34) \times 10^{-10}$	$(1.47 \pm 0.29) \times 10^{49}$
060614	0.13	-0.03	1150	32400	1.3	$(7.31 \pm 1.62) \times 10^{-12}$	$(3.30 \pm 0.73) \times 10^{44}$
060707	3.43	0.57	626	109000	1.4	$(7.08 \pm 1.56) \times 10^{-12}$	$(7.86 \pm 1.73) \times 10^{47}$
060714	2.71	0.33	350	4187	1.3	$(2.62 \pm 0.58) \times 10^{-11}$	$(1.65 \pm 0.37) \times 10^{48}$
060719	1.53	-0.18	221	6792	1.2	$(1.39 \pm 0.30) \times 10^{-11}$	$(2.15 \pm 0.47) \times 10^{47}$
060729	0.54	0.28	460	13200	-0.4	$(2.16 \pm 0.48) \times 10^{-11}$	$(2.55 \pm 0.57) \times 10^{46}$
060814	1.92	0.63	810	21200	1.5	$(1.34 \pm 0.30) \times 10^{-11}$	$(3.63 \pm 0.80) \times 10^{47}$
060906	3.69	0.31	932	11300	1.7	$(3.89 \pm 0.91) \times 10^{-12}$	$(5.15 \pm 1.20) \times 10^{47}$
060908	1.88	0.70	80	926	1.5	$(1.83 \pm 0.35) \times 10^{-10}$	$(4.71 \pm 0.90) \times 10^{48}$
061021	0.35	0.46	342	2716	0.8	$(8.19 \pm 1.70) \times 10^{-11}$	$(3.44 \pm 0.71) \times 10^{46}$
061121	1.31	0.18	203	1238	0.9	$(2.57 \pm 0.48) \times 10^{-10}$	$(2.70 \pm 0.51) \times 10^{48}$
061202	2.25	0.36	594	23300	1.7	$(1.55 \pm 0.34) \times 10^{-11}$	$(6.20 \pm 1.36) \times 10^{47}$
061222A	2.09	0.33	210	2398	1.0	$(2.04 \pm 0.44) \times 10^{-10}$	$(6.81 \pm 1.48) \times 10^{48}$
070129	2.34	0.15	1455	14700	1.0	$(3.66 \pm 0.86) \times 10^{-12}$	$(1.61 \pm 0.38) \times 10^{47}$
070306	1.50	0.09	606	18600	0.8	$(1.86 \pm 0.41) \times 10^{-11}$	$(2.74 \pm 0.60) \times 10^{47}$
070328	2.06	0.32	156	616	1.3	$(1.01 \pm 0.18) \times 10^{-09}$	$(3.25 \pm 0.57) \times 10^{49}$
070419B	1.96	0.51	533	7943	1.3	$(1.06 \pm 0.23) \times 10^{-10}$	$(3.02 \pm 0.67) \times 10^{48}$
070506	2.31	0.55	424	8140	-	$(6.53 \pm 1.41) \times 10^{-12}$	$(2.78 \pm 0.60) \times 10^{47}$
070508	0.82	0.72	221	1006	1.3	$(1.40 \pm 0.21) \times 10^{-09}$	$(4.60 \pm 0.70) \times 10^{48}$
070521	2.09	0.20	81	1402	1.2	$(1.88 \pm 0.42) \times 10^{-10}$	$(6.27 \pm 1.41) \times 10^{48}$
070802	2.45	0.18	524	8072	1.2	$(3.05 \pm 0.67) \times 10^{-12}$	$(1.50 \pm 0.33) \times 10^{47}$
070810A	2.17	0.39	102	1448	1.4	$(4.04 \pm 0.87) \times 10^{-11}$	$(1.48 \pm 0.32) \times 10^{48}$
071010B	0.95	0.66	6241	156128	-	$(5.49 \pm 1.20) \times 10^{-12}$	$(2.60 \pm 0.57) \times 10^{46}$
071021	2.45	0.53	668	22300	1.1	$(1.73 \pm 0.40) \times 10^{-11}$	$(8.52 \pm 1.96) \times 10^{47}$
080207	2.09	-0.21	130	339	1.8	$(2.78 \pm 0.42) \times 10^{-09}$	$(9.28 \pm 1.40) \times 10^{49}$
080310	2.43	0.17	682	10900	1.6	$(1.25 \pm 0.23) \times 10^{-10}$	$(6.03 \pm 1.10) \times 10^{48}$
080413B	1.10	0.50	135	335	0.9	$(2.50 \pm 0.48) \times 10^{-10}$	$(1.70 \pm 0.33) \times 10^{48}$
080430	0.77	0.47	285	33200	1.1	$(6.87 \pm 1.55) \times 10^{-12}$	$(1.93 \pm 0.44) \times 10^{46}$
080602	1.82	0.02	145	461	0.7	$(2.46 \pm 0.50) \times 10^{-10}$	$(5.84 \pm 1.19) \times 10^{48}$
080604	1.42	0.53	6397	371394	-	$(1.44 \pm 0.35) \times 10^{-13}$	$(1.85 \pm 0.45) \times 10^{45}$
080605	1.64	0.64	97	399	1.1	$(1.23 \pm 0.19) \times 10^{-09}$	$(2.26 \pm 0.34) \times 10^{49}$

TABLE 5.2: Summary data of the GRBs with an X-ray plateau. With s_1 and s_2 we indicate the plateau and post-plateau temporal slopes, respectively. t_i and t_f are the initial and the final time of the plateau. Errors on s_1, s_2, t_i and t_f can be found on the Swift public repository. The last two columns are the average flux and luminosity of the X-ray plateau.

GRB	z	s_1	t_i (s)	t_f (s)	s_2	$F_{0.3-10\,\mathrm{keV}}$ (erg cm $^{-2}$ s^{-1})	$L_{0.3-10\,\mathrm{keV}}$ (erg s^{-1})
080707	1.23	0.40	173	16300	1.3	$(3.01 \pm 0.70) \times 10^{-12}$	$(2.71 \pm 0.63) \times 10^{46}$
080721	2.60	0.62	113	357	0.9	$(3.77 \pm 0.51) \times 10^{-09}$	$(2.14 \pm 0.29) \times 10^{50}$
080905B	2.37	0.48	191	16000	2.4	$(8.78 \pm 1.94) \times 10^{-11}$	$(3.99 \pm 0.88) \times 10^{48}$
081007	0.53	0.70	226	31300	1.2	$(1.56 \pm 0.35) \times 10^{-11}$	$(1.76 \pm 0.39) \times 10^{46}$
081029	3.85	0.47	2711	17700	2.6	$(7.82 \pm 1.74) \times 10^{-12}$	$(1.14 \pm 0.25) \times 10^{48}$
081118	2.58	0.58	698	683657	-	$(2.22 \pm 0.49) \times 10^{-13}$	$(1.24 \pm 0.27) \times 10^{46}$
081210	2.06	0.66	3917	167000	2.4	$(1.35 \pm 0.20) \times 10^{-09}$	$(4.35 \pm 0.66) \times 10^{49}$
081221	2.26	0.65	223	695	1.3	$(4.53 \pm 0.71) \times 10^{-10}$	$(1.83 \pm 0.29) \times 10^{49}$
090404	3.00	0.20	284	16600	1.2	$(8.01 \pm 1.79) \times 10^{-12}$	$(6.45 \pm 1.44) \times 10^{47}$
090418A	1.61	0.44	127	2654	1.5	$(2.17 \pm 0.44) \times 10^{-10}$	$(3.81 \pm 0.78) \times 10^{48}$
090423	8.20	0.01	80	5140	1.4	$(9.01 \pm 1.79) \times 10^{-11}$	$(7.73 \pm 1.54) \times 10^{49}$
090424	0.54	0.74	255	1757	8	$(7.48 \pm 1.43) \times 10^{-10}$	$(8.84 \pm 1.69) \times 10^{47}$
090510	0.90	0.68	98	1396	2.1	$(1.52 \pm 0.30) \times 10^{-10}$	$(6.29 \pm 1.25) \times 10^{47}$
090529	2.63	0.70	1191	968777	-	$(7.52 \pm 1.93) \times 10^{-13}$	$(4.40 \pm 1.13) \times 10^{46}$
090530	1.27	0.61	151	52700	1.3	$(7.71 \pm 1.76) \times 10^{-12}$	$(7.51 \pm 1.71) \times 10^{46}$
090618	0.54	0.58	366	4008	1.3	$(5.72 \pm 0.90) \times 10^{-10}$	$(6.76 \pm 1.06) \times 10^{47}$
090709A	1.80	-0.03	179	1101	1.4	$(1.29 \pm 0.20) \times 10^{-09}$	$(2.98 \pm 0.46) \times 10^{49}$
090715B	3.00	-0.05	52	124	3.7	$(5.22 \pm 0.79) \times 10^{-09}$	$(4.20 \pm 0.63) \times 10^{50}$
090812	2.45	0.42	96	196	5.9	$(3.44 \pm 0.46) \times 10^{-09}$	$(1.69 \pm 0.23) \times 10^{50}$
090927	1.37	0.20	2144	10900	1.2	$(3.28 \pm 0.79) \times 10^{-12}$	$(3.86 \pm 0.93) \times 10^{46}$
091018	0.97	0.47	67	537	1.1	$(3.04 \pm 0.56) \times 10^{-10}$	$(1.51 \pm 0.28) \times 10^{48}$
091029	2.75	0.31	304	15600	1.16	$(1.52 \pm 0.34) \times 10^{-11}$	$(9.91 \pm 2.19) \times 10^{47}$
100219A	4.67	0.59	495	33400	3.6	$(1.34 \pm 0.30) \times 10^{-11}$	$(3.10 \pm 0.70) \times 10^{48}$
100302A	4.81	0.45	296	29300	0.9	$(5.01 \pm 0.78) \times 10^{-10}$	$(1.24 \pm 0.19) \times 10^{50}$
100316B	1.18	0.10	76	1061	1.2	$(1.43 \pm 0.32) \times 10^{-11}$	$(1.16 \pm 0.26) \times 10^{47}$
100316D	0.06	0.12	144	699	1.9	$(2.29 \pm 0.35) \times 10^{-09}$	$(2.00 \pm 0.30) \times 10^{46}$
100418A	0.62	-0.20	630	69000	1.4	$(7.87 \pm 2.02) \times 10^{-13}$	$(1.30 \pm 0.33) \times 10^{45}$
100425A	1.76	0.58	320	43900	1.2	$(1.60 \pm 0.38) \times 10^{-12}$	$(3.50 \pm 0.82) \times 10^{46}$
100615A	1.40	0.32	176	15600	1.2	$(3.90 \pm 0.87) \times 10^{-11}$	$(4.84 \pm 1.07) \times 10^{47}$
100621A	0.54	0.36	498	5942	1.2	$(1.12 \pm 0.25) \times 10^{-10}$	$(1.32 \pm 0.29) \times 10^{47}$
100814A	1.44	0.31	645	49200	3.9	$(1.45 \pm 0.32) \times 10^{-11}$	$(1.93 \pm 0.42) \times 10^{47}$
110213A	1.46	-0.24	144	1458	1.1	$(2.84 \pm 0.62) \times 10^{-10}$	$(3.91 \pm 0.85) \times 10^{48}$
110715A	0.82	0.56	97	1570	1.5	$(7.31 \pm 1.14) \times 10^{-10}$	$(2.40 \pm 0.37) \times 10^{48}$
110808A	1.35	0.71	378	830597	-	$(7.25 \pm 1.47) \times 10^{-13}$	$(8.22 \pm 1.67) \times 10^{45}$
111008A	4.99	0.01	334	3026	1.1	$(5.59 \pm 1.22) \times 10^{-11}$	$(1.51 \pm 0.33) \times 10^{49}$
111209A	0.68	0.24	425	935	1.2	$(8.18 \pm 0.58) \times 10^{-09}$	$(1.70 \pm 0.12) \times 10^{49}$
111228A	0.71	0.45	411	17200	2.9	$(3.15 \pm 0.70) \times 10^{-11}$	$(7.26 \pm 1.60) \times 10^{46}$
111229A	1.38	0.00	94	8749	2.9	$(1.05 \pm 0.23) \times 10^{-11}$	$(1.26 \pm 0.28) \times 10^{47}$
120118B	2.94	-0.33	314	2697	1.0	$(8.72 \pm 1.93) \times 10^{-12}$	$(6.68 \pm 1.48) \times 10^{47}$
120326A	1.80	0.20	251	68100	1.9	$(8.83 \pm 1.96) \times 10^{-12}$	$(2.04 \pm 0.45) \times 10^{47}$
120327A	2.81	0.62	215	2798	1.5	$(1.12 \pm 0.24) \times 10^{-10}$	$(7.69 \pm 1.63) \times 10^{48}$
120404A	2.87	0.12	514	2924	1.8	$(2.72 \pm 0.59) \times 10^{-11}$	$(1.97 \pm 0.43) \times 10^{48}$
120422A	0.28	0.30	374	169000	1.2	$(2.72 \pm 0.62) \times 10^{-13}$	$(6.81 \pm 1.54) \times 10^{43}$
120521C	6.00	0.71	343	70183	-	$(2.06 \pm 0.50) \times 10^{-12}$	$(8.58 \pm 2.09) \times 10^{47}$
120724A	1.48	0.40	818	24554	-	$(8.04 \pm 1.88) \times 10^{-13}$	$(1.14 \pm 0.27) \times 10^{46}$
120802A	3.80	0.36	264	17563	-	$(3.84 \pm 0.90) \times 10^{-12}$	$(5.45 \pm 1.27) \times 10^{47}$
120811C	2.67	0.47	242	2747	1.2	$(5.74 \pm 1.27) \times 10^{-11}$	$(3.48 \pm 0.77) \times 10^{48}$
120907A	0.97	0.40	94	1577	1.1	$(6.25 \pm 1.38) \times 10^{-11}$	$(3.11 \pm 0.69) \times 10^{47}$
121027A	1.77	0.36	829	132000	1.4	$(9.82 \pm 1.49) \times 10^{-10}$	$(2.18 \pm 0.33) \times 10^{49}$
121128A	2.20	0.56	154	1503	1.6	$(1.92 \pm 0.41) \times 10^{-10}$	$(7.27 \pm 1.54) \times 10^{48}$
121211A	1.02	0.30	115	1088	3.5	$(5.76 \pm 0.75) \times 10^{-09}$	$(3.25 \pm 0.42) \times 10^{49}$
130408A	3.76	0.45	154	3531	1.6	$(1.02 \pm 0.21) \times 10^{-10}$	$(1.41 \pm 0.29) \times 10^{49}$
130420A	1.30	0.73	743	36400	1.1	$(9.85 \pm 2.19) \times 10^{-12}$	$(1.02 \pm 0.23) \times 10^{47}$
130603B	0.36	0.15	63	380	0.8	$(8.37 \pm 1.66) \times 10^{-11}$	$(3.76 \pm 0.75) \times 10^{46}$
130702A	0.15	0.56	99	155000	1.2	$(9.99 \pm 2.08) \times 10^{-11}$	$(6.17 \pm 1.28) \times 10^{45}$
131103A	0.60	0.38	130	1610	1.1	$(3.34 \pm 0.44) \times 10^{-09}$	$(5.10 \pm 0.67) \times 10^{48}$
131105A	1.69	0.32	365	5915	1.2	$(2.58 \pm 0.57) \times 10^{-11}$	$(5.10 \pm 1.13) \times 10^{47}$

TABLE 5.3: Continued

biases. In panel (b) of Fig. 5.4 we show the comparison between the distribution of the plateau energy, the E_{iso} of GRBs with plateau and E_{iso} of the full sample of GRBs. These distributions are relative only to GRBs with available E_{iso}, which is taken by Jia et al., 2022. The sample of all GRBs with

GRB	z	s_1	t_i (s)	t_f (s)	s_2	$F_{0.3-10\,\mathrm{keV}}(\mathrm{erg\ cm^{-2}\ s^{-1}})$	$L_{0.3-10\,\mathrm{keV}}(\mathrm{erg\ s^{-1}})$
140206A	2.73	0.68	155	8669	1.7	$(2.55 \pm 0.35) \times 10^{-09}$	$(1.63 \pm 0.22) \times 10^{50}$
140301A	1.42	0.72	313	93080	-	$(1.19 \pm 0.22) \times 10^{-10}$	$(1.53 \pm 0.29) \times 10^{48}$
140304A	5.28	0.26	89	1524	2.6	$(2.09 \pm 0.43) \times 10^{-10}$	$(6.46 \pm 1.32) \times 10^{49}$
140419A	3.96	0.48	1177	3326	1.4	$(1.64 \pm 0.36) \times 10^{-10}$	$(2.57 \pm 0.56) \times 10^{49}$
140430A	1.60	0.64	413	33700	1.1	$(3.45 \pm 0.78) \times 10^{-12}$	$(5.96 \pm 1.35) \times 10^{46}$
140512A	0.73	0.72	266	6982	1.1	$(9.04 \pm 2.14) \times 10^{-09}$	$(2.23 \pm 0.53) \times 10^{49}$
140518A	4.71	0.24	257	3265	1.9	$(1.76 \pm 0.39) \times 10^{-11}$	$(4.16 \pm 0.92) \times 10^{48}$
140703A	3.14	-0.17	336	7430	1.7	$(4.49 \pm 1.00) \times 10^{-11}$	$(4.03 \pm 0.90) \times 10^{48}$
140903A	0.35	0.19	74	8035	1.2	$(1.59 \pm 0.33) \times 10^{-11}$	$(6.68 \pm 1.39) \times 10^{45}$
141121A	1.47	0.31	24500	308000	2.2	$(1.07 \pm 0.26) \times 10^{-12}$	$(1.50 \pm 0.37) \times 10^{46}$
150323A	0.59	0.43	469	11000	1.1	$(4.27 \pm 1.00) \times 10^{-12}$	$(6.25 \pm 1.46) \times 10^{45}$
150403A	2.06	0.38	81	517	0.6	$(3.72 \pm 0.58) \times 10^{-09}$	$(1.20 \pm 0.19) \times 10^{50}$
150821A	0.76	0.49	250	633	2.3	$(1.45 \pm 0.22) \times 10^{-09}$	$(3.95 \pm 0.60) \times 10^{48}$
150910A	1.36	0.19	231	977	0.8	$(4.88 \pm 0.77) \times 10^{-10}$	$(5.63 \pm 0.89) \times 10^{48}$
150915A	1.97	0.37	1592	126036	-	$(2.37 \pm 0.48) \times 10^{-13}$	$(6.84 \pm 1.37) \times 10^{45}$
151027A	0.81	0.06	538	1807	0.8	$(3.92 \pm 0.63) \times 10^{-10}$	$(1.25 \pm 0.20) \times 10^{48}$
151027B	4.06	0.65	342	46300	1.4	$(5.10 \pm 1.16) \times 10^{-12}$	$(8.47 \pm 1.93) \times 10^{47}$
151031A	1.17	0.67	443	105851	-	$(2.99 \pm 0.70) \times 10^{-12}$	$(2.37 \pm 0.56) \times 10^{46}$
160121A	1.96	0.32	212	20900	2.1	$(4.73 \pm 1.10) \times 10^{-12}$	$(1.35 \pm 0.31) \times 10^{47}$
160227A	2.38	0.23	1618	21800	1.7	$(1.94 \pm 0.43) \times 10^{-11}$	$(8.90 \pm 1.97) \times 10^{47}$
160509A	1.17	0.65	7271	40100	1.3	$(3.38 \pm 0.75) \times 10^{-11}$	$(2.68 \pm 0.59) \times 10^{47}$
160804A	0.74	0.29	1185	14700	0.9	$(4.39 \pm 1.01) \times 10^{-12}$	$(1.12 \pm 0.26) \times 10^{46}$
161014A	2.82	0.51	125	2037	1.6	$(2.62 \pm 0.51) \times 10^{-10}$	$(1.82 \pm 0.36) \times 10^{49}$
161017A	2.01	-0.10	68	190	1.4	$(4.02 \pm 0.61) \times 10^{-09}$	$(1.22 \pm 0.18) \times 10^{50}$
161117A	1.55	0.48	575	8871	1.2	$(3.37 \pm 0.74) \times 10^{-11}$	$(5.38 \pm 1.18) \times 10^{47}$
161219B	0.15	0.76	2517	214000	7.0	$(5.39 \pm 0.86) \times 10^{-10}$	$(3.33 \pm 0.53) \times 10^{46}$
170113A	1.97	0.48	327	4036	1.2	$(9.70 \pm 2.13) \times 10^{-11}$	$(2.80 \pm 0.61) \times 10^{48}$
170202A	3.65	-0.09	345	2228	1.1	$(3.59 \pm 0.80) \times 10^{-11}$	$(4.63 \pm 1.03) \times 10^{48}$
170604A	1.33	0.72	128	8375	1.2	$(4.50 \pm 0.89) \times 10^{-09}$	$(4.91 \pm 0.97) \times 10^{49}$
170705A	2.01	0.37	809	6966	1.6	$(5.42 \pm 1.21) \times 10^{-11}$	$(1.64 \pm 0.37) \times 10^{48}$
171205A	0.04	-0.15	5956	90800	1.1	$(9.13 \pm 2.14) \times 10^{-13}$	$(3.45 \pm 0.81) \times 10^{42}$
171222A	2.41	0.01	2228	27200	0.7	$(8.63 \pm 2.12) \times 10^{-13}$	$(4.08 \pm 1.00) \times 10^{46}$
180115A	2.49	0.65	271	8452	1.3	$(1.70 \pm 0.38) \times 10^{-11}$	$(8.71 \pm 1.94) \times 10^{47}$
180325A	2.25	0.24	237	2079	2.0	$(7.33 \pm 1.40) \times 10^{-10}$	$(2.93 \pm 0.56) \times 10^{49}$
180329B	2.00	0.38	174	7961	1.6	$(2.41 \pm 0.33) \times 10^{-09}$	$(7.22 \pm 0.98) \times 10^{49}$
180404A	1.00	0.28	237	17800	1.4	$(4.20 \pm 0.88) \times 10^{-12}$	$(2.26 \pm 0.47) \times 10^{46}$
180620B	1.12	0.53	459	47000	1.2	$(2.30 \pm 0.50) \times 10^{-11}$	$(1.64 \pm 0.36) \times 10^{47}$
180720B	0.65	0.55	1020	3176	1.4	$(2.50 \pm 0.38) \times 10^{-09}$	$(4.64 \pm 0.70) \times 10^{48}$
180728A	0.12	0.31	7316	22700	1.3	$(1.40 \pm 0.31) \times 10^{-10}$	$(5.32 \pm 1.18) \times 10^{45}$
181010A	1.39	0.65	97	2884	1.2	$(1.94 \pm 0.39) \times 10^{-10}$	$(2.36 \pm 0.48) \times 10^{48}$
181020A	2.94	0.00	5623	14200	2.5	$(4.32 \pm 0.96) \times 10^{-11}$	$(3.31 \pm 0.74) \times 10^{48}$
190106A	1.86	0.05	369	4852	1.1	$(8.43 \pm 1.83) \times 10^{-11}$	$(2.11 \pm 0.46) \times 10^{48}$
190114A	3.38	-0.01	410	2506	1.2	$(3.36 \pm 0.75) \times 10^{-11}$	$(3.60 \pm 0.80) \times 10^{48}$
190627A	1.94	0.11	122	21700	1.5	$(1.12 \pm 0.25) \times 10^{-11}$	$(3.11 \pm 0.70) \times 10^{47}$
190829A	0.08	0.57	103	140000	1.2	$(6.27 \pm 1.01) \times 10^{-10}$	$(1.00 \pm 0.16) \times 10^{46}$
191011A	1.72	0.30	84	874	1.3	$(2.38 \pm 0.53) \times 10^{-11}$	$(4.92 \pm 1.09) \times 10^{47}$
191221B	1.15	0.60	388	1291	1.5	$(7.06 \pm 1.07) \times 10^{-10}$	$(5.37 \pm 0.81) \times 10^{48}$

TABLE 5.4: Continued

available $E_{\rm iso}$ consists of 221 elements, 32 of which have an X-ray plateau. The plot shows no significant difference in the distribution of $E_{\rm iso}$ between GRBs with plateau and the full GRB sample. Moreover the distribution of the plateau energy is shifted at lower values by $\sim 1-1.5$ dex, but it is more scattered. The evidences shown above indicate that the plateau energy may be correlated both with the GRB duration and the isotropic prompt energy. In Fig. 5.5 (a) and (c) we show the scatter plots of $E_{\rm plateau} - t_{90}$ and $E_{\rm plateau} - E_{\rm iso}$. The correlation coefficient is $C_f = 0.11$ (p-value=0.16) for the $E_{\rm plateau} - t_{90}$ relation and $C_f = 0.68$ (p-value=1.8×10^{-5}) for the $E_{\rm plateau} - E_{\rm iso}$ relation. Once fitted with a power law relation $y \propto x^m$, we

find a best fit value $m = 0.59 \pm 0.06$ (1.39 dex of vertical scatter) for the $E_{\rm plateau} - t_{90}$ relation and $m = 0.99 \pm 0.04$ (1.21 dex of vertical scatter) for the $E_{\rm plateau} - E_{\rm iso}$ relation.
If the vertical scatter of the $L_p - t_p$ relation is mainly due to a large scatter on the plateau energy and the latter one is correlated with other observables, the $L_p - t_p$ relation can be re-normalised, with the aim of shrinking the scatter. We tried this first using the $E_{\rm plateau} - t_{90}$ relation. The re-normalisation is done introducing a third variable, combination of t_p and t_{90}:

$$\log u = k \log t_{90} + m \log t_p.$$

Analogously, the same procedure can be adopted exploiting the $E_{\rm plateau} - E_{\rm iso}$ correlation. In this case the new variable would be:

$$\log u = k \log E_{\rm iso} + m \log t_p.$$

The values of m and k are found minimising the vertical scatter of the $L_p - u$ relation. In the specific, the couple of values (m,k) which minimise the scatter is found adopting the following procedure:

1. we fit with a relation $\log L_p = A - \log u$ relation, keeping only A as free parameter;
2. we compute the dispersion as[3]
$$\delta(m,k) = \sum_i log[L_{p,i}/(A - \log u_i)];$$
3. we iterate the procedure until the absolute minimum of $\delta(m,k)$ is found.

In conclusion we find:

- For the $L_p - t_p - t_{90}$ relation the scatter is minimised for:
$$m = 0.86, k = -1.07.$$
The correlation coefficient (vertical scatter) increases (decreases) from $C_f = -0.71$ (1.58 dex) for the $L_p - t_p$ relation to $C_f = -0.74$ (1.27 dex) for the $L_p - t_p - t_{90}$ relation.

[3]The sum can be computed also as $\sum_i log[L_{p,i} - (A - \log u_i)]$, but this choice has no relevant impact on the final minimization of the correlation scatter.

- For the $L_p - t_p - E_{\rm iso}$ relation the scatter is minimised for:

$$m = 0.96, k = -0.80.$$

The correlation coefficient (vertical scatter) increases (decreases) from $C_f = -0.76$ (1.24 dex) for the $L_p - t_p$ relation[4] to $C_f = -0.87$ (0.83 dex) for the $L_p - t_p - E_{\rm iso}$ relation.

The fact that the $E_{\rm plateau} - E_{\rm iso}$ relation is more strongly correlated than the $E_{\rm plateau} - t_{90}$ one explains why the $L_p - t_p - E_{\rm iso}$ relation is less scattered that the $L_p - t_p - t_{90}$ one. Our results about the correlation between plateau and prompt emission parameters can be compared with the results presented in Ding et al., 2022. The authors extensively test the correlation between the X-ray plateau parameters (luminosity, starting and ending time) with the prompt emission parameters (e.g., $E_{\rm iso}$, peak luminosity, fluence). In the specific, their best fit parameters of the $L_p - t_p - E_{\rm iso}$ relation are $m = 0.95 \pm 0.07$ and $k = -0.71 \pm 0.06$, very close to the ones presented here. Moreover, among all the three-parameters tested by the authors, the $L_p - t_p - E_{\rm iso}$ relation results to be the one with highest correlation coefficient and one of the less scattered. Another interesting relation previously found in literature, which relates the prompt emission properties with the ones of the plateau, is the $L_p - t_p - L_{\rm peak}$, where $L_{\rm peak}$ is the peak luminosity during prompt emission (e.g., Dainotti et al. 2017). It is necessary to clarify that the significance reported for the analyzed correlations may depend on the sample size. This means that if, for selection reasons, the sample size is reduced, then the probability that the correlation is spurious is higher. Therefore the comparison of correlation significance is meaningful only for samples of comparable size.
The above considerations imply that it is possible to obtain a tighter correlation between L_p and t_p re-scaling the plateau luminosity by the prompt isotropic energy (or peak luminosity). Therefore, even if a non-negligible residual scatter remains ($\sim$1 dex), these results could indicate the existence of a quasi-common energy reservoir for the X-ray plateau, once renormalised to the prompt emission energetics. The origin of the residual scatter can be ascribed to the fact that a universal energy reservoir does not necessarily ensures a universal observed energy of the plateau. Indeed, a universal radiated energy in the plateau phase would require that 1) the radiation and dissipation processes are also common, 2) the efficiency in

[4]The correlation and vertical scatter of the $L_p - t_p$ relation are different from the values reported before because in this case the relation is limited only to GRBs with available estimate of $E_{\rm iso}$

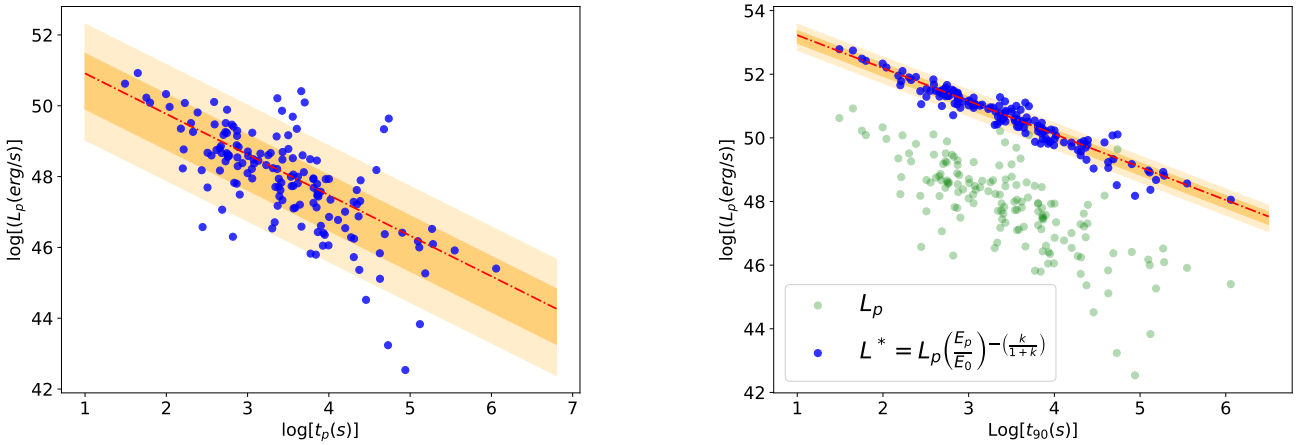

(a) (b)

FIGURE 5.6: Panel (a), the vertical scatter of the $L_p - t_p$ relation . The red dashed line is the best fit interpolation with a relation $L_p \propto t^n$. The light and dark shaded regions represent the 1σ and 2σ vertical scatter, respectively. Panel (b): comparison between the $L_p - t_p$ relation and the $L^* - t_p$ relation. The details about the choice of L^* are described in the text. Here E_p is the plateau energy, $k = 3$ and $E_0 = 10^{55}$ erg.

conversion from the energy reservoir to the radiated output is common, 3) the X-ray luminosity represents always a good proxy of the bolometric luminosity (not true if most of the energy is radiated at other wavelengths).

In order to address better this point, in the following we show whether a quasi-universal energy reservoir is compatible with the observed $L_p - t_p$ relation. To be as much general as possible, we do not specify which is the origin of the energy reservoir. For instance, for a scenario with magnetar-powered plateau emission, the reservoir is represented by the initial rotational energy of the NS. In the HLE from a structured jet, instead, the reservoir is related to the entire prompt energy released on the full surface of the jet. If the energy during the plateau is released in a time scale t_{res}, the relation between the observed X-ray plateau luminosity and the energy reservoir E_{res} can be written as:

$$L_p \sim \epsilon_r \epsilon_s E_{res} / t_{res},$$

where we introduce ϵ_r and ϵ_s as two conversion factors which take into account the fraction of the reservoir energy E_{res} which is radiated (which

mostly depends on the dissipation mechanism) and the fraction of radiated energy which falls in the observed band (which mostly depend on the dominant radiative process and the resultant spectrum). As a rough approximation, we assume that both ϵ_r and ϵ_s dominantly depend only on the reservoir energy E_{res} and mildly on other physical parameters. Therefore we can factorise $\epsilon_r \epsilon_s = \epsilon(E_{res})$, and we can write:

$$E_{\rm plateau} = \epsilon(E_{res}) E_{res}.$$

We highlight that, from a physical point of view, the conversion efficiency of a dissipation mechanism should not depend on the amount of the energy reservoir, but mainly on the specific microphysics of the process. Therefore is more plausible that most of the dependency of $\epsilon(E_{res})$ resides in ϵ_s, namely in the dependence of the spectral peak on the energy reservoir. Here we make a further ansatz, assuming that ϵ increases with E_{res} as:

$$\epsilon\left(E_{res}\right) = \begin{cases} \epsilon_{\rm max} & , E_{res} > E_{\rm max} \\ \epsilon_{\rm max} \left(\dfrac{E_{res}}{E_{\rm max}}\right)^{k} & , E_{res} < E_{\rm max} \end{cases}, \tag{5.2}$$

with $k > 0$ and $\epsilon_{\rm max} \leq 1$. This means that we can reverse the relation and obtain E_{res} as a function of the plateau energy. We can finally define a luminosity of the reservoir as:

$$L_{res} = E_{res}/t_{res} = L_p/\epsilon = L_p \left(\frac{E_{plateau}}{E_{max}}\right)^{-\frac{k}{1+k}}.$$

It can be shown that, if the vertical scatter of the $L_p - t_p$ relation is δ, then the corresponding scatter for the $L_{res} - t_p$ relation would be $\delta^{\frac{1}{1+k}}$. This means that the $L_{res} - t_p$ relation becomes a universal relation ($\delta \to 0$) only if $k \to \infty$. Though, this limit is un-physical, because it would require an efficiency ϵ which drastically depends on the initial energy reservoir. However, it is instructive to see how the $L_{res} - t_p$ relation would appear for reasonable values of k, if we make the substitution

$$L_p \to L_{res} = L^* = L_p \left(\frac{E_{plateau}}{E_{max}}\right)^{-\frac{k}{1+k}}.$$

In Fig. 5.6(b) we show the $L_p - t_p$ and $L^* - t_p$ relation fixing $k = 3$ and $E_{max} = 10^{55}$ erg. It is evident that the re-normalised plateau luminosity

L^* has a much stronger correlation with t_p and all the points are tightly clustered around a line with $E = L_* t_p \sim$const. Hence, this demonstrates that, in principle, the existence of a relation like eq. 5.2 would justify how a quasi-universal energy reservoir can be compatible with the observed $L_p - t_p$ relation.

5.2 Combined X-ray and optical analysis of the X-ray plateau

In this section we perform a systematic analysis of the X-ray and optical emission during and after the plateau phase. The aim is to carry out a time resolved spectral analysis in the X-rays and for each temporal bin test whether both X-rays and optical are compatible with a single synchrotron spectral component. Several GRBs show a plateau phase also at optical wavelengths (e.g. Si et al. 2018; Dainotti et al. 2020), but a comprehensive consistency check of X-ray and optical light curves within the afterglow model is still confined to a few cases (e.g. Gompertz et al. 2015; Zhang et al. 2018).
Regarding the sample selection, we start from the sample of GRBs with an X-ray plateau with available redshift, defined in the previous section. In addition, in order to select a plateau long enough to have a sufficient number of photons to perform a time-resolved spectral analysis, we also discard all GRBs where $t_f/t_i < 2$, where t_i and t_f are the initial and final time of the plateau, respectively.

5.2.1 X-ray plateau optical counterpart sample

In order to investigate on the broad-band properties of the plateau, in this work we focus on a sample subset with multi-band optical/NIR follow-up during the X-ray plateau phase. Specifically, we select GRBs for which multi-band data during the X-ray plateau and post-plateau phase are enough to perform a time resolved spectral analysis (see next section).

The optical sample is based on selection criteria and methods originally presented in Kann et al., 2006. The sample includes GRBs with afterglow, redshift and good coverage in the UV/optical/NIR domain and is based on the updated sample and analysis of works in preparation (Kann et al. 2023a,b,c, in prep.). For this work in particular, we have re-analyzed GRB 110213A, while the analysis of GRB 180728A is taken from Rossi et al. (in

prep.). Hereby, we assume achromaticity and that all bands follow the same temporal evolution. Such an assumption is justified both by theoretical and observational evidences. Indeed, several works demonstrated that the optical emission follows the same temporal trend, independently on the specific adopted filter (e.g., see Harrison et al. 1999; Xu et al. 2009; Filgas et al. 2011; Filgas et al. 2012; Greiner et al. 2013a). Any contribution to the afterglow flux from the presence of the GRB host galaxy and/or an associated supernova has been subtracted. The spectral energy distributions are fitted with local dust extinction laws (Pei, 1992), determining the intrinsic spectral slope β_0 and the extinction in the rest-frame V band A_V (in mag). Using the method of Kann et al., 2006, the light curves are then corrected for line-of-sight extinction. The achromatic nature of the light curves allows us to shift data from other bands to the common R_C band, creating a maximally dense light curve for each analyzed GRB afterglow. Please note that we use results based only on the optical/NIR SED. We report the A_V value of each GRB of our sample in Table 5.6. Most of these measurements are found in the work presented in Kann et al., 2010; Kann et al., 2011 and Kann et al. 2023a,b,c, in prep. There are a few cases (indicated in the table) where we refer to works dedicated to single events. Our final sample of GRBs with X-ray plateau and optical counterparts consists of 30 events. General information of the full GRB sample, including burst duration, redshift and energetics, are quoted in Tab. 5.5.

5.2.2 Data analysis

Our goal is to verify that both the optical and X-ray emission during the X-ray plateau are consistent at each time with a single synchrotron component. To achieve this goal we perform a time resolved spectral analysis in the XRT band, fitting the X-ray data with a single absorbed power law. From this analysis we derive the X-ray flux and the photon index. We then extrapolate the expected flux in the optical regime at the X-ray binning times (see below and Fig. 5.7), and we check whether the extrapolation is compatible with the optical observations shifted to the R_C band (see sec. 5.2.1).

X-ray time resolved spectral analysis

The X-ray light curves have been re-binned imposing that the number of counts per bin in the band (0.5-10) keV is above a certain threshold N_0 and we choose $N_0 > 500$ counts. For bins with $N_0 < 500$ the spectral analysis

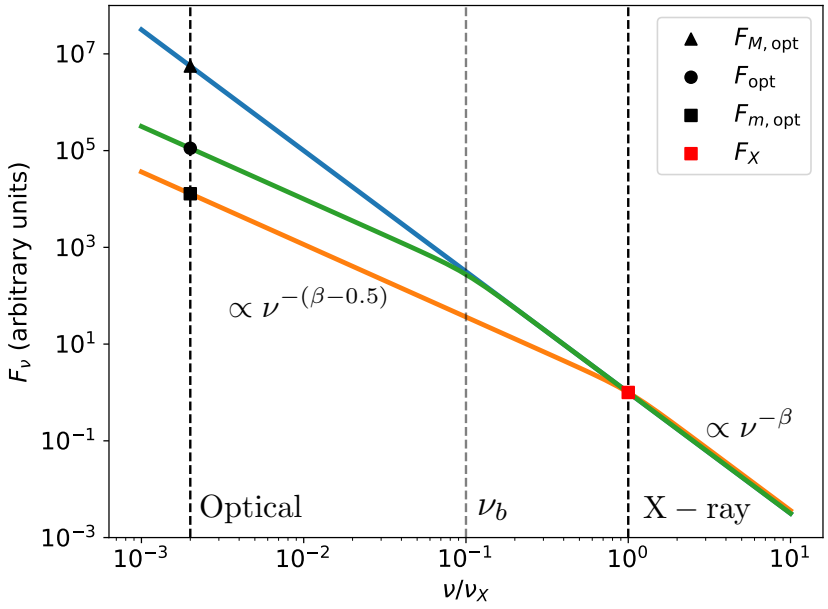

FIGURE 5.7: Schematic representation of the method used to compare X-ray and optical data. $F_{m,\mathrm{opt}}$ and $F_{M,\mathrm{opt}}$ are the minimum and maximum optical fluxes allowed by the standard afterglow model assuming that there is a single break $\nu_{\mathrm{opt}} < \nu_b < \nu_X$. F_X, F_{opt} and the X-ray spectral slope are derived from spectral analysis. Therefore, if $F_{m,\mathrm{opt}} < F_{\mathrm{opt}} < F_{M,\mathrm{opt}}$, we then consider that the optical counterpart is consistent with a single synchrotron spectrum and we can derive ν_b. The blue line has no break, the orange line has $\nu_b = \nu_X$, while the green line has a break between optical and X-ray.

gives too large errors on the parameters or the fit does not converge at all, due to the noisiness of the spectrum. Since the X-ray light curves present some observational gaps, the temporal length is not the same for all the bins. Moreover, given the criteria described above, the bin length tend to be larger in the post-plateau phase, where the count rate decreases.
We perform for each bin a spectral analysis using XSPEC, version 12.10.1 and PyXspec. We consider only photons in the band $E = 0.5 - 10$ keV. Each spectrum is modeled by adopting an absorbed power law and for the absorption we use the Tübingen-Boulder model (Wilms et al., 2000). Since for all the GRBs of our sample the redshift is known, we distinguish a Galactic absorber and the host galaxy absorber. The Galactic absorption is taken from Kalberla et al., 2005. The specific syntax in XSPEC is *tbabs*ztbabs*po*. The estimation of the host equivalent hydrogen column density N_H is performed on the time-integrated spectrum of the post-plateau phase, where

we do not expect strong spectral evolution, as verified by Butler and Kocevski, 2007 and Mu et al., 2016. Once the host N_H is determined, it is fixed to be the same for all the bins of the light curve. The only free parameters are photon index and normalization. Such a procedure is preferred to the case of leaving the host N_H as a free parameter, because of the degeneracy between photon index and column density.

Comparison of optical and X-ray data

In this section we show a method to derive the overall spectral properties of the plateau and post-plateau phases, exploiting the knowledge of the X-ray flux, the optical flux and the X-ray photon index. In the synchrotron scenario, two characteristic frequencies are defined: 1) the cooling frequency ν_c, which is associated with the cooling Lorentz factor $\gamma_c = \frac{6\pi m_e c}{\sigma_T t B^2}$, where the time t and the magnetic field B are defined in the comoving frame; 2) the frequency ν_m, associated with the minimum Lorentz factor γ_m of the electron energy distribution. In the following, we work in the assumption of a slow cooling regime, namely $\nu_m < \nu_c$, as commonly found in GRB afterglows. Indeed, computing the ratio between the cooling frequency ν_c and ν_m (Sari et al., 1998a), we have:

$$\frac{\nu_c}{\nu_m} \sim 10^5 \varepsilon_{B,-3}^{-2} E_{52}^{-1} n^{-1} \varepsilon_{e,-1}^{-2} t_d (1+Y)^{-2}, \tag{5.3}$$

where ϵ_B and ϵ_e are the fraction of energy that goes to magnetic field and electrons, respectively, E is isotropic kinetic energy, n the circum-burst density, t_d the time measured in days and the Y parameter indicated the relevance of the SSC component (we adopt the notation $Q_X = Q/10^X$). In Appendix C.1 we show how the ratio ν_c/ν_m depends of the Y parameter. We find that, for typical micro-physical values, it is more plausible to have $\nu_c > \nu_m$, even if the opposite regime cannot be rejected a priori (discussed later in this section) In the slow cooling regime, we expect that the flux density goes like:

$$F_\nu \propto \nu^{-\beta}$$

for $\nu > \nu_c$ and

$$F_\nu \propto \nu^{-(\beta-1/2)}$$

for $\nu < \nu_c$, where $\beta = p/2$ and p is the power law index of the particle distribution. If $\nu_c < \nu_{\rm opt}$ then optical and X-ray flux can be connected with

a single power law with spectral index β. In this case we define[5]:

$$F_{M,\mathrm{opt}} = F_X(\nu_{\mathrm{opt}}/\nu_X)^{-\beta}.$$

If, instead, $\nu_{\mathrm{opt}} < \nu_c < \nu_X$ the optical flux is below the spectral extrapolation from X-rays assuming a single power law, i.e. $F_{\mathrm{opt}} < F_{M,\mathrm{opt}}$. The minimum expected optical flux corresponds to the case in which $\nu_c \sim \nu_X$ or $\nu_c > \nu_X$ and in this case we define

$$F_{m,\mathrm{opt}} = F_X(\nu_{\mathrm{opt}}/\nu_X)^{-(\beta-1/2)}.$$

Therefore, whenever $F_{m,\mathrm{opt}} < F_{\mathrm{opt}} < F_{M,\mathrm{opt}}$, optical and X-ray emission are compatible with a synchrotron spectrum with $\nu_{\mathrm{opt}} < \nu_c < \nu_X$. In the case $\nu_{\mathrm{opt}} < \nu_c < \nu_X$, we can write

$$F_{\mathrm{opt}} = F_X \left(\frac{\nu_c}{\nu_X}\right)^{-\beta} \left(\frac{\nu_{\mathrm{opt}}}{\nu_c}\right)^{-(\beta-1/2)}.$$

Two other possibilities are:

1. $F_{\mathrm{opt}} > F_{M,\mathrm{opt}}$;
2. $F_{\mathrm{opt}} < F_{m,\mathrm{opt}}$.

In case 1) there is no way to justify optical and X-ray emission with a single synchrotron spectrum. Case 2) can be explained if we assume that $\nu_X < \nu_c$ and $\nu_{\mathrm{opt}} < \nu_m < \nu_X$. We recall that $F_\nu \propto \nu^{1/3}$ for $\nu < \nu_m$, but none of the analysed GRBs has an optical spectral index $\beta_{\mathrm{opt}} < 0$. On the other hand, we have to take into account that the spectral breaks in synchrotron are not sharp, namely the spectral slope $dF_\nu/d\nu$ has a smooth transition across the break. Therefore, if $\nu_m \sim \nu_{\mathrm{opt}}$ and no other break is present between ν_{opt} and ν_X, it is still possible to measure $\beta_{\mathrm{opt}} > 0$ and $F_{\mathrm{opt}} < F_{m,\mathrm{opt}}$. Hence, we conservatively consider case 2) as a case compatible with a single synchrotron spectrum.
In the case of $F_{m,\mathrm{opt}} < F_{\mathrm{opt}} < F_{M,\mathrm{opt}}$, since F_{opt}, F_X and β are known, we can estimate ν_c as follows:

$$\nu_c = \left(\frac{F_X}{F_{\mathrm{opt}}}\right)^2 \left(\frac{\nu_{\mathrm{opt}}}{\mathrm{keV}}\right)^{1-p} \mathrm{keV}. \tag{5.4}$$

[5]As reference, throughout the paper we consider ν_X =1 keV and $\nu_{\mathrm{opt}} = 1.88 \times 10^{-3}$ keV, corresponding to the central frequency of the R band.

The uncertainty on ν_c is derived through error propagation using the same formula. Based on the comparison of optical and X-ray data, we define two sub-samples:

- *Sample 1*: for all the temporal bins the optical flux satisfies the condition $F_{m,\mathrm{opt}} < F_{\mathrm{opt}} < F_{M,\mathrm{opt}}$ or $F_{\mathrm{opt}} < F_{m,\mathrm{opt}}$. In this case optical and X-ray emissions are compatible with a single synchrotron spectrum. 19 GRBs satisfy this condition.
- *Sample 2*: for at least one temporal bin $F_{\mathrm{opt}} > F_{M,\mathrm{opt}}$, which indicates an incompatibility with single component synchrotron origin. 11 GRBs fall within this case.

In the case of *Sample 1* we derive the temporal evolution of ν_c during and after the X-ray plateau. If the number of temporal bins where both X-ray and optical data are available is larger than 4, we fit the temporal evolution of ν_c with a power law $\nu_c \propto t^{-s}$. The adopted fitting formula is:

$$\log_{10}(v_c/\mathrm{keV}) = \mathrm{A} - \mathrm{s}\log_{10}(\mathrm{t}/\ \mathrm{sec}). \tag{5.5}$$

The results of the fit are reported in Tab. 5.9. In our sample there are 5 GRBs with s consistent with 0 within the errors, 11 with $s > 0$ and 3 with $s < 0$. The same analysis about the temporal evolution of the spectral break can be repeated relaxing the assumption that we are in slow cooling regime. All the considerations reported above still hold, but in fast cooling we have:

$$F_{m,\mathrm{opt}} = F_X(\nu_{\mathrm{opt}}/\nu_X)^{-1/2},$$

and the break frequency would be ν_m, which can be analogously derived and corresponds to

$$\nu_m = \left(\frac{F_X}{F_{\mathrm{opt}}}\right)^{2/(p-1)} \left(\frac{\nu_{\mathrm{opt}}}{\mathrm{keV}}\right)^{1/(1-p)} \mathrm{keV}. \tag{5.6}$$

The expression of $F_{M,\mathrm{opt}}$ is unchanged, since the spectral slope above the break is the same in both slow and fast cooling regime. This means that the selection condition $F_{\mathrm{opt}} \leqslant F_{M,\mathrm{opt}}$ would produce the same classification of *Sample 1* and *Sample 2* as in slow cooling. Comparing eqs. 5.4 and 5.6, we notice that the break frequency derived in the slow cooling regime ($\nu_{c,SC}$) and the one derived for the fast cooling regime ($\nu_{m,FC}$) are connected by the following relation:

$$\nu_{m,FC} \propto (\nu_{c,SC})^{\frac{1}{p-1}}.$$

Therefore, having fitted the temporal behaviour of $\nu_{c,SC}$ as $\propto t^{-s}$, in the assumption of a fast cooling regime we would have obtained

$$\nu_{m,FC} \propto t^{\frac{s}{1-p}}.$$

This implies that, for typical values of $p > 2$, if $\nu_{c,SC}$ decreases in time, $\nu_{m,FC}$ would decrease as well.

TABLE 5.5: General information of the full sample.

GRB	z	t_{90} (s)	$E_{iso}(10^{52}$ erg)	E_p(keV)	Ref.
050319	3.24	152 ± 11	$3.98^{+6.39}_{-0.59}$	$190.8^{+114.5}_{-182.3}$	(1)
050416A	0.65	6.7 ± 3.4	$0.08^{+0.05}_{-0.02}$	$24.8^{+8.3}_{-8.3}$	(1)
050730	3.97	155 ± 19	$5.89^{+8.07}_{-3.02}$	$973.8^{+2797}_{-432.3}$	(1)
050824	0.83	25 ± 5.6	$0.11^{+0.87}_{-0.04}$	$23.8^{+3.7}_{-21.9}$	(1)
051109A	2.35	37 ± 6	$0.95^{+1.50}_{-6.46}$	$466.8^{+388.1}_{-150.6}$	(1)
060526	3.21	298 ± 23	$4.90^{+5.72}_{-0.35}$	$307.4^{+635.9}_{-303.2}$	(1)
060605	3.8	80 ± 7	$1.91^{+3.11}_{-0.61}$	$677.8^{+1714}_{-238.7}$	(1)
060614	0.125	109 ± 3	$0.25^{+0.03}_{-0.02}$	$55.0^{+45.0}_{-45.0}$	(2)
060729	0.54	113 ± 22	$0.27^{+0.29}_{-0.06}$	$103.2^{+352.7}_{-38.5}$	(1)
061121	1.31	81 ± 5	$25.70^{+1.33}_{-2.48}$	$1402^{+208.3}_{-166.6}$	(1)
080310	2.43	363 ± 17	$4.90^{+10.71}_{-0.99}$	$75.4^{+72.0}_{-30.8}$	(1)
080413B	1.1	8 ± 2	$6.92^{+2.41}_{-6.89}$	$614.5^{+350.2}_{-154.5}$	(1)
080605	1.64	18 ± 1	$24.04^{+0.28}_{-0.28}$	$686.3^{+23.8}_{-26.4}$	(3)
081007	0.53	9.7 ± 4.9	$0.20^{+0.03}_{-0.03}$	$61.2^{+15.3}_{-15.3}$	(3)
081029	3.85	275 ± 49	$20.75^{+5.25}_{-3.45}$	$887.2^{+804.8}_{-290.9}$	(3)
090618	0.54	113 ± 1	$26.36^{+0.37}_{-0.36}$	$338.8^{+12.3}_{-12.3}$	(3)
091018	0.97	4.4 ± 0.6	$0.94^{+0.11}_{-0.09}$	$53.2^{+3.9}_{-7.9}$	(3)
091029	2.75	39 ± 5	$16.63^{+2.16}_{-1.98}$	$247.6^{+41.3}_{-37.5}$	(3)
100219A	4.67	27 ± 9	$2.67^{+1.50}_{-0.64}$	$696.2^{+2393.1}_{-293.1}$	(3)
100418A	0.62	7.9 ± 1.1	$22.23^{+2.37}_{-2.37}$	$259.6^{+33.9}_{-30.7}$	(3)
100621A	0.54	64 ± 2	$4.57^{+0.18}_{-0.17}$	$149.6^{+12.3}_{-10.8}$	(3)
100814A	1.44	177 ± 11	$7.52^{+0.19}_{-0.19}$	$242.1^{+20.9}_{-17.0}$	(3)
110213A	1.46	48 ± 16	$5.15^{+0.22}_{-0.20}$	$216.9^{+12.8}_{-12.8}$	(3)
110715A	0.82	13 ± 4	10.4^{+1}_{-1}	259^{+34}_{-31}	(3)
111228A	0.71	101 ± 5	$1.87^{+0.52}_{-0.36}$	$58.4^{+6.9}_{-6.9}$	(3)
120404A	2.87	39 ± 4	$10.91^{+1.70}_{-1.39}$	$271.4^{+81.4}_{-50.4}$	(3)
130702A	0.15	~ 59	$6.6^{+0.4}_{-0.4}$	-	(4)
140419A	3.96	80 ± 4	$254.68^{+16.34}_{-14.80}$	$1397.6^{+188.3}_{-188.3}$	(3)
150910A	1.36	112 ± 37	$5.20^{+0.49}_{-0.45}$	$535.4^{+113.2}_{-87.3}$	(3)
180728A	0.12	8.7 ± 0.3	$0.30^{+0.0002}_{-0.0002}$	$88.5^{+1.6}_{-1.6}$	(3)

(1) Kann et al., 2010, (2) Kann et al., 2011, (3) Kann et al. (in preparation), (4) Volnova et al., 2017.

TABLE 5.6: Optical general information

GRB	β_{opt}	A_V(mags)	t_1(s)	t_2(s)	Model
050319	0.74 ± 0.42	0.05 ± 0.09	381	400550	SMC
050416A	0.92 ± 0.3	0.21 ± 0.14	657	144815	SMC
050730	0.52 ± 0.05	0.1 ± 0.015	1555	12563	SMC
050824	0.45 ± 0.18	0.14 ± 0.13	634.7	34478	SMC
051109A	0.42	0.09 ± 0.03	167	44747	SMC
060526	0.65 ± 0.06	0	3080	462574	N/A
060605	0.6	0	86	23377	N/A
060614	0.41 ± 0.09	0.28 ± 0.07	4733	246090	SMC
060729	0.67 ± 0.07	0	18042	662500	N/A
061121	0.6	0	305	72360	N/A
080310	0.42 ± 0.12	0.19 ± 0.05	153	252216	SMC
080413B	0.74 ± 0.04	0	96	780506	N/A
080605	0.58 ± 0.35	0.51 ± 0.19	414	124475	SMC
081007	0.27 ± 0.11	0.82 ± 0.09	94	328979	SMC
081029	0.33 ± 0.05	0.24 ± 0.02	150	108578	SMC
090618	0.71 ± 0.02	0	405	454723	N/A
091018	0.61 ± 0.02	0	301	534067	N/A
091029	0.429 ± 0.026	0	311	188708	N/A
100219A	0.66 ± 0.14	0.13 ± 0.05	31708	398304	SMC
100418A	1.06 ± 0.02	0.09 ± 0.04	27742	476546	SMC
100621A	0.78 ± 0.09	3.72 ± 0.10	237	10974	SMC
100814A	0.41 ± 0.04	0.16 ± 0.02	526	960827	SMC
110213A	0.9 ± 0.07	0.132 ± 0.003	193	5546	SMC
110715A	0.63 ± 0.28	0.47 ± 0.22	217211	736849	SMC
111228A	0.69 ± 0.07	0.16 ± 0.04	349	663118	SMC
120404A	1.02	0.07 ± 0.02	730	19824	MW
130702A	0.71 ± 0.02	0	101088	335296	N/A
140419A	0.76 ± 0.08	0	280	10780	N/A
150910A	0.53 ± 0.14	0.17 ± 0.05	728	120966	SMC
180728A	0.67 ± 0.05	0	2072	180050	N/A

For GRBs 060605 and 061121 we assumed $\beta_{opt} = 0.6$ as in Kann et al., 2006. t_1(s) and t_2(s) define the interval within which the optical modelling has been obtained. For GRB 100219A , the values reported are from Thöne et al., 2013.

name	N ($\times$100 mJy)	a	b	$t_b/10^4 s$	χ^2/dof	$\log_{10}(\frac{L_X}{\mathrm{erg/s}})$	ph. index.	p-value
				Sample 1				
050319	0.07 ± 0.01	0.45 ± 0.04	1.90 ± 0.18	5.36 ± 1.15	65.7/82	$48.09^{+0.09}_{-0.11}$	1.92 ± 0.03	0.763
050416A	0.43 ± 0.30	0.32 ± 0.17	0.96 ± 0.05	0.10 ± 0.10	90.8/96	$46.79^{+0.09}_{-0.11}$	1.90 ± 0.04	0.765
050824	0.03 ± 0.02	0.04 ± 0.32	0.98 ± 0.17	3.75 ± 3.75	53.0/41	$45.66^{+0.10}_{-0.12}$	1.96 ± 0.07	0.078
051109A	0.94 ± 0.84	0.52 ± 0.39	1.34 ± 0.08	0.47 ± 0.46	151.7/151	$48.25^{+0.09}_{-0.11}$	2.12 ± 0.03	0.412
060526	0.02 ± 0.01	0.56 ± 0.06	2.25 ± 0.23	5.29 ± 1.45	92.4/37	$48.13^{+0.09}_{-0.11}$	1.98 ± 0.07	0.508
060605	0.14 ± 0.03	0.39 ± 0.10	2.45 ± 0.15	1.06 ± 0.17	48.7/63	$48.23^{+0.09}_{-0.11}$	2.00 ± 0.04	0.386
060729	0.26 ± 0.01	0.03 ± 0.02	1.53 ± 0.02	6.83 ± 0.39	867.3/675	$46.40^{+0.09}_{-0.11}$	1.93 ± 0.01	0.002(*)
061121	1.23 ± 0.16	0.34 ± 0.03	1.55 ± 0.03	0.77 ± 0.10	323.1/276	$48.39^{+0.07}_{-0.09}$	1.93 ± 0.02	0.001(*)
080413B	1.36 ± 0.71	0.51 ± 0.09	1.22 ± 0.04	0.15 ± 0.09	300.8/225	$48.09^{+0.08}_{-0.10}$	1.86 ± 0.02	0.226
080605	10.81 ± 2.58	0.40 ± 0.08	1.50 ± 0.03	0.06 ± 0.01	383.2/311	$49.31^{+0.06}_{-0.07}$	1.71 ± 0.02	0.194
090618	4.65 ± 0.54	0.33 ± 0.06	1.51 ± 0.02	0.41 ± 0.05	812.8/775	$47.66^{+0.07}_{-0.08}$	1.91 ± 0.01	$< 10^{-3}$(*)
091018	5.63 ± 0.79	-0.17 ± 0.26	1.25 ± 0.03	0.03 ± 0.01	155.0/115	$48.14^{+0.08}_{-0.10}$	1.92 ± 0.03	0.059
091029	0.17 ± 0.03	-0.06 ± 0.10	1.22 ± 0.04	0.83 ± 0.19	127.8/120	$47.78^{+0.09}_{-0.11}$	1.92 ± 0.04	0.558
100621A	0.11 ± 0.04	0.68 ± 0.03	1.69 ± 0.09	8.05 ± 2.48	249.5/178	$46.70^{+0.09}_{-0.11}$	2.37 ± 0.03	$< 10^{-3}$(*)
110213A	5.03 ± 0.37	-0.19 ± 0.06	1.90 ± 0.03	0.31 ± 0.02	245.0/229	$48.57^{+0.09}_{-0.11}$	2.04 ± 0.02	0.020(*)
111228A	0.57 ± 0.12	0.19 ± 0.07	1.28 ± 0.04	0.75 ± 0.19	195.4/150	$47.00^{+0.09}_{-0.11}$	1.97 ± 0.03	0.589
130702A	0.26 ± 0.10	0.10 ± 0.61	1.35 ± 0.10	8.93 ± 4.66	210.2/226	$44.81^{+0.09}_{-0.11}$	1.81 ± 0.03	0.343
140419A	1.21 ± 1.03	0.60 ± 0.20	1.55 ± 0.11	0.60 ± 0.46	201.6/198	$49.38^{+0.09}_{-0.11}$	1.88 ± 0.03	0.017(*)
180728A	1.78 ± 1.54	0.69 ± 0.17	1.44 ± 0.07	2.12 ± 1.71	583.5/500	$45.76^{+0.09}_{-0.11}$	1.76 ± 0.02	0.055
				Sample 2				
050730	2.64 ± 0.33	-0.02 ± 0.22	2.62 ± 0.05	0.76 ± 0.06	481.8/334	$49.54^{+0.09}_{-0.11}$	1.55 ± 0.02	$< 10^{-3}$(*)
060614	0.09 ± 0.01	-0.06 ± 0.06	2.16 ± 0.06	5.21 ± 0.40	119.8/153	$44.49^{+0.09}_{-0.11}$	1.77 ± 0.03	0.098
080310	0.13 ± 0.03	0.32 ± 0.09	1.81 ± 0.09	1.42 ± 0.32	148.8/77	$48.07^{+0.09}_{-0.11}$	1.92 ± 0.05	$< 10^{-3}$(*)
081007	0.01 ± 0.01	0.68 ± 0.05	1.56 ± 0.17	11.34 ± 7.17	76.1/64	$46.32^{+0.09}_{-0.11}$	1.87 ± 0.05	0.453
081029	0.08 ± 0.01	0.18 ± 0.10	3.00 ± 0.22	1.80 ± 0.21	95.3/76	$48.08^{+0.09}_{-0.11}$	1.86 ± 0.05	0.297
100219A	0.04 ± 0.01	0.53 ± 0.06	3.00 ± 0.29	2.77 ± 0.56	42.3/23	$48.55^{+0.09}_{-0.11}$	1.58 ± 0.06	0.973
100418A	0.02 ± 0.00	-0.45 ± 0.15	1.63 ± 0.11	7.18 ± 1.78	27.9/26	$45.15^{+0.10}_{-0.13}$	1.76 ± 0.09	0.441
100814A	0.05 ± 0.00	0.50 ± 0.02	2.38 ± 0.09	21.53 ± 1.47	731.6/293	$47.25^{+0.09}_{-0.11}$	1.84 ± 0.02	0.049(*)
110715A	24.76 ± 1.15	-0.80 ± 0.32	1.00 ± 0.01	0.01 ± 0.00	452.1/247	$48.57^{+0.06}_{-0.07}$	1.85 ± 0.02	$< 10^{-3}$(*)
120404A	0.42 ± 0.17	-0.16 ± 0.38	1.97 ± 0.14	0.28 ± 0.09	29.7/36	$48.31^{+0.09}_{-0.11}$	1.78 ± 0.06	0.001(*)
150910A	1.92 ± 0.15	0.34 ± 0.02	2.49 ± 0.06	0.67 ± 0.04	487.1/328	$48.72^{+0.06}_{-0.07}$	1.52 ± 0.02	$< 10^{-3}$(*)

TABLE 5.7: Results relative to the temporal fit of the X-ray light curve. The first four columns are the best fit parameters. t_b is in the observer frame. The fifth column is the reduced χ^2 and L_X is the average X-ray luminosity during the plateau. Further details are specified in the text. Errors are given at the 1 sigma level of confidence. The last two columns report the average X-ray photon index and the corresponding p-value of the fit with a constant of the photon index as a function of time. Cases denoted with $(^*)$ have a p-value < 0.05, indicating that the photon index temporal trend significantly deviates from a constant.

name	N ($\times$100 mJy)	a	b	$t_b/10^4$s	χ^2/dof	$\log_{10}(L_{\rm opt}$(erg/s))
			Sample 1			
050319	0.9 ± 0.1	0.53 ± 0.02	2.85 ± 0.30	41.57 ± 3.40	39.9/37	$46.26^{+0.06}_{-0.05}$
050416A	11.9 ± 2.1	-0.31 ± 0.32	0.92 ± 0.07	0.05 ± 0.02	40.1/28	$44.36^{+0.05}_{-0.05}$
050824	4.2 ± 0.1	0.66 ± 0.01	-	-	58.9/27	-
051109A	17.2 ± 0.3	0.81 ± 0.02	-	-	25.0/21	-
060526	2.5 ± 0.2	0.60 ± 0.01	2.64 ± 0.10	15.78 ± 0.85	199.0/43	$46.56^{+0.05}_{-0.05}$
060605	12.0 ± 1.6	0.80 ± 0.03	3.00 ± 0.17	2.45 ± 0.18	165.5/29	$47.42^{+0.04}_{-0.04}$
060729	31.0 ± 2.1	0.02 ± 0.03	1.60 ± 0.03	8.16 ± 0.72	305.0/41	$44.99^{+0.06}_{-0.05}$
061121	4.9 ± 4.2	0.53 ± 0.08	1.26 ± 0.14	4.09 ± 3.93	58.2/30	$45.98^{+0.12}_{-0.09}$
080413B	1.5 ± 0.1	0.43 ± 0.01	3.00 ± 0.27	40.12 ± 2.46	213.7/25	$45.42^{+0.04}_{-0.04}$
080605	8.0 ± 0.1	0.64 ± 0.01	-	-	172.4/39	-
090618	44.3 ± 10.9	0.51 ± 0.05	1.45 ± 0.04	1.72 ± 0.43	43.2/43	$45.26^{+0.03}_{-0.03}$
091018	1.2 ± 0.1	0.91 ± 0.01	2.84 ± 0.32	12.51 ± 0.88	42.5/36	$45.97^{+0.03}_{-0.03}$
091029	3.8 ± 0.8	0.39 ± 0.03	1.63 ± 0.13	5.87 ± 1.43	48.6/37	$46.08^{+0.05}_{-0.04}$
100621A	32.2 ± 2.7	0.22 ± 0.02	2.41 ± 0.18	4.00 ± 0.40	2560.6/29	$45.32^{+0.02}_{-0.02}$
110213A	290.4 ± 5.6	0.20 ± 0.01	2.01 ± 0.02	1.52 ± 0.04	2645.9/41	$47.09^{+0.02}_{-0.02}$
111228A	29.4 ± 2.6	0.25 ± 0.03	1.54 ± 0.04	1.91 ± 0.20	72.5/39	$45.28^{+0.05}_{-0.04}$
130702A	320.1 ± 24.6	1.31 ± 0.02	-	-	41.8/40	-
140419A	15.1 ± 0.2	1.06 ± 0.01	-	-	119.6/34	-
180728A	123.7 ± 1.7	1.08 ± 0.01	-	-	92.5/39	-
			Sample 2			
050730	74.9 ± 13.0	-0.22 ± 0.28	1.58 ± 0.08	0.74 ± 0.19	236.9/18	$47.13^{+0.02}_{-0.02}$
060614	8.6 ± 0.6	0.03 ± 0.06	2.47 ± 0.08	7.55 ± 0.46	48.4/22	$42.81^{+0.05}_{-0.04}$
080310	175.7 ± 5.0	-0.60 ± 0.10	1.16 ± 0.01	0.18 ± 0.01	795.5/43	$46.93^{+0.03}_{-0.03}$
081007	8.9 ± 0.1	0.73 ± 0.01	-	-	272.4/38	-
081029	197.6 ± 3.0	-1.31 ± 0.06	1.90 ± 0.02	0.86 ± 0.02	316.7/30	$47.36^{+0.02}_{-0.02}$
100219A	6.9 ± 0.2	0.99 ± 0.02	-	-	73.1/21	-
100418A	21.6 ± 0.8	-0.32 ± 0.03	1.66 ± 0.04	5.72 ± 0.33	200.0/31	$44.58^{+0.04}_{-0.03}$
100814A	8.2 ± 0.2	0.09 ± 0.01	3.90 ± 0.15	39.14 ± 0.70	3100.6/47	$45.68^{+0.02}_{-0.02}$
110715A	9.6 ± 1.3	0.52 ± 0.01	2.87 ± 0.30	37.49 ± 3.19	123.4/30	$46.12^{+0.06}_{-0.05}$
120404A	147.0 ± 3.0	-1.65 ± 0.11	1.60 ± 0.04	0.26 ± 0.01	22.3/38	$46.79^{+0.06}_{-0.05}$
150910A	315.1 ± 11.6	-4.00 ± 0.34	1.26 ± 0.01	0.11 ± 0.00	75.3/36	$46.20^{+0.12}_{-0.10}$

TABLE 5.8: Results relative to the temporal and spectral optical analysis. The first four columns are the best fit parameters. t_b is in the observer frame. The fifth column is the reduced χ^2 and $L_{\rm opt}$ is the average optical luminosity during the plateau, if present. The reported parameters are specified in the text. Errors are given at 1 sigma level of confidence. When the fit with a broken power law does not converge, we fit with a single power law and therefore only the value of the slope a is reported.

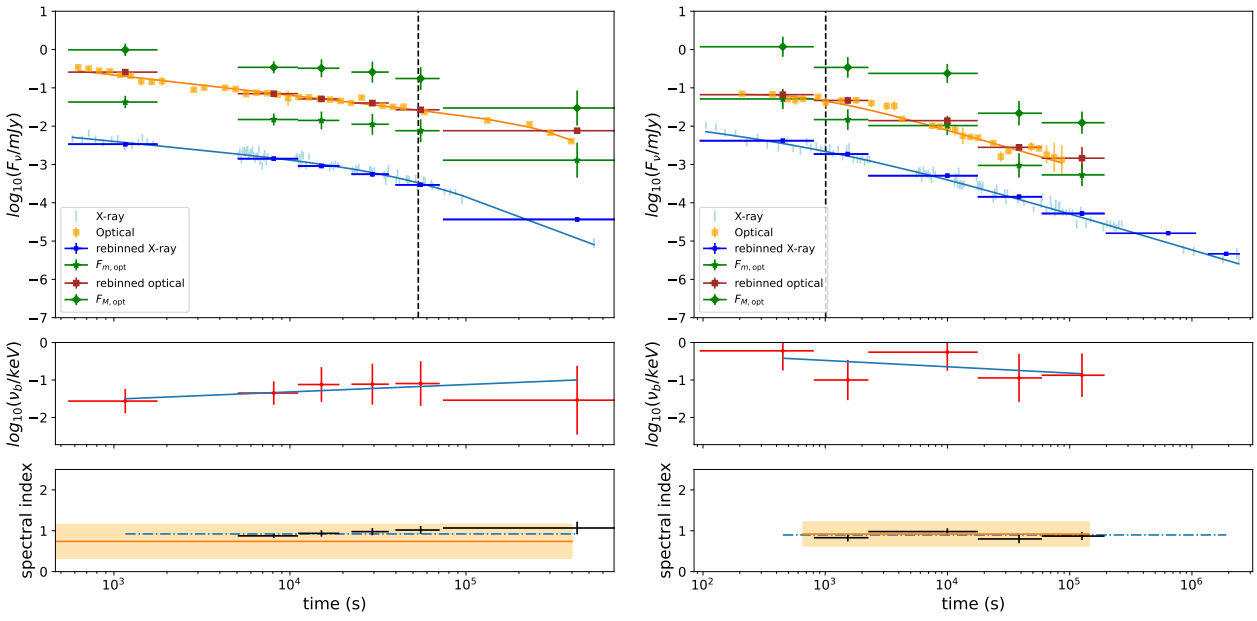

(a) 050319

(b) 050416A

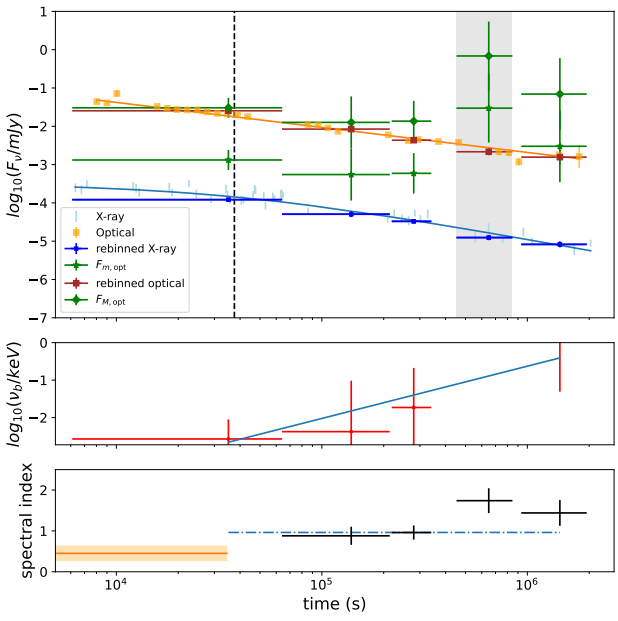

(c) 050824

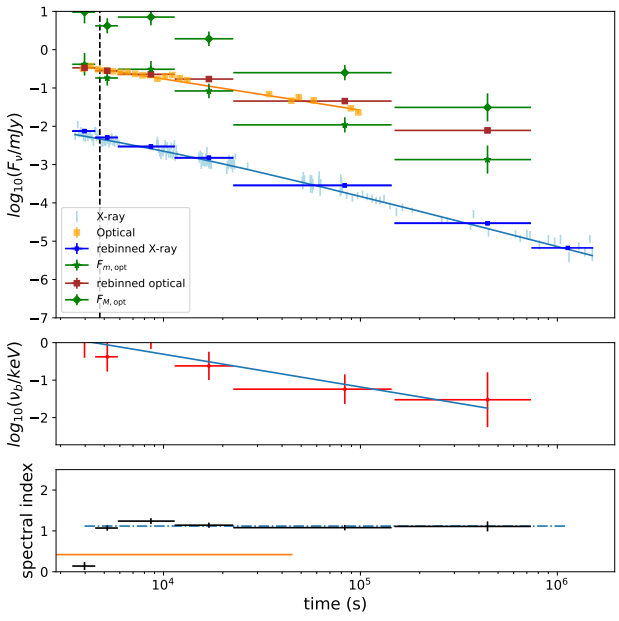

(d) 051109A

FIGURE 5.8: Summary plots of the simultaneous optical/X-ray spectral analysis for the first sample (*Sample 1*), where optical and X-ray are compatible with a single synchrotron spectrum. The top panel shows the X-ray (blue points) and the optical (orange points) light curves. The X-ray flux is computed at 1 keV, while the optical flux in the R band. The solid blue and orange lines are the best fit curves that interpolate the X-ray and optical light curves, respectively. f_m is the optical flux density extrapolated from X-ray flux assuming a spectral break $\nu_b = \nu_X$, while f_M is the optical flux density extrapolated from X-ray flux assuming no spectral break. Gray vertical band indicates when $f_{opt} < f_m$. The vertical dashed line indicates the end of the plateau. In the middle panel we report the evolution of the break frequency ν_b as a function of time (red error bars), while the blue line indicates the best fit with a power law ($n_b \propto t^s$). In the bottom panel, we show the X-ray spectral index for each temporal bin with black error bars, while the dot-dashed line is the time-averaged value. In the same sub-plot, we also report the optical spectral index with an orange line (the yellow band is the uncertainty interval).

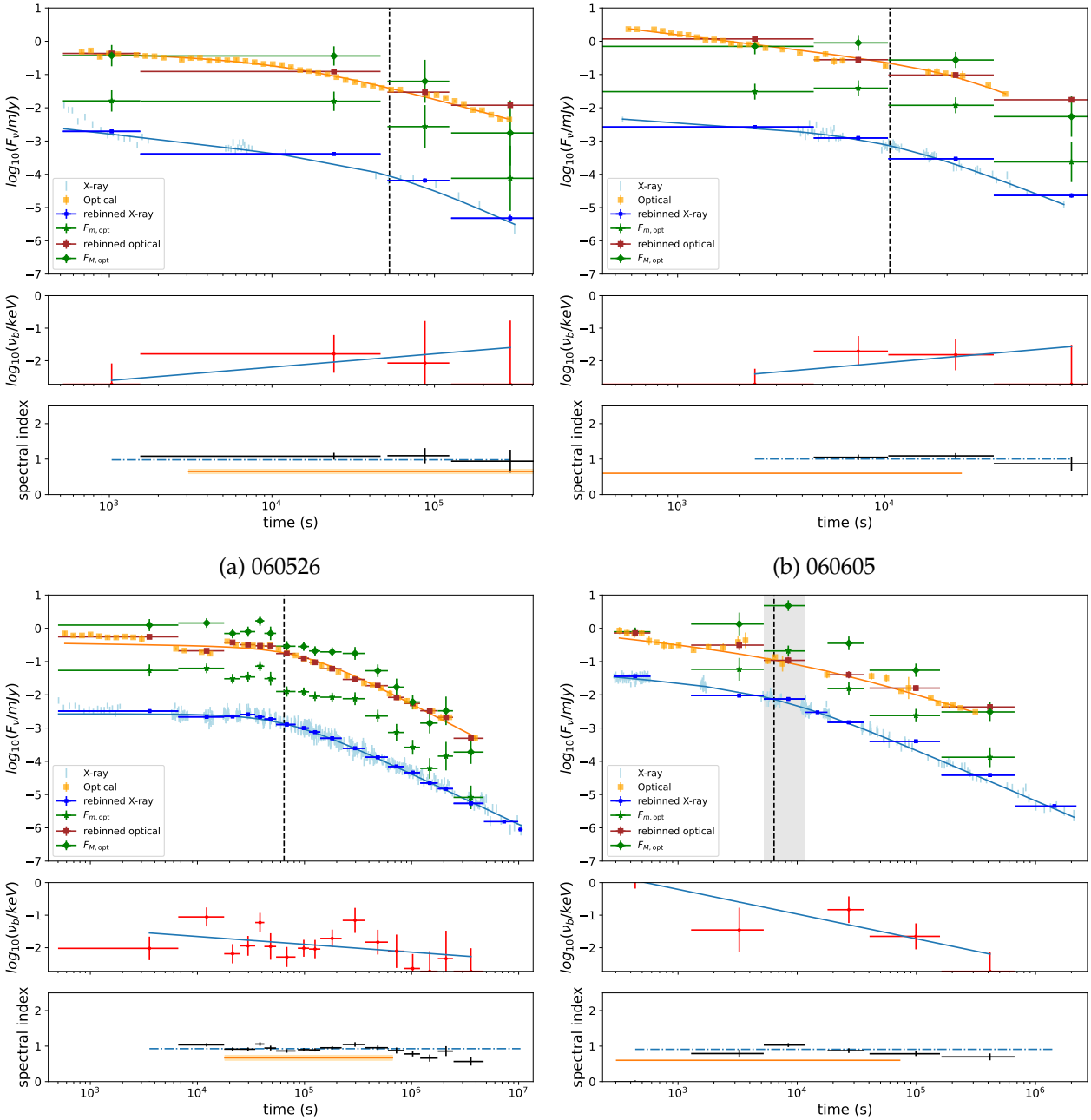

(a) 060526

(b) 060605

(c) 060729

(d) 061121

FIGURE 5.9: *Sample 1* - continued

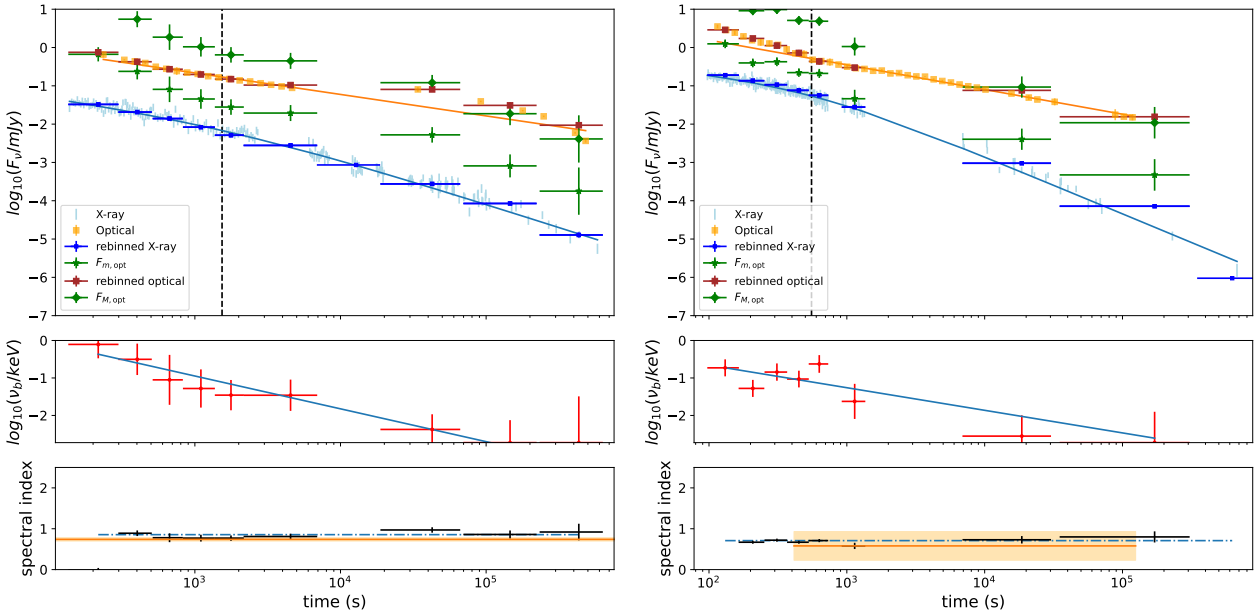

(a) 080413B

(b) 080605

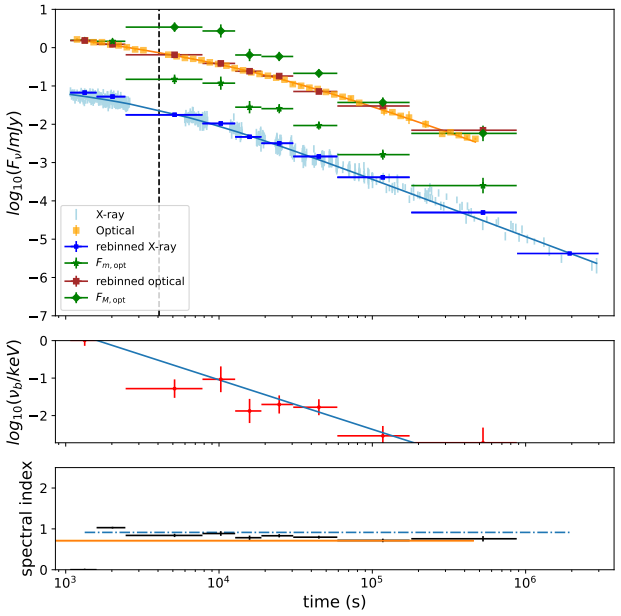

(c) 090618

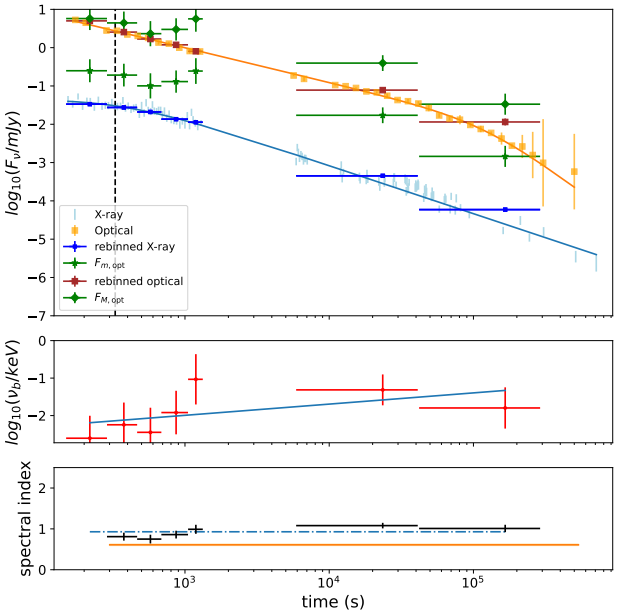

(d) 091018

FIGURE 5.10: *Sample 1* - continued

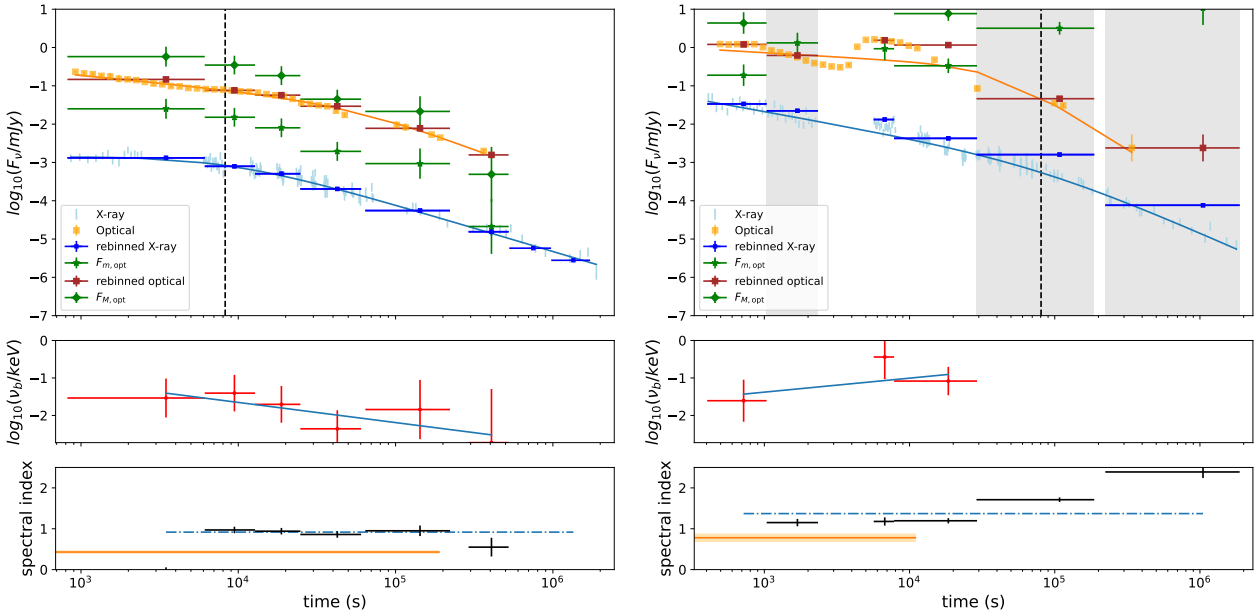

(a) 091029

(b) 100621A

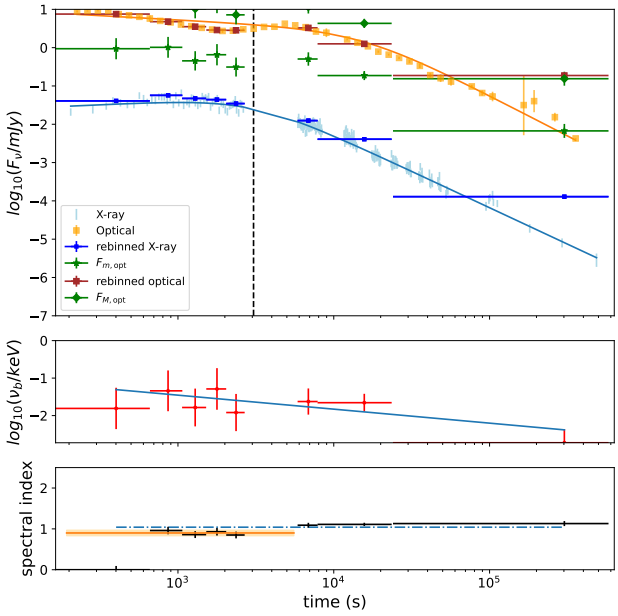

(c) 110213A

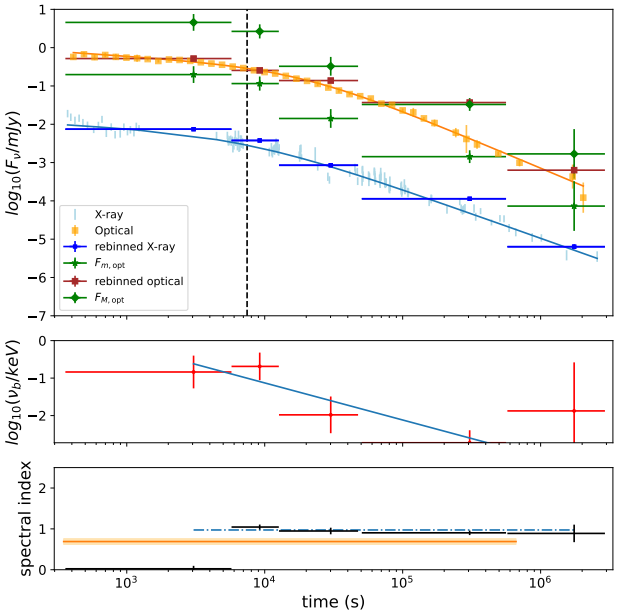

(d) 111228A

FIGURE 5.11: *Sample 1* - continued

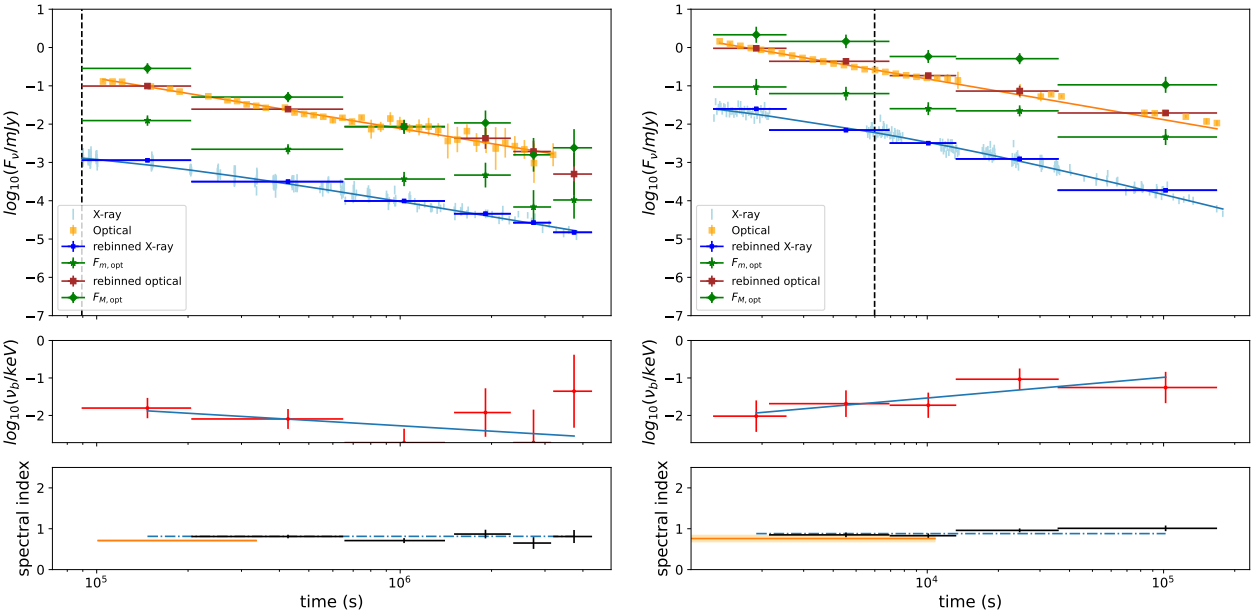

(a) 130702A (b) 140419A

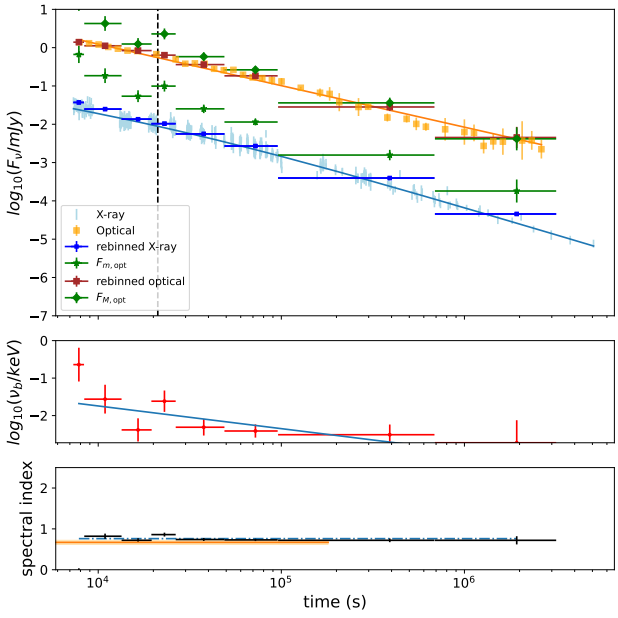

(c) 180728A

FIGURE 5.12: *Sample 1* - continued

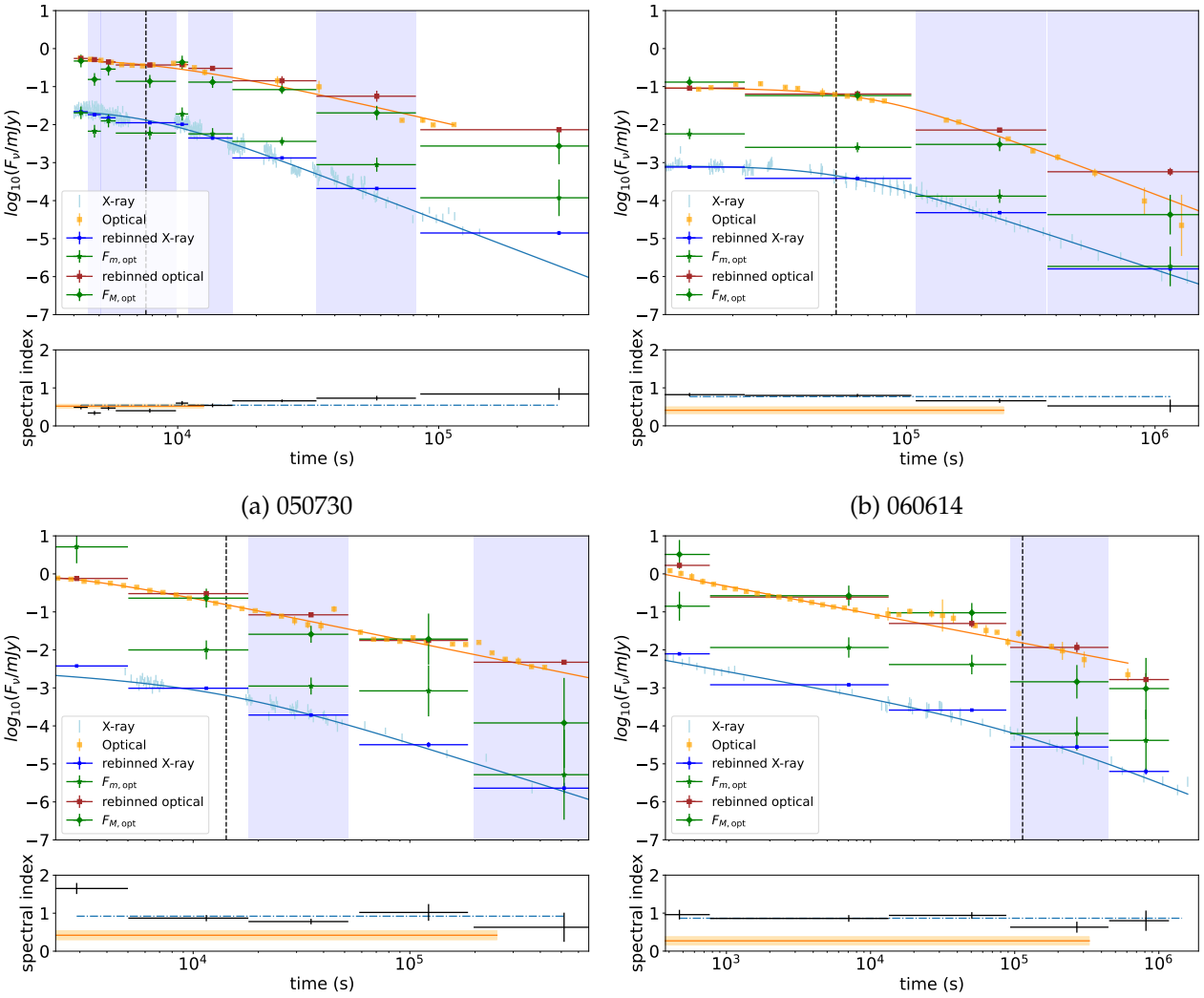

(a) 050730

(b) 060614

(c) 080310

(d) 081007

FIGURE 5.13: Summary plots of the second sample of GRBs (*Sample 2*) where for at least one temporal bin the optical flux is above f_M, indicating that optical and X-ray data are not compatible with a single synchrotron spectrum. The symbols are the same as in Fig. 5.8 and we indicate with a vertical light-blue band the temporal bin where $f_{opt} > f_M$. The lower panel shows the temporal evolution of the X-ray photon index.

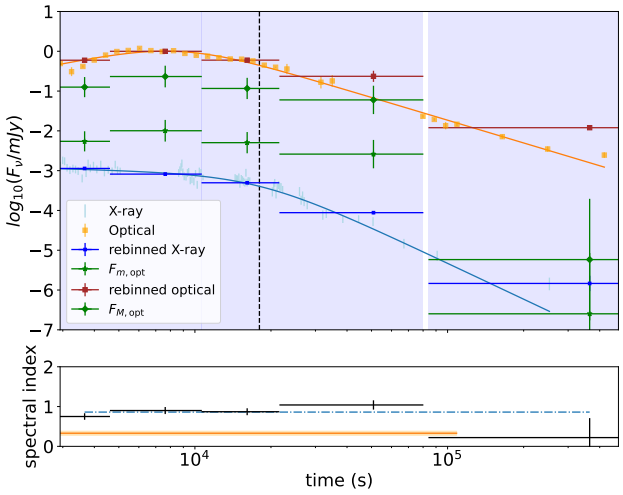

(a) 081029

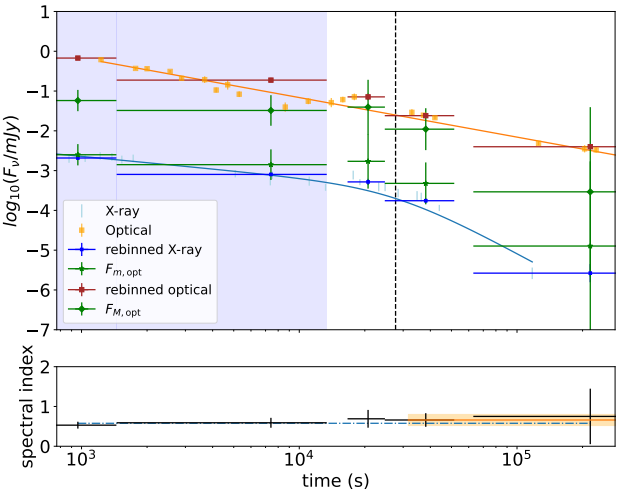

(b) 100219A

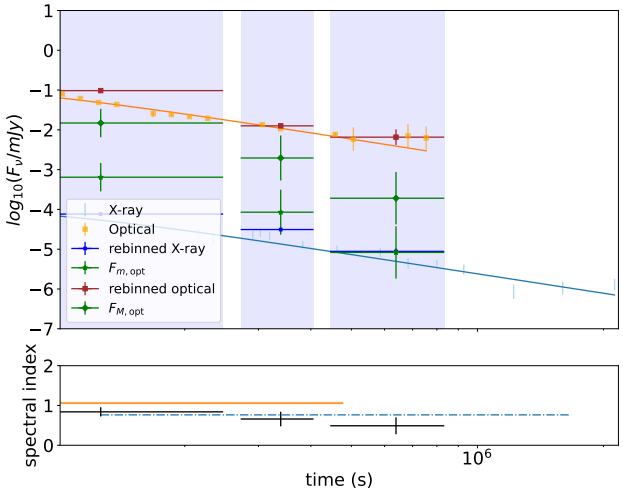

(c) 100418A

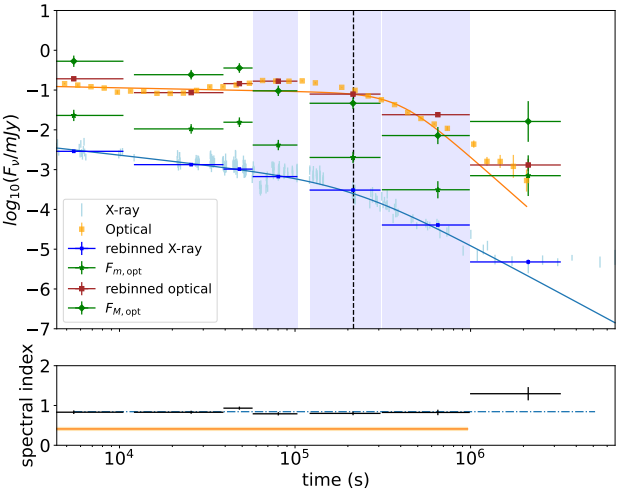

(d) 100814A

FIGURE 5.14: *Sample 2* - continued

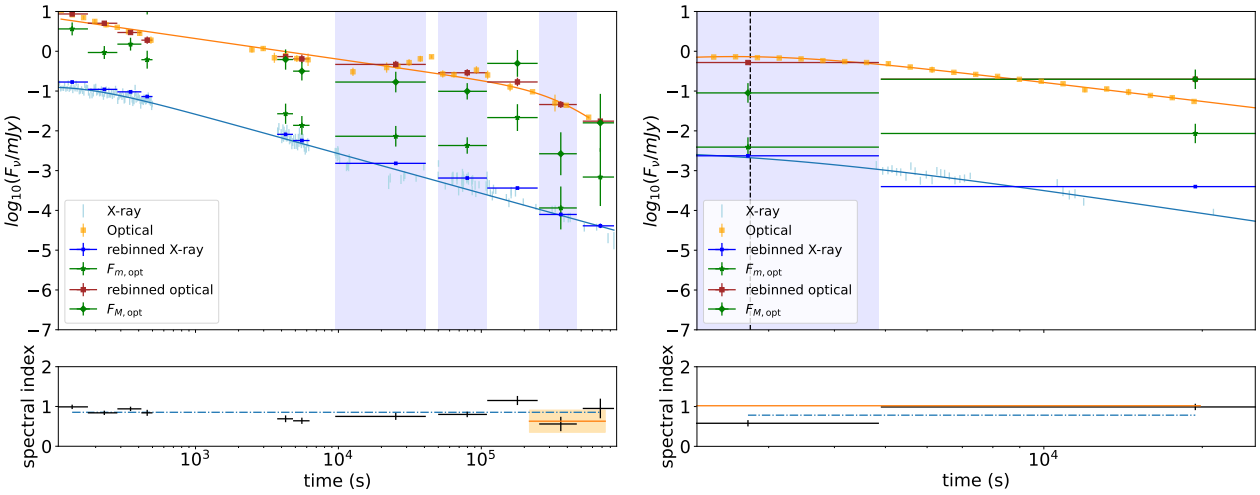

(a) 110715A

(b) 120404A

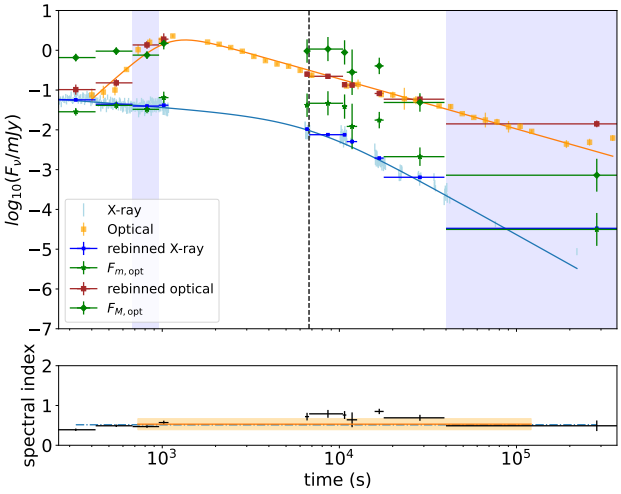

(c) 150910A

FIGURE 5.15: *Sample 2* - continued

GRB	A	s	class
050824	-8.99 ± 4.45	-1.39 ± 0.91	(1)
050319	-2.16 ± 1.07	-0.21 ± 0.27	(2)
050416A	0.03 ± 1.09	0.17 ± 0.28	(2)
051109A	3.19 ± 1.35	0.87 ± 0.31	(3)
060526	-3.84 ± 2.04	-0.41 ± 0.51	(2)
060605	-4.26 ± 2.37	-0.55 ± 0.60	(2)
060729	-0.71 ± 0.64	0.24 ± 0.13	(3)
061121	2.07 ± 0.61	0.76 ± 0.16	(3)
080413B	1.68 ± 0.60	0.88 ± 0.17	(3)
080605	0.55 ± 0.51	0.60 ± 0.19	(3)
090618	4.24 ± 0.38	1.32 ± 0.10	(3)
091018	-2.81 ± 0.76	-0.27 ± 0.20	(1)
091029	0.50 ± 1.92	0.54 ± 0.45	(3)
100621A	-2.50 ± 1.86	-0.37 ± 0.48	(2)
110213A	-0.34 ± 0.69	0.37 ± 0.17	(3)
111228A	2.83 ± 1.08	0.99 ± 0.24	(3)
130702A	0.59 ± 2.17	0.48 ± 0.38	(3)
140419A	-3.74 ± 1.23	-0.55 ± 0.30	(1)
180728A	0.68 ± 0.88	0.61 ± 0.19	(3)

TABLE 5.9: Results of the fit of the temporal behaviour of ν_c. The fitting function is $\log_{10}(\nu_c/\mathrm{keV}) = \mathrm{A} - \mathrm{s}\log_{10}(\mathrm{t/s})$. Errors are given at the 1 sigma level of confidence. The last column identifies three classes, considering the value of s within the errors: (1) if $s < 0$, (2) if $s = 0$, (3) if $s > 0$.

5.2.3 Temporal fit of X-ray and optical light curves

In order to check if the X-ray plateau has a corresponding plateau phase in the optical, we fit both X-ray and optical light curves of GRBs in *Sample* 1 and *Sample* 2 with an empirical broken power law, in the form:

$$F(t) = \frac{N}{(t/t_b)^a + (t/t_b)^b}.$$

This functional form is valid if the temporal decay before the break is shallower than the one after the break. This condition is always satisfied for all the X-ray and optical light curves, with the exception of the optical light curve of GRB 140419A. In this case we adopt the following functional form:

$$F(t) = N((t/t_b)^a + (t/t_b)^b).$$

In the case of optical light curves we rebin the data points as follows: if t_i and t_f are the initial and final times of the optical data, we rebin using a grid of 50 bins spaced logarthmically in the interval $[t_i - t_f]$. The fit is performed using the python function *curvefit*, which is based on least squares minimisation. If the fit does not converge, i.e. if one of the parameters of the model cannot be constrained, we fit with a single power law. The results are reported in Tab. 5.7 and 5.8 for X-ray and optical light curves, respectively. The best fit curves are reported as solid blue (X-ray) and orange (optical) lines in Fig. 5.8 and 5.16. In all the cases, the fit of X-ray light curves gives a reasonably good value of χ^2. Instead, for some optical light curves $\chi^2 \gg 1$, indicating the presence of more complex temporal structures that cannot be approximated by a simple broken power law. The cases showing the worst agreement are GRB 100621A (Greiner et al., 2013b), GRB 110213A (Cucchiara et al., 2011) and GRB 100814A (Nardini et al., 2014), which clearly exhibit the superposition of a bump over the power law decay. Such behaviour is expected, for instance, in the case of a structured jet viewed slightly off-axis. Indeed, as shown by Beniamini et al., 2020a, for particular combinations of structure profile and viewing angle, the X-ray light curve shows a plateau phase, while at optical wavelentghts a bump can appear in the light curve.
Looking at Tab. 5.8, 8 GRBs have an optical light curve compatible with a single power law with $a \in [-0.8, 0.8]$. Therefore, the light curves of these GRBs significantly show the presence of a plateau phase. All the other GRBs have an optical light curve compatible with a broken power law where the flatter segment has a shallow temporal slope in the interval

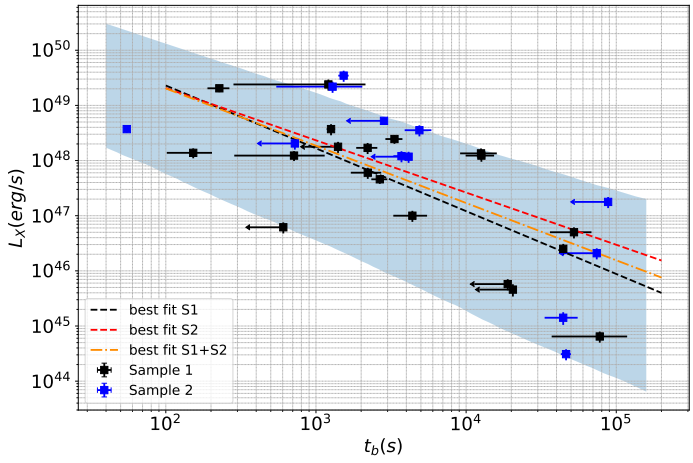

(a)

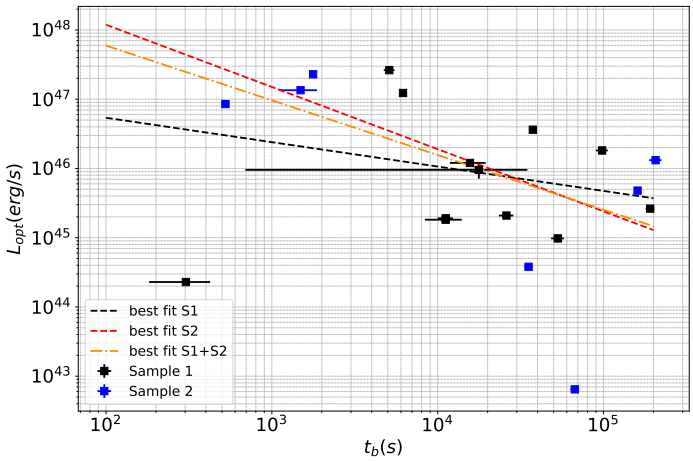

(b)

FIGURE 5.16: Panel (a): relation between the X-ray luminosity and duration of the plateau. We distinguish *Sample 1* and *Sample 2* with black and blue points, respectively. Arrows indicate upper limits. Time is reported in the rest frame of the source. The black (red) dashed line is the best fit line for the *Sample 1* (*Sample 2*), where the fitting function is $\log_{10}(L_X) = N + \lambda \log_{10}(t_b)$. The orange dot-dashed line is the corresponding best fit for the union of *Sample 1* and *Sample 2*. Panel (b) shows the analogous relation between optical luminosity and duration of the plateau.

	X-ray		Optical	
	λ	N	λ	N
Sample 1	-1.14 ± 0.03	0.08 ± 0.03	-0.35 ± 0.03	-0.97 ± 0.01
Sample 2	-0.95 ± 0.03	0.42 ± 0.03	-0.90 ± 0.01	-0.72 ± 0.01
Sample 1+Sample 2	-1.04 ± 0.02	0.23 ± 0.02	-0.79 ± 0.01	-0.81 ± 0.01

TABLE 5.10: Best fit values of the relation between the plateau luminosity and the plateau duration, in X-ray and optical. The values of λ and N are specified in the text.

$a \in [-0.8, 0.8]$. The only exceptions are GRB 091018 (with $a > 0.8$), GRB 081029 and GRB 150910A (with $a < -0.8$). Therefore 19/30 GRBs show a plateau both in X-ray and optical.
For all the GRBs that show a plateau in optical and/or in X-ray, we compute the X-ray/optical luminosity during the plateau as:

$$L_{X,opt} = \left\langle F_{X,\mathrm{opt}} \right\rangle \times 4\pi D_L(z)^2,$$

where $\left\langle F_{X,\mathrm{opt}} \right\rangle$ is the average flux in the specific band. The duration of the plateau is approximated with the break time. Such an approximation is valid in the limit in which the initial time of the plateau satisfies the condition $t_i \ll t_b$, which is usually the case.
The relation between X-ray plateau luminosity and duration is shown in Fig. 5.16a. The points, even if quite scattered, seem to follow the Dainotti relation (Dainotti et al., 2010), which is reported in the plot with a light blue band. The width of the band is computed taking into account the uncertainty on both the slope and normalisation of the Dainotti relation. We fitted the $L_X - t_b$ relation with the function:

$$\log_{10} \frac{L_x}{10^{47}\mathrm{ergs}^{-1}} = N + \lambda \log_{10} \frac{t_b}{10^4\,\mathrm{s}}. \tag{5.7}$$

We show in Fig. 5.16b the analogous relation between plateau luminosity and duration in the optical. Also in this case we fit the same power law relation of eq. 5.7. The best fit parameters of the $L_X - t_p$ and $L_{\mathrm{opt}} - t_p$ relations are reported in Tab. 5.10. The value of the slope of the $L_X - t_b$ relation found by Dainotti et al., 2013 is $\lambda = -1.32 \pm 0.28$, steeper but still compatible with our values. For the $L_{\mathrm{opt}} - t_b$ relation, instead, Dainotti et al., 2020 report $\lambda = -1.12 \pm 0.26$, significantly steeper than our values. We note however that in Dainotti et al., 2020 L_X is defined slightly different as the

luminosity at the end of the plateau.
In addition to the $L_X - t_p$ relation, previous works have shown that the properties of the X-ray plateau could correlate with the prompt emission energetics of the burst (Margutti et al., 2013; Dainotti et al., 2017; Tang et al., 2019). The investigation of these relations could give further details about the origin of plateau. Indeed, as pointed out by Beniamini et al., 2020d, in the case of a plateau as a result of a structured jet, the X-ray plateau luminosity should correlate with the plateau duration as $L_p \propto E_{iso} t_p^{-1}$, where E_{iso} is isotropic equivalent energy. Such a relation, instead, does not necessarily hold for the energy injection scenario, where the plateau energy is tightly connected to the additional energy transferred to the external shock, but not to the energy released during the prompt phase. Therefore we tested for the GRBs analysed here if there are significant correlations between the isotropic energy E_{iso} and the plateau luminosity, both in the optical and X-rays. The correlation between plateau luminosity in X-rays and E_{iso} has a Pearson coefficient $C_P = 0.58$ (p-value$= 7 \times 10^{-4}$), while the correlation between plateau luminosity in optical and E_{iso} has a Pearson coefficient $C_P = 0.45$ (p-value$= 0.06$). These results show that the $L_X - E_{iso}$ relation is more strongly correlated with respect to the $L_{opt} - E_{iso}$ one. These two relations are shown in panel (a) and (b) of Fig. 5.17.

We also tested the correlation between L_X/E_{iso} and $t_{b,X}$, as well as L_{opt}/E_{iso} and $t_{b,opt}$. The $L_X - t_{b,X}$ relation has a Pearson correlation coefficient $C_P = -0.71$ (p-value$= 6.6 \times 10^{-6}$), while the $L_X/E_{iso} - t_{b,X}$ relation has $C_P = -0.64$ (p-value$= 9.5 \times 10^{-5}$). In the optical, instead, the $L_{opt} - t_{b,opt}$ relation has a Pearson correlation coefficient $C_P = -0.25$ (p-value$= 0.32$), while the $L_X/E_{iso} - t_{b,X}$ relation has $C_P = -0.41$ (p-value$= 0.08$). Also in this case, the $L_X/E_{iso} - t_{b,X}$ relation results much more correlated than the $L_{opt}/E_{iso} - t_{b,opt}$ one, as evident from panels (c) and (d) of Fig. 5.17. Finally, for the sub-sample of GRBs with a plateau in both optical and X-ray bands, we show in Fig. 5.18 the relation between the duration of the plateau in optical and X-rays. There is a clear indication that optical plateaus tend to be longer than X-ray plateaus, which is in line with our findings on ν_{opt} being smaller than ν_c is most of the cases. Among all the the analysed GRBs with both an X-ray and optical plateau, only a few have $t_{b,X} \simeq t_{b,opt}$, implying that the majority shows a chromatic plateau. There are two particular cases, GRBs 110715A and 080413B, which are in the bottom right corner of the plot, indicating an optical break of the plateau at much later times with respect to the X-ray break. Such a behaviour seems to significantly deviate from the average trend, but looking at Figs. 5.15a and 5.10a it is possible that a simple broken power law does not describe

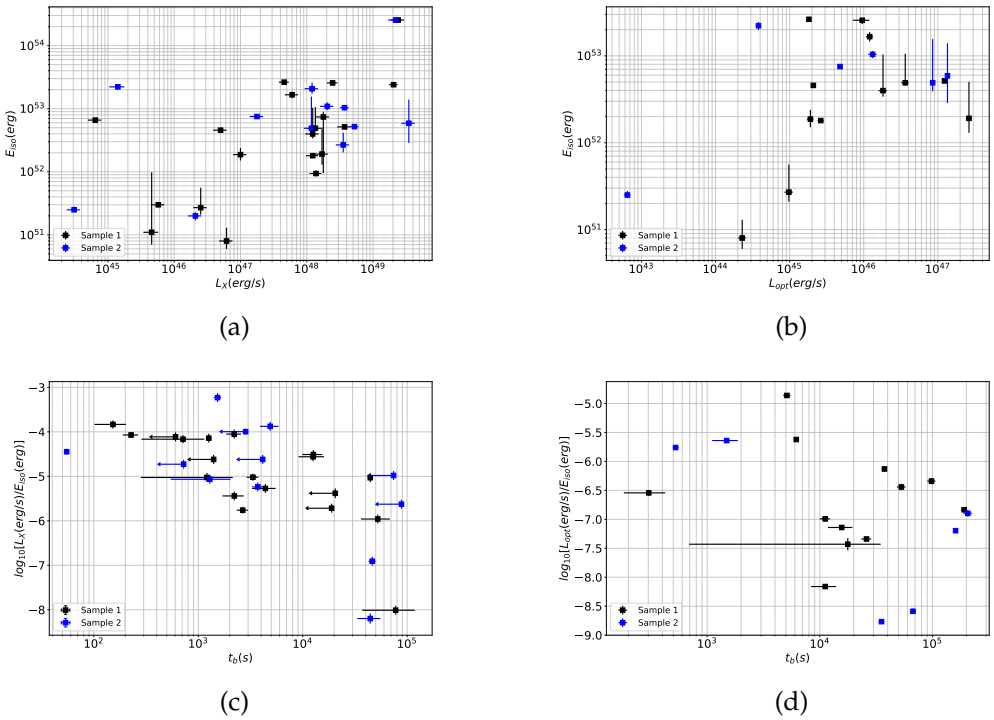

FIGURE 5.17: In panel (a) (panel (b)) we show the correlation between the X-ray (optical) plateau luminosity and the isotropic energy E_{iso}. In panel (c) (panel (d)) we show the relation between luminosity and duration of the X-ray (optical) plateau, where the luminosity is corrected by the isotropic energy.

sufficiently well the temporal structure of the optical light curve, therefore giving a possibly biased estimation of the optical break. Apart these two exceptions, $t_{b,X}$ and $t_{b,opt}$ show a correlation. Excluding GRBs 110715A and 080413B, we derive a Pearson correlation coefficient $C_P = 0.78$ and a 2-tailed p-value of 3.4×10^{-4}.

5.2.4 Discussion

The results of our analysis show that in 19 out of 30 GRBs the plateau has an optical-to-X-ray spectrum fully consistent with synchrotron emission from a single population of shock-accelerated electrons (*Sample 1*). The comparison of the temporal properties of the X-ray and optical plateaus further confirms this interpretation. Indeed, the fact that the optical flux densities lie within the allowed range of values extrapolated from X-ray fluxes assuming a single synchrotron spectrum, allows us to infer $\nu_{\rm opt} < \nu_c < \nu_X$.

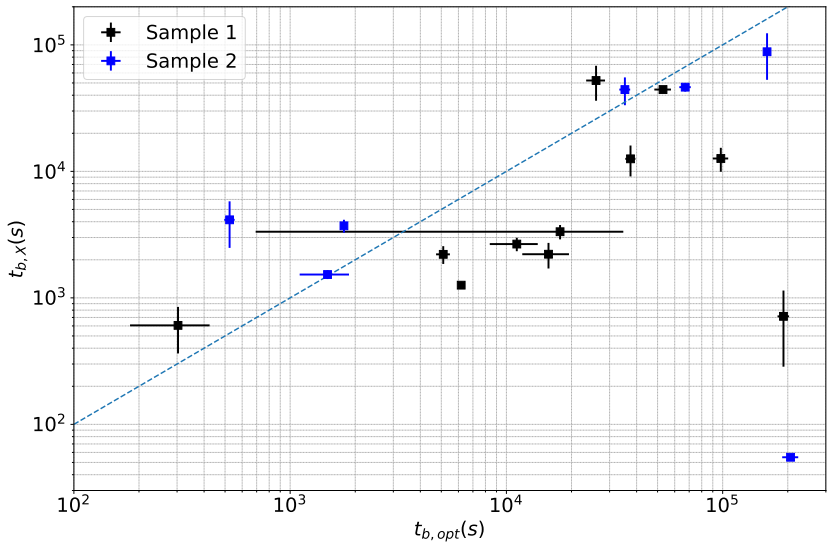

FIGURE 5.18: Relation between the duration of the X-ray and optical plateau. We distinguish *Sample 1* and *Sample 2* with black and blue points, respectively. Time is reported in the rest frame of the source. The blue dashed line is corresponds to $t_{b,\mathrm{opt}} = t_{b,X}$.

This condition implies a slower evolution of the optical plateau than the X-ray one, in agreement with our findings that $t_{b,o} > t_{b,X}$ in most of the GRBs belonging to *Sample 1* (see fig. 5.18). In order to test whether the transition of ν_c across the optical band is simultaneous to a steepening of the optical light curve, we estimate the time t^* for which $\nu_c(t^*) = \nu_{\mathrm{opt}}$ and we compare it with $t_{b,opt}$, reported in Tab. 5.8. The value and the uncertainty of t^* is estimated inverting the relation 5.5, namely:

$$t^* = \left(\frac{10^N}{\nu_{\mathrm{opt}}/\mathrm{keV}}\right)^{1/s} \mathrm{sec.}$$

In Tab. 5.11 we compare t^* and $t_{b,opt}$ of all the GRBs of *Sample 1* which have $s > 0$. The only case where t^* and $t_{b,opt}$ are not compatible is GRB 090618. In all other cases, we have three possibilities: 1) we have an estimate of both t^* and $t_{b,opt}$ and they are compatible, 2) only a lower limit on t^* is available, but still compatible with $t_{b,opt}$, 3) no break in the optical is observed, possibly indicating that the break may occur later than the available data. While cases 2) and 3) are inconclusive, only for the first case (GRBs 061121, 080413B and 111228A) we can conclude that

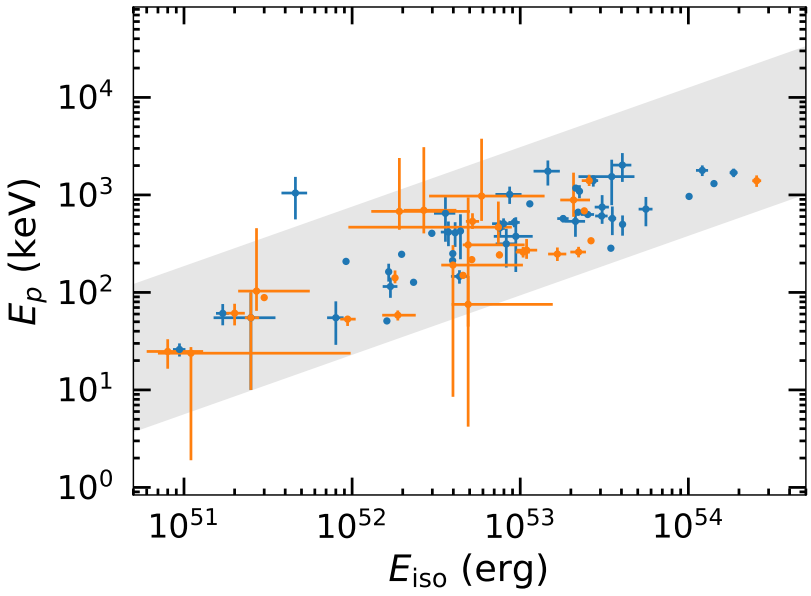

FIGURE 5.19: Location in the $E_p - E_{\rm iso}$ plane of the GRB sample selected in our work (orange points, see Tab. 5.5). The blue points are taken from Nava et al., 2012 and the gray region is the corresponding 3σ band.

$t^* \simeq t_{b,opt}$, indicating that the optical temporal break is in agreement with the transition of the cooling frequency across the optical band.

If the condition $\nu_{\rm opt} < \nu_c < \nu_X$ is satisfied, no spectral evolution is expected in the X-rays. We tested the presence of spectral evolution fitting the X-ray photon index temporal trend with a constant. In Tab. 5.7 we report the average photon index (the average is taken over the whole available data) and the p-value of the fit. Among 19 cases, 6 GRBs have a p-value < 0.05 showing significant deviation from a constant trend. For three of them (GRBs 060729, 061121 and 090618) the deviation is given by the hardening of the X-ray spectrum at late times. For GRBs 100621A, 110213A and 140419A there is evidence of spectral softening. For all these six cases, except for GRB 140419A, Tab. 5.9 shows that the derived ν_c decreases in time. In this scenario, a softening of the X-ray spectrum is expected as $F_\nu \propto \nu^{-(p-1)/2}$ for $\nu < \nu_c$ and $F_\nu \propto \nu^{-p/2}$ for $\nu > \nu_c$. Since the synchrotron spectral shape has smooth transitions between a power law segment and the other, a temporal decrease of ν_c would produce a gradual spectral softening. On the contrary, a decreasing trend of ν_c is not in agreement with

name	$\log_{10}(t^*)$	$\log_{10}(t_{b,opt})$
050416A	>3.64	$2.70^{+0.15}_{-0.22}$
051109A	$6.77^{+6.16}_{-2.92}$	-
060729	>3.65	$4.20^{+0.16}_{-0.26}$
061121	$6.27^{+2.69}_{-1.75}$	$4.61^{+0.29}_{-1.41}$
080413B	$4.98^{+2.04}_{-1.38}$	$5.60^{+0.03}_{-0.03}$
080605	$5.41^{+3.75}_{-1.95}$	-
090618	$5.26^{+0.74}_{-0.64}$	$4.23^{+0.18}_{-0.32}$
091029	>1.29	$4.77^{+0.09}_{-0.12}$
110213A	>3.09	$4.18^{+0.01}_{-0.01}$
111228A	$5.58^{+3.23}_{-1.97}$	$4.28^{+0.04}_{-0.05}$
130702A	>1.30	-
180728A	$5.54^{+4.60}_{-2.42}$	-

TABLE 5.11: Comparison between t^* and $t_{b,opt}$. $t*$ is the time at which ν_c crosses the optical band.

the evidence of spectral hardening. In this regard, we point out that in the derivation of the temporal evolution of ν_c we assumed that the spectral slopes above and below ν_c are constant in time. If there is an additional process which induces an intrinsic variation of the spectral slope, the estimation of the temporal trend of ν_c can be biased. Hence, we conclude that the results shown for the evolution of the cooling frequency are fully reliable for the GRBs that do not show significant spectral evolution in the X-rays. Among the 12 cases of *Sample 2*, seven of them have a p-value < 0.05 (GRBs 050730, 080310, 100814A, 110715A, 120404A, 140419A and 150910A), but none of them shows a clear trend which points towards a softening or a hardening of the X-ray spectrum.

The consistency of the optical and X-ray data with a single spectrum can be interpreted as an indication that both X-ray and optical photons originate from the same emission region. Moreover, the process responsible for the X-ray plateau should also explain the observed evolution of the cooling frequency. In the standard scenario of a forward shock decelerating through the circumburst medium, the predicted temporal evolution of the characteristic synchrotron frequencies is (Granot and Sari, 2002):

$$\nu_c \propto \epsilon_B^{-3/2} n_0^{-1} E_{52}^{-1/2} t_{\rm days}^{-1/2} \tag{5.8}$$

for an ISM with uniform particle density n_0, and

$$\nu_c \propto \epsilon_B^{-3/2} E_{52}^{1/2} t_{\rm days}^{1/2} \tag{5.9}$$

for a medium with a wind-like density profile. With E_{52} we indicate the isotropic energy in units of 10^{52} erg. The flux density, instead, is expected to decline like $F_\nu \propto t^{-a}$ and the predicted values are, in slow cooling regime (e.g., see Zhang et al. 2006b):

$$a = \frac{3}{4}(p-1) \text{ for } \nu < \nu_c,\ a = \frac{3p-2}{4} \text{ for } \nu > \nu_c$$

for the ISM scenario and

$$a = \frac{3p-1}{4} \text{ for } \nu < \nu_c,\ a = \frac{3p-2}{4} \text{ for } \nu > \nu_c$$

for the wind scenario. Since the values of p are likely above 2, the standard picture predicts afterglow light curves not flatter than $t^{-3/4}$. Therefore, even if the observed temporal evolution of ν_c can be compatible with the temporal behavior specified in eq. 5.8 and 5.9, the observed temporal slope of the X-ray and optical plateaus are incompatible with the standard FS scenario.
Modifications to the standard picture have been proposed in the literature (Misra et al., 2021), which invoke the possible temporal evolution of the shock microphysical parameters, such as ϵ_B. In the specific case, assuming a temporal evolution in the form $\epsilon_B \propto t^\mu$ and a circum-burst medium with a density profile $\rho \propto r^{-k}$, the cooling frequency evolves as $\nu_c \propto t^{-s}$, with:

$$s = \frac{4 + 12\mu - 3k(1+\mu)}{2(4-k)}.$$

Moreover, considering the ordering $\nu_{\rm opt} < \nu_c < \nu_X$, the optical and X-ray flux densities are expected to evolve like $F_{\rm opt} \propto t^{a_o}$ and $F_X \propto t^{a_X}$, with

$$a_o = \frac{1}{2}\left(\mu + \frac{k}{k-4}\right) + \frac{p-1}{2}\left(\frac{4 + 12\mu - 3k(1+\mu)}{2(k-4)}\right)$$

and

$$a_X = \frac{1}{2}\left(\mu + \frac{k}{k-4}\right) + \frac{p}{2}\left(\frac{4 + 12\mu - 3k(1+\mu)}{2(k-4)}\right).$$

In order to check the validity of this scenario, we compare, simultaneously,

the expected values of a_o, a_X and s with the observed ones. In particular, we search for a combination of μ and k such that the following relations are simultaneously satisfied:

$$a_{o,th} \in [a_{o,obs} - \Delta a_o, a_{o,obs} + \Delta a_o],$$

$$a_{X,th} \in [a_{X,obs} - \Delta a_X, a_{X,obs} + \Delta a_X],$$

$$s_{th} \in [s_{obs} - \Delta s, s_{obs} + \Delta s],$$

where we indicate with X_{th}, X_{obs} and ΔX the expected value, the observed value and the error of the quantity X, respectively. The intersection of these three conditions defines a region in the $k - \mu$ plane, which is in agreement with observations. We verified for all the GRBs of *Sample 1* that a combination of k and μ that satisfies the above conditions does not exist.
Another solution invokes the presence of additional energy injected into the forward shock at late times. A single emitting region is compatible with the energy injection scenario, where additional energy is transferred to the external shock due to the late-time activity of the central engine. In this scenario, the dynamical evolution of the blast wave is determined by the rate of energy injection and the efficiency of conversion from injected energy to jet kinetic energy. Hence, the deceleration in the ISM is less severe and the flux drop is shallower. The injection of energy modifies the dynamical evolution of the external shock but it does not have influence on the dominating radiative mechanisms responsible for the dissipation of the particles' energy. Therefore, the spectral energy distribution should be the same of that in the standard scenario of particles dissipating through synchrotron radiation. We notice that, if the energy injection has impact only on the blast wave dynamics, the plateau should be achromatic (e.g. Fan and Piran 2006). This would imply that the temporal break corresponding to the transition from plateau to post-plateau phase should be the same in optical and X-rays. Though, as pointed out before, this is not the case if a spectral break is between the two bands.
Adopting the standard prescription of a injected luminosity in the form:

$$L_{inj} \propto t^{-q},$$

the temporal slope of the afterglow light curve at any frequency ν_{obs} can be predicted depending on the position of ν_{obs} relative to the synchrotron characteristic frequencies (ν_m and ν_c). Moreover the temporal behavior of

these last are modified consequently and read:

$$\nu_m \propto t^{-(2+q)/2},\ \nu_c \propto t^{(q-2)/2} \tag{5.10}$$

for the ISM scenario (jet propagating into a ISM with constant density), and

$$\nu_m \propto t^{-(2+q)/2},\ \nu_c \propto t^{(2-q)/2} \tag{5.11}$$

for the wind scenario (jet propagating into a medium with density $n \propto r^{-2}$). Therefore, if $q < 2$ ($q > 2$) the energy injection model predicts a decreasing cooling frequency in the ISM scenario (wind scenario).
One of the possible sources of energy responsible for the jet refreshing is the long-lived highly magnetized neutron star (magnetar) left after the production of the GRB (Dai and Lu, 1998a; Zhang and Mészáros, 2001a; Dall'Osso et al., 2011). The magnetar looses rotational energy through spin down radiation and the associated released luminosity in the standard scenario of a rotating magnetic dipole depends on the rotational frequency as $L_{sd} \propto \Omega^4$. The temporal evolution of the spin down luminosity is:

$$L_{\rm sd}(t) = \frac{L_0}{\left[1 + \frac{t}{\tau}\right]^2}.$$

This relation can be further extended including deviations from the standard picture of simple dipole radiation. This modification leads to a spin down luminosity in the form $L_{sd} \propto \Omega^{4-2\alpha}$, where α is related to the braking index n as $n = 3 - 2\alpha$ and $0 < \alpha < 1$. The corresponding temporal behavior of the spin down luminosity is:

$$L_{\rm sd}(t) = \frac{L_0}{\left[1 + (1-\alpha)\frac{t}{\tau}\right]^{\frac{2-\alpha}{1-\alpha}}}$$

For $t \gg \tau$, the spin down luminosity evolves as $L_{sd} \propto t^{-q}$, with

$$q = \frac{2-\alpha}{1-\alpha} \geqslant 2 \tag{5.12}$$

and the forward shock afterglow emission dominates. Indeed, following Dall'Osso et al., 2011, the luminosity evolution in the relativistic external shock can be obtained from the balance between radiative losses and energy injection from the spinning down magnetar. Fitting this model on the observed X-rays light curves provides a very good description of the

plateau and post-plateau phases, with reasonable values of the magnetic field strength and spin period (e.g., Dall'Osso et al. 2011; Bernardini et al. 2012; Stratta et al. 2018). In this scenario, the post-plateau afterglow spectral properties follow the standard forward shock prescriptions, in good agreement with the majority of the GRBs in *Sample 1*. Since the majority of the GRBs in *Sample 1* (16/19) show a preference for ν_c decreasing in time after the plateau phase, even in the magnetar scenario we can apply eqs. 5.8 and 5.9 and find agreement with a forward shock propagating in an ISM medium. For the remaining three GRBs, ν_c increases with time, with a slope compatible with $t^{0.5}$, indicating a preference for wind-like density profile.
If the X-ray plateau is a direct consequence of additional energy injected in the forward shock, this would also impact the ratio between the jet kinetic energy E_{kin} (inferred by afterglow light curve) and prompt isotropic energy E_{iso}. The ratio $\epsilon_{pr} = E_{iso}/E_{kin}$ represents the prompt emission efficiency and, if the injection of energy in the forward shock tends to increase E_{kin}, then the inferred ϵ_{pr} should be lower with respect to average cases where no energy injection operates. In order to verify this point we follow the method adopted by D'Avanzo et al., 2012, which use the X-ray luminosity at 24 hr after the burst ($L_{X,24\,hr}$) as direct proxy of E_{kin}. In Fig. 5.20 we show the relation between $L_{X,24\,hr}$ and E_{iso}, comparing our GRB sample with the average relation reported in Fig. 2 by D'Avanzo et al., 2012, where the authors consider a complete sample of GRBs detected by Swift with no specific selection about the presence of an X-ray plateau. Our plot shows that our sample of GRBs is characterised by a ratio $L_{X,24\,hr}/E_{iso}$ larger than the average, which could be an indication of a larger ratio E_{kin}/E_{iso}. Notice that the last implication is based on the adoption of a specific afterglow model for converting $L_{X,24\,hr}$ in E_{kin}. The conversion factor depends on all the microphysical parameters, therefore the conclusion that the ratio E_{kin}/E_{iso} is larger for our sample holds in the assumption that all GRBs (with and without plateau) share similar microphysical parameters.
Alternatively to the energy injection scenario, the emission from the forward shock can still produce a plateau phase if the blast wave is stratified in velocity (Rees and Mészáros, 1998). In the specific, if the faster component of the ejecta is launched later, it catches the slower one, resulting in a refreshed shock wave. If the stratification is given by a smooth distribution in Lorentz factor, the effect is a flattening of the light curve, while in the limit of two distinct shells launched at different speeds the light curve could show a re-brightening, followed again by standard forward shock decay. Though, notice that also in this scenario the broad band emission should be compatible with a single synchrotron component.

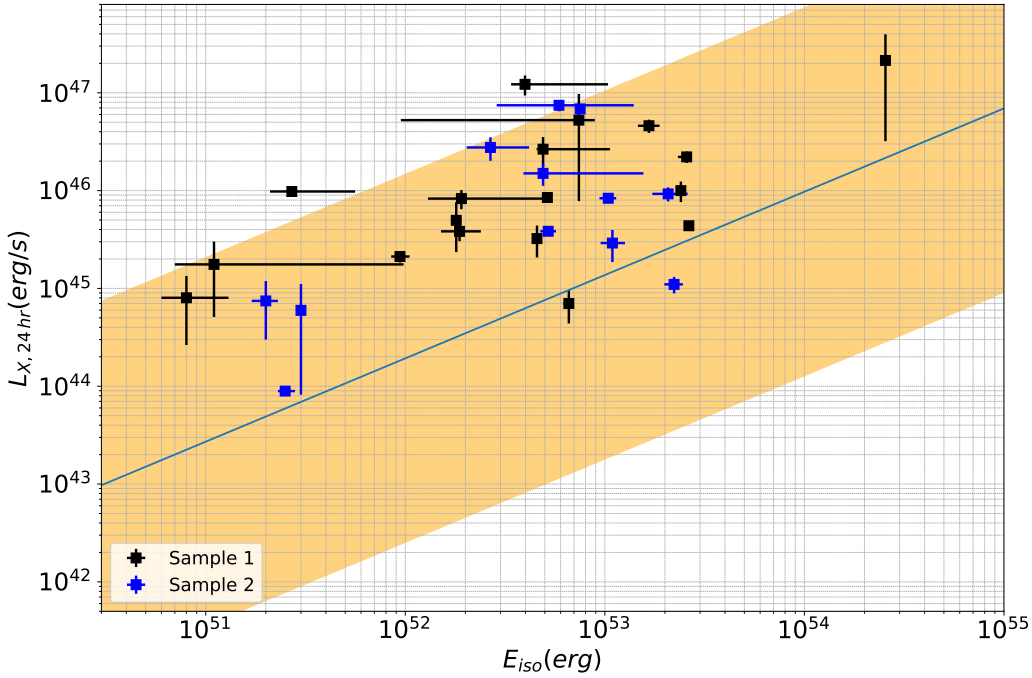

FIGURE 5.20: Comparison between the isotropic equivalent energy E_{iso} and the X-ray luminosity at 24 hr after the trigger. The blue solid line and the yellow band are the best fit and 3σ dispersion, respectively, of the same relation reported by D'Avanzo et al., 2012 for a complete sample of GRBs observed by Swift.

All the scenarios described so far assume that the afterglow emission is dominated by the forward shock emission. Alternatively, provided that the forward shock radiative efficiency is sufficiently low, also the reverse shock emission can dominate as well . Uhm and Beloborodov, 2007 demonstrate that the reverse shock emission from a stratified blast wave can easily produce a flat segment in the X-ray light curve, without assuming any injection of energy in the forward shock (see also Genet et al. 2007). Moreover the reverse shock emission is sensible to the change of density of the external medium, which corresponds to a re-brightening of the optical light curve, as observed for several GRBs, both in *sample 1* (GRBs 100621A, 110213A) and in *sample 2* (GRB 100814A).

Another interesting scenario considers the possibility that the plateau phase occurs in the coasting phase of the jet propagation, namely before the blast wave deceleration (Granot et al., 2006; Shen and Matzner, 2012). Following this idea, Dereli-Bégué et al., 2022 claim that the plateau can be

still explained in the classical fireball model, provided that the jet is propagating in a wind environment and with a rather low value of bulk Lorentz factor ($\sim$ few tens). This last condition ensures to have a long enough coasting phase and a corresponding light curve whose temporal slope is close to the ones observed during the plateau. Though, in order to have the jet dissipation above the photospheric radius, such low values of Lorentz factor require a not too large isotropic luminosity and a minimum variability time scale of $\sim$ few seconds. Moreover, the transparency requirement is satisfied if rather high values of ϵ_B (> 0.1) are assumed. Therefore, also this scenario requires further investigation.

The HLE from a structured jet, as well, provides a viable explanation for the presence of a plateau phase in the X-ray light curves of GRBs. In the approach of Oganesyan et al., 2020b, the photons emitted during the prompt emission at large angles with respect to the jet core arrive to the observer at late times and less Doppler boosted. According to this model, if the energy spectrum in the shock comoving frame is the same along the jet ring, then also the observed spectrum at each time should reflect the same spectral shape of the prompt emission. Though, since the Doppler boosting decreases at higher latitudes, the observed spectral peak should decrease with time as well. Therefore, also in the HLE scenario, we expect an optical and X-ray emission compatible with a single synchrotron component, whose characteristic frequencies (ν_m and ν_c) decrease in time due to the Doppler effect. The specific rate of temporal decrease of the characteristic frequencies depends on the jet structure. We note here that HLE would be dominant over the afterglow from forward shock emission throughout the light curve, still being compatible with a single synchrotron component.

Another approach based on the HLE from a structured jet is the one adopted by Beniamini et al., 2020c; Beniamini et al., 2020a, where the photons responsible for the plateau emission are produced in the deceleration phase of the forward shock. In particular, in Beniamini et al., 2022, the authors show also the predictions of the temporal evolution of the cooling frequency. As shown in Fig. 1 and in Tab. 1 of Beniamini et al., 2022, the model predicts

$$-1 < s = -\frac{3k-4}{2} < 2, \text{ for } 0 < k < 2,$$

for the pre-deceleration and the angular structure dominated phase, while

$$-1/2 < s = -\frac{3k-4}{8-2k} < 1/2, \text{ for } 0 < k < 2,$$

for the post deceleration phase. As before, $\rho \propto r^{-k}$. These ranges of s are fully consistent with the ones reported in Tab. 5.9. In this class of models, the plateau appears when the jet is observed slightly off-axis, namely at $\theta_{obs} \gtrsim \theta_j$, where θ_j is the opening angle of the jet core. In Fig. 5.19 the plateau sample shows no significant deviation from the average $E_{iso} - E_p$ correlation, which is largely consistent with the condition $\theta_{obs} \sim \theta_j$.

Among the GRBs in *Sample 1*, the case of GRB 100621A shows several peculiarities (Greiner et al., 2013b). The optical light curve clearly shows a bump around $5 \times 10^3 - 2 \times 10^4$ s, while the X-ray light curve is well fitted by a broken power law. Moreover, the X-ray spectrum shows an evident softening at late times. Such a softening imposes the introduction of an additional spectral break between optical and X-rays, in order to explain the broad band emission with a single synchrotron component. If this spectral break is identified with ν_m, the observations would imply a ν_m which increases with time. This increase is hardly explained in the framework of standard forward shock theory, even including an energy injection term (see eqs. 5.10 and 5.11). Hence, even if GRB 100621A satisfies the conditions to be in *Sample 1*, the shape of the optical light curve and the X-ray spectral softening are hardly explained in the context of standard synchrotron emission from a single emission zone.

For the GRBs belonging to *Sample 2*, optical and X-ray data are incompatible with a single synchrotron spectrum in at least one temporal bin. In at least two events (GRB 100814A and GRB 150910A), the optical light curve has a shape which differs substantially from the X-ray one. In a few cases, though, the two light curves behave in a similar way, yet the optical emission appears to be a factor of a few above the maximum extrapolated from the X-ray flux (e.g., GRB 060614, GRB 081007 and GRB 100418A). When the optical light curve shows substantial differences with the X-ray one, a single synchrotron-emitting region cannot explain the observed broad-band spectrum. One viable explanation is that the HLE associated to the prompt phase and external shock emission from a structured jet can simultaneously contribute to the broad-band spectrum. The HLE can dominate in the X-rays, while the optical would be dominated by external shock. If this last option is valid, this means that the two components cannot have the same spectral energy distribution, otherwise one of them would dominate in both the bands, which is not the case. Moreover, if the component that dominates in the optical is characterised by a non-thermal spectrum, we should expect an optical spectral index softer than the X-ray one. Indeed, in order to have an excess flux in optical, the spectral component dominating in optical should have a steeper spectral slope. If in optical $F_\nu \sim \nu^{-\beta_{\rm opt}}$

and in X-rays $F_\nu \sim \nu^{-\beta_X}$, this would translate in $\beta_{\rm opt} > \beta_X$. Though, comparing the optical spectral slopes with the X-ray spectral index for *Sample 2*, we verified that they have compatible values. A possible solution would be that the optical flux is dominated by a component with a non-thermal spectrum and a cut-off at energies $\nu_{\rm opt} < \nu_{\rm cut-off} < \nu_X$, or, alternatively, by a thermal component with a characteristic temperature $kT \sim h\nu_{\rm opt}$.
The analysis described in this section is reported in Ronchini et al., 2022b.

5.3 Conclusions

The origin of the plateau phase in the X-ray light curve of GRBs is still matter of debate. In this chapter we first defined a complete sample of GRBs with X-ray plateau, presenting the statistical properties and correlations between the observables. Secondly, starting from the same sample we restricted our analysis to those cases where also optical data are available simultaneously to the X-ray plateau. We performed a time-resolved spectral analysis in the X-rays and we compared X-ray and optical data to verify if they are compatible with a single synchrotron spectrum. While the majority of the cases show compatibility with a single component synchrotron origin of the multi-band emission, we collect evidence that some GRBs ($\sim 1/3$ of the entire sample) are incompatible with the standard forward shock emission from a single dissipation zone.
For the sample of GRBs compatible with a single zone emission, we derive the temporal evolution of the cooling frequency and we compare it with the predictions from several models. We show that the majority of the GRBs shows a cooling frequency which decreases in time. For the GRBs which show a plateau both in X-ray and in optical (19 over 30), this leads to a duration of the optical plateau larger than the X-ray one. Moreover, we verify that the transition of the cooling frequency across the optical band is compatible with a simultaneous steepening of the optical light curve. We find that both an energy injection model and the scenario of HLE from a structured jet predict a temporal decay slope in optical/X-ray and trend of the cooling frequency compatible with the observations. This is due to the fact that both scenarios assume classic synchrotron emission. However, while in energy injection this would come from the afterglow (external shock), the HLE emission model would imply that everything comes from the prompt emission region, while the external shock would always remain subdominant. A model in which the plateau is produced by the external shock viewed off-axis, like the one proposed by Beniamini et al., 2022, would be

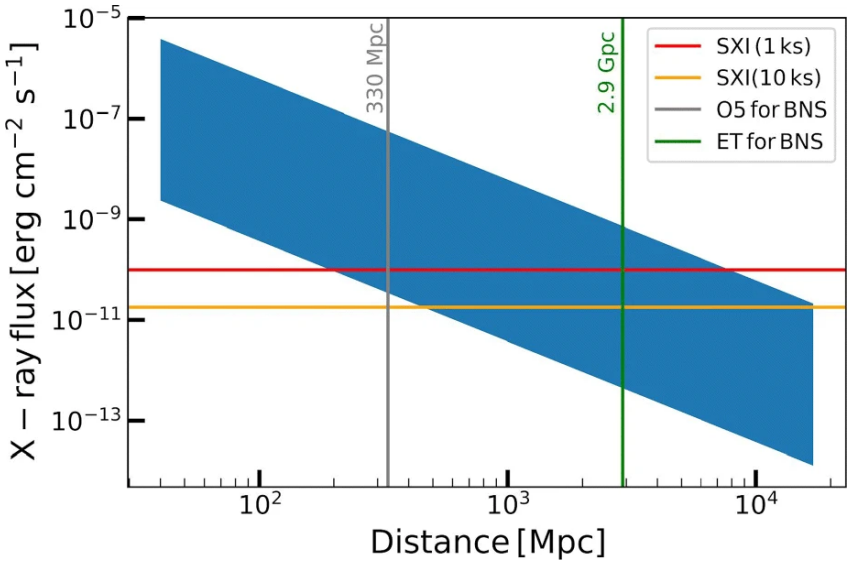

FIGURE 5.21: Range of X-ray flux expected during the plateau phase of short GRBs. THESEUS-SXI flux limits are shown for two exposure times, 1 ks and 10 ks. The LVK O5 and ET ranges for BNS detection are show as well. Image adapted from Ciolfi et al., 2021.

degenerate with energy injection in the framework of our study.
Concerning the second sample of GRBs not compatible with a single synchrotron spectrum, the optical emission lies above the extrapolation inferred from the X-ray analysis. Neither the energy injection model nor the HLE model alone can account for this behaviour, while an interplay of both process can be a plausible solution.

5.3.1 Further studies of the GRB plateau: perspectives for future instruments in the multi-messenger context

In this chapter we explored and investigated the properties of the X-ray plateau in GRBs, through a statistical analysis of its occurrence and a detailed comparison of optical/X-ray light curves and spectral evolution. This is of crucial importance when we need to perform reliable predictions about the detectability of the X-ray afterglow with future instruments. The impact of our work can be summarised as follows:

- The results of the first part of this chapter help us to enrich our knowledge of the average occurrence and properties of the plateau phase. Knowing the typical duration, luminosity and morphology of the

X-ray light curve is important to validate empirical models for the prediction of future detections of GRBs in the high-energy domain. Moreover, such validation can be even more reliable if internal correlations between the prompt emission and the plateau properties are taken into account.

- From the second part of this chapter we concluded that for a considerable fraction of the analysed cases, the optical and X-ray data are not compatible with a single synchrotron emission component. We find that typically the optical flux is above the range expected from X-rays. This has a fundamental consequence for the detectability with future instruments. Indeed, since the models currently adopted for the production of synthetic afterglow light curves usually adopt synchrotron emission (sometimes with the inclusion of SSC), the resulting predicted optical flux could be under-estimated. This requires the development of a model which correctly takes into account the observed optical excess during the X-ray plateau. Additionally, a more refined estimation of the optical afterglow brightness and duration would allow us to infer the probability of obtaining a precise measurement of the GRB redshift.

The X-ray plateau has also interesting applications in the multi-messenger context, which are the following:

1. If the remnant of a BNS mergers is a long lasting highly magnetised NS, there could be a post-merger emission of continuous GWs due to the deformation of the NS induced by the re-arrangement of the internal magnetic field (Dall'Osso et al., 2015). This process tends to change the spin axis of the NS until the quadrupolar moment is maximised. Provided that the spin-down process does not dominate the loss of angular momentum, the emission of GWs can be efficient. The authors estimate that with 3G GW detectors, such as the Einstein Telescope, such kind of emission could be potentially detectable up to $\sim$ 300 Mpc. Since such a process can produce simultaneously a spin-down emission and a GW emission, the detection of GWs in correspondence of an X-ray plateau of a short GRB would represent a strong indication of the magnetar origin of this last.

2. In the interpretation of the X-ray plateau as signature of a magnetar wind, the emission could be potentially quasi-isotropic. Therefore it could represent a potential EM counterpart associated to BNS

mergers, even if the relativistic jet is highly off-axis. Notice that the same would not be true if the plateau is related to the jet structure. Indeed, in this last case the off-axis emission would be much fainter than the on-axis one. Nevertheless, as showed by Ascenzi et al., 2020c, future instruments such as THESEUS will be potentially able to detect the structured jet emission up to very large viewing angles (e.g., $\theta_{max} \sim 30^\circ - 40^\circ$ for a GRB at z=0.5, though this strongly depends on the assumptions about the structure, as well as radiation efficiency and opacity at large inclination angles). The results of our investigation on the X-ray plateau have been exploited to perform a detailed assessment of the future potentialities of THESEUS regarding the detection of EM transients associated to CBMs. In particular our statistical study of the plateau properties have been used to predict the detectability of the plateau phase with THESEUS-SXI, as a function of the source distance. The result is shown in Fig. 5.21, where the expected flux during the plateau is derived considering the average plateau luminosity of all the short GRBs with known redshift. For comparison also the LVK O5 and ET ranges for BNS detections are shown. Assuming an exposure of 1 ks, THESEUS would detect about 90% (30%) of all X-ray plateaus up to 330 Mpc (2.9 Gpc), which is the typical 2G (ET) GW detection range for a randomly oriented BNS merger. These results, together with all the other multi-messenger aspects of the THESEUS scientific return, are reported in (Ciolfi et al., 2021).

3. The plateau phase is expected to be associated with high energy neutrinos emission, which can be detected by IceCube in spatial and temporal coincidence with GRBs. In this regard, the sample defined in this chapter has been exploited to perform a single source and a stacked search on 10 years of IceCube data, adopting a weighting factor which is physically motivated by observational constraints. The expected neutrino flux scales with the isotropic fluence of the source, therefore, if we limit our study to the afterglow phase of GRBs, X-ray plateaus, along with X-ray flares, are the most promising candidates, thanks to a flux which is kept almost constant up to $10^4 - 10^5$ s. In general, if the plateau is associated to the emission from the external shock, the expected neutrino flux is not large, since it scales with the inverse of the size of the emission region. On the other hand, if the origin of plateau is conneted to an internal dissipation and the bulk motion is not highly relativistic, the efficiency of neutrino production

is enhanced (e.g., Kimura 2022). Despite our study does not confirm any neutrino-GRB coincidence, it allows us to infer important constraints on the emission site properties, such as the baryon loading, the Lorentz factor or the magnetic field strength. This work has been published in Lucarelli et al., 2022.

Chapter 6

Joint detection of GWs and high-energy signals from BNS mergers

The detection of short GRBs associated with GW signals from BNS mergers is currently limited by the sensitivity of the LIGO, Virgo and KAGRA detectors, and by the small probability to detect systems with the beamed GRB emission pointing to Earth. To increase the efficiency of the GRB/GW search, the LVK collaboration performs a triggered search for GWs in the time window and position of observed GRBs. Section 6.1 describes this analysis, my contribution to this search within the LVK collaboration and the results obtained analysing the data taken during the first, second and third runs of observations of LIGO and Virgo. The results of this work have been published in Abbott et al., 2022a.
The combined observation of GW170817/GRB170817A represents the only case of joint detection of a short GRB and GWs, so far. The invaluable wealth of information and new insights obtained by this event show the enormous potential of BNS mergers as multi-messenger sources. Within this context, this chapter focuses on the joint detection of GWs and high-energy (γ and X-ray) signals from BNS mergers by the next generation detectors. The advent of the Einstein Telescope (ET), together with other 3G GW detectors, will revolutionise the BNS study enabling to detect $\sim 10^5$ mergers per year up to high redshift. The high-energy emission will be essential for the identification of the counterpart at high redshifts, where the optical emission is too faint to be detected. Understanding how to optimise the joint detection probability is a crucial key to maximise the multi-messenger scientific return of each GW detection. Section 6.2 presents the work done to evaluate the ET detection and parameter estimation capabilities as well as the synergy beween ET and future high-energy telescopes in terms of number of joint detections, observational strategy and science impact. Methodology and results are published in Ronchini et al., 2022a.

6.1 Current status: searches for GWs in coincidence with GRBs

The type of signal of GWs expected in correspondence to GRBs depends on the GRB progenitor:

- in the case of a CBM, the inspiral and merger GW signal is well modelled, using numerical simulations of general relativity. Hence, the modelled search of a GW signal is performed through a direct comparison of data with a template bank of waveforms.
- in the case of a collapsar-driven GRB, a GW signal could be detectable as long as the SNa explosion has a relatively large level of asymmetry. In this case the GW waveform is highly uncertain due to the difficulty of simulating with sufficient precision the micro-physics acting in a supernovae explosion. The search of GWs, therefore, is limited to the search of an excess of power measured as signal amplitude with respect to the noise (unmodelled search).

In both cases the significance of a signal is expressed in terms of signal-to-noise ratio (SNR). A detection is claimed once the SNR exceeds a given minimum threshold and the detection significance is estimated through a Bayesian approach. As well known, the addition of further information on the source can modify the priors probability distribution, making the search more effective. The GW search that uses external information (typically electromagnetic or neutrino events) from the possible GW source is called triggered search (Abbott et al., 2008). In the case of a GRB the position and time of the GRBs can be used in the GW analysis. Thus, if the GW search is restricted to a specific time window and a specific region of the sky, a given GW signal can have higher significance compared to an all-sky search. Furthermore, if the GRB distance is known, the GW search can be restricted to a parameter space which is even more reduced. The search for joint GW/GRB detection is done in real time when the GRB alerts are sent but also off-line by re-analysing all the data. The off-line analysis benefits of better estimation of the noise and the possibility of performing the analysis exploring all the source parameter space. If there is an event exceeding a significance of 5σ, the joint GW/GRB detection can be claimed. I participated in the off-line analysis of the O3 data in coincidence of GRBs detected by Fermi and Swift. In particular I was responsible of the analysis of 5 GRBs.
For the off-line search of GW signals in coincidence with merger-driven

GRBs, the *PyGRB* pipeline is used (Williamson et al., 2014). In this case, in order to select events more likely associated with binary merger of compact object, short GRBs with a duration $t_{90} < 2$s are selected. The time window for the GW search is restricted to the range $[t_{GRB} - 5s, t_{GRB} + 1s]$, where t_{GRB} is the GRB trigger time. The asymmetry of the interval is due to the fact that some scenarios predict the formation of a relativistic jet and the consequent dissipation via prompt emission can be delayed with respect to the merger time. The exact value of the delay may strongly depend on the nature and life-time of the remnant, as well as on the specific time needed by the jet to propagate and break through the ejecta. An additional interval of time of 90 s, centred around the GRB trigger, is used for the estimation of the GW background. *PyGRB* exploits a matched-filter approach, based on a comparison of real data with signals from a template bank, where a wide parameter space of the binary system is explored (e.g. component masses, orbital plane inclination, spins). Additionally the sensitivity of the search is evaluated injecting and recovering artificial signals. The sensitivity is quantified by the 90% exclusion distance D_{90}, namely the distance within which 90% of the injected signals are recovered. The larger the D_{90} is, the more efficient is the search, mainly affected by the number of active interferometers, the background noise present around the GRB trigger and the GRB orientation in the sky with respect to the instrument antenna pattern.
As standard procedure, the GW search first is done on a time interval that excludes the central window around the GRB trigger and this procedure creates a so called *closed box*. The analysis of the closed box enables us to verify the quality of data (through injected/recovered signals) and possible issues in the background, e.g. if the noise deviates from a Gaussian distribution. Once the quality of the closed box is checked, the central time window is included in the analysis and this creates the so called *open box*. The analysis of the open box gives the final result about the loudest event (higher SNR) and associated false alarm probability. For the search of GWs in coincidence to merger-driven GRBs, I run the PyGRB pipeline for GRB 200327A, on behalf of the LVK GRB/FRB group.
For the off-line search of GW signals associated to collapsar-driven GRBs, the *Xpipeline* is used (Sutton et al., 2010). This pipeline searches for coherent excess power in the available operating interferometers during the GRB trigger. Here the search is extended on a wider time range corresponding to $[t_{GRB} - 600\,s, t_{GRB} + \max(t_{90}, 60\,s)]$, due to the larger uncertainties on the physical process at the origin of GW emission in the case of a star collapse. The coherent excess power search is based on the comparison of the frequency-time maps of different interferometers. A GW with unknown

waveform is expected to produce the same power in different interferometers, for a fixed frequency, but with a delay time due to the separation in space of the instruments. For the un-modelled search I run the Xpipeline on behalf of the LVK GRB/FRB group for four different GRBs. The results of my analysis contribute to the LVK publication Abbott et al., 2022a. Apart GW170817, in none of the three LVK observing runs a GW/GRB association has been confirmed (Abbott et al., 2017e; Abbott et al., 2019; Abbott et al., 2021c; Abbott et al., 2022b), neither with the use of PyGRB or Xpipeline. The main results of the GW/GRB search in the O3b run, reported in Abbott et al., 2022a, are the following:

- A total of 17 GRBs have been analysed with the modelled search and 86 with the unmodelled search. For each group a cumulative histogram of the exclusion distance D_{90} has been obtained. The main difference with O3a results is that the median D_{90} is larger, mainly attributed to the inclusion of the autogating, a technique able to remove more efficiently glitches in the data.

- The non-detection of coincidence of GW/GRB signals allows us to impose constraints of the shape of the GRB luminosity function. This has been done assuming a given parametric function for the luminosity function, described by a triple power law. The parameters of this functions are three slopes, two break luminosities and one low-luminosity cutoff. In this work only the low-luminosity slope and cutoff are left as free parameters, while the others parameters are fixed to the ones derived by Wanderman and Piran, 2015. Following a maximum likelihood approach and imposing that during all the GW runs the only joint GW/GRB detection is given by GW170817, a posterior distribution can be derived for the low-luminosity parameters of the luminosity function. The resulting luminosity function, marginalised over the posterior, is shown in Fig. 6 in Abbott et al., 2022a.

- The combined analysis of the targeted search during all the three observing runs leads to an estimation of future joint GW/GRB detections in O4 equal to $N_j = 1.04^{+0.26}_{-0.27}\mathrm{yr}^{-1}$.

.

6.2 Future prospects: joint detection of GWs-short GRBs in the Einstein Telescope era

In this section we explore the potentialities of the ET for the joint GW/EM detection of short GRBs, with a particular focus on the high-energy (X-ray and γ-ray) EM counterparts and the role of wide field telescopes. High-energy observatories will become more and more crucial to work in synergy with GW detectors which will make it possible to reach even larger distances. They represent a unique way to detect high redshift counterparts. Being intrinsically fainter than the high energy emission, the kilonova emission will be hardly detected at distances larger than a redshift of 0.3 even with next generation optical wide FOV observatories, such as the Vera Rubin Observatory (see e.g., Maggiore et al. 2020). Larger distances can be reached with extremely large telescopes, such as ELT, but only arcmin-arcsec localised GW sources can be effectively pointed by these telescopes. The next generation of GW detectors observing with sensitive wide FOV high-energy satellites will enable *i)* to build large samples of joint detections, *ii)* to have joint detections at high redshift, and *iii)* to observe, in the local Universe, counterparts from larger viewing angles with respect to the jet axis which will enable precise parameter estimation of the source progenitor properties. This will allow us to deeply investigate the connection between BNS mergers and short GRBs, to unveil the jet structure (Beniamini et al., 2019a; Hayes et al., 2020; Biscoveanu et al., 2020), to estimate how many BNS mergers produce jets (Salafia et al., 2022), how the production of the jet is connected to the progenitor properties, and what is the relation between merger remnants and the properties of the high-energy emission. Accessing a large sample of joint detections at high-redshift will enable us to evaluate cosmological parameters, including the Hubble constant and the dark energy equation of state (Zhao and Wen, 2018; de Souza et al., 2022; Yu et al., 2021; Chen et al., 2021), and test modified gravity at cosmological distances by comparing the GW luminosity distance and the one derived from the electromagnetic side (Belgacem et al., 2019; Mancarella et al., 2022). Identifying the BNS host galaxies and having a redshift will be of primary importance for these science cases. γ-ray and X-ray telescopes can potentially give precise (arcmin-arcsec) sky localisation to drive the ground-based follow-up.

Here we work in the assumption that the majority of short GRBs are produces by BNS mergers, thus neglecting the contribution from the NS-BH channel. The reasons are two-fold: 1) The estimated rate of NS-BH is $\sim$

1/10 the BNS rate, even if the current uncertainties are quite large (Abbott et al., 2020a); 2) The probability that a NS-BH system is able to launch a relativistic jet depends on the amount of accreted mass, which is not directly swallowed by the BH. Therefore the production of a short GRB is expected only for a specific combination of binary mass ratio and BH spin. The combination of these two factors justify our choice to consider BNS mergers as primary progenitors of short GRBs (see also Pannarale and Ohme 2014).
The population synthesis model for the cosmic BNS merger rate density, the GW detector configurations and the modeling of the GW signal, the modeling and calibration of the prompt and afterglow emission are described in Sec. 6.2.1. In Sec. 6.2.2 and 6.2.4 we show the predictions for joint detection of GW along with prompt and afterglow emission exploring several observational strategies. We consider ET as single observatory and in different networks of 3G GW detectors observing together with future high-energy facilities, which can operate in survey and pointing modes. We conclude highlighting the perspectives for joint GW and high-energy detections, discussing the optimal instruments and observational strategies to completely exploit the synergy between 3G GW detectors and $\gamma-$ and X-ray satellites, and the impact on the multimessenger science case.

6.2.1 Modeling and data analysis

In order to produce reliable estimations of joint GW/EM detection with future detectors, a complete and observation-based theoretical modelling is necessary. The logical steps behind the theoretical setup and the following analysis are listed here:

1. The cosmic rate density of BNS mergers is simulated with a state-of-the-art method, based on population synthesis model.

2. The high-energy EM signal associated to each BNS is predicted through the development of a phenomenological model, which works in the assumption of a universal jet structure.

3. The EM model is calibrated imposing that it is able to reproduce the statistical properties of short GRBs observed so far. Additionally the internal parameters are tuned in such a way that, independently on the local BNS merger rate, the average short GRB rate observed by Fermi is reproduced.

4. Once the model is calibrated, the temporal and spectral properties of the prompt and afterglow emission are self-consistently predicted, as a function of the jet viewing angle.

5. The detectability of the EM emission is evaluated considering currently operating and future high-energy telescopes.

6. The detectability and parameter estimation of the GW signal is performed adopting a Fisher matrix approximation.

7. Several observing strategies are taken into account, which also exploit the knowledge of GW parameters.

The BNS population model

The cosmic rate density of BNS mergers adopted in this work has been simulated using the approach detailed in Santoliquido et al., 2021. The catalogue of isolated compact binaries is generated with MOBSE (Mapelli et al., 2017; Giacobbo et al., 2018; Giacobbo and Mapelli, 2018), which is a population synthesis-code taking into account the metallicity dependence of mass-loss rate of massive stars, the uncertainty related to the common envelope evolution, natal kicks and mass transfer efficiency. The BNS merger rate density as a function of redshift is obtained with the COSMO$\mathcal{R}$ATE code (Santoliquido et al., 2020). The details about the adopted prescriptions and assumption are reported in Appendix D.1. For the NS mass we assume a uniform distribution in the range $[1 - 2.5]$ $M_\odot$ and no correlation exists between one mass the the one of the companion. The assumption of a uniform and broad mass distribution is consistent with the last results from GW observations (The LIGO Scientific Collaboration et al., 2021b). The specific shape of the NS mass distribution can have a relevant impact on the GW detection efficiency and hence on the portion of the accessible Universe. This, in turn can impact also our results of the estimation of the joint GW/EM detection rate. In Appendix D.4 we describe how the GW detection efficiency depends on the assumption about the mass function, in particular assuming using a mass distribution sharply peaked around 1.33 $M_\odot$ as observed in Galactic double neutron-star systems (Özel and Freire, 2016). The uniform mass assumption is the most optimistic one, since more system with higher chirp mass are expected.
With the adopted simulation setup described above, the entire population consists of $\sim 9 \times 10^5$ BNS mergers per year (observed at Earth by an ideal

instrument), and the local BNS merger rate ($R_{BNS} = 365\,\mathrm{Gpc^{-3}yr^{-1}}$) is consistent with the most updated constraints provided by GW observations during the first, second and third run of observations by the Advanced LIGO and Virgo detectors ($R_{BNS} \in [10 - 1700]\mathrm{Gpc^{-3}yr^{-1}}$, The LIGO Scientific Collaboration et al. 2021a; The LIGO Scientific Collaboration et al. 2021b; Abbott et al. 2021a; Abbott et al. 2021b). Moreover, the local rate assumed here is perfectly consistent with the collection of local BNS merger rates given by Mandel and Broekgaarden, 2021 and including both observed (from GW, kilonovae, SGRBs, and Galactic pulsar binaries' observations) and theoretically predicted rates. The BNS systems are injected with an isotropic distribution in the sky.

GW detector configuration, GW signal modeling and parameter estimation

In this work, we consider three GW detector configurations:

1. ET as a single detector located in Sardinia (Italy)
2. ET in a network with CE (40 km arms) located in the LIGO-Livingston site
3. ET in a network with 2CE of 40 km arms, with the second CE located in Australia

We assume the full sensitivity configuration for ET (referred as ET-D configuration, Hild et al. 2011). For CE we use the sensitivity of the 40 km arms detector given by Evans et al., 2021b. For CE as well as for each of the three combinations of high and low frequency interferometers of ET we assume a duty cycle of 0.85. Starting from the BNS population described in Section 6.2.1, we inject GW signals constructed using a post-Newtonian formalism, in particular assuming a TaylorF2 waveform (Buonanno et al., 2009). Since the spin is expected to be small in binaries of neutron stars that merge within a Hubble time (Burgay et al., 2003), the effects due to spins are neglected. The signal-to-noise ratio (S/N) of each inspiral is then computed through a matched-filter. A network S/N threshold equal to 8 is used to select GW detections.
The parameter estimation is obtained using the *GWFish* code (Dupletsa et al., 2022) and computing the elements of the inverse of the Fisher matrix (Grimm and Harms 2020). The code, for which I participated in the testing and development, is publicly available at this repository[1]. In *GWFish* the

[1] `https://github.com/janosch314/GWFish`

BOX 6.1: HOW *GWFish* WORKS

GWFish is a code which is able, starting from an injected GW and a given detector configuration, to evaluate the detection significance in terms of SNR, as well as to perform a full parameter estimation. Standard GW parameter estimation involves a full Bayesian-based procedure using posterior sampling and Monte Carlo techniques. However, this procedure, even if numerically reliable, is computationally expensive. Therefore, if we need to explore the detector capabilities over a complete population of sources distributed across the Universe, a large amount of signals have to be processed (the average merger rate both for BNS and BBH can exceed 10^6 yr^{-1}). With this purpose, *GWFish* has been conceived to radically reduce the parameter estimation computational time, working in the high SNR limit, where a Fisher matrix approach is valid.
The elements of the Fisher matrix are defined as

$$\mathcal{F}_{ij} = \sum_{k=1}^{N} \left\langle \partial_{x_i} h^k \mid \partial_{x_j} h^k \right\rangle ,$$

where the sum is extended to all the operating interferometers, h is the modelled signal and x_i are the parameters of the model. Here, the scalar product is defined as:

$$\langle a \mid b \rangle = 4 \int_0^\infty \mathrm{d}f \frac{\mathrm{Re}\left(a(\vec{x}, f) b^*(\vec{x}, f)\right)}{S_\mathrm{n}(f)},$$

where $S_\mathrm{n}(f)$ is the power spectral density of the detector noise, which is assumed to be Gaussian and stationary. It can be shown that in the high SNR limit, the inverse of the Fisher matrix well approximates the covariance matrix, from which parameters uncertainty can be derived as the diagonal elements:

$$\sigma_i \sim \sqrt{d_i^{-1}},$$

where $d_i = \mathcal{F}_{ii}$. *GWFish* works in the frequency domain, under the stationary phase approximation. This allows to accurately take into account also the time-dependent position and orientation of the detectors, which is relevant especially when long-lasting signals (e.g. BNS inspirals) are considered. Accessing lower frequencies makes the signal stay for longer time in the 3G detector band, which is even more crucial for ET. This advantage, together with about one order magnitude improvement at all detectable frequencies and with the inclusion of current GW detectors, make the parameter estimation much more precise thanks to the larger SNR.

waveforms, modeled in frequency domain, are implemented from scratch and the code includes an interface with LALSimulation[2].

Detector networks consider Earth's rotation, which has an impact on the localisation capabilities. The most important computational aspects (waveform derivatives and Fisher matrix inversion) are carried out using an hybrid approach for derivatives (analytic and numeric) and a combination

[2] `https://lscsoft.docs.ligo.org/lalsuite/lalsimulation/`

of matrix normalization and singular value decomposition for matrix inversion (which takes care of the quasi singularity of the Fisher matrices). Such an approach approximates the true likelihood with a Gaussian profile, which is valid in the limit of a high information content in the data. In this regime the likelihood is highly peaked and the role of priors is negligible. Hereafter, the uncertainty on the sky localisation $\Delta\Omega$ is given as 90% credible region, while the uncertainty on other GW parameters, such as θ_v and luminosity distance, is given at 1σ confidence level.

Prompt emission modeling

In this section we describe a method to predict the main features of the prompt γ-ray emission produced by the BNS merger. The basic dissipation mechanism behind prompt emission is still poorly understood. Since no specific process is strongly favoured over the others, we do not make any assumption on the physical origin of the prompt emission. The model we propose is phenomenological, namely it directly predicts physical observables, without making strong assumption about their physical origin. In this way, the model can be calibrated with a direct comparison with real observed data.
As described in Section 3.3, several conditions are necessary such that a relativistic and collimated outflow is produced after a BNS merger. Moreover, even if a jet is launched, it must be able to break through the ejecta in order to release a detectable γ-ray emission. Several efforts have been spent to carefully model how the jet launch and successful break out may depend on the initial condition (e.g. Salafia et al. 2020a), but many uncertainties still affect these approaches, making any prediction strongly model dependent. Therefore we decide to parametrise the probability that a jet is able to penetrate the post-merger ejecta and to successfully break-out introducing a parameter f_j. This is a free parameter of our model and it is defined as the fraction of BNS which are able to produce a jet. Hence, if $\dot{\rho}_{sGRB}(z)$ and $\dot{\rho}_{BNS}(z)$ are the cosmic rate densities (in units of events per comoving volume per comoving time) of the sGRB and BNS populations, respectively, then:

$$\dot{\rho}_{sGRB}(z) = f_j \dot{\rho}_{BNS}(z).$$

We notice that, in principle, f_j could depend on the properties of the binary system, such as the component masses and spins, but here we do not assume any dependency.

BOX 6.2: THE ASSUMED UNIVERSAL JET STRUCTURE

The properties of the γ-ray and X-ray emissions are evaluated in the assumption of a universal jet structure (Lipunov et al. 2001, Salafia et al. 2015b, Salafia et al. 2019b, Salafia et al. 2020b), which is the same of GRB 170817A. In particular, we adopt:

$$\epsilon(\theta) = \frac{dE}{d\Omega} \propto \frac{1}{1 + (\theta/\theta_c)^{s_\epsilon}} \tag{6.1}$$

and

$$\Gamma(\theta) = 1 + \frac{\Gamma_0 - 1}{1 + (\theta/\theta_c)^{s_\Gamma}}, \tag{6.2}$$

where $\epsilon(\theta)$ is the angular structure of the local emissivity and $\Gamma(\theta)$ the bulk Lorentz factor profile (θ is the polar angle measured from the jet symmetry axis). The choice of θ_c and Γ_0 influences the number of prompt emission detections, while the off-core specific shape of the jet has more impact on the brightness of the afterglow component and the prompt tail. From the modeling of radio afterglow of GRB 170817A (Ghirlanda et al., 2019c), the best fit parameters of the jet structure are the following:

$$s_\epsilon = 5.5^{+1.3}_{-1.4},\ s_\Gamma = 3.5^{+2.1}_{-1.7},\ \theta_c = (3.4 \pm 1.0)\ \text{deg}. \tag{6.3}$$

For our modeling, we fix for simplicity $s_\epsilon = s_\Gamma = s$ and we adopt:

$$s = 4,\ \theta_c = 3.4\ \text{deg}. \tag{6.4}$$

Moreover, we fix $\Gamma_0 = 500$, which is in agreement with usual values inferred for GRBs (e.g., Ghirlanda et al. 2018). These parameters are the same for the modeling of both prompt and afterglow emission. A broader structure with $s = 2$ and same θ_c is also tested (Rossi et al., 2002a). Hereafter we refer to *Stru1* for the case $s = 4$ and $\theta_c = 3.4$ deg and *Stru2* for the case $s = 2$ and $\theta_c = 3.4$ deg.
The dependency of our results on the choice of the structure parameters is discussed later in In Sec. 6.2.2 and 6.2.4. The aperture angle assumed here is consistent with the values found in SGRBs with well constrained jet break (typical values of θ_c are in the interval $\sim 1^\circ - 8^\circ$, see Fong et al. 2014, Jin et al. 2018 and references within). Similar values are found in hydrodynamical simulations of jet propagation in NS mergers, for example Lazzati et al. 2018b predicts a jet aperture angle of $\sim 5^\circ$ (see also Geng et al. 2019, Wu and MacFadyen 2018). Also Lamb et al., 2022b find a rather small jet core ($\theta_c \sim 2.2^\circ$) and a jet profile compatible with eq. 6.1 and 6.2, with best fit values $s_\epsilon \sim 3.1$ and $s_\Gamma \sim 1.8$.

Hereafter, we assume that all the jets share a common structure, described in Box 6.2, and they differ only in the energy content, prompt emission duration and comoving spectral properties. We define E_t the beaming corrected energy budget of the jet, which is connected to the isotropic energy measured by an observer aligned to the jet (on-axis) in the following

way:

$$E_{\rm iso} = \frac{4\pi}{\Delta\omega} E_t, \tag{6.5}$$

where $\Delta\omega \sim 4\pi(1-\cos(\theta_c))$. E_t is related to $\epsilon(\theta)$ through the following relation:

$$E_t = \int_\Omega \epsilon(\theta) d\Omega.$$

We note that E_t does not represent the energy content of the jet, but rather the energy which is converted into radiation through dissipation mechanisms (such as internal shocks or magnetic reconnection). We extract the value of E_t from the following probability distribution:

$$P\left(E_t/E^*\right) \propto \left(E_t/E^*\right)^{-\lambda_E} e^{-E^*/E_t}, \tag{6.6}$$

which is a power law with a low-energy exponential cut-off. The choice of this specific functional form is justified as follows. As shown in Appendix A.2, if the core luminosity follows a power law distribution[3] in the form $P(L) \propto L^{-k}$, then the luminosity function of a structured jet is well approximated by a broken power law:

$$\phi(L) \propto \begin{cases} L^{-\alpha} & , L < L_* \\ L^{-k} & , L > L_* \end{cases},$$

where α depends only on the specific assumed structure. Therefore the assumed functional form reported in eq. 6.6 is in agreement with a broken power law profile of the luminosity function, strongly favoured from past populations studies of short GRBs (Wanderman and Piran, 2015; Ghirlanda et al., 2016b).

The prompt emission spectrum is assumed to be angle-independent in the jet comoving frame and follows a smoothly broken power law, with low- and high-energy photon indices of 2/3 and 2.5, respectively. These are typical values measured for SGRBs (Nava et al., 2011). For an on-axis observer in the rest frame of the source, we assume that the spectral peak energy has a log-normal distribution, that is to say:

$$P(\log(E_p)) \propto \exp\left(-\frac{(\log(E_p) - \log(\mu_E))^2}{\sigma_E^2}\right), \tag{6.7}$$

[3]Both E_t and core luminosity follow the same probability distribution in the approximation that the emission duration is highly peaked around a single value

where μ_E and σ_E are the mean value and the standard deviation of the distribution, respectively. The assumed distribution function corresponds to that adopted by Ghirlanda et al., 2016b. Such distribution in the observer frame is equivalent to assume a monochromatic distribution of E'_p in the jet comoving frame and a log-normal distribution of Γ_0 (indeed $E_p = \Gamma_0 E'_p$).
For the computation of the burst duration, we compute the time t_{90} such that the energy emitted from 0 to t_{90} is equal to the 90% of the total energy released by the GRB [4]. The light curve is approximated with a linear rising phase from $t = 0$ to the peak time $t = t_p$, followed by a decreasing phase which evolves according to high latitude emission (HLE). Therefore we assume that a single pulse dominates the SGRB emission. For t_p we consider a log-normal distribution as well, as measured in the rest frame of the burst from an on-axis observer:

$$P(\log(t_p)) \propto \exp\left(-\frac{(\log(t_p) - \log(\mu_\tau))^2}{\sigma_\tau^2}\right). \tag{6.8}$$

The functions introduced above fully describe the prompt emission observables for an on-axis observer. To predict the viewing angle-dependent observables, we follow the approach described in Appendix B.1. Specifically, we work in the approximation of an infinitesimal duration emission at a fixed radius R_0, namely the burst duration in the rest frame is negligible compared to the time needed by the jet to propagate up to R_0. The presence of a jet structure like the one adopted here produces an X-ray light curve with a steep decay followed by a shallower phase, known as plateau. As mentioned in the introduction of Chapter 5 and in Appendix B.2, the core radius R_0 and the aperture angle θ_c are the two structure parameters that determine the duration of the plateau and larger values of R_0 and θ_c produce a longer plateau. In order to find a fiducial value for R_0, we considered all the SGRBs from the *Swift*-XRT catalog with a plateau phase. We verified that the end time of the plateau typically spans in the range $10^2 - 10^3$ s. Having fixed $\Gamma_0 = 500$ and $\theta_c = 3.4$ deg, we therefore adopted $R_0 = 5 \times 10^{14}$ cm in order to obtain a typical plateau duration around few hundred seconds.
Once the on axis parameters and the viewing angle are known, the off-axis

[4] As well known, the t_{90} is an instrument-dependent quantity, therefore our computation takes into account the specific instrument that we use to calibrate our model. In particular, given the detection threshold of the instrument, we compute t_{90} taking into account the portion of the light curve which is above the detection limit.

observables can be obtained from the angle-dependent light curve. Unfortunately, when the light curve has to be computed by numerical methods for a large amount of injected BNS, the computational time can grow significantly. Therefore, to reduce the computational time, we introduce for each observable X an auxiliary function $F_X(\theta_v, t)$ (derived in Appendix D.3) which describes how the off-axis observable depends on the on-axis one evaluated at the light curve peak time. Namely, once the jet structure is fixed and the on-axis observable X is derived by the random sampling of the distributions mentioned above, the off-axis observable and the relative temporal evolution can be computed as

$$X(t, \theta_v) = F_X(\theta_v, t) X(t = t_p, \theta_v = 0).$$

Such simplification is extremely helpful when the model has to be calibrated through the use of Monte Carlo techniques, which involve $\sim 10^6$ evaluations of the prompt emission observables.[5] In the modelling setup described so far, also the transparency of the emitting region has to be taken into account. Indeed, in the computation of the observed flux, we need to verify that the each patch of the emitting region is optically thin. A detailed treatment of the compactness issue and how it has been taken into account in our work can be found in Appendix B.3.
With this approach we are able to predict the prompt emission output, as well as the contribution at later time given by the jet wings due to HLE effects, which can be relevant for the detectability of the SGRB afterglow, especially in the X-rays and for off-axis observers.

Calibration of the prompt emission model

Here, we describe the procedure for the calibration of the prompt emission model and the setup of the joint GW/prompt detection simulation, which can be summarised in the following steps:

1. For the comparison between model and data, we consider the sample of short GRBs defined in Ghirlanda et al., 2016b, from which we extract the probability distribution $P(X_o)$ of each observable, which are the peak energy, duration, peak flux and fluence. With X_o we indicate the observed quantity, while with X_p the one predicted by our model. The calibration sample is obtained by selecting SGRBs in the *Fermi*

[5] As described later, the convergence of the parameter estimation needs to produce at least 10^4 different realisations of the model and for each realisation order of 100 GRBs are simulated, for a total of $\sim 10^6$ evaluations of the model.

parameter	prior interval
λ_E	[1,12]
$\log_{10}(E_*/10^{49}\mathrm{erg/s})$	[-2,$\log_{10}(50)$]
$\log_{10}(\mu_E/\mathrm{keV})$	$[\log_{10}(700), \log_{10}(3000)]$
σ_E	[0.05,1]
$\log_{10}(\mu_\tau/s)$	$[-2, \log_{10}(4)]$
σ_τ	[0.05,1]
$\log_{10} f_j$	[-3,0]

TABLE 6.1: Prior intervals for the prompt emission model. For λ_E, σ_E and σ_τ we consider a flat prior distribution, while for the others the distribution is flat in logarithm.

parameter	Stru 1	Stru 2
λ_E	$6.7^{+3.6}_{-3.3}$	$6.4^{+3.7}_{-3.5}$
$\log_{10}(E_*/10^{49}\mathrm{erg/s})$	$-0.30^{+0.40}_{-0.34}$	$-0.23^{+0.48}_{-0.69}$
$\log_{10}(\mu_E/\mathrm{keV})$	$3.2^{+0.1}_{-0.1}$	$3.2^{+0.1}_{-0.1}$
σ_E	$0.36^{+0.10}_{-0.09}$	$0.37^{+0.10}_{-0.10}$
$\log_{10}(\mu_\tau/s)$	$0.05^{+0.24}_{-0.31}$	$0.02^{+0.09}_{-0.10}$
σ_τ	$0.60^{+0.10}_{-0.11}$	$0.59^{+0.09}_{-0.10}$
$\log_{10} f_j$	$-0.59^{+0.37}_{-0.32}$	$-0.95^{+0.52}_{-0.41}$

TABLE 6.2: Prompt emission model parameters from the MCMC sampling for the two jet structures analysed in the present work. The interval of confidence from the posterior distribution of the prompt emission parameters is given as 1σ.

catalogue with peak flux $F_p > 5$ ph cm^{-2} s^{-1} to ensure the completeness of the sample.

2. Our model depends on the set of parameters

$$\omega = [\lambda_E, E^*, \mu_E, \sigma_E, \mu_\tau, \sigma_\tau, f_j].$$

For each realisation of ω, a sample of 100 GRBs is simulated and the probability distribution of the simulated observable $P(X_p)$ is calculated. In order to quantify the predictive power of the model, we introduce a likelihood function defined as $\log \mathcal{L} =$

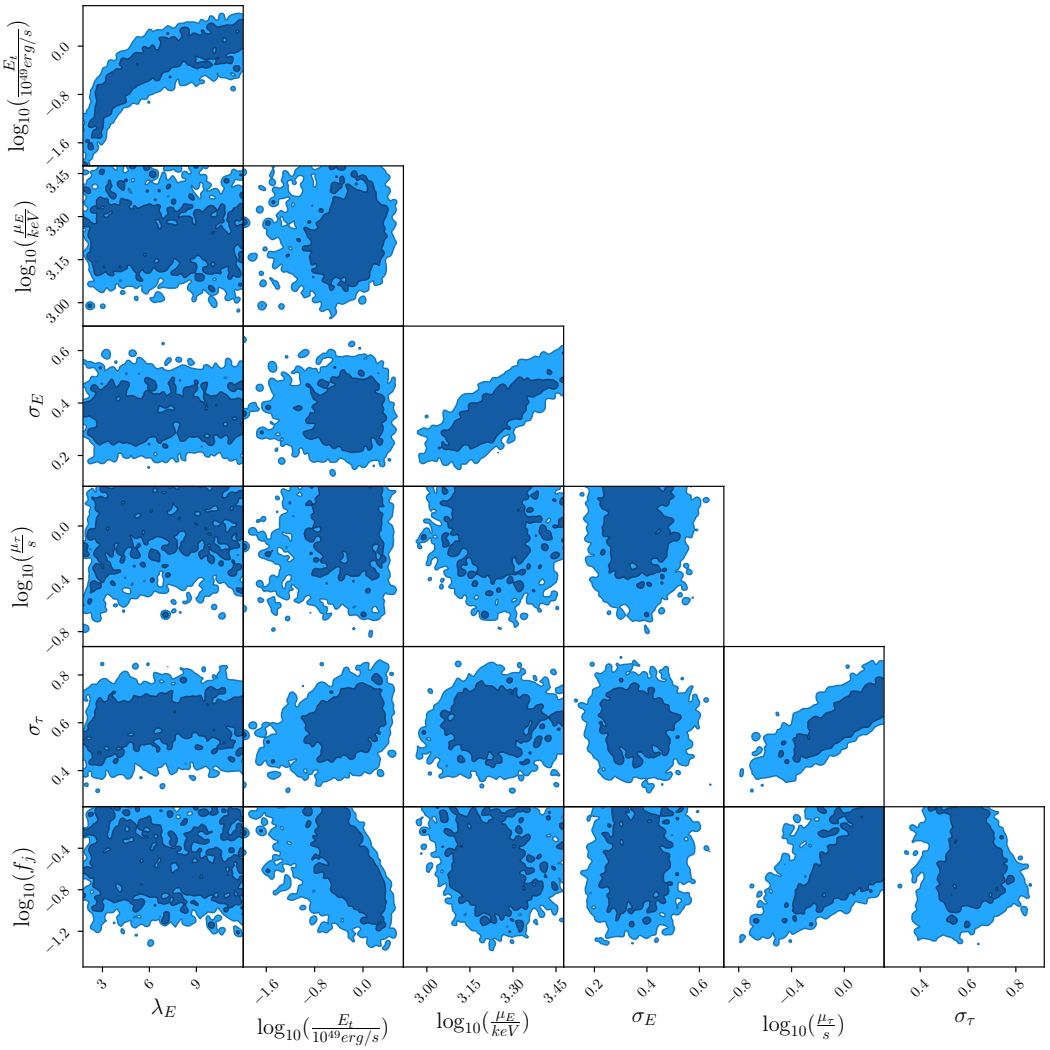

FIGURE 6.1: Corner plot of the posterior distribution of the parameters adopted for the prompt emission model. The assumed structure is *Stru1*. The number of MCMC steps is chosen such that the auto-correlation time reaches a plateau, as described in Foreman-Mackey et al., 2013.

$\log\left(P_C(N_{\rm pre}|N_{\rm det})\right) + \sum_{i=1}^{4} \log(P_{\rm KS,i})$, where $P_C(N_{\rm pre}|N_{\rm det})$ is the Poissonian probability that *Fermi*-GBM detects N_{pre} SGRBs per year given that the average observed number is N_{det}, while $P_{KS,i}$ is, for each observable i, the Kolmogorov-Smirnov probability that the predicted and observed distributions come from the same population.

3. Adopting the likelihood defined above, the parameter estimation

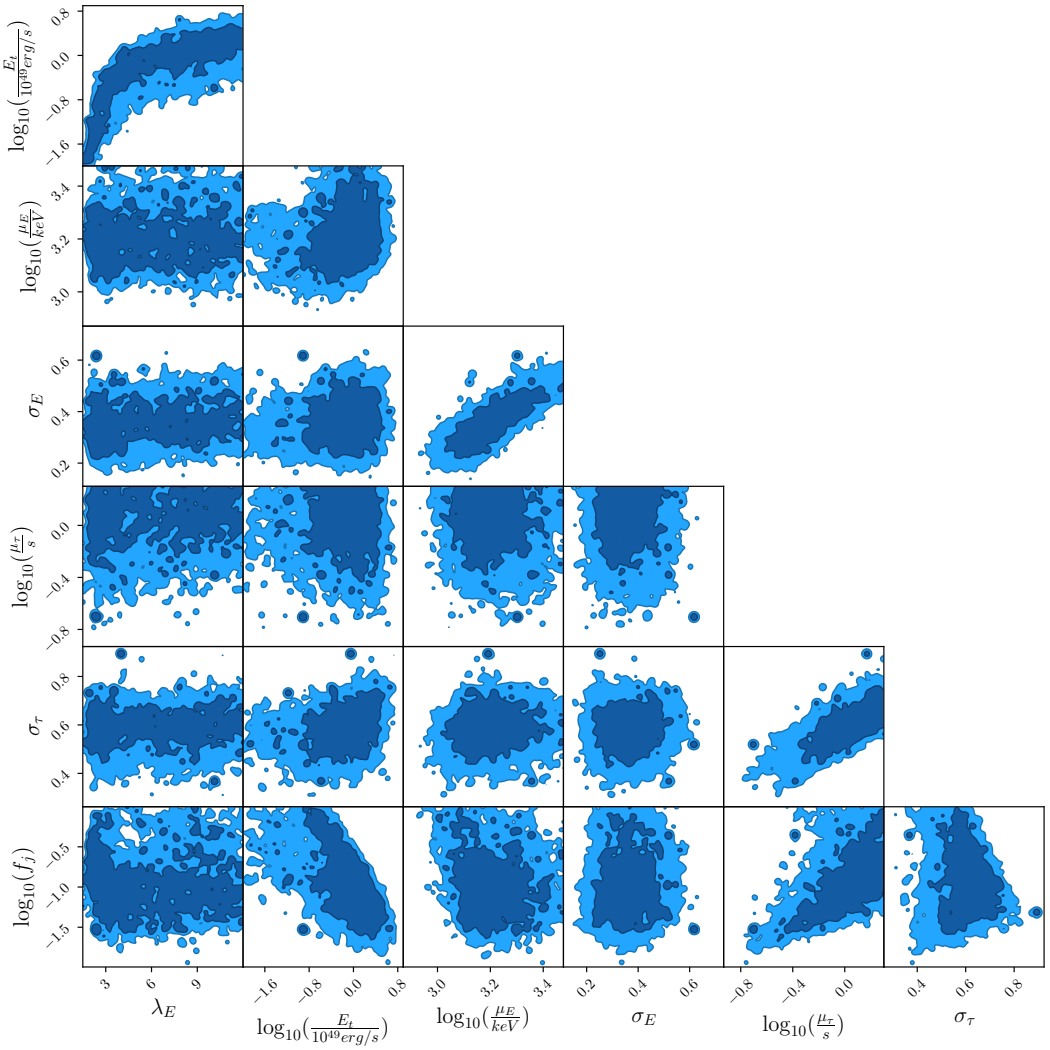

FIGURE 6.2: Same as Fig. 6.1, adopting *Stru2*.

is performed adopting the Goodman & Weare's Affine Invariant Markov chain Monte Carlo (MCMC) Ensemble sampler[6].

4. The MCMC defines our fiducial posterior distribution for ω. Each realisation of ω corresponds to a different GRB population. The calibration is set up in such a way that the statistical properties of the

[6]We adopted 16 walkers and 30000 steps

observables, averaged over many realisations of ω, converge to the statistical properties of the real short GRB sample.[7]

The detection rate of SGRBs $R_{\rm SGRB,det}$ can be related to the BNS rate $R_{\rm BNS}$ as:

$$R_{\rm SGRB,det} = \int [\frac{dN_{\rm SGRB}}{dzdt}|_{\rm det}]dz, \tag{6.9}$$

where

$$\frac{dN_{\rm SGRB}}{dzdt}|_{\rm det} = \langle \Omega_{\rm obs} \rangle \times \phi_{\rm det}(z) \times f_j \frac{dN_{\rm BNS}}{dzdt}. \tag{6.10}$$

We note that $\langle \Omega_{\rm obs} \rangle$ is the time-averaged sky coverage of the instrument and f_j is the fraction of BNS able to form a jet. The quantity $\frac{dN_{\rm BNS}}{dzdt}$ is the number of BNS mergers observed at Earth per unit time and redshift and it is provided by the population synthesis model. $\phi_{\rm det}(z)$ is the variable that combines the detection efficiency of the instrument (which takes into account the k-correction) and the beaming of the SGRB emission. Namely, $\phi_{\rm det}(z)$ represents the probability that a SGRB at redshift z is detectable by a given instrument at Earth, that is to say:

$$\phi_{\rm det}(z) = \frac{N_{\rm SGRB}(F > F_{\rm lim}, z)}{N_{SGRB}(z)},$$

where $N_{\rm SGRB}(z) = \frac{dN_{\rm SGRB}}{dzdt}$, $N_{\rm SGRB}(F > F_{\rm lim}, z) = \frac{dN_{\rm SGRB}}{dzdt}(F > F_{\rm lim})$ and $F_{\rm lim}$ is the limiting flux in the band of the instrument. In turn, $N_{\rm SGRB}(F > F_{\rm lim}, z)$ depends on the luminosity function of SGRBs, their average spectral properties, as well as on the jet structure.

The inclusion of f_j as free parameter of our model makes our estimates of absolute numbers of detections independent on the overall normalization of the BNS population model which is still subject to large uncertainties (Santoliquido et al., 2021). Indeed the likelihood function is written in such a way that, whatever the BNS merger rate normalization is, the value of f_j is optimized to reproduce the current average rate of *Fermi*-GBM detections. Namely, in eq. 6.10 the quantity $\frac{dN_{BNS}}{dzdt}$ is uniquely determined by the BNS population model, $\phi_{det}(z)$ depends on the prompt emission model and therefore the MCMC converges to that value of f_j that reproduces $R_{\rm SGRB,det}$,

[7] For instance, for one specific realisation of ω, the isotropic energy distribution may deviate from the observed one, but the distribution, averaged over many realisation of ω, converges to the observed one.

which is known.
This approach therefore implies that the full calibration of the model, and hence the specific fiducial values of the adopted parameters, depend on the definition of $\frac{dN_{BNS}}{dzdt}$. In Appendix D.2 we show how, under the assumption of a fixed luminosity function, the parameters f_j changes if we adopt a different BNS population. In the assumption that the new BNS population differs from the one adopted here only for the local rate ρ_0 (and not in the redshift distribution), then we trivially obtain that $f_j \propto \rho_0^{-1}$. If this assumption does not hold, the derivation of f_j is less straightforward (see Appendix D.2).

The MCMC sampling has been performed for two different jet structures *Stru1* and *Stru2*. For both structures, we obtain the posterior distribution of the model parameters. The prior intervals are reported in Tab. 6.1. The confidence intervals of the parameters are reported in Tab. 6.2, while the corner plots of the posterior distributions are reported in Figs. 6.1 and 6.2 for *Stru1* and *Stru2*, respectively. The modification of the off-core slope of the jet structure does not influence the best fit parameters, except for f_j, which tends to be smaller for $s = 2$. Such result is justified by the fact that a broader structure implies a larger detectability of the prompt emission at larger viewing angles, which corresponds to a larger number of off-axis detections. Therefore, for a given BNS population and an average SGRB detection rate, a broader structure requires a smaller fraction of BNS to be able to produce SGRB. The confidence interval we obtain for f_j is not particularly tight and it is compatible with other works which combine EM observations of SGRBs and BNS rates from GW observations (Ghirlanda et al., 2019c; Salafia et al., 2022; Sarin et al., 2022; Beniamini et al., 2019b; Lamb and Kobayashi, 2017b).
Recent observations revealed that CBMs can actually produce a GRB with a duration longer than two seconds (Rastinejad et al., 2022; Mei et al., 2022b). This means that, in principle, there could exist a sub-population of long GRBs powered by a CBM and our estimations of joint detections could have an additional contribution related to that sub-sample of events.

Forward shock modeling

The forward shock (FS) light curves are produced using the Python package *afterglowpy* (Ryan et al., 2020b). This semi-analytical code adopts a simplified equation of state and prescription for the lateral spreading, making it a precise prediction tool in the ultra-relativistic regime. Compared with fully

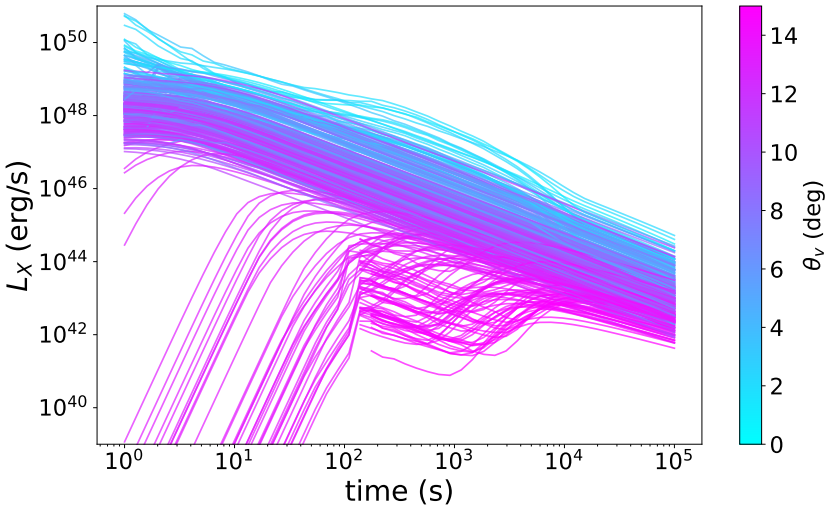

FIGURE 6.3: X-ray light curves of SGRBs with viewing angle $0° < \theta_v < 15°$ predicted by our model. The lines are produced with a random extraction from the posterior distribution of prompt parameters. In the computation we assume *Stru1* and we include both HLE and FS (configuration *FS-SGRB*). The color of each line indicates the viewing angle. The X-ray luminosity is computed at 5 keV.

numerical codes, such as *BoxFit* (van Eerten et al., 2012), Afterglowpy successfully agrees at late times, while at early times the discrepancy is below a factor of 50%. For the jet kinetic structure we assume the same profile adopted for the structure of the comoving frame emissivity reported in the prompt emission modeling (see eq. 6.1). This implies that we are assuming that the conversion efficiency from kinetic energy to radiated energy has no angular dependence. The detectability of X-ray emission is evaluated for both *Stru1* and *Stru2*. *Afterglowpy* includes the parameter θ_w which is the angular extension of the jet wings. For *Stru1* we assume $\theta_w = 15$ deg, while for *Stru2* we assume $\theta_w = 30$ deg. The impact of the choice of θ_w on the detectability of X-ray emission is discussed later in the text. The model depends also on the micro-physical parameters n_0, p, ϵ_e and ϵ_B which are the ISM density, the slope of the electron energy distribution, the fraction of energy carried by electrons and the fraction of energy carried by the magnetic field, respectively. In the following, we perform our simulation using two setups of parameters:

1. $n_0 = 2.5 \times 10^{-4}\,\mathrm{cm}^{-3}$, $p = 2.2$, $\epsilon_e = 0.1$ and $\epsilon_B = 1.3 \times 10^{-4}$, which are the best fit values obtained from the multiwavelength (X-ray, optical, radio) modeling of the X-ray afterglow of GRB 170817A

(Ghirlanda et al. 2019c). These values are also consistent with the confidence intervals reported by Wu and MacFadyen, 2019b. We call this configuration *FS-GW17*.

2. For the ISM density we take the fiducial interval derived by Fong et al., 2015b $n_0 \in (3-15)\times 10^{-3}$ cm^{-3}. The other parameters are fixed to $p = 2.2$, $\epsilon_e = 0.1$ and $\epsilon_B \in [0.01-0.1]$. n_0 and ϵ_B are uniformly extracted from the confidence intervals reported above. This configuration is more representative for SGRB population with respect to *FS-GW17*, and we call it *FS-SGRB*.

If we call η the fraction of kinetic energy which is transformed into radiation, then $E_{\rm rad}/E_{\rm kin} = (1-\eta)/\eta = \tilde{\eta}$ and we assume $\tilde{\eta}$ randomly distributed in the interval $[0.01-0.1]$. Fig. 6.3 shows a collection of X-ray light curves produced with our model at different viewing angles, including both HLE and FS (configuration *FS-SGRB*). The curves are obtained with a random extraction from the probability distributions of the prompt parameters described in sec. 6.2.1 and the parameter of each distribution is extracted from the Monte Carlo posterior described in sec. 6.2.1.

Simulation setup

Here we summarise how the predictions about the joint detections of GWs and short GRBs are simulated, considering first the γ-ray prompt emission and later the X-ray emission from the contribution of both forward shock afterglow and HLE from the structured jet. The fiducial posterior ranges of the joint detection rates are obtained as follows:

1. For each BNS we derive SNR and parameter estimation with *GWFish*. To each BNS we assign a viewing angle θ_v.

2. The value of the parameter vector ω, defined in Sec. 6.2.1, is randomly extracted from the posterior distribution defined by the MCMC.

3. Once ω is defined, f_j is known as well. Then a random number n is drawn between 0 and 1, and if $n < f_j$, the jet is successful and we proceed with the simulation, otherwise we go back to point 1.

4. All the observables, related to both prompt and afterglow, are computed at a viewing angle $\theta = \theta_v$. The detection in the EM domain is evaluated once the sensitivity of the specific instrument is known.

5. Steps 3 and 4 are repeated for all the injected BNS, thus obtaining a single population of short GRBs, once ω is fixed. This defines a fraction $S_{GW} = N_{GW}/N_{inj}$ of BNS that have a detectable GW and a fraction $S_{EM}(\omega) = N_{EM}(\omega)/N_{inj}$ of BNS with a detectable EM emission (γ-ray and/or X-ray), as well as a fraction of joint detections $S_{EM+GW}(\omega) = N_{EM+GW}(\omega)/N_{inj}$.

6. The quantities $S_{EM}(\omega)$ and $S_{EM+GW}(\omega)$ are computed for N different realisations[8] of ω. The average value and relative uncertainties of $S_{EM}(\omega)$ and $S_{EM+GW}(\omega)$ are reported quoting the 50^{th} percentile and the 16^{th}-84^{th} percentile as the median and 1σ range, respectively.

For computational efficiency reasons, the viewing angle θ_v is drawn from a uniform distribution in $\cos(\theta_v)$ in the interval $\arccos(\theta_{max}) < \cos(\theta_v) < 1$, where θ_{max} is the maximum angle at which the EM emission can be detected. This means that if N_{inj} is the total number of BNS injected for one year of observations, the above distribution of θ_v implies that we are simulating a corresponding period of $1\ \mathrm{yr}/(1-\cos(\theta_v))$. Namely, for a fixed period of observations, the simulation time is reduced by a factor $1/(1-\cos(\theta_v))$. Notice that θ_{max} depends on redshift, so we conservatively take θ_{max} calculated at the minimum redeshift of the BNS population.

6.2.2 Joint detection of GWs and the prompt emission

For the detection of the prompt emission from our SGRBs population, we consider the following γ-ray instruments: the Gamma-ray Burst Monitor on board of *Fermi* (*Fermi*-GBM, Meegan et al. 2009b), the *Swift*-Burst Alert Telescope (*Swift*-BAT, Barthelmy et al. 2005), the Gravitational wave high-energy Electromagnetic Counterpart All-sky Monitor (GECAM, Li et al. 2020), the ECLAIRs telescope and the Gamma-Ray burst Monitor (GRM) on board of the Space-based multi-band astronomical Variable Objects Monitor (SVOM, Cordier et al. 2015; Götz and SVOM Collaboration 2012), the X/Gamma-ray Imaging Spectrometer (XGIS) on board of the Transient High-Energy Sky and Early Universe Surveyor (THESEUS, Amati et al. 2018; Amati et al. 2021; Ciolfi et al. 2021; Rosati et al. 2021), the Gamma-ray Transient Monitor (GTM) on board of the Transient Astrophysical Probe (TAP, Camp et al. 2019), and the High Energy Rapid Modular Ensemble of

[8] N depends whether we are considering prompt emission or X-ray afterglow, depending on the computational time required, much larger for the X-ray afterglow, for which the full light curve has to be simulated for each source. See details in the respective sections later.

INSTRUMENT	band MeV	$F_{\rm lim}$ erg cm^{-2} s^{-1}	FOV/4π	loc. acc.	Joint ET +γ-ray	N_{JD}/N_γ	Joint (ET+CE) +γ-ray	N_{JD}/N_γ
Fermi-GBM	0.01 - 25	0.5(*)	0.75	5 deg (^{a})	33^{+14}_{-11}	68^{+13}_{-18}%	47^{+14}_{-14}	95^{+5}_{-7}%
Swift-BAT	0.015 - 0.15	2×10^{-8}	0.11	1-3 arcmin	10^{+3}_{-3}	62^{+11}_{-14}%	13^{+5}_{-4}	94^{+6}_{-7}%
GECAM	0.006 - 5	2×10^{-8}	1.0	1 deg	121^{+84}_{-48}	57^{+8}_{-10}%	205^{+145}_{-72}	92^{+4}_{-5}%
SVOM-ECLAIRs	0.004 - 0.250	1.792(*)	0.16	$<$ 10 arcmin	3^{+1}_{-1}	69^{+10}_{-9}%	4^{+1}_{-1}	95^{+5}_{-4}%
SVOM-GRM	0.03 - 5	0.23(*)	0.16	$\sim$ 5 deg	9^{+4}_{-3}	59^{+6}_{-6}%	14^{+6}_{-4}	92^{+3}_{-3}%
THESEUS-XGIS	0.002 - 10	3×10^{-8}	0.16	$<$ 15 arcmin	10^{+5}_{-4}	63^{+13}_{-13}%	15^{+6}_{-4}	94^{+6}_{-7}%
HERMES	0.05 - 0.3	0.2(*)	1.0	1 deg	84^{+42}_{-30}	61^{+10}_{-11}%	139^{+54}_{-36}	94^{+6}_{-6}%
TAP-GTM	0.01 - 1	1(*)	1.0	20 deg	60^{+24}_{-24}	67^{+13}_{-14}%	84^{+30}_{-24}	95^{+5}_{-6}%

(^{a}) The value indicates the 50% percentile of the localisation error of the fourth *Fermi*-GBM catalog (von Kienlin et al., 2020). 90% of the GRBs detected by Fermi have a localisation error below 15 deg.
(*) expressed in ph cm^{-2} s^{-1}.

TABLE 6.3: Number of joint GW+γ-ray detections for different combinations of γ-ray instruments. Columns 5 and 7 give the number of joint GW+γ-rays detections during one year of observation with ET alone, and the network of ET+CE, respectively. Column 6 and 8 give N_{JD}/N_γ, the fraction of γ-ray detections which have also a GW counterpart for ET and ET+CE, respectively. The jet structure *Stru1* is assumed.

Satellites (HERMES, Fiore et al. 2020). The first three are currently operating missions; *Swift* and *Fermi* have been observing for more than 10 years, and GECAM was launched in 2020. SVOM is expected to be launched in 2023. Nominally they are not expected to be operative in mid '30s and '40s when ET and CE will start observations, but we take them as reference instruments. THESEUS, TAP, and HERMES are mission concepts. The HERMES-Pathfinder project consisting in the deployment of six cube-satellites is expected to be operative in the next few years (Fiore et al., 2021). In this work we consider the final HERMES as a full constellation of cube-satellites. In order to establish whether the prompt emission is detected, we compute the peak flux during 1 second exposure and we compare this value with the detection threshold of the instrument.

The results relative to one year of joint GW+γ-ray detections are reported in Tabs. 6.3 and 6.4 for *Stru1* and *Stru2*, respectively, where we considered ET and ET+CE as GW networks. The uncertainty intervals are computed simulating 1000 years of observations and for each year the prompt emission parameters are randomly extracted from the Monte Carlo posterior distribution. In the computation of the absolute numbers, we took into account the FOV of each instrument, assuming that the probability of

INSTRUMENT	band MeV	$F_{\rm lim}$ erg cm^{-2} s^{-1}	FOV/4π	loc. acc.	Joint ET +γ-ray	N_{JD}/N_γ	Joint (ET+CE) +γ-ray	N_{JD}/N_γ
Fermi-GBM	0.01 - 25	0.5(*)	0.75	5 deg (^{a})	36^{+14}_{-14}	70^{+16}_{-14}%	47^{+18}_{-14}	95^{+5}_{-7}%
Swift-BAT	0.015 - 0.15	2×10^{-8}	0.11	1-3 arcmin	9^{+6}_{-3}	64^{+11}_{-13}%	14^{+7}_{-4}	94^{+6}_{-7}%
GECAM	0.006 - 5	2×10^{-8}	1.0	1 deg	163^{+175}_{-60}	60^{+7}_{-8}%	253^{+271}_{-96}	92^{+3}_{-4}%
SVOM-ECLAIRs	0.004 - 0.250	1.792(*)	0.16	<10 arcmin	3^{+1}_{-1}	71^{+15}_{-10}%	4^{+1}_{-1}	95^{+5}_{-4}%
SVOM-GRM	0.03 - 5	0.23(*)	0.16	~5 deg	11^{+6}_{-4}	60^{+13}_{-6}%	15^{+10}_{-5}	92^{+3}_{-3}%
THESEUS-XGIS	0.002 - 10	3×10^{-8}	0.16	<15 arcmin	11^{+7}_{-4}	66^{+12}_{-16}%	16^{+7}_{-5}	94^{+6}_{-7}%
HERMES	0.05 - 0.3	0.2(*)	1.0	1 deg	96^{+60}_{-31}	64^{+12}_{-12}%	151^{+66}_{-48}	94^{+4}_{-6}%
TAP-GTM	0.01 - 1	1(*)	1.0	20 deg	66^{+24}_{-24}	69^{+15}_{-14}%	90^{+30}_{-24}	95^{+5}_{-7}%

TABLE 6.4: As in Tab. 6.3, assuming the jet structure *Stru2*.

detection is FOV/4π, which implicitly assumes an optimistic duty cycle of 100%. In the case of *Fermi*-GBM, *Swift*-BAT and SVOM, we adopt a more realistic value of sky-averaged FOV, which takes into account Sun and Moon occultations (Burns et al., 2016). In the case of THESEUS-XGIS the FOV we assumed ($\sim$ 2 sr) is relative to the energy band 2-150 keV. Since the FOV in the energy band above 150 keV is 2π sr, the reported number of joint detections is a conservative estimate. Our results show that, already with ET alone, $\sim 60-70$% of all the SGRBs will have a detectable GW counterpart, and this fraction approaches 100% if we consider ET operating with CE. The less steep structure profile of *Stru2* increases the number of joint detections for the majority of the satellites.
Depending on the properties of each satellite, Tabs. 6.3 and 6.4 show instruments giving a few tens of detections per year and other hundreds of detections per year. While instruments such as GECAM are optimal for statistical studies by giving a large number of detections, instruments with a smaller number of detections but able to localise the source, such as THESEUS-XGIS, are crucial for science cases requiring the identification of the host galaxy, the knowledge of the source redshift, and the complete multiwavelength characterisation of the source emission. Furthermore, the sensitivity of the instruments considered for the detection of the prompt emission maximises in different energy bands. While instruments such as GECAM are appropriate for detecting GRBs with a harder spectrum, GRBs less energetic (intrinsically or because viewed off-axis) will peak at lower energies (soft/hard X-rays) and for them instruments such as XGIS are more suitable. The presence of multiple instruments will be extremely valuable to cover the entire energy range typical of the prompt emission of short GRBs.

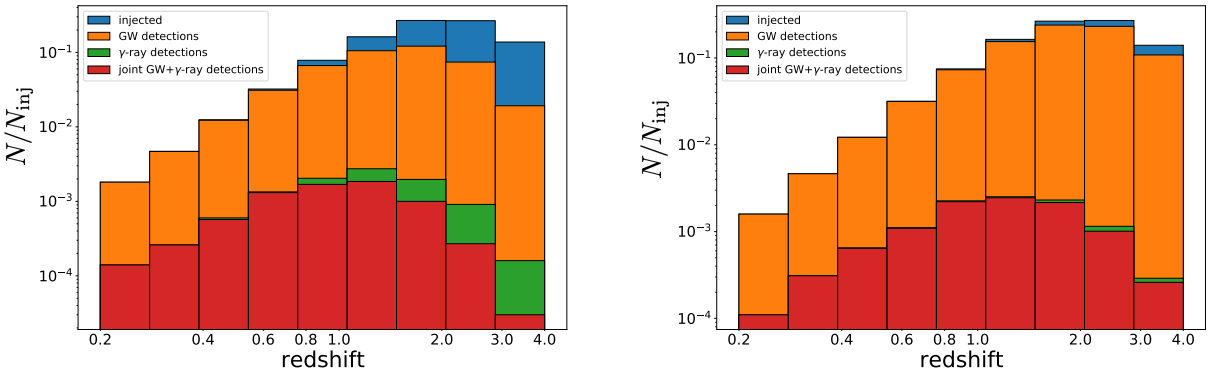

(a) (b)

FIGURE 6.4: In panel (a) we show the histogram of the joint ET+*Fermi*-GBM detections (red), together with the distribution of injected BNS (blue), the mergers detected by ET (orange), the mergers detected by *Fermi*-GBM (green). The histogram is normalised to $N_{inj} = 10^5$, which is the number of injected BNS mergers in the angle range $0^\circ < \theta_v < 15^\circ$ and in the redshift range $0 < z < 4$. The same histogram is shown for ET+CE in panel (b). For visualisation purposes, the fraction of BNS producing a jet, f_j, has been assumed to be one.

Figs. 6.4a and 6.4b show the distribution in redshift of the joint detections, in the specific case of *Fermi*-GBM in synergy with ET and ET+CE, respectively. These figures are produced injecting 10^5 BNS mergers (extracted from the BNS population, and thus following the astrophysical merger rate evolution with z), with the viewing angle uniformly distributed in the range $0^\circ - 15^\circ$. Even if we distribute the injections over a wider range of angles, the number of joint detections (given as fraction of γ-ray detections having an associated GW counterpart) does not change, since, while there are GW sources detectable at $\theta_v > 15^\circ$, there are no γ-ray detections for $\theta_v > 15^\circ$ (see Fig 6.5 and Fig 6.6). For better visibility, Figs. 6.4a and 6.4b are produced fixing $f_j = 1$. The value of f_j shifts the green and red histograms vertically but does not change their relative ratio. In the case of ET alone, the GW detector is so sensitive that up to $z \simeq 0.8 - 1.0$ the probability that a SGRB has a detectable GW counterpart is close to 100%. Adding CE to the network, the GW detection efficiency remains close to 100% for redshifts above the BNS merger peak. In this section we do not include the results for ET+2CE, since the addition of another CE would not further increase the joint detection efficiency in the redshift range accessible to γ-ray instruments for SGRBs.

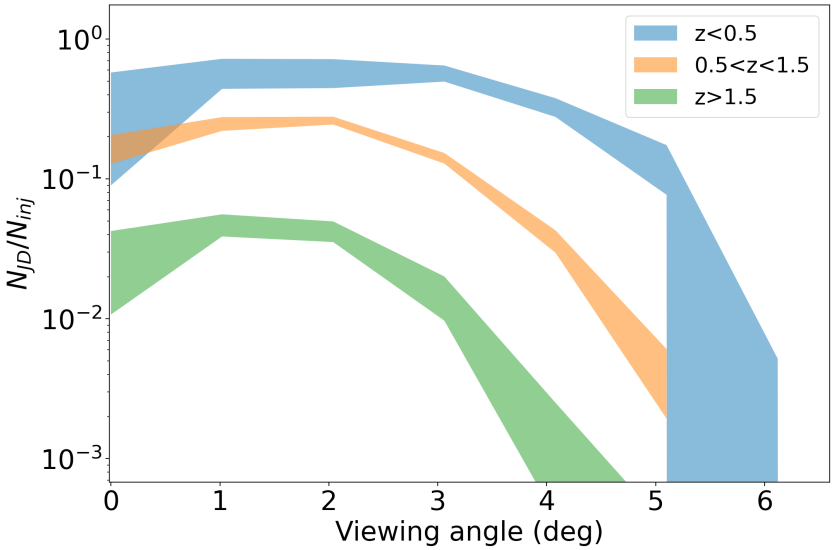

FIGURE 6.5: Angle dependency of the joint GW+γ-ray detections for three redshift bins, considering ET+*Fermi*-GBM. The bands are obtained with random realisations extracted from the MCMC posterior samples. For each redshift bin, the y-axis gives the number of joint detections normalised to 5×10^4 BNS injections with viewing angle $0^\circ < \theta_v < 15^\circ$. We assume that all BNS produce a jet ($f_j = 1$).

The γ-ray missions that are more suited to maximise the joint detection rates are those with large FOV and best sensitivity around MeV energies. However, another parameter to take into account is the localisation accuracy by the γ-ray detectors (given in Tables 6.3 and 6.4), which defines what are the instruments that are able to drive the follow-up observations by ground-based telescopes, crucial for obtaining the source redshift and to completely characterise the multiwavelength emission of the source.
Fig. 6.5 shows the distribution of the ET+γ-ray joint detections as a function of the viewing angle, assuming *Stru1*, for three redshift bins: $z < 0.5, 0.5 < z < 1.5, z > 1.5$. Fig. 6.6 shows the same, but assuming *Stru2*. Again, as example, we consider *Fermi*-GBM as γ-ray detector, but we obtain consistent results for the other γ-ray satellites considered in the present paper. On the y axis we report the ratio $N_{\rm JD}/N_{\rm inj}$ between the joint detections over the total injected BNS (assuming $f_j = 1$) per redshift bin and viewing angle bin. For the viewing angle we consider a linearly spaced grid, where the width of the single bin is $\theta_c/3$. The uncertainty bands are obtained with 15 random extractions of the prompt parameters and each realization considers 5×10^4 BNS injections with viewing angle $0^\circ < \theta_v < 15^\circ$. As before, a different assumed value of f_j just shifts the bands vertically. The

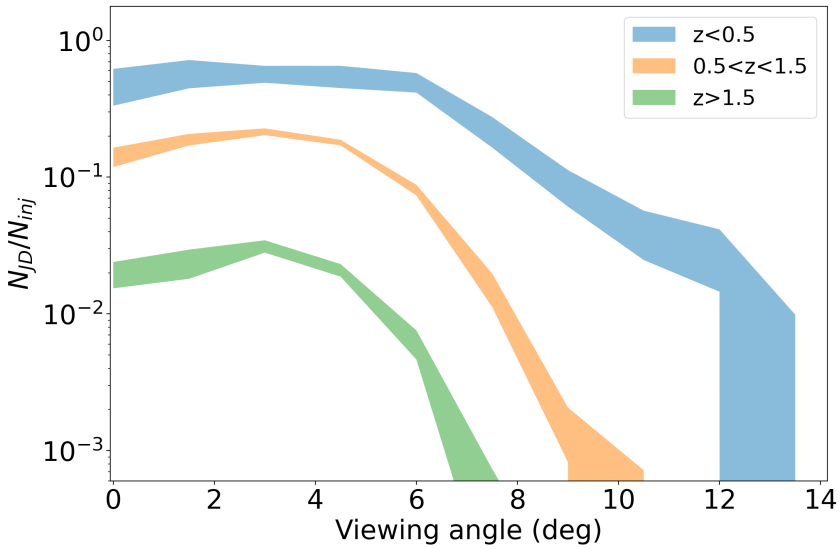

FIGURE 6.6: Same as Fig. 6.5, but for *Stru2*.

plot shows a mild decrease of the ratio $N_{\rm JD}/N_{\rm inj}$ for very small viewing angles ($\theta_v \lesssim \theta_c/3$). Such effect is due to the fact that SGRB viewed on-axis have very high values of peak energy, meaning that the bulk of the flux is above the *Fermi*-GBM band. Therefore, considering two identical SGRBs at the same redshift, the one viewed at $\theta_v \sim \theta_c$ appears slightly brighter than the one viewed at $\theta_v \sim 0$. Moreover, the number of sources per unit angle scales as $\sin(\theta_v)$, therefore the small decrease of $N_{\rm JD}/N_{\rm inj}$ around $\theta_v \sim 0$ is related to the paucity of sources contained in the first angle bin.

6.2.3 Joint detection of GWs and γ-rays from cocoon shock break-out

In the derivation of the joint GW+γ-ray detections, we have assumed that all the SGRBs share a common jet structure and that the γ-ray emission is given by the dissipation of the internal energy of the jet. However, for GRBs observed at large viewing angles, namely $\theta_v \gg \theta_c$, the γ-ray emission from the shock break-out (SBO) of the jet should be taken into consideration. Indeed, even if the formation and successful break-out of a relativistic jet through the post-merger ejecta is not guaranteed, the formation of a cocoon at very wide angles is commonly expected in the BNS mergers (Ramirez-Ruiz et al., 2002; Nakar and Piran, 2017b; Gottlieb et al., 2018e). The shocks driven by the mildly relativistic expansion of the cocoon can produce γ-ray

TABLE 6.5: Maximum luminosity distance $D_{\rm L,max}$ and number of joint GW+γ-ray detections of a SBO with the same properties of the γ-ray flash observed in coincidence with GW 170817.

instrument	$D_{\rm L,max}$ (Mpc)	$N_{\rm det}$
Fermi-GBM	76.4	< 1
Swift-BAT	123	3
GECAM	210	12
THESEUS-XGIS	114	2
HERMES	121	3
TAP-GTM	80	1

emission which is potentially detectable at least in the local Universe. Moreover, several studies found a remarkable agreement among the properties of the gamma-ray emission of GW 170817 and the shock-breakout model (Kasliwal et al., 2017; Gottlieb et al., 2018c; Nakar et al., 2018; Bromberg et al., 2018; Pozanenko et al., 2018). The γ-ray emission detected is not emitted by the wings of a structured jet, but rather by the shock breakout of the cocoon produced by the interaction of the jet with the NS merger ejecta (Gottlieb et al., 2018c; Bromberg et al., 2018).
In order to investigate this scenario, as a reference, we take the spectrum (cut-off power law with photon index $\alpha = 0.62 \pm 0.40$ and cut-off energy $E_c = 185 \pm 62$ keV) and the *Fermi*-GBM peak flux ($(3.1 \pm 0.7) \times 10^{-7}$ erg cm^{-2} s^{-1}) of the γ-ray flash associated to GW 170817 (Goldstein et al., 2017b) and we compute the maximum distance $D_{\rm L,max}$ at which this emission can be detected by the γ-ray instruments considered in the present work. In a first order approximation, the SBO emission can be considered isotropic, therefore we do not include any angle dependency in our treatment. In order to evaluate the number of γ-ray detections associated to SBO, we compute the number of BNS at a luminosity distance $D_L < D_{\rm L,max}$. In our derivation, we assume that each BNS produces a SBO. Since the detection efficiency of any 3G GW detector is $\sim$ 100% for distances $D_L < D_{\rm L,max}$, the number of γ-ray detections per year that we report corresponds also to the number of joint GW+γ-ray detections associated to SBO from BNS mergers. The results are reported in Tab. 6.5.

	ET	ET+CE	ET+2CE
$N_{\rm det}$	12970	23600	25668
$N_{\rm det}(\Delta\Omega < 1\ {\rm deg}^2)$	0	20	636
$N_{\rm det}(\Delta\Omega < 10\ {\rm deg}^2)$	2	845	13673
$N_{\rm det}(\Delta\Omega < 100\ {\rm deg}^2)$	69	17049	23935
$N_{\rm det}(\Delta\Omega < 1000\ {\rm deg}^2)$	526	21564	25367

TABLE 6.6: Number of GW detections per year with sky localisation better than 1, 10, 100, and 1000 deg^2. The reported numbers are relative to BNS mergers with $\theta_v < 15^\circ$. The numbers of GW detections per year are obtained assuming a duty cycle of 0.85 as described in the text.

6.2.4 Joint detection of GWs and X-ray emission

In this section, we evaluate the detectability of the afterglow emission with future X-ray telescopes. Specifically, we show the expected rate of BNS mergers which will have both a detectable GW signal and an X-ray emission associated to the afterglow phase of the SGRB. For the X-ray emission, we consider two components: 1) the standard forward shock (FS) emission, 2) the HLE associated to the last photons emitted during the prompt phase. Under the assumption of a structured jet, the HLE produces an X-ray flux which can be comparable or even dominant with respect to the FS emission (Oganesyan et al., 2020a; Panaitescu, 2020). We evaluate the joint X-ray and GW detections considering satellites in survey mode as well as satellites pointing to the GW source. For the pointing strategy, we use the localisation capabilities of ET alone and in the network of 3G observatories. Since the number of sources suitable for pointing observations result to be high (especially for network of 3G detectors), we also evaluate other source parameters estimated from the GW signals, such as viewing angle and distance, which can be used to down-select sources to be observed.

Wide-FOV X-ray telescopes: survey and pointing observations

For the detection of the afterglow emission from our SGRBs population, we consider the following X-ray instruments: the Einstein Probe (EP, Yuan et al. 2018) which is scheduled for launch by the end of 2022, the ECLAIRs instrument on board of SVOM (Cordier et al., 2015) which is scheduled for launch in 2023, and three mission concepts, THESEUS (Amati et al. 2018;

BOX 6.3: GW SKY LOCALISATION

Here we summarise the results about the GW sky localisation, relative to our BNS population. Fig. 6.8 shows the sky localisation of ET, ET+CE and ET+2CE. The figures show the error on sky position, expressed in $\deg^2$, as a function of redshift for one year of BNS injections. The injections are extracted from the BNS population described in Sect. 6.2.1, thus following the same redshift evolution of the merger rate. We show the sky localisation both for sources with $0 < \theta_v < 15^\circ$ and for sources with all the orientations. We chose θ_v maximum equal to 15° as it is consistent with the largest viewing angle up to which the X-ray emission from a *Stru1* jet is observable by the analysed WFX-ray satellites (see Fig. 6.12). For the combination ET+CE (ET+2CE), a considerable fraction of sources detected at $z < 1$ ($z < 3$) has a sky localisation smaller than 10 $\deg^2$, which is small enough to enable prompt and efficient multiwavelength search for EM counterparts.

In Tab. 6.6 and 6.7 we summarize the sky localisation capabilities of ET, ET+CE and ET+2CE for systems observed with $\theta_v < 15^\circ$ and for systems observed at all angles, respectively. The tables list the number of detections per year with sky localisation uncertainty $\Delta\Omega < 1, 10, 100, 1000$ $\deg^2$. Fig. 6.10 shows the redshift distribution of $\Delta\Omega$ as scatter plot with a color code indicating the S/N for ET, ET+CE and ET+2CE, considering cases with $\theta_v < 15^\circ$ and cases with no selection on θ_v.

Fig. 6.7 shows the cumulative distribution of the S/N for BNS detected with ET, ET+CE and ET+2CE with a sky uncertainty $\Delta\Omega < 100$ $\deg^2$, for $\theta_v < 15^\circ$ (panel a) and without selection on θ_v (panel b). The S/N distribution shows that, even adopting a larger S/N threshold, for instance S/N> 12, the number of sources with $8 <$ S/N < 12 is negligible and therefore not relevant for the evaluation of the joint GW+X-ray detection rate at least for well localised sources.

Amati et al. 2021), the Wide Field Imager on board of TAP (Camp et al. 2019), and the *Gamow Explorer* (White et al., 2021). The launch date of this last is expected to be in 2028-2032.
If the instrument operates in survey mode, the probability of detecting the source (if the flux is above the sensitivity limit) is given by $\sim$FOV$/4\pi$. Instead, if the instrument operates only in pointing mode, the light curve is monitored only after a time $t_{\rm resp}$ from the trigger time, which is the sum of the time to respond to a trigger from ground and the time to repoint the instrument. In order to evaluate how each instrument will sample the afterglow temporal evolution, we use the sensitivity curve (the sensitivity curve of EP is taken here[9], while for all the other X-ray missions, we use the sensitivity curves reported in the references cited at the beginning of this section), which relates the minimum detectable flux as a function of

[9] https://sci.esa.int/documents/34375/36249/1567258027270-ESA-CAS-workshop1_20140225_7__Einstein_Probe-exploring_the_dynamic_X-ray_Universe__Yuan.pdf

TABLE 6.7: Same as Tab. 6.6, but without any selection on θ_v.

	ET	ET+CE	ET+2CE
$N_{\rm det}$	143970	458801	592565
$N_{\rm det}(\Delta\Omega < 1\ {\rm deg}^2)$	2	184	5009
$N_{\rm det}(\Delta\Omega < 10\ {\rm deg}^2)$	10	6797	154167
$N_{\rm det}(\Delta\Omega < 100\ {\rm deg}^2)$	370	192468	493819
$N_{\rm det}(\Delta\Omega < 1000\ {\rm deg}^2)$	2791	428484	585317

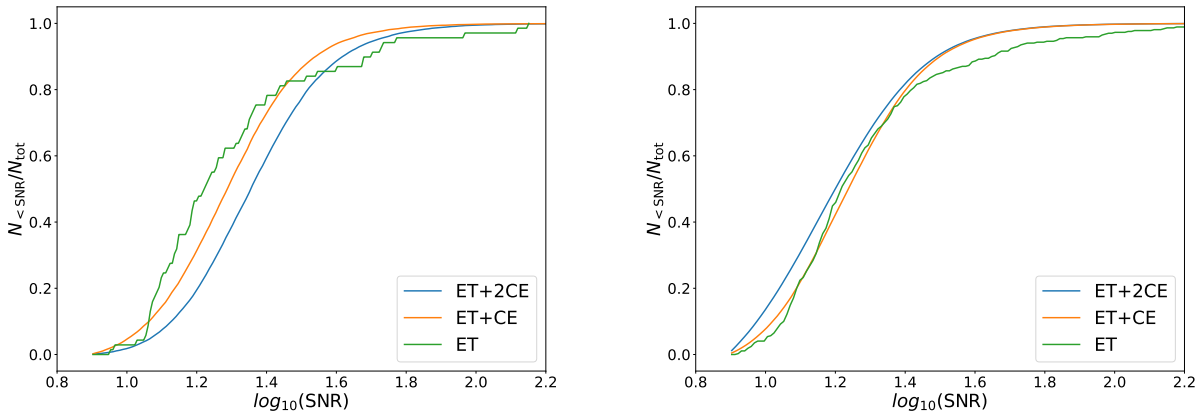

(a) (b)

FIGURE 6.7: Cumulative distribution of the S/N for BNS mergers localized better than 100 deg^2 for the three GW networks considered in this work. Panel (a) shows cases with $\theta_v < 15°$, while in panel (b) all angles are considered.

the exposure time. The temporal sampling is computed using an iterative approach. Starting from the beginning of the light curve, we determine the length ΔT of each bin at time t_i such that

$$\frac{1}{\Delta T}\int_{t_i}^{t_i+\Delta T} F(t)dt > F_{\rm lim}(\Delta T), \tag{6.11}$$

where $F_{\rm lim}(\Delta T)$ is derived from the sensitivity curve. The afterglow light curve is classified as undetectable if, even increasing ΔT, the eq. 6.11 is never satisfied. For *Gamow*, THESEUS and EP we consider sensitivity curves including a median Galactic absorption $N_H = 5 \times 10^{20}{\rm cm}^{-2}$. For

BOX 6.4: VIEWING ANGLE AND LUMINOSITY DISTANCE FROM GWS

Here, we explore how the GW observations can give constraints about the viewing angle with respect to the axis perpendicular to the BNS orbital plane (assumed to be parallel to the jet axis) and the luminosity distance of the system. Fig. 6.9 shows how the detected sources are distributed in the plane $\Delta\theta_v - \theta_v$, considering ET, ET+CE and ET+2CE. $\Delta\theta_v$ is the 1σ error on the viewing angle. Only sources at $z < 1$ and with $\Delta\theta_v < 40$ deg are shown. For all the networks, a considerable fraction of sources have $\Delta\theta_v/\theta_v < 0.1$. Moreover, since the gradient of the GW amplitude is maximum at $\theta_v = 90$ deg, the θ_v parameter is better constrained when the source is seen edge-on. This result is particularly important to prioritise the BNS events to be followed-up. Indeed, in the era of 3G GW detectors we expect hundreds of BNS detections per day. Due to the limited observational time at each observatory, with a pointing strategy only a limited fraction of GW-detected signals can be followed up. For example, aiming at detecting the high-energy emission, one can exclude all the sources edge-on for which the viewing angle estimate is more precise from the GW parameter estimation.

Fig. 6.11 shows the distribution in redshift of $\Delta D_L/D_L$, where ΔD_L is 1σ error on the luminosity distance D_L. We consider ET, ET+CE and ET+2CE. Only sources with $\Delta D_L/D_L < 1$ are shown. For ET operating alone the relative error can be below 10% only for sources with $z \lesssim 0.2$, while for ET+CE and ET+2CE the same is true for $z \lesssim 1.5$ and $z \lesssim 3$, respectively. The plots also show that the constraint on distance is tighter for sources seen edge on. This is due to the strong degeneracy between luminosity distance and viewing angle and therefore the error on the first is significantly reduced when the second is well constrained.

TAP the published sensitivity curve does not include this information.

For all the results reported in this section, we simulate 25 realizations of one year of BNS mergers, each with parameters extracted randomly from the MCMC posterior distributions. For each realization we consider a number of injections $N_{\rm inj} = \min(N_{\rm req}, 10^4)$, where $N_{\rm req}$ is the number of BNS in one year that satisfy the selection criteria (e.g., about S/N, θ_v and $\Delta\Omega$). The choice $N_{\rm inj} = \min(N_{\rm req}, 10^4)$ is made in order to have enough statistics and such that the full parameter space is correctly covered. Then the number of detections correspondent to one year is obtained re-scaling by the factor $N_{\rm req}/N_{\rm inj}$. The parameters of the prompt model influence the afterglow light curve because both the FS and HLE brightness depend on the $E_{\rm iso}$ which is predicted by our model. First we evaluate the expected rate of joint GW+X-ray detections, considering the telescopes operating in survey mode. The results are reported in Tab. 6.10. Due to the good sensitivity down to 2 keV and the large FOV, THESEUS-XGIS can contribute substantially to the total amount of X-ray detections. Thanks to the larger FOV (1.1 sr) and the better sensitivity, EP gives a larger number

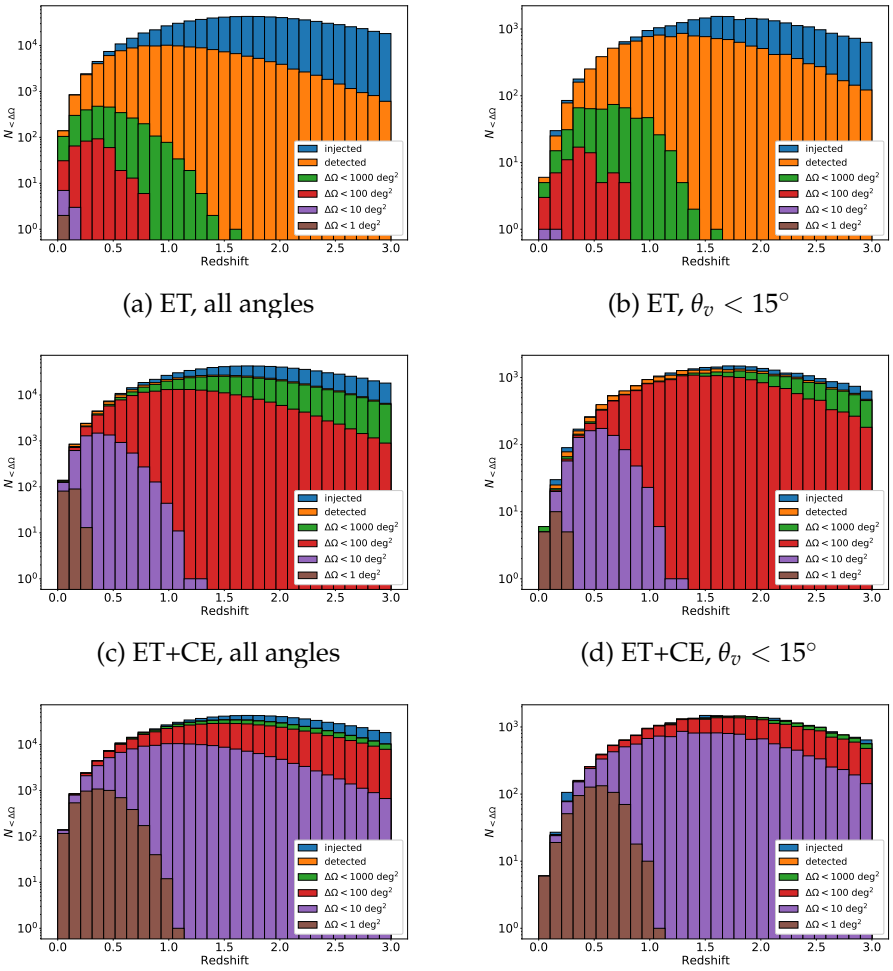

(a) ET, all angles

(b) ET, $\theta_v < 15°$

(c) ET+CE, all angles

(d) ET+CE, $\theta_v < 15°$

(e) ET+2CE, all angles

(f) ET+2CE, $\theta_v < 15°$

FIGURE 6.8: Redshift distribution of the sky-localisation uncertainty (given as 90% credible region) for three detector configurations: ET, ET+CE and ET+2CE. The absolute numbers are relative to one year of observation and assuming a duty cycle of 0.85 as described in the text. Plots on the right show BNS systems with a viewing angle $0 < \theta_v < 15°$.

of detections compared to THESEUS-SXI and TAP.

The probability of detection can be increased considering the possibility to point GW sources localised with enough precision through the GW signal. In such case, wide field X-ray (WFX-ray) telescopes can point to the sky error box and start the search of the X-ray counterpart. We explore this

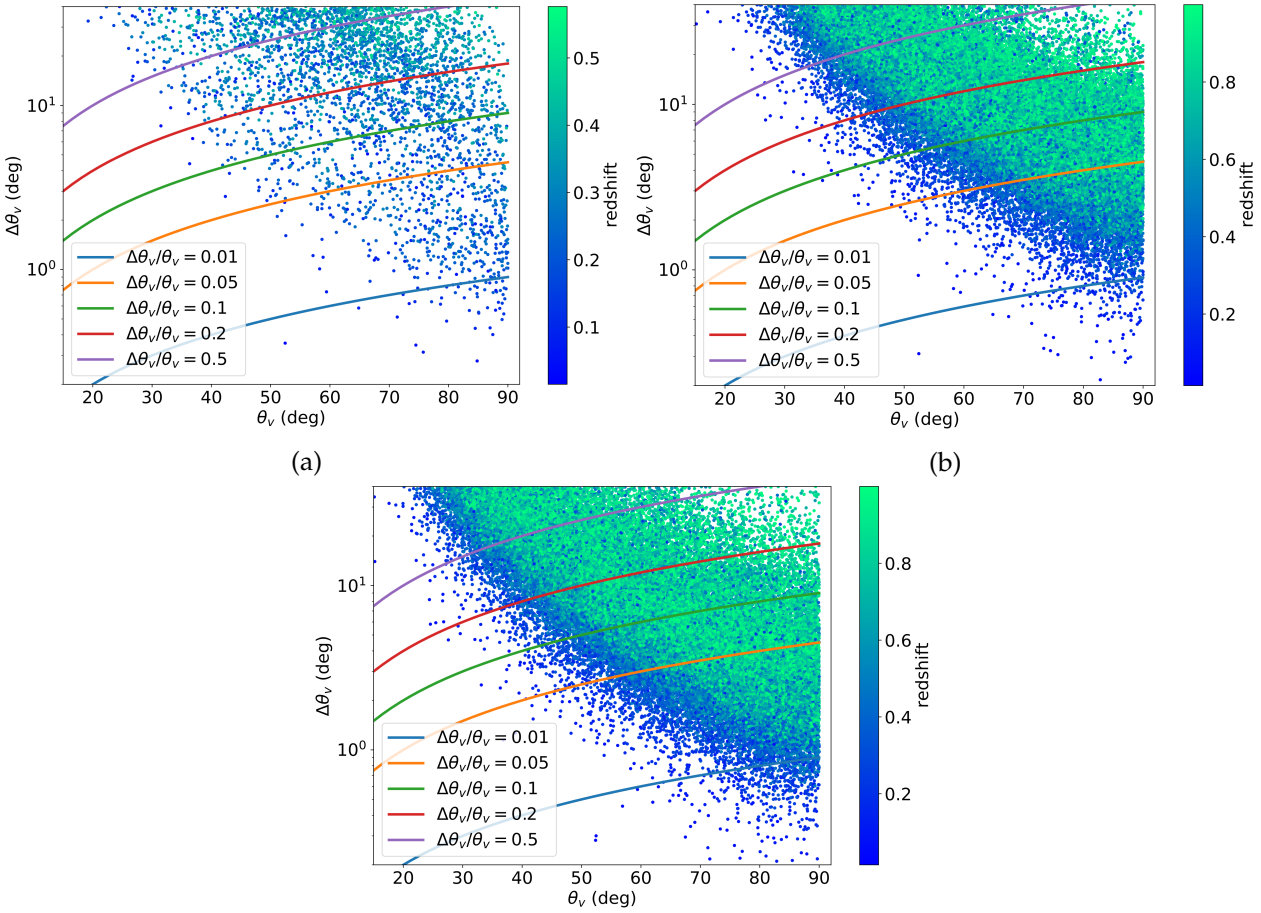

FIGURE 6.9: Distribution of $\Delta\theta_v$ vs θ_v relative to one year of observation, in the case of ET (a), ET+CE (b) and ET+2CE (c). The color bar indicates the redshift. We report only BNS mergers detected at $z < 1$ and with a $\Delta\theta_v < 40^\circ$. A duty cycle of 0.85 has been assumed for the GW detectors as described in the text.

scenario simulating one year of BNS mergers and selecting only those that are detected with an error on sky position better than 100 deg^2. The typical FOV of WFX-ray telescopes is larger than 1 sr, so an error region of 100 deg^2 can be well contained inside the FOV of the instrument. A sky region of 100 deg^2 is around 1/10 of a typical FOV of a WFX-ray telescope. If, instead, we select sources localised better than 1000 deg^2 and considering that the bulk of sources detectable in the X-rays are at $z \lesssim 1$, we expect, with respect to the cases with $\Delta\Omega < 100$ deg^2: 1) a factor ~ 10 more joint GW+X-ray detections with ET; 2) no substantial variation for ET+CE, since sources with

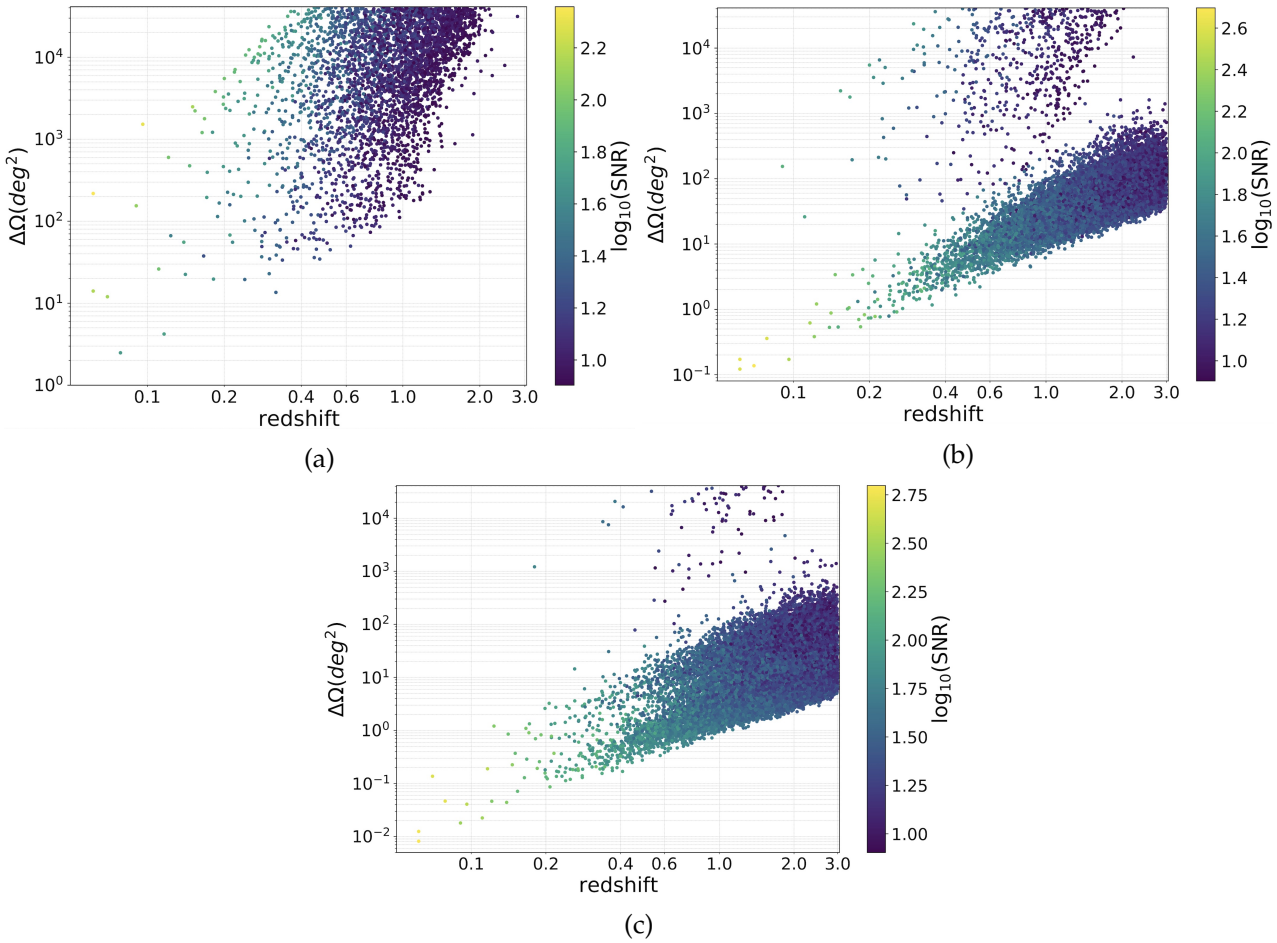

FIGURE 6.10: Sky localization (90% credible region in deg^2) as a function of the redshift for one year of BNS injections with viewing angle in the range $0^\circ < \theta_v < 15^\circ$ and considering ET (a), ET+CE (b) and ET+2CE (c). The color bar indicates the S/N of each detection. A duty cycle of 0.85 has been assumed for the GW detectors as described in the text.

100 deg^2 $< \Delta\Omega <$ 1000 deg^2 are located at $z \gtrsim 1$; 3) no substantial variation for ET+2CE, since $N(\Delta\Omega < 100 \text{ deg}^2) \sim N(\Delta\Omega < 1000 \text{ deg}^2)$ for $z \lesssim 1$.

For the selected sub-sample of well localised sources, we predict the X-ray emission and we check if it is detectable with the telescopes listed before. The numbers of THESEUS-SXI and *Gamow* are identical since we consider for them the same sensitivity, and the slightly different FOV does not influence pointing observations. In Tab. 6.11 we show the number of expected joint GW+X-ray detections for one year of observation with ET, ET+CE and ET+2CE. We consider the configuration *FS-SGRB* for the FS

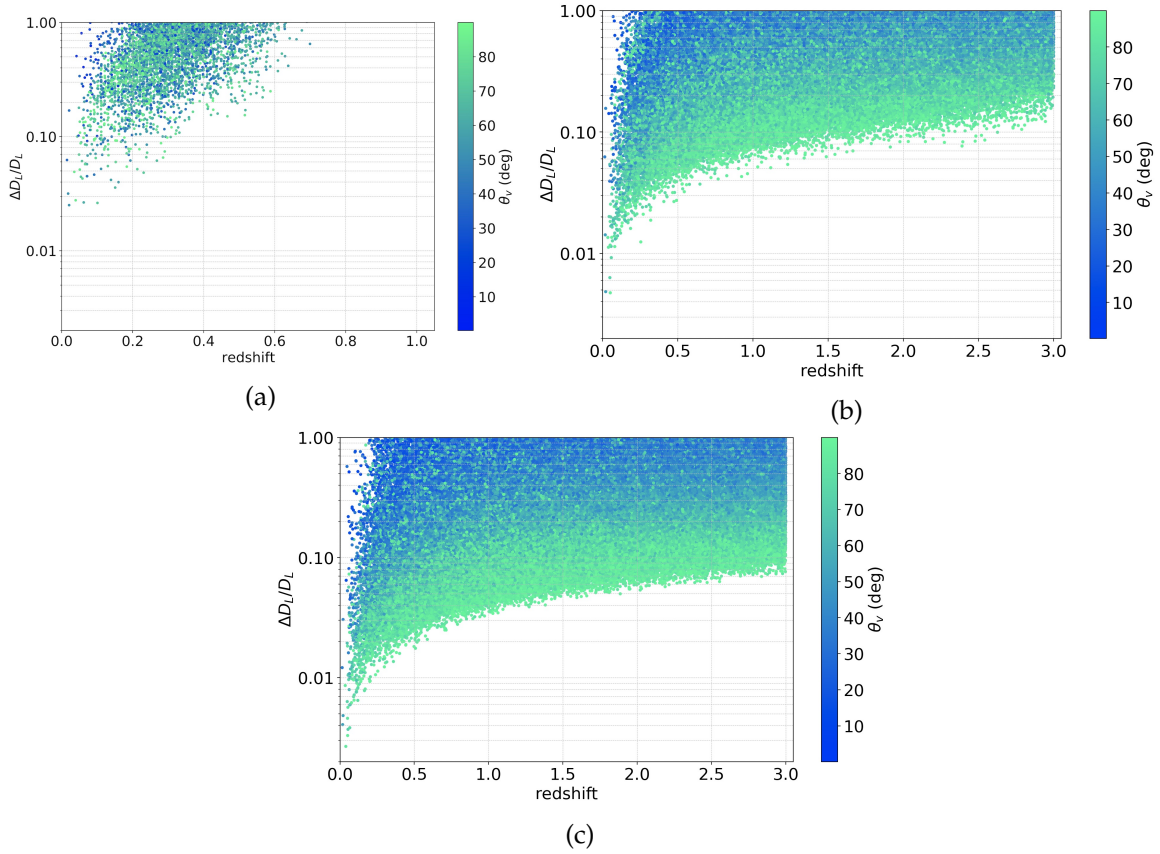

FIGURE 6.11: Distribution of the relative error on the luminosity distance D_L as a function of redshift relative to one year of observation, in the case of ET (a), ET+CE (b) and ET+2CE (c). The color bar indicates the viewing angle. Only cases with $\Delta D_L/D_L < 1$ and at $z < 3$ are shown. A duty cycle of 0.85 has been assumed for the GW detectors as described in the text.

parameters and we assume that the X-ray telescopes are able to point toward the sky position provided by GW detectors within 100 s from the BNS merger. A response time of 100 s is a short amount of time to communicate the trigger from the ground to the satellites, but the possibility of accessing lower frequencies by the next generation GW detectors will make it possible pre-merger alerts. We evaluated that, in the case of ET, a fraction of $\sim$30% and $\sim$60% of sources localised better than 100 deg^2 at the merger are above the detection threshold (S/N=8) and with a sky-localisation better than 1000 deg^2, which is well within the FOV of the satellites analysed here, 20 and 10 minutes before the merger, respectively (see tab. 6.8). For ET+CE (ET+2CE) this fraction is $\sim$5% (6%) 10 minutes before the merger, leaving

	$N_{\Delta\Omega<1000\,\mathrm{deg}^2,t_{\mathrm{pre}}}/N_{\Delta\Omega<100\,\mathrm{deg}^2,t_{\mathrm{merger}}}$			
	S/N> 8		S/N> 7	
t_{pre}	10 min	20 min	10 min	20 min
ET	63%	29%	68%	37%
ET+CE	5%	0.5%	5%	0.7%
ET+2CE	6%	0.5%	6%	0.6%

TABLE 6.8: Pre-merger sky localization. We show the fraction $N_{\Delta\Omega<1000\,\mathrm{deg}^2,t_{\mathrm{pre}}}/N_{\Delta\Omega<100\,\mathrm{deg}^2,t_{\mathrm{merger}}}$ of BNS localized better than 100 deg^2 at the merger that are localized better than 1000 deg^2 at a pre-merger time t_{pre}, for ET, ET+CE and ET+2CE. We show both cases that are detected with S/N> 8 and S/N> 7 at the pre-merger time. We consider only BNS observed at a viewing angle $\theta_v < 15^\circ$.

	FOV (sr)	loc. accuracy (arcmin)
Einstein Probe	1.1	5
Gamow	0.4	1-2
THESEUS-SXI	0.5	1-2
TAP-WFI	0.4	1

TABLE 6.9: Field of view and localisation accuracy of the WFX-ray telescopes considered in this work.

the absolute number of triggers to be followed up of order of several hundreds. The typical exposure time for detection in X-rays is $t_{\mathrm{exp}} = 66^{+249}_{-42}$ s for SXI and *Gamow*, $t_{\mathrm{exp}} = 96^{+219}_{-29}$ s for TAP, $t_{\mathrm{exp}} = 239^{+171}_{-173}$ s for EP, where the uncertainties are reported at 1σ level of confidence and they are computed considering a random sampling of the MCMC posterior distribution.

Considering ET alone and FS configuration (*FS-SGRB*), Tab. 6.10 and 6.11 show that the survey mode is more promising than the pointing mode in terms of number of GW+X-ray detections per year. For ET+CE and ET+2CE, due to the larger number of well localised sources, the number of joint detections is considerably larger than the survey mode case. Hence, the exploitation of sky localisation provided by GW detectors can enhance

	ET	ET+2CE
SVOM-ECLAIRs	4 ± 2	5 ± 2
Einstein Probe	50^{+15}_{-16}	64^{+12}_{-20}
Gamow	9^{+2}_{-2}	10^{+3}_{-3}
THESEUS-SXI	11^{+3}_{-3}	13^{+4}_{-3}
THESEUS-(SXI+XGIS)	23^{+6}_{-5}	27^{+7}_{-5}
TAP-WFI	16^{+3}_{-4}	17^{+6}_{-3}

TABLE 6.10: Expected number of joint GW+X-ray detections in survey mode. The numbers are relative to one year of observations, for different X-ray instruments operating in survey mode. The assumed structure is *Stru1* and the FS configuration is *FS-SGRB*.

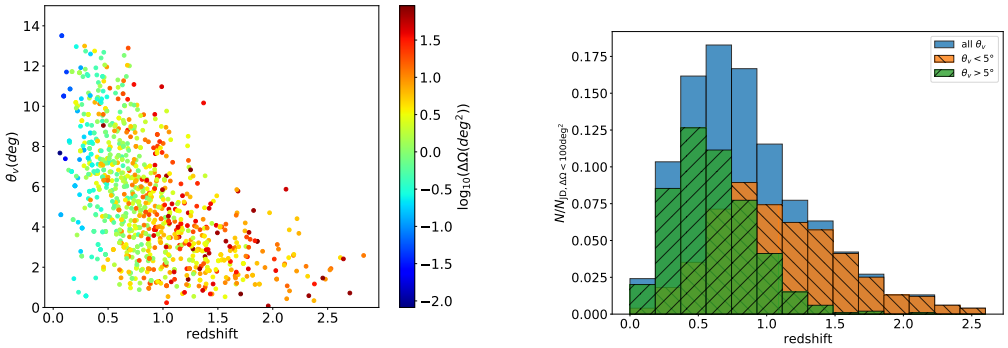

(a) (b)

FIGURE 6.12: Redshift distribution of the joint GW+X-ray detections. Panel (a) shows the distribution of the viewing angle as a function of redshift for a sample of 1000 joint GW+X-ray detections, considering ET+2CE and SXI and under the assumption *Stru1*. Only BNS detections with GW sky localisation $\Delta\Omega < 100$ deg^2 are selected. The assumed jet core angle is $\theta_c = 3.4$ deg. The color bar indicates the GW sky localisation uncertainty of each detection. Panel (b) shows the distribution in redshift of the same sample, where we distinguish between detections with $\theta_v < 5^\circ$ and $\theta_v > 5^\circ$. The histogram is normalised to the number of total joint detections with $\Delta\Omega < 100$ deg^2.

substantially the probability of identifying the EM counterpart of BNS mergers. We point out that the reported numbers for pointing mode do not take into account the duty factor of the instruments, which is assumed

	ET	ET+CE	ET+2CE
Einstein Probe	9^{+5}_{-3}	294^{+80}_{-59}	359^{+168}_{-110}
THESEUS-SXI/ *Gamow*	7^{+5}_{-3}	95^{+43}_{-14}	122^{+41}_{-23}
TAP-WFI	8^{+5}_{-3}	182^{+43}_{-31}	225^{+76}_{-72}

TABLE 6.11: Expected number of joint GW+X-ray detections in pointing mode. The numbers are relative to one year of observations, for different X-ray instruments operating in pointing mode. We consider BNS mergers with sky-localisation uncertainty $\Delta\Omega < 100$ deg^2 and with a detectable X-ray emission, assuming a $t_{\rm resp} = 100$ s. The assumed structure is *Stru1* and the FS configuration is *FS-SGRB*.

	100 s	1 hr	4 hr
Einstein Probe	359^{+168}_{-110}	48^{+24}_{-15}	17^{+15}_{-10}
THESEUS-SXI/ *Gamow*	122^{+41}_{-23}	12 ± 7	< 9
TAP-WFI	225^{+76}_{-72}	50^{+20}_{-10}	17^{+10}_{-5}

TABLE 6.12: As in Tab. 6.11, but considering different delay times between the merger and the beginning of X-ray observation. In this table, we consider ET+2CE as GW network.

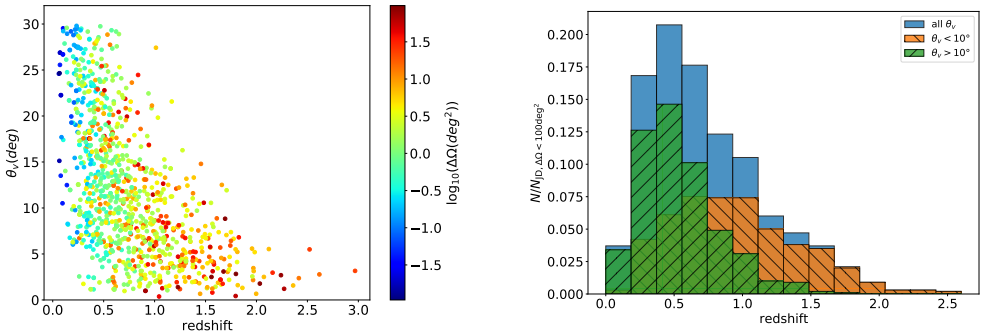

(a) (b)

FIGURE 6.13: Same as in Fig. 6.12, but for *Stru2*.

	HLE +FS-SGRB	FS-SGRB	HLE +FS-GW17
Einstein Probe	359^{+168}_{-110}	344^{+106}_{-95}	67^{+14}_{-17}
THESEUS-SXI/ *Gamow*	122^{+41}_{-23}	98^{+34}_{-31}	22^{+7}_{-6}
TAP-WFI	225^{+76}_{-72}	174^{+94}_{-27}	33^{+12}_{-8}

TABLE 6.13: As in Tab. 6.11, but considering different assumptions for the computation of the X-ray light curve. In this table we consider ET+2CE as GW network and $t_{\rm resp} = 100$ s.

	Stru1	*Stru2*
Einstein Probe	359^{+168}_{-110}	383^{+131}_{-112}
THESEUS-SXI/ *Gamow*	122^{+41}_{-23}	128^{+73}_{-61}
TAP-WFI	225^{+76}_{-72}	219^{+128}_{-73}

TABLE 6.14: Comparison between *Stru1* and *Stru2* for the prediction of joint GW+X-ray detections in pointing mode, considering ET+2CE. Both HLE and FS are included. The FS configuration is *FS-SGRB* and we assume $t_{\rm resp} = 100$ s.

to be 100%. Moreover, each X-ray mission, depending on the scientific objectives, can dedicate only a limited amount of time for the follow-up of GW triggers. Therefore, if we call $\epsilon_{\rm GW}$ the fraction of observational time dedicated to GW follow-up and $\epsilon_{\rm DC}$ the duty cycle, a more realistic estimate of the number of joint detections would be $N_{\rm JD,real} = \epsilon_{\rm GW}\epsilon_{\rm DC}N_{\rm JD}$, where $N_{\rm JD}$ are the numbers reported in this section about the pointing mode. Regarding the survey mode, instead we just have $N_{\rm JD,real} = \epsilon_{\rm DC}N_{\rm JD}$. Another pivotal point of the future pointing strategy, which can strongly influence the real joint detection efficiency, is the trigger selection. As shown in Table 6.6, the number of sources localised better than 100 deg^2 are of order of 100 for ET and of 10^5 for ET+CE and ET+2CE. In order to not lose observational time, the triggers to be observed will require to be prioritised. A strategy based on the knowledge of the satellite detection efficiency, the distance and viewing angle from the GW signals (see Boxes 6.4 and 6.3) will be mandatory to select the triggers with a higher chance of

joint detection. Therefore the reported numbers for pointing mode should be considered as potential detections, which can be achieved only provided that an efficient selection of the GW triggers is performed to restrict the follow-up to cases with highest probability of detection.

In Tab. 6.12 we consider longer response time (relaxing the assumption of $t_{\rm resp} = 100$ s) and we show how the detection rate significantly decreases if the telescope needs more time to respond to the trigger and point the GW localisation. The significant decrease of the chance to detect the afterglow emission pointing with one hour delay is due to a combination of the rapid decline of the GRB X-ray flux and the sensitivity of wide field X-ray instruments. Among the population of detected BNS, nearby events similar to GW170817 are a tiny fraction, while the large majority of joint detections comes from on-axis (or slightly off-axis) short GRBs distributed at cosmological distances, with an afterglow light curve which peaks at early times and followed by rapid drop of the flux. For these cases a rapid response is fundamental to catch the first decaying part of the X-ray emission. In Tab. 6.13, we show how the prediction of joint GW+X-ray detections depends on the assumption of FS parameters and on the inclusion of HLE. In this case, we assume ET+2CE as GW network and $t_{\rm resp} = 100$ s. In the specific, we test three possible setups, where we compute the X-ray light curve: 1) including HLE + FS emission, with *FS-SGRB* configuration; 2) including HLE + FS emission, with *FS-GW17* configuration; 3) including only FS emission, with *FS-SGRB* configuration. Our results show that the assumption of FS parameters like GW 170817 leads to less bright FS emission, mainly due to lower value of ϵ_B. Moreover, the tables show that the inclusion of HLE is non negligible in the estimation of detectability of the X-ray afterglow. The reasons are mainly twofold: 1) the HLE produces an initial steep decay phase which is well visible in X-rays and exceeds the FS contribution at least in the first tens of seconds, 2) the HLE associated to a structured jet typically produces a plateau phase for sources observed at $\theta_v \lesssim \theta_c$ and this contribution can be as relevant as the FS emission itself.

Finally, we test how the expected joint detection rate of GW+X-rays from BNS mergers depends on the assumption of the jet structure. The specific structure *Stru1* assumed so far, namely the one derived from GW 170817, has a very steep off-core profile, meaning that the probability of detecting prompt and/or afterglow emission from SGBRs viewed at $\theta_v > \theta_c$ is lower than the one of detecting a shallower off-core jet profile, such as *Stru2*. Tab. 6.14 shows the difference in joint GW+X-ray detections in pointing

mode assuming *Stru1* and *Stru2*. The overall rate of joint GW+X-ray detections for *Stru2* is, within the uncertainties, comparable with the one of *Stru1*. This is due to the fact that, though the X-ray emission is detectable at larger viewing angles for *Stru2*, the best fit value for the fraction of BNS producing a jet, f_j, derived from the Monte Carlo is smaller for *Stru2* than the one of *Stru1*. Fig. 6.12 and 6.13 show the distribution of viewing angle of GW+X-rays joint detections as a function of redshift, adopting the jet structure *Stru1* and *Stru2*, respectively. For each detection, we use a color code for the sky-localisation uncertainty. The plot is realized simulating 1000 GW+X-rays detections (ET+2CE + SXI) which satisfy the requirement $\Delta\Omega < 100$ deg^2, assuming $t_{\rm resp} = 100$ s and *FS-SGRB* configuration. Below $z \sim 0.5 - 1$, for both the structures, the X-ray emission is detectable up to viewing angles much larger than $\theta_c = 3.4$ deg.
In the bottom panel of Fig. 6.12, we show how the GW+X-rays joint detections are distributed in redshift and we distinguish between cases detected at $\theta_v < 5^\circ$ and $\theta_v > 5^\circ$. We adopt $\theta_v = 5^\circ$ as a threshold because, according to Fig. 6.5, this is the maximum angle up to which prompt emission is detectable by *Fermi*-GBM (similarly for XGIS onboard of THESEUS), considering an average on redshift. This implies that all the sources detected in X-rays at $\theta_v > 5^\circ$ have a non detectable prompt emission in γ-ray. In the case of *Stru1*, sources with $\theta_v > 5^\circ$ represent $\sim 40\%$ of all the GW+X-rays joint detections. Similarly, for *Stru2* the threshold angle for detectability of prompt emission is $\theta \sim 10^\circ$ and $\sim 50\%$ of all the GW+X-rays joint detections is above this limit.
Independently on the assumption on the jet structure, this result means that there is a significant number of off-axis events concentrated below $z \sim 0.5 - 1$ which are only detectable with WFX-ray instruments. In terms of absolute numbers of off-axis GW+X-rays joint detections, a combination of ET+2CE + SXI would observe few a tens of such events per year. For TAP and Einstein Probe a similar fraction ($\sim 40 - 50\%$) of events are expected to be observed off-axis. This result demonstrates the fundamental role of WFX-ray telescopes in synergy with GW detectors for the detection of off-axis emission from BNS mergers that would be otherwise undetactable for γ-ray instruments. We finally evaluated how the choice of a larger value of the angular extension of the jet wings, θ_w (used in *Afterglowpy*), could increase the number of detections. Increasing θ_w also the maximum viewing angle at which the source is detectable increases. We estimated that increasing θ_w from 15 deg (30 deg) to 45 deg, the number of joint detections increases of a factor $< 5\%$ ($\sim 10\%$) for *Stru1* (*Stru2*).

Medium and small-FOV sensitive X-ray observatories

When the GW sources are localised at the level of arcminutes the X-ray afterglow can be directly detected by pointing small-FOV instruments. However, there are no BNSs localised at arcminute precision through the GW signal when ET is operating as a single detector, and the number is also negligible when ET is in a network of 3G detectors. When the GW localisation is of order of 1-10 deg^2, medium-FOV X-ray instruments can scan the entire localisation region by performing mosaic observations. Considering the GW sources localised better than 10 deg^2 from Table 6.7, the sources that can be followed-up by medium-FOV instruments are around 10 when ET is operating as a single detector, but several thousands (hundred of thousands) when the ET+CE (ET+2CE) network is observing. However, in the case of ET+CE, the distances of these sources are limited to $z < 1.2$. For larger z the way to detect the X-ray counterpart remains through the use of wide-FOV γ-ray and/or X-ray satellites. In this case, the more sensitive small-FOV satellites can operate at a later time by pointing the precise localisation provided by the wide-FOV satellites, following-up and characterising the detected counterparts.

During the activity period of 3G GW detectors, the mission Athena is expected to be operative (Nandra et al., 2013). The exceptional sensitivity of Athena X-ray telescope and its focal plane instruments will allow us to detect the faint afterglow emission from SGRBs and GW counterparts hours to years (for closer events) after the merger and to make high resolution spectra (Piro et al., 2021). Athena will host the Wide Field Imager (WFI) with a FOV of 0.4 deg^2 and the X-IFU high resolution spectrometer with a FOV of 5 arcmin equivalent diameter. The WFI is able to directly point GW signals with sky localisation uncertainties smaller than its FOV (a few tens per year for ET+CE and thousands for ET+2CE considering all the orientations of the binary systems), and in addition is capable to carry out a mosaic of sky regions extended up to 10 deg^2. On the other hand, X-IFU requires a precise localisation ($\simeq$2 arcmin) to directly point the source. Even considering a GW network with ET+2CE, there are no sources with such a small uncertainty on the GW sky location. Therefore, instead of being directly triggered by the GW detection, X-IFU can be used either for following up precise localisations delivered by WFX-ray telescopes or by the Athena WFI itself. Taking into account that Athena will likely have a Time of Opportunity (TOO) response time of 4 hours, we find that the totality of the sources jointly detected by ET+2CE and the

WFX-ray telescopes can be detected and followed-up by Athena X-IFU.

In order to evaluate the Athena-WFI capabilities to detect GW counterparts, we consider the sources localised by the GW detectors within a region of 10 deg^2. We assume an average number of exposures to fully cover the GW sky region equal to $N_{\rm exp} \sim \Delta\Omega_{\rm GW}/{\rm FOV}_{\rm WFI}$, where ${\rm FOV}_{\rm WFI}$ = 0.4 deg^2, and an exposure time $T_{\rm exp} = 10^4$ s for each mosaic observation. For simplicity, we work in the approximation that the source is randomly located within the 90% GW error region and that each position is equi-probable. This implies that, if the GW region is tiled in $N_{\rm exp}$ subregions, the probability that the source is located inside the k^{th} subregion is $P(k) = 1/N_{\rm exp}$ and is the same for all the subregions. We consider a TOO response time $T_{\rm TOO}$ of 4 hr and we include a dead time interval T_d of 30 minutes corresponding to the time necessary to slew from one subregion of the mosaic to the adjacent one[10]. Hence, the time necessary to point and detect the source is $T(k) = T_{\rm TOO} + k \times (T_{\rm exp} + T_d)$. Operatively, for each source we extract a random number k in the range $[0, N_{\rm exp}]$ and we check if at time $T(k)$ after the GW trigger the X-ray afterglow emission is above the sensitivity of Athena-WFI corresponding to 10^4 s of exposure.

Given the several science goals of Athena, only a fraction of its observational time can be realistically dedicated to the follow-up of GWs; specifically we assume one month over one year of observations. While for ET alone the number of sources with $\Delta\Omega < 10$ deg^2 is around 10, and all of them can in principle be followed up by Athena in this total amount of time, the number of the sources detected by ET+CE with $\Delta\Omega < 10$ deg^2 is of several thousands. In order to maximise the effectiveness of the search and not lose time on sources without any chance of detection, a further selection of the sources to be followed-up results to be necessary. We select the sources by excluding all those with $\theta_v > 50^\circ$ (for which the error on θ_v is relatively small, see Fig. 6.9, and thus can be reliably considered off-axis) and $z > 0.5$. We select randomly among these sources ($\sim$ 130) up to reach a total amount of time of one month of observation, and find that Athena-WFI is able to detect $N_{\rm GW+Athena} = \epsilon_{\rm FOR} \times (6^{+2}_{-3})$ events per year, where $\epsilon_{\rm FOR}$ is a factor that takes into account the TOO efficiency and it corresponds to a field of regard of $\sim$ 50% (i.e., only a fraction $\epsilon_{\rm FOR}$ of the events can be successfully followed-up by Athena). Including another CE in the

[10] https://www.cosmos.esa.int/documents/400752/400864/Athena+Mission+Proposal/18b4a058-5d43-4065-b135-7fe651307c46

GW network does not increase significantly the number of Athena detections ($N_{\rm GW+Athena} = \epsilon_{\rm FOR} \times 8^{+3}_{-2}$ detections per year), because even increasing the number of sources well localised, the maximum number of Athena detections is anyway limited by the time dedicated to TOO. If we exclude more sources by lowering the threshold on the viewing angle to $\theta_v < 30^\circ$ instead of $\theta_v < 50^\circ$, the number of joint detection increases to $\epsilon_{\rm FOR} \times 14^{+4}_{-3}$/yr ($\epsilon_{\rm FOR} \times 27^{+3}_{-3}$/yr) for ET+CE (ET+2CE). The knowledge about the luminosity distance and the viewing angle coming from GW analysis can considerably help for the selection of a golden sample of events that have a larger probability to be detected, giving the possibility to maximise the GW+X-ray joint detection efficiency.

6.2.5 Discussion

Our study evaluates the perspectives for multimessenger astronomy in the ET era focusing on the search of high-energy signals, which is a unique way to detect EM counterparts of GW signals at high redshift. The methodology and results described here have been published in Ronchini et al., 2022a. We estimate the expected rate of joint detections of GWs and γ-ray and/or X-ray signals from BNS mergers considering prompt and afterglow emissions, different GW detector configurations (ET, ET+CE, ET+2CE), and different observational strategies (survey and pointing mode) for several satellites. Our theoretical framework starts from an astrophysically-motivated population of BNS mergers and predicts the high-energy signals associated with these mergers making the BNS population able to reproduce all the statistical properties of currently observed SGRBs. This approach makes it possible to reproduce not only the observational features of SGRBs, such as luminosity, duration and spectral properties, but also the average detection rate with current γ-ray instruments, such as *Fermi*-GBM. This enables us to normalise the number of joint detections, evaluate the fraction of BNS producing a jet, and be less dependent of the BNS merger absolute number, which is still largely uncertain.

Summary of our results

- Regarding the joint detection of GWs and γ-ray emission, we find that already considering ET alone, more than 60% of all the SGRBs having a detectable prompt emission will also have a detectable GW

counterpart. This percentage approaches 100% if we include CE as an additional interferometer in the network. From a few tens to hundred joint detections are expected per year, mainly depending on the FOV of the high energy-satellites. However, although increasing the number of joint detections is important for statistical studies, characterising the sources and identifying the host galaxies is of primary importance. As shown by *Swift* in many years of observations, this is possible and effective when the source is localised at arcmin level enabling to drive the follow-up of ground-based telescopes. Mission concepts such as THESEUS-XGIS, will be essential to detect and localise high-energy counterpart of BNS mergers with enough precision (arcmin uncertainty). This is particularly important when the sources are located at large redshift, namely $z > 1$ where also in the optimistic scenario of a network of 3G GW detectors, the GW sky localisation will be larger than 1 deg^2 from the GW signals. Instruments such as HERMES (full constellation of cube-satellites) can also be a good compromise of number of detections and sky localisation uncertainties which are however order of a few deg^2.

- Considering the possible shock breakout of the cocoon produced by the interaction of the jet with the NS merger ejecta, we show that sensitive (more than the current ones) and wide FOV γ-ray instruments are required.

- Regarding the joint detection of GWs and X-ray emission, we demonstrate the important role of WFX-ray missions, such as SVOM, Einstein Probe, *Gamow*, THESEUS, and TAP. We predict tens of detections per year when these instruments operate in survey mode. The joint detection rate in survey mode is limited by the chance of having the source inside the FOV at the moment of the merger. We propose an additional observational strategy, the pointing strategy, which could in principle enhance the probability of joint detection exploiting the information about sky localisation provided by GW instruments (see below).

- ET operating as a single observatory can detect several hundreds of BNS mergers per year with $\Delta\Omega < 100$ deg^2, among them about ~ 70 BNS/yr have a viewing angle $\theta_v < 15^\circ$, namely sources with potentially detectable high-energy emission. The inclusion of CE in the network significantly improves the localisation capabilities by reaching several thousands (hundreds with $\theta_v < 15^\circ$) of BNS detections per

year with $\Delta\Omega < 10$ deg^2. The network of CE+ET is able to localise a few hundreds (a few tens with $\theta_v < 15^\circ$) with $\Delta\Omega < 1$ deg^2 up to redshift 0.3. This number increases to thousands (hundreds on-axis) per year up to redshift 1 with the network of ET+2CE.

- Considering WFX-ray telescopes slewing to the sky position provided by GW detectors for sources with a good sky localisation (better than 100 deg^2), we evaluate that the X-ray afterglow emission from ten to hundreds SGRBs could be detected during one year of observation assuming a response time $t_{\rm resp}$ =100 s.

- A rapid communication of the GW sky location and a rapid repointing of the high-energy satellites is crucial to maximise the efficiency of the pointing strategy. Indeed, due to the typical rapid decline of the X-ray flux of SGRBs, we showed that a longer delay time between the merger and the beginning of X-ray monitoring would decrease the probability of detection by a factor ~ 10 or more going from $t_{\rm resp}$ =100 s to $t_{\rm resp} = 1$ hr. The low-frequency sensitivity of ET will make it possible to provide a good sky localisation even several minutes before the merger (Banerjee et al., 2022; Chan et al., 2018; Li et al., 2022; Nitz and Dal Canton, 2021). This will allow us to send information about the sky location of the source well before the merger and X-ray telescopes can realistically start earlier the slewing procedure. We evaluate that a not negligible fraction of GW events, localised within 100 deg^2 at merger, are detectable tens of minutes before the BNS merger with a sky localisation well within the FOV of the WFX-ray satellites.

- While the number of detections for WFX-ray satellites in survey mode is reliable, the number of detections in pointing is optimistic and relies on a perfect prioritization of the trigger to be followed (see below).

- We show that using WFX-ray instruments makes it possible to detect a significant fraction of BNS mergers which are too off-axis to have a detectable γ-ray emission and that would be otherwise missed in absence of these instruments. The presence of WFX-ray monitors is also fundamental to provide the spectral coverage at smaller energies than γ-rays and to precisely localise the source. The WFX-ray telescopes can provide sky location accuracy of $\sim$ arcmin, which enables to trigger follow-up observations by ground-based optical telescopes, radio arrays and exceptionally sensitive X-ray instruments, such as

the X-IFU instrument onboard of Athena. We evaluate that the totality of the sources jointly detected by the GW detectors and the WFX-ray telescopes can be detected and followed-up by the Athena X-IFU.

- The networks of ET+CE and ET+2CE are expected to localise a large number of BNS signals with $\Delta\Omega < 10$ deg^2. An instrument such as the WFI (FOV of 0.4 deg^2) on-board of Athena is able to carry out a mosaic of these sky regions by detecting from a few to a few dozen signals by using 1 month of Athena observations. The joint detection number comes from an observational strategy which maximises the chance of detections by removing the BNS signals with smaller probability to have observable jet. In particular, this is done by removing BNS with larger viewing angles and distances.

- Due to the high number of BNS events expected to be released by the next generation GW detectors, for the pointing observational strategy, it will be crucial to select and prioritise the ones to be followed-up. The selection based on sky-localisation will not be enough to avoid to lose observational time of the high-energy satellites when the network ET+CE and ET+2CE will operate. On the basis of the different scientific science goals, specific selection based on the GW source parameters such as distance and viewing angles, but also pre-merger sky localisation, will be mandatory to maximise the joint detection efficiency. This shows the importance in the ET era to send in low-latency (updating) information about GW parameter estimation.

6.2.6 Application of the methodology to other studies

In this section we describe how the method and simulation setup presented in the previous sections have been applied in other works, related to the assessment of the detection capabilities of mission concepts, as well as to the evaluation of how the ET performances depend on the adopted design.

Proposals for future missions to answer to the 2021 ESA call

The model and simulations developed in my thesis have been used also to evaluate the performances in the multi-messenger context of the mission concepts Astrogam (De Angelis et al., 2021), GRINTA and THESEUS[11].

[11] At the moment of writing only THESEUS succeeded in the phase two selection process

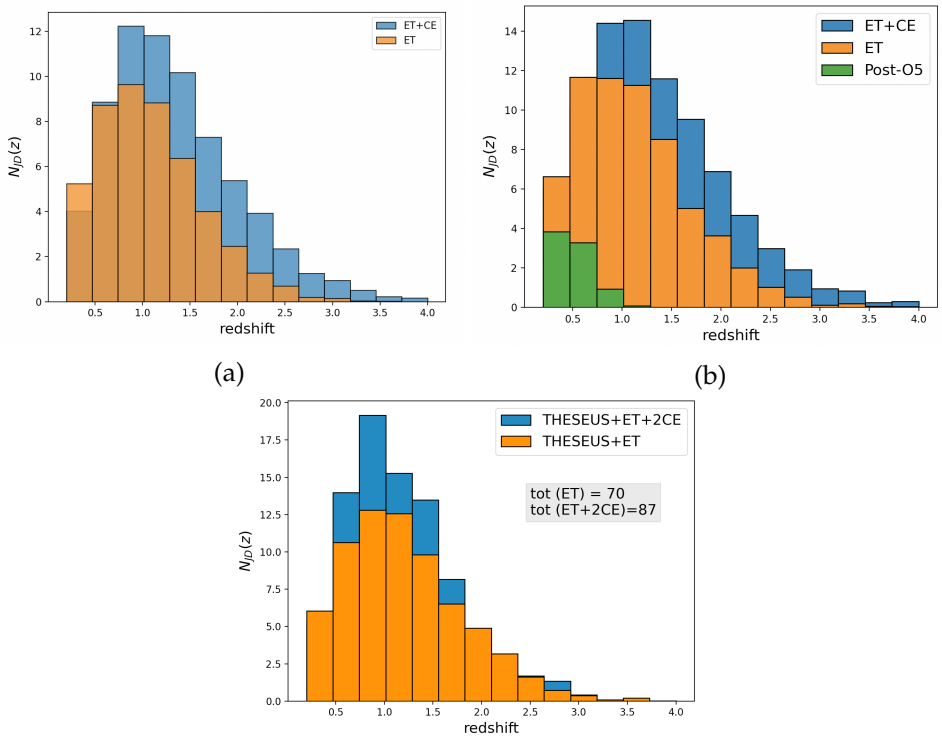

FIGURE 6.14: Redshift distribution of joint GW/γ-ray detections for Astrogam (a), GRINTA (b) and THESEUS (c), reported in the relative ESA proposals. The histograms are normalised to 3 yr, 1 yr and 3.5 yr of observations, respectively.

GW detectors	XGIS+SXI	XGIS-prompt	SXI-afterglow	(SXI+XGIS)-afterglow
ET	$70[56-87]$	$22[13-34]$	$28[21-36]$	$55[43-70]$
ET+2 CE	$87[72-107]$	$34[25-47]$	$34[26-44]$	$65[53-82]$

TABLE 6.15: Expected rates of joint detections with THESEUS, during 3.5 years of operation. The number in square brackets are the 1 σ confidence intervals.

These missions have been proposed for the 2021 ESA selection of medium-size and fast missions. All the three missions represent a great opportunity for the future of multi-messenger astrophysics. Their ability of continuously monitoring the sky at high-energy is crucial for the systematic GW/EM association. The capabilities of these three missions for the joint GW/GRB detection have been evaluated considering different GW detector networks, including both post-O5 scenarios and 3G detectors.

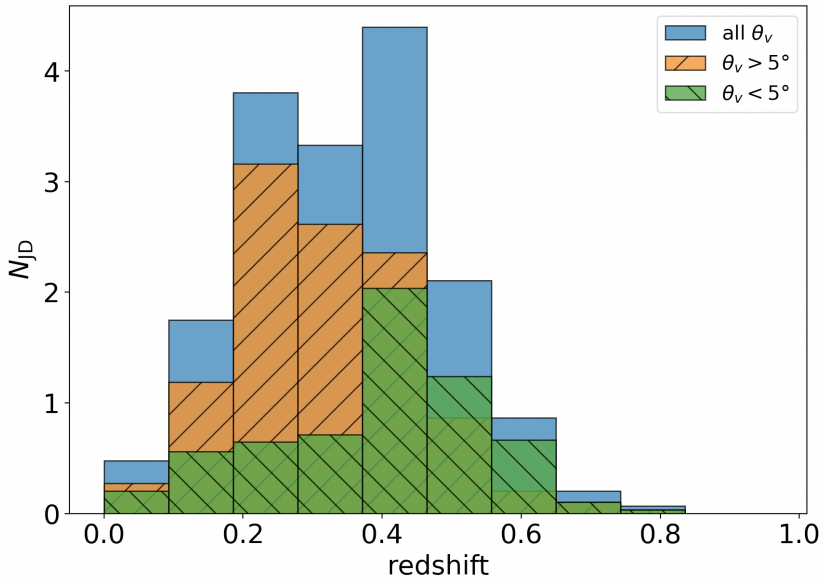

FIGURE 6.15: Redshift distribution of the joint GW/X-ray detections with GRINTA-HXI, distinguishing between on-axis and off-axis cases.

Scenario	GW network	N_{JD}	N_{JD}/N_γ
2G+	LIGO-L + LIGO-H + LIGO-I + Virgo + Kagra	1^{+2}_{-1}	$< 2\%$
Post O5	3 Voyager + Virgo + Kagra	9 ± 4	$12^{+6}_{-4}\%$
ET	Einstein Telescope	63^{+12}_{-17}	$65 \pm 8\%$
ET+CE	Einstein Telescope + Cosmic Explorer	86^{+21}_{-17}	$94^{+3}_{-4}\%$

TABLE 6.16: Estimated rates of joint GW/γ-ray detections with GRINTA-TED. The rated are relative to one year of observation. Several GW networks are shown.

The advantage of Astrogam is the exquisite sensitivity around and above MeV energies, for an accurate characterisation of the temporal and spectral properties of the prompt emission. GRINTA, despite the reduced dimensions, is an ideal compromise between costs and performances, perfectly optimised for the detection of GRBs and for multi-messenger applications. Indeed, the presence on board of both a γ-ray and wide-FOV X-ray instruments is an advantageous combination, following the same working principle of Swift. Thanks to the approach presented in this section, we

demonstrated that the fast repointing capabilities of GRINTA can be exploited both to catch the early X-ray emission following the initial γ-ray trigger, or to point directly the GW sky region for the search of the EM counterpart. THESEUS, as well, shares a similar configuration, with the difference that the instrument XGIS, dedicated to the detection of prompt emission, is more sensitive to lower energies (compared to the γ-ray modules of Astrogam and GRINTA). Moreover, THESEUS mounts an optical/IR telescope for the direct multi-wavelength inspection of the afterglow phase.
A reliable estimation of the detection performances of these missions is essential to assess which combination of instruments is ideal for the multi-messenger detection of GWs and GRBs. Figs. 6.14 and 6.15 summarise the performances of the three missions in terms of total joint GW+(γ-ray/X-ray) detections and how they are distributed in redshift. In Tab. 6.15 we report the expected rates of joint detection with both XGIS and SXI onboard of THESEUS. In Tab. 6.16 we show the expected rates of joint GW/γ-ray detection with GRINTA-TED. We also test the capabilitied of GRINTA-HXI in response to an external GW trigger. In this regard, selecting only the GW events localised better than 50 deg^2 and assuming a response time of the instrument of 5 minutes (1 hour), we estimate a rate of joint detections of 17^{+9}_{-7} (4^{+2}_{-2}).

Evaluation of the multi-messenger perspective for different ET designs.

At the moment of writing, the ET has reached substantial achievements since has been included in the the European Strategy Forum on Research Infrastructures (ESFRI) demonstrating its unique scientific relevance and its priority in European infrastructures. Among the most urgent and demanding tasks, the scientific community has to determine which is the best ET design, in relation to the corresponding cost of realisation. The aim of this study consists in comparing the scientific output of ET assuming several geometrical configurations of the detector arms, always considering as common requirement a detector working underground and with a xylophone configuration[12]. The configurations considered in this study are reported in Box 6.5. All the configurations are evaluated considering both high frequency (HF) and low frequency (LF) instruments, as well as HF alone. This study has been performed in the context of the activities of the

[12]The xylophone configuration consists of a part of the instrument tuned towards low frequencies (LF) and another towards high frequencies (HF). Only the low frequency one works at cryogenic temperatures.

BOX 6.5: ET CONFIGURATIONS CONSIDERED IN THIS STUDY

1. Δ configuration (triangular shape), with:
   (a) arm length of 10 km
   (b) arm length of 15 km
2. Two interferometers with L geometry (perpendicular arms), misaligned by 45°, one located in Sardinia, the other in the Meuse-Rhine region in Germany, with:
   (a) arm length of 15 km
   (b) arm length of 20 km

Observational Science Board (OSB) of ET, which is in charge of developing the Science Cases and the analysis tools relevant for ET. In particular, I lead the evaluation of the multi-messenger perspectives of ET operating with the high-energy satellites and contributed to the evaluation of the corresponding cosmology perspectives. This work is detailed in Branchesi, Maggiore et al. 2023 (under internal ET review).
The results and methodology presented in this chapter have been extensively exploited to perform a detailed evaluation of the different ET designs, with particular attention to multi-messenger observations, pre-merger sky localisation and applications for cosmological studies. For this purpose, we tested the performance of configurations 1. and 2. reported in Box 6.5, both HF+LF and HF alone.
As we deeply emphasised before, the good estimation of the GW sky localisation can significantly help in the search and identification of the EM counterpart. In this regard, the performance of configurations 1) and 2) have been investigated, finding that the Δ 15 km gives better results in sky localisation, with respect to the Δ 10 km. The exclusion of the LF part drastically worsen the sky-localisation performance. Regarding the sky localisation, we explored also the possibility of localising the source before the merger (30 min, 5 min, and 1 min before the merger) finding that the Δ 15 km performs similarly to 2L 20 km, and better than the other configurations.

Regarding the joint GW/GRB detection, we explored the detectability of both prompt and afterglow emission, analogously to the approach followed in Ronchini et al., 2022a. For the detection of the prompt phase, we considered Fermi-GBM, GECAM, HERMES, GRINTA-TED and THESEUS-XGIS. In the simulation setup, we need caution in the processing of the injections,

Full (HFLF cryo) sensitivity detectors

Instrument	Δ10	Δ15	2L 15	2L 20	Δ10	Δ15	2L 15	2L 20
Fermi-GBM	31^{+9}_{-9}	42^{+11}_{-13}	39^{+11}_{-9}	44^{+13}_{-11}	61^{+12}_{-11}%	83^{+9}_{-10} %	79^{+8}_{-11} %	89^{+4}_{-8}%
GECAM	61^{+39}_{-25}	89^{+54}_{-34}	81^{+51}_{-32}	96^{+52}_{-36}	51^{+5}_{-6}%	74^{+5}_{-5}%	70^{+3}_{-6}%	80^{+4}_{-4}%
HERMES	86^{+31}_{-28}	120^{+40}_{-31}	117^{+37}_{-34}	132^{+34}_{-34}	55^{+9}_{-7}%	78^{+8}_{-7}%	74^{+9}_{-9}%	85^{+5}_{-6}%
GRINTA-TED	77^{+31}_{-25}	107^{+31}_{-28}	98^{+31}_{-25}	114^{+34}_{-28}	57^{+10}_{-9}%	79^{+8}_{-8}%	74^{+9}_{-9}%	85^{+5}_{-5}%
THESEUS-XGIS	10^{+3}_{-3}	13^{+3}_{-3}	13^{+3}_{-3}	15^{+3}_{-4}	57^{+9}_{-10} %	79^{+8}_{-9}%	73^{+11}_{-7}%	85^{+7}_{-5}%

HF sensitivity detectors

Instrument	Δ10	Δ15	2L 15	2L 20	Δ10	Δ15	2L 15	2L 20
Fermi-GBM	20^{+8}_{-7}	33^{+9}_{-9}	29^{+11}_{-9}	38^{+12}_{-10}	39^{+11}_{-8}%	64^{+12}_{-11}%	60^{+12}_{-11}%	76^{+9}_{-9}%
GECAM	35^{+21}_{-15}	62^{+38}_{-22}	58^{+38}_{-22}	77^{+47}_{-30}	29^{+4}_{-5}%	54^{+4}_{-5}%	49^{+4}_{-7}%	66^{+4}_{-6}%
HERMES	52^{+21}_{-18}	91^{+30}_{-29}	83^{+28}_{-28}	107^{+40}_{-31}	33^{+7}_{-8}%	58^{+10}_{-8}%	53^{+10}_{-8}%	71^{+8}_{-8}%
GRINTA-TED	46^{+22}_{-16}	80^{+31}_{-25}	74^{+28}_{-25}	94^{+33}_{-23}	34^{+9}_{-9}%	61^{+9}_{-11} %	55^{+9}_{-10} %	72^{+9}_{-9}%
THESEUS-XGIS	6^{+2}_{-2}	10^{+3}_{-3}	9^{+3}_{-3}	12^{+3}_{-3}	34^{+8}_{-9}%	59^{+10}_{-8}%	54^{+10}_{-9}%	71^{+9}_{-9}%

TABLE 6.17: Columns 2-5 give the numbers of joint GW+γ-ray detections during one year of observation for different combinations of γ-ray instruments operating in survey mode together with different ET full sensitivity configurations. The absolute numbers do not assume duty cycle for the satellites. Columns 6-9 give the fraction of detected short GRBs which will have a GW counterparts.

such that the ET configurations are all compared in a equal and consistent way. This requires that the injected BNS population is the same for all the configurations, as well as the EM output is imposed to be the same. Namely, for all the BNS of the population, the same GW and EM signal is assigned and all the ET configurations are observing the same Universe[13]. Apart from the absolute number of joint detections, which depends on the specifics of the γ-ray instrument, it is instructive to compare the ET configurations in terms of fraction of GRBs with detected GW emission. This quantity is in the interval 51%-61% for Δ 10 km (as we saw in tab. 6.3), increasing up to 80%-89% for 2L 20 km. Also here the exclusion of the LF contribution decreases the joint detection efficiency. The difference between the ET geometries is appreciable also in terms of redshift distribution

[13]On the other hand, in order to reproduce a realistic scenario, the duty factor of the GW instruments is kept as a random parameter, independent for each configuration

Full (HFLF cryo) sensitivity detectors

Instrument	Δ10	Δ15	2L 15	2L 20
THESEUS-SXI survey	10^{+3}_{-2}	13^{+3}_{-4}	12^{+3}_{-3}	12^{+3}_{-3}
THESEUS-(SXI+XGIS) survey	21^{+6}_{-7}	21^{+8}_{-6}	20^{+7}_{-5}	21^{+7}_{-7}

HF sensitivity detectors

Instrument	Δ10	Δ15	2L 15	2L 20
THESEUS-SXI survey	8^{+2}_{-3}	11^{+2}_{-4}	10^{+2}_{-3}	11^{+2}_{-2}
THESEUS-(SXI+XGIS) survey	16^{+6}_{-5}	19^{+8}_{-5}	19^{+4}_{-5}	21^{+8}_{-6}

TABLE 6.18: Numbers of joint GW+X-ray detections during one year of observation for THESEUS operating in survey mode considering the instrument SXI and the combination of SXI and XGIS.

Instrument	Δ10 cryo	2L 20 km cryo	Δ10 HF	2L 20 km HF
THESEUS-SXI pointing	6^{+4}_{-4}	11^{+6}_{-5}	1^{+2}_{-1}	7^{+4}_{-4}

TABLE 6.19: Numbers of joint GW+X-ray detections during one year of observation for THESEUS operating in pointing mode considering the instrument SXI

of joint GW/GRB detections, shown in Fig. 6.16, where HERMES has been considered as γ-ray detector.
For the detection of the afterglow phase, only the THESEUS mission has been considered, including both the SXI and XGIS instruments. The results reported in Tab. 6.18 on the survey mode show that no significant difference appears between the four ET geometries[14], since the majority of joint GW/afterglow detection occurs at low redshift ($z \lesssim 1$), where the GW detection efficiency is close to 100 % for all the ET geometries. On the other hand, following the pointing strategy (Tab. 6.19) the difference is more evident, especially for those configurations that perform better in the source localisation[15].
The results on the joint GW/GRB detection have been used as well for

[14]but the exclusion of LF, as was already evident for the joint GW/prompt detection, reduce the detection efficiency in a non negligible way.

[15]Though, notice that given the extremely large amount of GW triggers, the pointing strategy could be not so efficient. A prioritisation scheme is necessary to optimise the candidates selection.

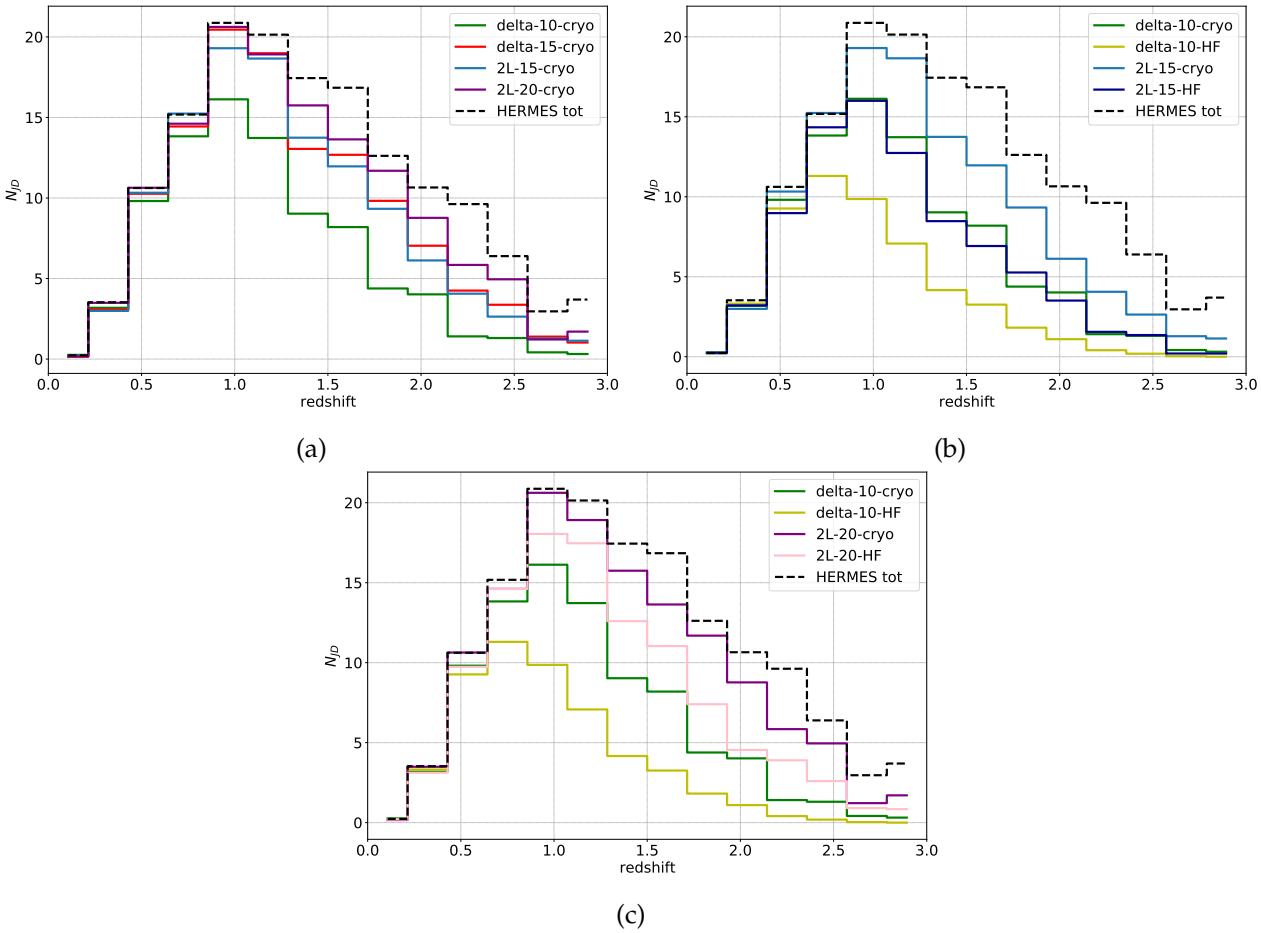

FIGURE 6.16: Histogram of the joint detection of ET and HERMES observing in survey mode during one year. Panel (a) aims at comparing all the 4 ET configurations, including both HF and LF. In panel (b) and (c) we compare HF+LF with LF alone.

the cosmological studies. For this aim, only the detections obtained with THESEUS-XGIS are taken into account, given the high probability that a spectroscopic determination of the redshift is available, thanks to the good sky-localisation capability of THESEUS. The number of total BNS injections is such that we obtain 75 joint GW/GRB detections with the 2L 20 km configuration, corresponding to $\sim$ 5 yr of observations. The simulation is set up in such a way that all the four configurations observe the same sample of BNS, with the same EM output, on the same range of time. With the combined knowledge of the luminosity distance, inferred by GWs, and redshift, inferred by the EM counterpart, cosmological studies can be performed,

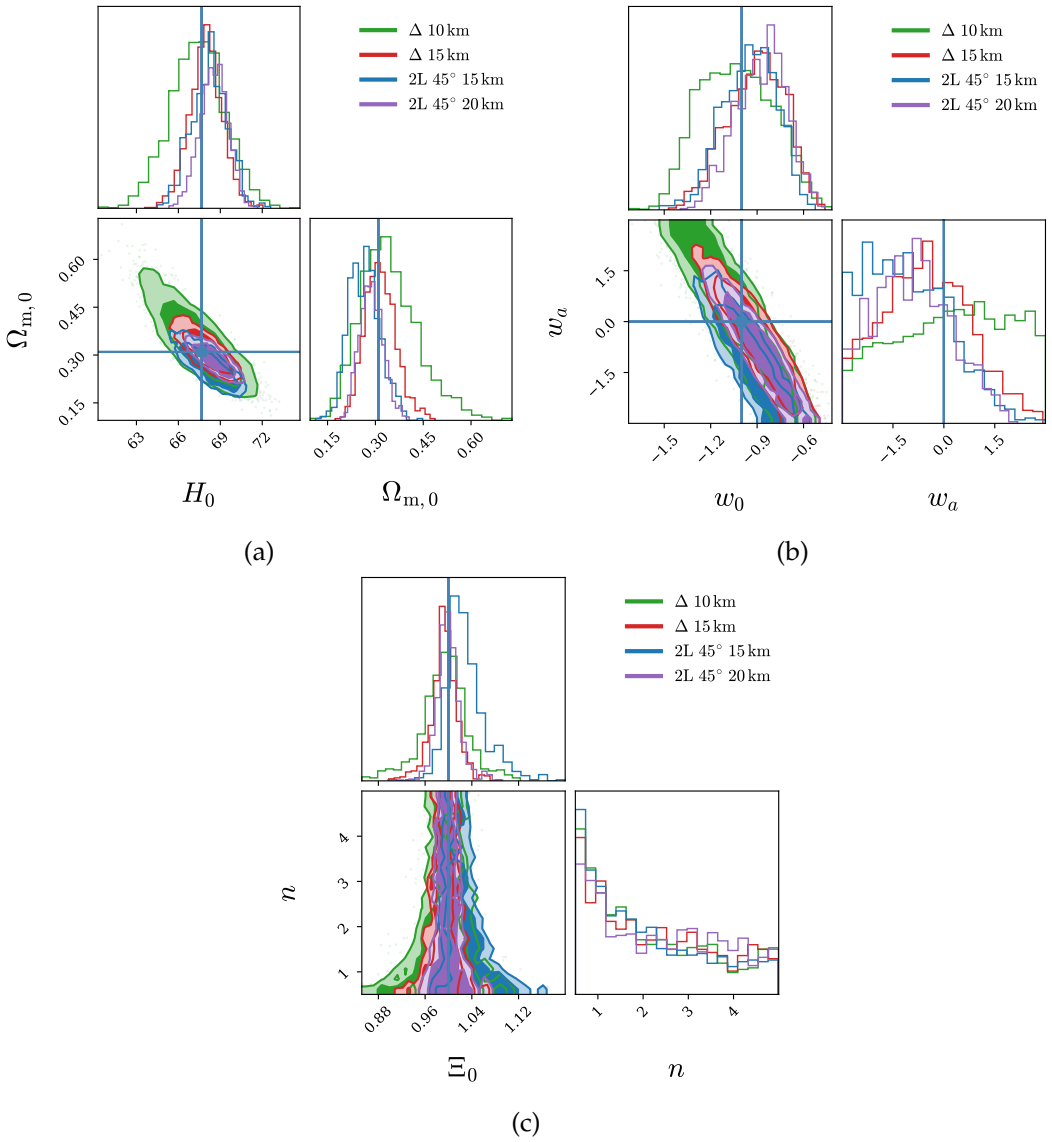

FIGURE 6.17: Reconstruction of cosmological parameters from the joint GW+EM events obtained with ET+THESEUS in 5 yr of observations, for the different geometries of ET shown, all with their HFLF-cryo sensitivity. In panel (a) the estimation of H_0 and Ω_M in ΛCDM, in panel (b) the reconstruction of the dark energy equation of state parameters w_0 and w_a, while in panel (c) the reconstruction of the parameters Ξ_0 and n for GW propagation in modified gravity.

both on a local Universe for the determination of the Hubble constant H_0, as well as on high-z Universe where the action of dark energy equation of

state is non negligible.
In particular, working in a flat ΛCDM scenario, the cosmological parameters H_0 and Ω_M can be derived through the following relation:

$$d_L(z) = \frac{c}{H_0}(1+z)\int_0^z \frac{d\tilde{z}}{\sqrt{\Omega_M(1+\tilde{z})^3+\Omega_\Lambda}}. \tag{6.12}$$

We find that for all the configurations, the relative error of H_0 reaches few %, going to sub-% including priors from other probes, such as SNe, barionic acoustic oscillations and CMB. The posterior reconstruction of H_0 and Ω_M is shown in Fig. 6.17a.
The test of dark energy EoS can be done considering again eq. 6.12 and relaxing the assumption that Ω_Λ is constant in time. This introduces a redshift dependence, which can be parametrised as:

$$w_{\rm DE}(z) = w_0 + \frac{z}{1+z}w_a,$$

where $w_{\rm DE}(z)$ relates pressure and density as $p_{\rm DE}(z) = w_{\rm DE}(z)\rho_{\rm DE}(z)$. The reconstruction of the dark energy EoS parameters can be obtained from a sample of joint GW/GRB detections, once the other parameters of eq. 6.12, H_0 and Ω_M, are assumed to be known from other EM probes, with negligible uncertainty. The results are shown in Fig. 6.17b.
As a final test, we investigated the possibility of probing possible deviations from general relativity (GR) in the propagation of gravitational waves. As shown in Belgacem et al., 2018, there exist a class of gravity models which predict a GW propagation equation which differs from the GR version from the introduction of a friction term. This translates not in a deviation of GW speed from the speed of light (which is already tightly constrained from GW170817), but rather in a deviation in the GW amplitude suppression as it propagates towards the observer. This would mean that, while in GR both EM and GW radiation fluxes decay as D_L^{-2}, for this class of modified gravity the GW flux drops more rapidly. Hence, EM luminosity distance $D_L^{\rm em}$ deviates from the one derived from GWs $D_L^{\rm gw}$ and the difference can be parametrised as:

$$\frac{D_L^{\rm gw}(z)}{D_L^{\rm em}(z)} = \Xi_0 + \frac{1-\Xi_0}{(1+z)^n}.$$

GRBs are optimal sources to test the GW propagation and test modified gravity at cosmological scale, since the GW/GRB temporal coincidence is

maintained to confirm the signals' association and the EM luminosity distance can be estimated from the host galaxy to be compared with the luminosity distance from the GW signal. The reconstruction of Ξ_0 and n with our sample of 5 yr of joint GW/GRB detections is shown in Fig. 6.17c. As a general result, we find that all the four ET configurations give very similar results on the estimation of cosmological parameters, with the best performance by 2L 20 km, followed by 2L 15 km and Δ 15 km, and finally by Δ 10 km.

6.2.7 Conclusions

Our work shows that in order to maximise the scientific return of 3G GW detectors in the multimessenger era, it is necessary to develop sensitive wide-FOV high-energy instruments able to detect but also localise a large number of short GRBs. Instruments, such as THESEUS, combining γ-ray and WFX-ray telescopes, are of primary importance to guarantee the observation of γ-ray and X-ray counterparts, by detecting $\sim 10 - 100$ well localised SGRBs up to high redshifts, for which also the host galaxy can be identified. This is of primary importance for evaluating the cosmological parameters and testing general relativity at cosmological scales. WFX-ray telescopes are required to detect GRB off-axis and make it possible to explore the jet structure, its interconnection with the ejecta, and the nature of low-luminosity SGRBs with a unique level of detail.
Medium-size X-ray instruments, such as Athena WFI, will become effective (operating mosaic of the GW sky localisation) for the X-ray counterpart search when a network of GW detector will observe. Mosaic observations with deep exposure by Athena WFI can enhance the possibility to detect off-axis X-ray emission. Sensitive instruments such as Athena X-IFU will be crucial to follow-up and characterise the X-ray emission at later times with respect to the merger.
The methodology presented in this section is a powerful and versatile tool, which can be systematically used to forecast the performance of current and future GW detectors, in cooperation with γ-ray and X-ray detectors. The simulation setup can be easily adjusted with the introduction of other CBM populations, as well as with other more sophisticated models for the prediction of the EM signal. For instance, it is possible that with future joint GW/GRB detections we will have a much more clear understanding of how the progenitor properties (component masses and spins, nature of the remnant) impact on the EM output. Hence, a more detailed and reliable model of the high-energy EM signal can be developed, starting from the

merger properties inferred from GW analysis.
The usefulness and applicability of our procedure has been extensively demonstrated in the completion of the ET OSB study for the assessment of the possible design of the ET. Our study explores in detail advantages and drawbacks of different ET configurations for the multi-messenger detection of CBMs, adopting the several observing strategies investigated in this section. Our predictions have been exploited as well for the comparison between different ET designs regarding cosmological studies, highlighting the wide impact of ET also in this sector.

Chapter 7

Summary

In this thesis, multiple aspects of the physics and phenomenology of GRBs have been addressed, with a special focus on the multi-messenger potential of these energetic events. Our analysis made use of both multi-band data analysis and development of theoretical and phenomenological models. The first part of the work described in chapters 4 and 5 took the advantage of the wealth of information provided by the Swift GRB catalog and data archive built over almost 20 years of observations, to extract new insights about open problems in the interpretation of the GRB X-ray emission. The second part of the thesis described in chapter 6 analysed the GRBs in the multi-messenger context by using the current observations of LIGO and Virgo and by evaluating the perspectives of the next generation GW observatories operating in synergy with high-energy satellites.

Exploring the origin and properties of the GRB X-ray emission: initial steep decay and plateau

Most of the X-ray light curves of GRBs are characterised by a steep-to-shallow transition, not in agreement with the predictions from the standard forward shock emission from a decelerating blast wave. The steep X-ray decay represents the final tail of the prompt emission. Since the spectrum gradually shifts towards lower energies, the prompt tail is better monitored in X-rays, rather than γ-rays. Therefore, the specific evolution of the spectral shift, combined with the evolution of the flux decay, contains useful hints about the prompt emission process, especially at the moment of its final phases, when the jet stops to dissipate its internal energy and enters in the deceleration phase.
Despite the importance of exploring steep decay, which is directly related to the central engine physics, there was little work which systematically

investigated this peculiar phase. Taking the advantage of almost 20 years of observations of Swift, this thesis provides for the first time an exhaustive examination of the X-ray steep decay, considering all the GRBs in the Swift catalogue with a sufficiently high quality of data. This systematic search enabled us to discover a unique relation between the flux and the spectral index, pointing to a common physical process at its origin. Even if the light curves are in agreement with the standard interpretation of the steep decay phase being due to the high-latitude emission, the inclusion of the spectral information highlights an inconsistency with this scenario. Following a thorough modelling of the combined spectral-temporal behaviour during the steep decay, we concluded that an intrinsic evolution of the spectrum needs to be invoked and the most favoured process driving it is the adiabatic expansion of the outflow. In the context of the origin of prompt emission, this finding has deep consequences. The dominance of adiabatic losses strongly suggests that the radiating particles are unable to efficiently cool on the dynamical time scale. In turn, this evidence gives insight into the nature of the emitting particles (pointing to protons rather than electrons), as well as on the physical conditions (e.g., regarding the evolution and strength of the magnetic field) that characterise the prompt emission site (Ronchini et al., 2021).

Another compelling phase of the X-ray light curve is the plateau, characterised by a very shallow decline of the X-ray flux and whose duration can last up to $10^3 - 10^5$ s. The origin of this feature remains under debate. In chapter 5 we defined a complete sample of GRBs with X-ray plateau to derive the overall statistical properties and to identify a sub-sample where both optical and X-ray data are available during the plateau phase. The systematic broad-band spectral analysis of the plateau phase can provide clues about its origin, possibly discerning between the available scenarios. We performed a joint X-ray/optical time-resolved spectral analysis, in order to test whether both X-ray and optical data are compatible with a single synchrotron emission component, as predicted from the standard forward shock scenario. We find that a considerable fraction of the analysed GRBs shows an optical emission in excess with respect to a single synchrotron emission. The results demonstrate that the broad-band emission during the X-ray plateau, at least in some cases, is the combination of multiple components, possibly arising from different emission sites. Mixed scenarios are a viable explanation, where a magnetar wind, the forward shock emission and the prompt HLE from a structured jet simultaneously contribute to the

overall spectral and temporal evolution (Ronchini et al., 2022b). In the future, observations at intermediate wavelengths between optical and X-ray bands could help in constraining better the overall spectral shape during the plateau phase. Additionally, measurements of the level of X-ray polarization can give further insigths about the specific nature of the radiative process.
Both the study of the steep decay and plateau in the X-ray light curves are a step forward in our understanding of the afterglow phenomenology and its connection with the prompt emission nature. The knowledge of the emission processes during these phases has been used to develop reliable population models and to evaluate the detectability of GRBs with current and future facilities (next section).

Prospects for the multi-messenger detection of GRBs

A large part of my thesis work has been devoted to the evaluation of the perspectives for multi-messenger astronomy using GRBs, in particular the evaluation of joint EM/GW detections, the definition of the best observational strategies, the identification of the best operation and technical requirements for the high-energy satellites and GW detectors to maximise the multi-messenger science. This work required to develop expertise in both the electromagnetic and gravitational wave data analysis, as well as in CBMs and GRBs modelling.

I participated in the search for GW signals in coincidence with GRBs detected during the third run of observations of LIGO, Virgo and KAGRA. Both the un-modelled search for generic gravitational-wave transients (used to analyse 86 events) and the modelled search for binary mergers including at least one neutron star (used to analyse 17 events), found no significant evidence for gravitational-wave signals associated with any GRB. The work (including data from the first to the third run of LIGO, Virgo and KAGRA observations) gives constraints on the population of low-luminosity short GRBs showing accordance with the local binary neutron star merger rate (Abbott et al., 2022a).

The tools, theoretical models and results presented in chapter 4 and 5 are propaedeutic for the methodology developed in chapter 6, where the most updated knowledge of the prompt and afterglow phenomenology enabled us to explore the future prospects of GRB detection in the multi-messenger era of 3G GW detectors. We particularly focus on the Einstein Telescope,

which is expected to revolutionise our knowledge of BNSs by detecting $\sim 10^5$ CBMs per year. Wide field γ-ray and X-ray telescopes will ensure a constant monitoring of the transient sky, allowing us to associate the EM counterpart, up to high redshift, to GW events detected by 3G instruments. In this thesis I investigated in detail several combinations of GW/EM facilities, assessing the efficiency of different observing strategies. We found that almost all detected short GRBs will have a GW counterpart making multi-messenger astronomy a mainstream. Depending on the different gamma-ray satellites, tens to hundreds of detections per year are expected. Among them, we highlight the importance of instruments providing arcmin sky localisation which are able to drive the EM follow up with ground-based optical facilities.

We demonstrated the importance of X-ray telescopes, both wide- and narrow-field of view, to increase the number of short GRB detections, to detect off-axis events and GRBs intrinsically sub-luminous in the γ-rays, located in the nearby Universe. We showed how an exploitation of the GW parameter estimation can help in defining a prioritisation scheme, which is mandatory when the number of GW transients will significantly increase. In addition, we evaluated the potential of pre-merger parameter estimation which will be realistically feasible with 3G GW detectors (Ronchini et al., 2022a). Synergy between GW observatories, γ-ray and X-ray telescopes is vital for the systematic detection of BNS up to high redshifts, allowing to confirm the GW/EM association, for the redshift determination and subsequent full characterisation of the multi-wavelength emission .

Observing CBMs along the cosmic history will open new frontiers in the fields of relativistic astrophysics, stellar evolution and populations, nuclear physics, gravitational physics and cosmology, enabling to connect the mergers to the properties (star formation and metalicity) and evolution of the Universe. My thesis work evaluates the multi-messenger and cosmology perspectives by developing a versatile theoretical approach able to reproduce all the current high-energy and GW osbervations of GRBs and BNS, and to evaluate joint detections for different ET designs, different network of GW detectors operating with different high energy satellites (including mission concepts such as ASTROGAM, THESEUS, GRINTA or mission such as HERMES and ATHENA).

A list of publications which regard my research activity during the PhD is reported in the following.

List of publications

Here we report the short-author list publications produced during my PhD.

1. Ronchini et al., 2021, Nature Communications: study of the spectral evolution during the X-ray steep decay. Results described in chapter 4

2. Ronchini et al., 2022b, under review in Astronomy & Astrophysics: combined optical/X-ray analysis during the X-ray plateau. Results described in chapter 5

3. Ronchini et al., 2022a, Astronomy & Astrophysics: multi-messenger perspectives for the joint GRB/GW detection in the era of 3G GW detector. Results described in chapter 6

4. Ghirlanda et al., 2021, Experimental Astronomy: I evaluated the capabilities of the THESEUS in

    - detecting and analysing the steep decay and related spectral evolution.
    - observing the effects of the jet structure in the X-ray light curve, both for an on-axis and an off-axis observer.

5. Ciolfi et al., 2021, Experimental Astronomy: my systematic analysis of the Swift-XRT catalogue has been used to predict the detectability horizon of THESEUS for the plateau phase.

6. Dupletsa et al., 2022, Astronomy and Computing: I contributed in the development and testing of the code *GWFish*. I also participated in the consistency check of our code with similar Fisher matrix codes (Iacovelli et al., 2022; Li et al., 2022).

7. Banerjee et al., 2022, Astronomy & Astrophysics : I contributed in the simulations performed to evaluate the pre-merger parameter estimation of 3G GW detectors, in synergy with future generation Cherenkov detectors.

8. Lucarelli et al., 2022, under review in Astronomy & Astrophysics: the plateau sample defined in my thesis work has been used for the systematic search of neutrino signals in IceCube, in coincidence with GRBs

9. Branchesi et al. (under internal review within the ET collaboration): I contributed to study the scientific performances of different design configurations of the ET, providing simulations of future joint GW/GRB detections and their impact on cosmological studies.

10. Oganesyan et al., 2021 under review in Nature Astronomy, Mei et al., 2022a, Astrophysical Journal, Mei et al., 2022c, Nature: I supported the data interpretation and for the last one I produced the graphic illustration in Fig. 5.

Finally, as member of the LVK collaboration I co-authored 29 papers. My main contribution is described in chapter 6 and published in Abbott et al., 2022a.

Appendix A

In this appendix we report some calculations useful for the concepts presented in Chapters 2 and 3, regarding the BNS merger rate and the relation between the jet structure and luminosity function. These results will be also taken into account in Chapter 6 for the modelling of the short GRB population .

A.1 Relation between SFR and BNS merger rate

Here we show how to derive the formula 3.6 from first principles. Let us consider a volume ΔV located at redshift z, corresponding to a time t_0 . We need to compute all the mergers that occur in that volume during the interval of time $[t_0, t_0 + \Delta t]$. We divide the temporal line before t_0 in single bins of duration $\Delta\tau$. The number of stars born during this interval is $N(\tau) = \dot{\rho}_*(t_0 + \tau)\Delta\tau\Delta V$, where R_* is the star forming rate. The probability that during an interval of time between τ and $\tau + \Delta\tau$ a fraction ϵ of stars ends with a merger is given by the binomial distribution:

$$\mathcal{B}(N, \epsilon N, p) = \begin{pmatrix} N \\ \varepsilon N \end{pmatrix} p^{\varepsilon N}(1-p)^{N(1-\varepsilon)},$$

where

$$p = p(\tau) = \int_{\tau}^{\tau+\Delta t} P(\hat{\tau}) d\hat{\tau}.$$

The average number of mergers occurring at time t_0 whose progenitors are originated at time $t_0 + \tau$ is pN. Therefore, the total number of mergers occurring in the time interval $[t_0, t_0 + \Delta t]$ is given by

$$N_{\rm tot} = \sum_i p\left(\tau_i\right) N\left(\tau_i\right).$$

The merger rate is therefore:

$$\frac{N_{tot}}{\Delta V \Delta t} = \sum_i p\left(\tau_i\right) \dot{\rho}_*\left(t_0 + \tau_i\right) \frac{\Delta \tau}{\Delta t}.$$

In the limit of $\Delta V, \Delta t \to 0$, we have $p(\tau) \to P(\tau)\Delta t$:

$$\frac{N_{tot}}{\Delta V \Delta t} \to \dot{\rho}(t_0) = \int P\left(\tau\right) \dot{\rho}_*(t_0 + \tau) d\tau.$$

A.2 Jet structure and luminosity function

In this section we show how to derive the luminosity function in the case of a structured jet. In the case of a universal structure, we can write the luminosity as:

$$L(\vartheta) = L_0 S(\vartheta),$$

where $S(\vartheta)$ is the structure and L_0 is constant. Hereafter we denote with $P_x(x)$ the probability density function of the random variable x. For a generic function $y = y(x)$ such that $x(y)$ can be defined:

$$P_y(y) = \frac{d}{dy} \int_{-\infty}^{x(y)} P_x(x) dx.$$

For an isotropic distribution

$$P_\vartheta(\vartheta) = \begin{cases} \sin\vartheta, & 0 < \vartheta < \pi/2 \\ 0, & \text{otherwise} \end{cases}.$$

Therefore:

$$\begin{aligned} \phi(L) = P_L(L) &= \frac{d}{dL}\left[\cos\vartheta\Big|_{\vartheta(L)}^{0}\right] = \sin\vartheta(L) \cdot \frac{d\vartheta(L)}{dL} \\ &= \sin\vartheta(L) \cdot \frac{1}{dL/d\vartheta}\Big|_{\vartheta(L)} \end{aligned}.$$

In the case of a Gaussian jet $L = L_0 e^{-(\vartheta/\vartheta_c)^2}$

$$\vartheta(L) = \vartheta_c \sqrt{\ln\left(\frac{L_0}{L}\right)}$$

$$\frac{dL}{d\vartheta} \propto -2\vartheta e^{-(\vartheta/\vartheta_c)^2} \propto L\sqrt{\ln\left(\frac{L_0}{L}\right)}$$

$$\phi(L) \propto \sin\vartheta_c \sqrt{\ln\left(\frac{L_0}{L}\right)} \cdot \frac{1}{L\sqrt{\ln\left(\frac{L_0}{L}\right)}} \underset{L\sim L_0}{\longrightarrow} L^{-1}.$$

For $L \ll L_0$ (i.e., $\vartheta \gg \vartheta_c$), since $\sin x < x$, $P_L(L)$ has a shallower decay, namely

$$\frac{d\log P_L}{d\log L} \gtrsim -1.$$

Analogously one can repeat the exercise far a power law structure in the form

$$S(\vartheta) = \begin{cases} 1 & \vartheta < \vartheta_c \\ (\vartheta/\vartheta_c)^{-k} & \vartheta > \vartheta_c \end{cases},$$

obtaining

$$\phi(L) \propto \left(\frac{L_0}{L}\right)^{1+\frac{1}{k}} \sin\left[\vartheta_c \left(\frac{L_0}{L}\right)^{1/k}\right]$$
$$\underset{L\sim L_0}{\longrightarrow} L^{-1-\frac{2}{k}}$$
$$\underset{\vartheta\sim\pi/2}{\longrightarrow} L^{-1-\frac{1}{k}}.$$

So far we worked in the assumption $L_0 = \text{const}$, namely $L(\vartheta = 0) = \text{const}$ for all the GRBs. Here we extend the treatment considering a probability distribution for L_0. In order to compute $\phi(L)$, we remind that if $y = AB$ and both A and B are random variables, then:

$$P_y(y) = \int_{-\infty}^{+\infty} P_A(A) \cdot P_B\left(\frac{y}{A}\right) \cdot \frac{1}{|A|} dA$$

. Therefore we can write:

$$P_L(L) = \int P_S(S) P_{L_0}\left(\frac{L}{S}\right) \frac{dS}{S}.$$

Using

$$P_S(S)dS = \frac{dN}{dS}dS = \frac{dN}{d\vartheta}d\vartheta = P_v(\vartheta)d\vartheta,$$

we arrive to

$$\phi(L) = \int_0^{\pi/2} d\vartheta \frac{\sin\vartheta}{S(\vartheta)} P_{L_0}\left(\frac{L}{S(\vartheta)}\right).$$

Appendix B

In this appendix we explicit all the useful calculations regarding the jet structure, including the HLE for an on-axis and off-axis observer, the properties of the plateau induced by jet structure and estimation of the jet transparency as a function of the viewing angle.

B.1 Prompt HLE from a structured jet, viewed from an on-axis observer

In this section we derive the properties of the light curve produced by a structured jet, in the approximation of an instantaneous prompt emission flash. Starting from eq. (B.8) in Ascenzi et al., 2020c, we have that the time dependence of the observed flux can be written as:

$$F_\nu(t) \propto \int_{EATR} \frac{\epsilon(\theta) S(\nu/\mathcal{D}) \mathcal{D}^3 P(\alpha, \tau) \mathrm{d}l}{|\nabla h|},$$

which is valid in the generic case of a structured jet seen off axis. Here:

- the integral is computed along the equal arrival time ring, defined as the intersection between the jet surface and a plane $\perp$ to the line of sight;
- $\epsilon(\theta)$ is the comoving emissivity;
- The Doppler factor is

$$\mathcal{D} = \mathcal{D}(\theta, \psi) = \frac{1}{\Gamma(\theta)(1 - \beta(\theta)\cos(\psi))},$$

  where ψ is the angle between the direction of propagation of the jet patch with respect to the line of sight;

- the projection factor is

$$P(\alpha, \tau(\theta)) = \begin{cases} 1, & \tau(\theta) \ll 1 \\ \cos\alpha, & \tau(\theta) \gg 1 \end{cases},$$

  where τ is the angle-dependent optical depth and the angle α is measured between the $\perp$ to the jet surface and the line of sight;

- $S(\nu)$ is the comoving spectral shape;

- $h = \mathcal{D}(\theta, \psi)\Gamma(\theta)t - t_{em}$.

The above expression simplifies in the limit of on-axis observer, giving:

$$F_\nu(t) \propto \frac{\epsilon(\theta) S(\nu/\mathcal{D}) \mathcal{D}^3 P(\alpha, \tau)}{|\nabla h|} R(\theta) \sin\theta,$$

where

$$|\nabla h| = \frac{\mathcal{D}\Gamma}{c} \frac{|\partial_\theta (R\cos\theta)|}{\sqrt{(\partial_\theta R)^2 + R^2}}.$$

Assuming that the jet is propagating at a constant speed $\beta(\theta)$, we can write:

$$R(\theta) \sim c t_{em} \beta(\theta).$$

Therefore:

$$\begin{aligned} F_\nu(t) \propto & \frac{D^2(\theta)}{\Gamma(\theta)} \epsilon(\theta) S[\nu/\mathcal{D}(\theta)] \frac{\sqrt{(\partial_\theta \beta(\theta))^2 + \beta^2(\theta)}}{|\partial_\theta(\beta(\theta)\cos\theta)|} \beta(\theta)\sin\theta \\ & \times \begin{cases} 1 & , \tau(\theta) \ll 1 \\ \dfrac{1}{\sqrt{(\partial_\theta \beta(\theta))^2 + \beta^2(\theta)}} \partial_\theta(\beta(\theta)\sin\theta) & , \tau(\theta) \gg 1 \end{cases}. \end{aligned} \tag{B.1}$$

Here the angular variable θ is related to the observer time by $t = t_{em}(1 - \beta(\theta)\cos\theta)$. Therefore to each observer time we can associate a specific angle $\theta(t)$. In the limit of $\tau(\theta) \gg 1$, the above expression does not corresponds to the eq. (A6) of Oganesyan, 2020 (O20), since the authors, in eq. (A1) and (A2), approximate i) the projection factor $P(\theta) = \cos\theta$, and ii) the element of surface as $dS = R^2 \sin\theta d\theta$, obtaining

$$F_\nu(t) \propto \int I'_{\nu'} D^3(\theta) P(\theta) dS \propto \int I'_{\nu'} D^3(\theta) R^2 \sin\theta\cos\theta d\theta.$$

Though, conditions i) and ii) are valid only in the limit of a spherical approximation $R(\theta)$ =const. Taking correctly into account the jet curvature, the quantity $R^2 \cos\theta \sin\theta$ should be replaced with the more generic one $\partial_\theta(R(\theta)\sin\theta)R(\theta)\sin\theta$. Indeed, as a consistency check, it can be verified that, for $\tau \gg 1$, eq. (A6) of O20 corresponds to eq. B.1 in the limit of

$$\partial_\theta(\beta(\theta)\sin\theta) \to \beta(\theta)\cos(\theta),$$

valid only if $\beta(\theta) \sim$ const and not true for structured jets. The contribution of the term $\partial_\theta(\beta(\theta)\sin\theta)$ becomes not negligible when $\partial_\theta(\beta(\theta)\sin\theta) \to 0$, namely when the azimuthal height of the jet $y(\theta) = R(\theta)\sin\theta \sim$ const and the jet surface is tangent to the line of sight. Notice that neither in the limit $\tau \ll 1$, (A6) of O20 corresponds to eq. B.1, since

$$P(\theta)dS = R^2\sqrt{1+(\partial_\theta \ln R)^2}\sin\theta d\theta \neq R^2 \sin\theta\cos\theta d\theta.$$

Hereafter, if not specified otherwise, we adopt eq. B.1 in the limit of optically thin medium.

B.2 Features of the X-ray plateau from a structured jet

Here we show how to derive basic relations between the jet structure parameters and the X-ray plateau characteristics, such as duration and luminosity. For the computation of the luminosity, we notice that the appearance of the plateau in the HLE light curve occurs always after a steep decay phase. In the HLE framework, the steep decline is expected in the limit of a spherical surface, therefore the transition between steep decay and plateau occurs when the jet structure starts to deviate from the spherical approximation. If the jet core is identified by a characteristic value θ_c, such that $\Gamma(\theta < \theta_c) \sim$ const, then the plateau luminosity will be roughly the luminosity of the light curve at $t = t(\theta_c)$. Hence

$$\frac{F_\nu\left(t\left(\theta_c\right)\right)}{F_\nu\left(t\left(\theta_0\right)\right)} \sim \cos\theta_c \left(\frac{1-\beta}{1-\beta\cos\theta_c}\right)^{1+s} \underset{\beta\sim1,\theta_c\ll1}{\longrightarrow} \left(\theta_c\Gamma_0\right)^{-2(1+s)},$$

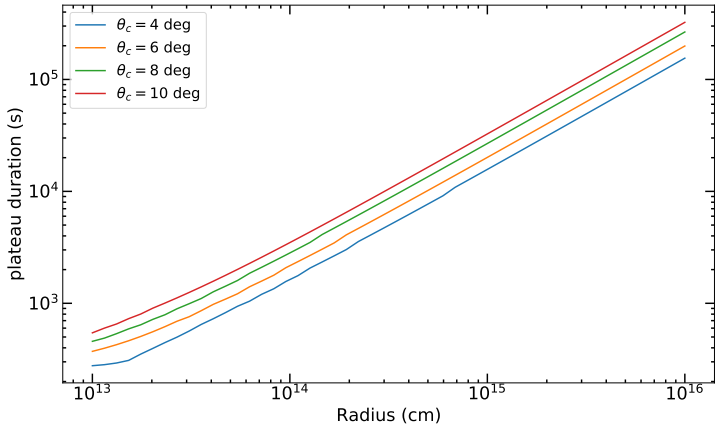

FIGURE B.1: Dependence of the plateau duration on both the core radius R_0 and the core aperture θ_c.

with $\Gamma_0 = \Gamma(\theta = 0)$ and s is the low-energy spectral slope of the prompt emission spectrum [1]. Since the average value of the low-energy photon index is ~ 1, then it is reasonable to take $s \sim 0$. The expression above allows us to write the X-ray plateau luminosity as a function of the peak prompt luminosity as

$$L_X \sim \lambda(s, \nu_p) L_{peak} \left(\theta_c \Gamma_0\right)^{-2},$$

where $\lambda(s, \nu_p)$ is the fraction of prompt energy that is emitted in X-rays. Thus, the plateau luminosity appears to be strongly dependent on θ_c and Γ_0, but the dependence on the assumed jet structure outside the core is negligible.

On the other hand, it turns out that the plateau duration depends on all the parameters of the jet structure. By the use of numerical evaluation of eq. B.1, one can verify that, once the structure profile is fixed, the plateau duration mainly depends on $R_0 = R(\theta = 0)$ and more mildly on the core aperture angle. The dependence on Γ_0 is completely negligible. It can be verified numerically than the following relation holds:

$$t_p \propto R_0^n \theta_c^m,$$

with $n \sim 1$ and $0.5 \lesssim m \lesssim 1$. As an example, we show in Fig. B.1 the dependence of the plateau duration on both the core radius R_0 and the core

[1] The expression is valid as long as the peak energy $\nu_p \gg \nu_X$ throughout the steep decay

	Ghirlanda et al., 2019b	Mooley et al., 2022
θ_v	$15^{+1.5}_{-1.0}$	$21.89^{+3.35}_{-2.89}$
θ_c	$3.4^{+1.0}_{-1.0}$	$4.9^{+1.2}_{-1.2}$
s	$3.5^{+2.1}_{-1.7}$	$1.8^{+3.20}_{-1.53}$
$\log \Gamma_0$	$2.4^{+0.5}_{-0.4}$	$2.93^{+0.95}_{-1.35}$

TABLE B.1: Jet structure best fit values adopted in this section, taken from Ghirlanda et al., 2019a and Mooley et al., 2022.

aperture θ_c. For the structure we assume a power law profile with slope $s = 2.5$ and $\Gamma_0 = 100$.

B.3 On the compactness related to the prompt emission from a structured jet

Here we specify what are the physical conditions such that a patch of a structured jet is optically thin and therefore the emitted radiation can escape from the medium. Hereafter we follow the approach of Matsumoto et al., 2019. Let us consider a jet with a given Lorentz factor structure $\Gamma(\hat{\theta})$. The jet axis is inclined by an angle θ_v with respect to the line of sight. We define the polar coordinate θ measured from the line of sight, while $\hat{\theta}$ is measured from the jet axis (i.e., $\hat{\theta} = \theta + \theta_v$). At each angle, three main sources of opacity should be considered during the prompt emission: A) $\gamma\gamma$ annihilation, B) scattering due to pair production, C) electron scattering.

For a jet with a given structure and luminosity, the combination of this components defines an effective angle-dependent optical depth $\tau(\theta, \Gamma(\theta))$, given by eq. 23 in Matsumoto et al., 2019. Hence, the regions of the jet which contribute to the observed emission are those that satisfy $\tau(\theta, \Gamma(\theta)) > 1$. In other words, the last condition defines a region in the (Γ, θ) plane for which $\tau > 1$ and the radiation can escape.

As an exercise, we test whether the γ-ray flash observed for GRB 170817A can be indeed produced by a structured jet seen off-axis. For the estimation of the jet structure and viewing angle we use the results from Ghirlanda et al., 2019b and Mooley et al., 2022, which are the ones that include in their

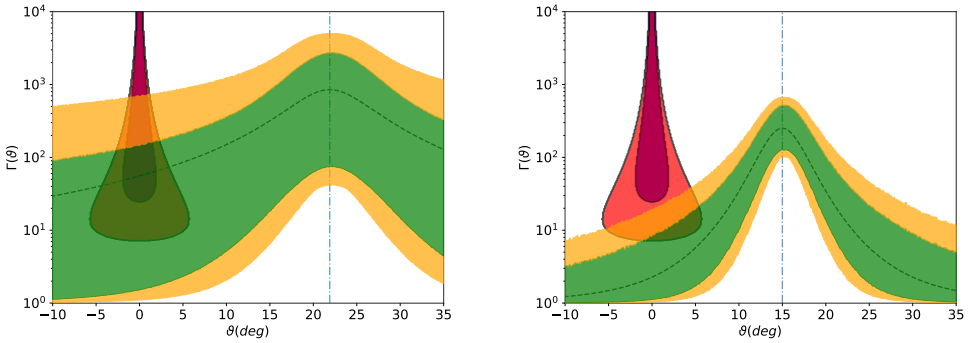

FIGURE B.2: Intersection between the allowed region imposed by the transparency condition (light and dark red contours) and the confidence region of the plane $\Gamma - \theta$ found in Ghirlanda et al., 2019c (right) and Mooley et al., 2022 (left). The green and yellow bands define the 68% and the 95% confidence regions for the structure $\Gamma(\theta)$.

analysis both multi-band afterglow data and VLBI measurement of the radio image centroid. Both the works assume a power law structure in the form:

$$\Gamma(\theta) = 1 + (\Gamma_0 - 1)\,\frac{1}{\left[1 + \left(\frac{\vartheta}{\vartheta_c}\right)^a\right]^{s/a}},$$

with $a = 1$ for the first work and $a = 2$ for the second one. The results are reported in Fig. B.2. The green and yellow bands define the 68% and the 95% confidence regions for the structure $\Gamma(\theta)$. They are obtained extracting randomly the structure parameters and the viewing angle, assuming for each parameter a uniform distribution in the 1σ confidence interval. The dashed line is the fiducial structure profile. The vertical dot-dashed line is the fiducial viewing angle. With dark- and light-red we report the allowed (Γ, θ) region defined by conditions B) and C) mentioned above, respectively, which are the most stringent for low-luminosity events like GRB 170817A. For the computation of the optical depth, we use the same parameters adopted in Matsumoto et al., 2019 for GRB 170817. In this specific case, the region defined by condition C) is completely enclosed by the region defined by condition B). The absence of an intersection between the (Γ, θ) allowed region and the structure confidence region would mean that from no part of the jet the radiation can escape, implying that the γ-ray flash cannot be originated from a structured jet seen off-axis. On the other hand, if an intersection exists, such region defines an interval of angles $\theta \in [\theta_{\rm min}, \theta_{\rm max}]$

from which the radiation can escape and arrive to the observer. We notice that for the jet structure and viewing angle derived from Ghirlanda et al., 2019b, there is no intersection with condition C), while for the parameters of Mooley et al., 2022 the intersection exists[2]. In this last case, the observed γ-ray flash would be produced by a small region (few deg wide) of the jet aligned along the line of sight, provided that this patch of the jet moves at $\Gamma(\theta_v) \gtrsim 8$ ($\Gamma(\theta_v) \gtrsim 20$) considering case B (case C).
This example could be extended for a generic GRB with a given jet structure and given observational properties. In general, when the prompt emission from a structured jet is computed, an additional term $e^{-\tau(\theta,\Gamma(\theta))}$ should be taken into account. Therefore the observed flux would be given by:

$$F_\nu(t) = \int_{\text{EATS}} R^2(\theta) I'_\nu e^{-\tau(\theta)} \mathcal{D}^3(\theta) \sin\theta \cos\theta d\theta,$$

where I'_ν is the comoving emissivity.

[2]This occurs because in the second work a much larger uncertainty on Γ_0 is derived. corresponding to an uncertainty of almost two orders of magnitude for $\Gamma(\hat{\theta} = \theta_v)$

Appendix C

Here we report some additional computations used in Chapter 5, in particular regarding the contribution of Synchrotron self Compton for the cooling of particle during the afterglow phase. The following results are necessary to justify our assumptions regarding the dominating cooling regime during the plateau phase.

C.1 The role of the Y parameter

Following Sari and Esin, 2001, here we estimate how the Y parameter adopted in eq. 5.3 can influence the ratio ν_c/ν_m and hence determine the cooling regime. The Y parameter is defined as the ratio between the SSC and synchrotron luminosities:

$$Y = \frac{L_{\rm SSC}}{L_{\rm syn}} = \frac{\eta_e \epsilon_e}{\epsilon_B (1+Y)},$$

where

$$\eta_e = \begin{cases} 1, & \text{fast cooling} \\ \left(\frac{\gamma_c}{\gamma_m}\right)^{2-p}, & \text{slow cooling} \end{cases},$$

from which

$$Y = \begin{cases} \frac{\eta_e \epsilon_e}{\epsilon_B}, & \frac{\eta_e \epsilon_e}{\epsilon_B} \ll 1 \\ \left(\frac{\eta_e \epsilon_e}{\epsilon_B}\right)^{1/2}, & \frac{\eta_e \epsilon_e}{\epsilon_B} \gg 1 \end{cases}$$

Let us define $\nu_c/\nu_m = (\gamma_c/\gamma_m)^2 = R$. Since R depends on Y, which in turn can depend on R, we check a posteriori the value of R, depending on the value of Y. As reference, we assume as fiducial values $\epsilon_e = 0.1$ and $\epsilon_B = 10^{-3}$.

1. Let us assume that we are in slow cooling. Then $R > 1$. We can have:

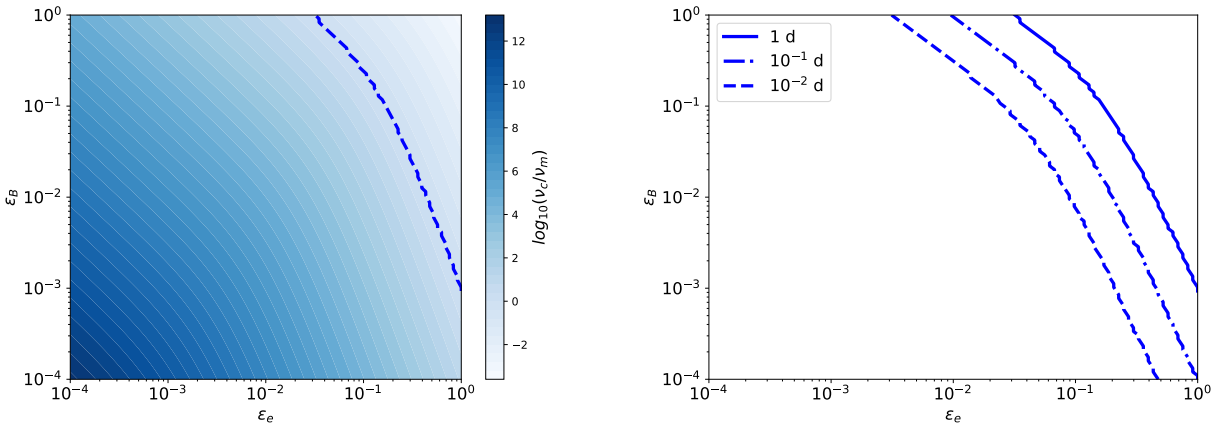

(a) (b)

FIGURE C.1: Panel (a): Contour plot of the value of $R = \nu_c/\nu_m$ as a function of ϵ_e and ϵ_B. The dashed line correspond to the combination of ϵ_e and ϵ_B which give R=1. The region on the right identifies the fast cooling regime. Panel (b): Lines in the $[\epsilon_e, \epsilon_B]$ plane where $R = \nu_c/\nu_m = 1$. Each line is computed at different times. The region of the plane on the right of the line identifies the combinations of $[\epsilon_e, \epsilon_B]$ which give a fast cooling regime..

(a) $Y \ll 1$, namely $\eta_e \epsilon_e/\epsilon_B \ll 1$, which gives $R \ll \left(\frac{\epsilon_e}{\epsilon_B}\right)^{\frac{2}{p-2}}$. This condition, for $p > 2$, is compatible with the value of R derived from eq. 5.3 (R$\sim 10^5$), hence not is contradiction with a slow cooling regime. In other words, slow cooling and negligible SSC can co-exist in the condition $1 < R \ll \left(\frac{\epsilon_e}{\epsilon_B}\right)^{\frac{2}{p-2}}$.

(b) $Y \gg 1$, namely $\eta_e \epsilon_e/\epsilon_B \gg 1$, leading to $R \gg \left(\frac{\epsilon_e}{\epsilon_B}\right)^{\frac{2}{p-2}} \gg 1$. Though, if we plug the expression of $Y = \sqrt{R^{\frac{2-p}{2}} \frac{\epsilon_e}{\epsilon_B}}$ into eq. 5.3, we obtain

$$R \sim \left(10^5 \frac{\epsilon_B}{\epsilon_e}\right)^{\frac{1}{2-p/2}} \ll \left(\frac{\epsilon_e}{\epsilon_B}\right)^{\frac{2}{p-2}}$$

which brings to a contradiction. This means that, for the assumed values of ϵ_e and ϵ_B, the condition $Y \gg 1$ is incompatible with a slow cooling regime.

2. Let us assume that we are in fast cooling. Therefore $\eta_e = 1$ and $Y =$

$\sqrt{\epsilon_e/\epsilon_B} = 10$. Substituting Y in eq. 5.3 we get $R \sim 10^3$, which is contradiction with the assumption of a fast cooling

Summarising, with the assumed values of ϵ_e and ϵ_B, the only acceptable combination is $Y \ll 1$ and slow cooling regime.
More generally, the value of R can be found as a function of ϵ_e and ϵ_B solving numerically the implicit function defined by eq. 5.3, where $R = R(\epsilon_e, \epsilon_B, Y(R, \epsilon_e, \epsilon_B))$. The result is shown in Fig. C.1(a), where we have fixed $t_d = 1$ and $n = 1$ cm^{-3}. The color bar indicates the ratio R and the blue dashed line divides the plane between the slow cooling (bottom left) and the fast cooling (top right) regimes. The plot shows that, for the assumed fiducial values $\epsilon_e = 0.1$ and $\epsilon_B = 10^{-3}$, we are on the left of the dashed line, therefore in the slow cooling regime. Fig. C.1(b) shows the same dividing line at three different times, $t = 10^{-2}$ d, $t = 10^{-1}$ d and $t = 1$ d. It is evident that at early times the region of the $[\epsilon_e, \epsilon_B]$ plane which gives a fast cooling is larger. Though, for the assumed fiducial values $\epsilon_e = 0.1$ and $\epsilon_B = 10^{-3}$ at early times we are still in slow cooling regime. Notice that the results shown in this section do not rule out the fast cooling regime, but rather demonstrate that the slow cooling is more plausible, since there exist more combinations of ϵ_e and ϵ_B which give $\nu_c > \nu_m$. For this reason, since the fast cooling cannot be rejected, in section 5.2.2 we interpret our data in both cooling regimes.

Appendix D

Here we report further details about the theoretical modelling adopted in Chapter 6, specifically for the BNS population and how it relates with the short GRB population, the computation of the prompt emission obsevables and the dependence of our results on the NS mass distribution.

D.1 BNS population synthesis model

Here, we specify the details of the assumptions adopted for the population synthesis model. The simulated BNS population is produced following the method described in Santoliquido et al., 2021. The authors make use of the COSMO$\mathcal{R}$ATE code, which adopts the star formation rate density and average metallicity evolution of the Universe from Madau and Fragos, 2017. We assume a metallicity spread $\sigma_Z = 0.3$. Redshift evolution and overall normalization of BNS merger density depend on several assumptions regarding the common envelope prescription (parametrized by the common envelope ejection efficiency α_{CE}), the natal kick model, the supernova explosion, the mass transfer via accretion, and the shape of the initial mass function. Here, we describe electron-capture supernovae as in Giacobbo and Mapelli, 2019 and assume the delayed supernova model (Fryer et al., 2012) to decide whether a core-collapse supernova produces a black hole or a neutron star.
When a neutron star forms from either a core-collapse or an electron-capture supernova, we randomly draw its mass according to an uniform distribution between 1 and 2.5 $M_\odot$. We generate the natal kicks according to $v_{kick} \propto m_{ej}/m_{rem}\, v_{H05}$, where m_{ej} is the mass of the ejecta, m_{rem} is the mass of the compact remnant (neutron star or black hole) and v_{H05} is a random number extracted from a Maxwellian distribution with one-dimensional root-mean square $\sigma = 265$ km s^{-1} (Hobbs et al., 2005). This formalism ensures low kicks for most electron-capture and ultra-stripped supernovae (Giacobbo and Mapelli, 2020). We assume a value of $\alpha_{CE} = 3$ for common envelope, we calculate the concentration parameter λ as in

Claeys et al., 2014 and the mass transfer formalism from Hurley et al., 2002. We draw the mass of the progenitor primary star from a Kroupa mass function (Kroupa, 2001). For the initial mass ratios, orbital periods and eccentricities we use the distributions inferred by Sana et al., 2012.

D.2 How fj depends on the BNS population

f_j is defined as the fraction of BNS which gives a successful jet. Thus, defining $\dot{\rho}_{\rm BNS}\,(z)$ the merger rate density in units of $Gpc^{-3}yr^{-1}$, then the GRB rate density is

$$\dot{\rho}_{GRB} = f_j \dot{\rho}_{BNS}.$$

The observed rate of GRB detection is:

$$R \propto \int dz f_j \frac{\dot{\rho}_{\rm BNS}}{1+z} \cdot \frac{dV_c}{dz} \int_{L_{\rm min}\,(z)}^{\infty} \varphi(L) dL, \tag{D.1}$$

where $\varphi(L)$ is the luminosity function and L_{min} is defined as:

$$L_{min}(z) = 4\pi D_L^2(z) k(z) S,$$

with S the minimum detectable flux of the instrument and $k(z)$ the k-correction. In our approach, the model is calibrated in such a way that $\langle R \rangle$ corresponds to the average rate observed by Fermi. This method defines the best value of f_j as well as the other model parameters and once they are known $\varphi(L)$ is uniquely defined. Hence the derived f_j and $\varphi(L)$ depend on the assumed $\dot{\rho}_{BNS}(z)$.
Here we show how f_j changes adopting a different $\dot{\rho}_{BNS}(z)$. Without rerunning the Monte Carlo for the full exploration of the parameter space, we can provide an order-of-magnitude estimate through analytical computations. Let us call $\hat{\rho}_{\rm BN\,S}(z) = \hat{\rho}_0 \cdot \hat{r}(z)$ the new population, such that $\hat{\rho}_0$ defines the local rate and $\hat{r}(z = 0) = 1$. Imposing the condition $R\Big|_{\rho_{\rm BNS}} = R\Big|_{\hat{\rho}_{\rm BNS}}$

$$\Rightarrow \int dz f_j \frac{\rho_{\rm BNS}}{1+z} \frac{dV_c}{dz} \int dL \varphi(L) = \int dz \hat{f}_j \frac{\hat{\rho}_{\rm BNS}}{1+z} \frac{dV_c}{dz} \int dL \varphi(L).$$

Notice that f_j and $\varphi(t)$ are degenerate, namely for a given ρ_{BNS} and $\langle R \rangle$,

there is not a unique combination of f_j and $\varphi(L)$ that satisfies eq. D.1. Therefore we assume for simplicity that $\varphi(L)$ is known a priori [1]. Under this assumption, we can distinguish two cases:

1. $r(z) = \hat{r}(z)$ but $\rho_0 \neq \hat{\rho}_0$, hence

$$\Rightarrow f_j \rho_0 = \hat{f}_j \hat{\rho}_0 \Rightarrow \hat{f}_j = f_j \, (\rho_0 / \hat{\rho}_0) \, ;$$

2. both $r(z) \neq \hat{r}(z)$ and $\rho_0 \neq \hat{\rho}_0$, in which case:

$$\Rightarrow \hat{f}_j = f_j \frac{\rho_0}{\hat{\rho}_0} \frac{\int dz \frac{r(z)}{1+z} \frac{dV_c}{dz} \int \varphi(L) dL}{\int dz \frac{\hat{r}(z)}{1+z} \frac{dV_c}{dz} \int \varphi(L) dL}.$$

D.3 Computation of the observables in the structured jet scenario

In this section we show how the peak flux, the fluence and the isotropic energy are derived in the structured jet framework. The derivation is done assuming a unique jet structure, with fixed values of R_0 and Γ, defined in the main text. For a given viewing angle θ, we write the rest frame photon spectrum as

$$N(E, \theta, t) = N_0(\theta, t) f(E / E_0(\theta, t)), \tag{D.2}$$

where we included the time dependency only in the normalization, assuming that there is not a strong spectral evolution during the GRB pulse. $f(E/E_0(\theta))$ is the spectral shape and it is assumed to be a smoothly broken power law, whose spectral slopes are assumed to be angle independent. f is normalized in such a way that $f(1) = 1$. $E_0(\theta, t)$ is the peak energy and we express it as

$$E_0(\theta, t) = E_0(\theta, t = t_p) P_E(t/t_p, \theta), \tag{D.3}$$

where t_p is the peak time of the pulse and $P(t/t_p\theta)$ describes the temporal profile, in principle angle-dependent. Analogously, we express the time behaviour of the photon spectrum normalization as:

$$N_0(\theta, t) = N_0^p(\theta) P_N(t/t_p, \theta). \tag{D.4}$$

[1] reliable parameters can be taken from Ghirlanda et al., 2016b

In both cases, we approximate the temporal profiles of peak energy and normalization as

$$P_X(t) = \begin{cases} t/t_p & 0 < t < t_p \\ (t/t_p)^{-\alpha_X(\theta)} & t > t_p \end{cases} \quad X = E, N. \tag{D.5}$$

At the peak time we write the photon spectrum as

$$N^p(E,\theta) = N_0^p(\theta) f(E/E_0(\theta)). \tag{D.6}$$

We define also

$$R_E(\theta) = E_0(\theta)/E_0(\theta = 0) = E_0(\theta)/\hat{E}_0 \tag{D.7}$$

and

$$R_F(\theta) = \frac{N^p(\theta)|_{E=E_0(\theta)}}{\hat{N}^p|_{E=\hat{E}_0}}. \tag{D.8}$$

The functions $\alpha_E(\theta)$, $\alpha_N(\theta)$, $R_E(\theta)$ and $R_F(\theta)$ are computed numerically using the structured jet model. Hereafter the notation $\hat{x}$ indicates that the quantity x is evaluated at viewing angle $\theta = 0$. In the observer frame, the peak photon spectrum is:

$$N^p(E,\theta) = (1+z)^2 N_0^p(\theta) f\left(\frac{1}{R_E}\frac{(1+z)E}{\hat{E}_0}\right) \tag{D.9}$$

and using eq. D.8

$$N^p(E,\theta) = (1+z)^2 \hat{N}_0^p R_F f\left(\frac{1}{R_E}\frac{(1+z)E}{\hat{E}_0}\right). \tag{D.10}$$

The value of $\hat{N}_0^p$ is derived from the rest frame on-axis isotropic energy $\hat{E}_{\rm iso} = E_t/(1-\cos\theta_c)$, where E_t is extracted from the assumed probability distribution defined in the main text. In the specific,

$$\hat{E}_{\rm iso} = 4\pi D_L^2 \int dt \int_{1\ {\rm keV}}^{10^4\ {\rm keV}} F_\nu(t) dE, \tag{D.11}$$

where D_L is the luminosity distance and F_ν is the flux density. Using eq. D.6:

$$\hat{E}_{\rm iso} = 4\pi D_L^2 \int dt \hat{N}_0(t) \hat{E}_0^2(t) \int_{1\ {\rm keV}/\hat{E}_0(t)}^{10^4\ {\rm keV}/\hat{E}_0(t)} x f(x) dx, \tag{D.12}$$

which can be written as

$$\hat{E}_{\rm iso} = 4\pi D_L^2 \hat{N}_0^p \int \hat{P}_N(t/t_p)\hat{E}_0^2(t) I_E(t) dt, \tag{D.13}$$

where $I_E(t) = \int_{1\ {\rm keV}/\hat{E}_0(t)}^{10^4\ {\rm keV}/\hat{E}_0(t)} x f(x) dx$.

This procedure allows us to write $\hat{N}_0^p$ in terms of known quantities, namely

$$\hat{N}_0^p = \frac{\hat{E}_{\rm iso}}{4\pi D_L^2 \int \hat{P}_N(t/t_p)\hat{E}_0^2(t) I_E(t) dt}. \tag{D.14}$$

Once $\hat{N}_0^p$ is determined, the peak photon flux integrated in the energy band of a given instrument is

$$F_p(\theta) = \int_{(1+z)E_1}^{(1+z)E_2} N^p(E,\theta) dE \tag{D.15}$$

$$= (1+z)\hat{N}_0^p R_F(R_E \hat{E}_0) \int_{(1+z)E_1/R_E\hat{E}_0}^{(1+z)E_2/R_E\hat{E}_0} f(x) dx. \tag{D.16}$$

The duration of the burst t_{90} is computed imposing that the 10-1000 keV fluence accumulated up to t_{90} is 90% of the total fluence, namely

$$\int_0^{t_{90}} dt \int_{(1+z)\ {\rm keV}}^{(1+z)10^4\ {\rm keV}} EN(E,\theta,t) dE \tag{D.17}$$

$$= 90\% \int_0^{\infty} dt \int_{(1+z)\ {\rm keV}}^{(1+z)10^4\ {\rm keV}/} EN(E,\theta,t) dE. \tag{D.18}$$

For computational reasons, the last integral in time is performed up to a time t_{max}, which is the maximum time for which the γ-ray emission is still detectable by the instrument. Finally the isotropic luminosity is defined as $E_{\rm iso}/t_{90}$.

D.4 Detection efficiency for different neutron-star mass distribution

In Fig. D.1 we show the detection efficiency (detected signals over injected ones) of ET as a function of redshift for a Gaussian mass distribution as observed in Galactic double neutron-star systems in radio (Özel and Freire,

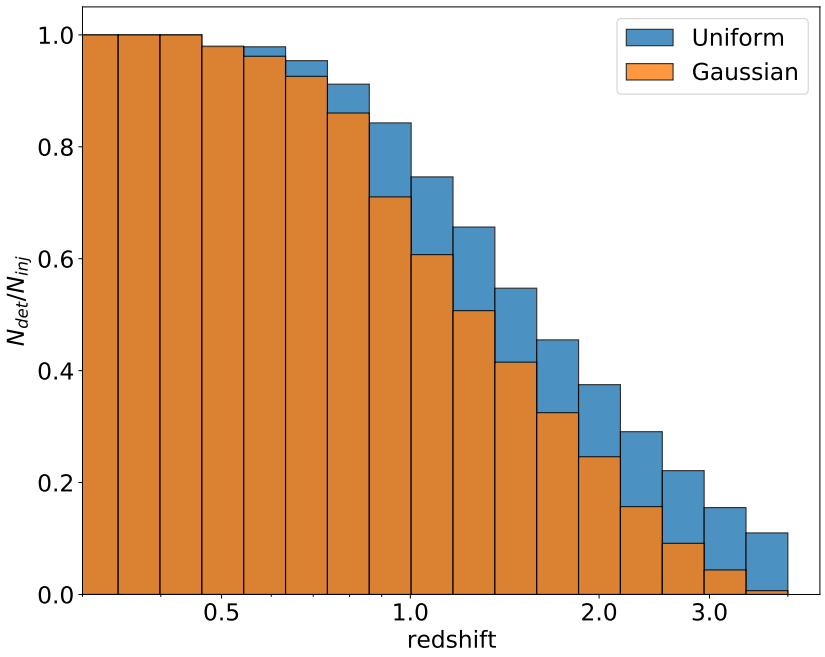

FIGURE D.1: Detection efficiency of ET as a function of redshift assuming a Gaussian distribution ($\langle M \rangle = 1.33 M_{\odot}$, $\sigma_M = 0.1 M_{\odot}$) and a uniform distribution ($M \in [1.0 - 2.5] M_{\odot}$). Only cases with $\theta_v < 15°$ are considered. A duty cycle of 0.85 has been assumed for the GW detectors as described in the text. The ratio between the orange bars and the blue bars corresponds to the function $\phi(z)$ defined in the text.

2016) and a uniform distribution of NS mass consistent with gravitational waves observations (The LIGO Scientific Collaboration et al., 2021b). For the Gaussian distribution we fixed the mean value to $\langle M \rangle = 1.33 M_{\odot}$ and the standard deviation to $\sigma_m = 0.1 M_{\odot}$. The detection efficiency obtained with the two distributions is consistent up to a redshift equal to 0.5, and then the Gaussian distribution leads to a lower number of GW detections accountable by the fact that the GW signal amplitude scales with the mass.

In order to evaluate the impact on joint detections, we estimate, as example, the loss of joint GW+γ-rays detections with ET+*Fermi-GBM*. We assume the probability of having a joint detection as

$$P_{JD}(z) = P_{EM}(z) P_{GW}(z),$$

where $P_{EM}(z)$ is the probability of detecting the EM counterpart, and

$P_{GW}(z)$ the probability of detecting the associated GW signal. Each probability corresponds to the ratio between the number of detected and injected sources.

$$P_i(z) = \frac{N_{det,i}(z)}{N_{inj}(z)},\ i = GW, EM.$$

The assumption of NS mass distribution only affects $P_{GW}(z)$, since we specified in the main text that we neglect any dependence on the NS mass for the formation of a jet. We call $P_{GW,flat}(z)$ and $P_{GW,Gauss}(z)$ the GW detection efficiency for flat and Gaussian distributions, respectively. The variation on the rate of joint detections can be computed as

$$\frac{dN_{JD,Gauss}}{dz}(z) = \frac{dN_{inj}(z)}{dz} P_{JD,Gauss}(z) =$$

$$= \phi(z) \frac{dN_{inj}(z)}{dz} P_{EM}(z) P_{GW,flat}(z) = \phi(z) \frac{N_{JD,flat}}{dz},$$

where we wrote $P_{GW,Gauss}(z) = \phi(z) P_{GW,flat}(z)$. The total variation, integrated in redshift, is

$$N_{JD,Gauss} = \int \phi(z) \frac{N_{JD,flat}}{dz} dz.$$

In Fig.D.1 the function $\phi(z)$ corresponds to the ratio between the two histograms. Finally, knowing the function $\phi(z)$ and the redshift distribution of joint detections, we derive the variation in joint detection rate for a Gaussian mass distribution. We obtain that the joint GW+γ-rays detections with ET+*Fermi-GBM* decreases of a factor $\sim$ 27% (from 33/yr to 24/yr), assuming a Gaussian mass distribution.

Bibliography

Abbott, B. et al. (June 2008). "Astrophysically triggered searches for gravitational waves: status and prospects". In: *Classical and Quantum Gravity* 25.11, 114051, p. 114051. DOI: 10.1088/0264-9381/25/11/114051. arXiv: 0802.4320 [gr-qc].

Abbott, B. P. et al. (Feb. 2016). "Observation of Gravitational Waves from a Binary Black Hole Merger". In: 116.6, 061102, p. 061102. DOI: 10.1103/PhysRevLett.116.061102. arXiv: 1602.03837 [gr-qc].

Abbott, B. P. et al. (Feb. 2017a). "Exploring the sensitivity of next generation gravitational wave detectors". In: *Classical and Quantum Gravity* 34.4, 044001, p. 044001. DOI: 10.1088/1361-6382/aa51f4. arXiv: 1607.08697 [astro-ph.IM].

Abbott, B. P. et al. (Oct. 2017b). "Gravitational Waves and Gamma-Rays from a Binary Neutron Star Merger: GW170817 and GRB 170817A". In: 848, L13, p. L13. DOI: 10.3847/2041-8213/aa920c. arXiv: 1710.05834 [astro-ph.HE].

— (Oct. 2017c). "GW170817: Observation of Gravitational Waves from a Binary Neutron Star Inspiral". In: *Physical Review Letters* 119.16, 161101, p. 161101. DOI: 10.1103/PhysRevLett.119.161101. arXiv: 1710.05832 [gr-qc].

— (Oct. 2017d). "Multi-messenger Observations of a Binary Neutron Star Merger". In: 848, L12, p. L12. DOI: 10.3847/2041-8213/aa91c9. arXiv: 1710.05833 [astro-ph.HE].

Abbott, B. P. et al. (June 2017e). "Search for Gravitational Waves Associated with Gamma-Ray Bursts during the First Advanced LIGO Observing Run and Implications for the Origin of GRB 150906B". In: 841.2, 89, p. 89. DOI: 10.3847/1538-4357/aa6c47. arXiv: 1611.07947 [astro-ph.HE].

Abbott, B. P. et al. (Nov. 2019). "Search for Gravitational-wave Signals Associated with Gamma-Ray Bursts during the Second Observing Run of Advanced LIGO and Advanced Virgo". In: 886.1, 75, p. 75. DOI: 10.3847/1538-4357/ab4b48. arXiv: 1907.01443 [astro-ph.HE].

Abbott, B. P. et al. (Sept. 2020a). "Prospects for observing and localizing gravitational-wave transients with Advanced LIGO, Advanced Virgo

and KAGRA". In: *Living Reviews in Relativity* 23.1, 3, p. 3. DOI: 10.1007/s41114-020-00026-9.

Abbott, B. P. et al. (Sept. 2020b). "Prospects for observing and localizing gravitational-wave transients with Advanced LIGO, Advanced Virgo and KAGRA". In: *Living Reviews in Relativity* 23.1, 3, p. 3. DOI: 10.1007/s41114-020-00026-9.

Abbott, R. et al. (Apr. 2021a). "GWTC-2: Compact Binary Coalescences Observed by LIGO and Virgo during the First Half of the Third Observing Run". In: *Physical Review X* 11.2, 021053, p. 021053. DOI: 10.1103/PhysRevX.11.021053. arXiv: 2010.14527 [gr-qc].

Abbott, R. et al. (May 2021b). "Population Properties of Compact Objects from the Second LIGO-Virgo Gravitational-Wave Transient Catalog". In: 913.1, L7, p. L7. DOI: 10.3847/2041-8213/abe949. arXiv: 2010.14533 [astro-ph.HE].

Abbott, R. et al. (July 2021c). "Search for Gravitational Waves Associated with Gamma-Ray Bursts Detected by Fermi and Swift during the LIGO-Virgo Run O3a". In: 915.2, 86, p. 86. DOI: 10.3847/1538-4357/abee15. arXiv: 2010.14550 [astro-ph.HE].

Abbott, R. et al. (Apr. 2022a). "Search for Gravitational Waves Associated with Gamma-Ray Bursts Detected by Fermi and Swift during the LIGO-Virgo Run O3b". In: 928.2, 186, p. 186. DOI: 10.3847/1538-4357/ac532b. arXiv: 2111.03608 [astro-ph.HE].

— (Apr. 2022b). "Search for Gravitational Waves Associated with Gamma-Ray Bursts Detected by Fermi and Swift during the LIGO-Virgo Run O3b". In: 928.2, 186, p. 186. DOI: 10.3847/1538-4357/ac532b. arXiv: 2111.03608 [astro-ph.HE].

Abdalla, H. et al. (Nov. 2019). "A very-high-energy component deep in the γ-ray burst afterglow". In: 575.7783, pp. 464–467. DOI: 10.1038/s41586-019-1743-9. arXiv: 1911.08961 [astro-ph.HE].

Abdo, A. A. et al. (Nov. 2009). "Fermi Observations of GRB 090902B: A Distinct Spectral Component in the Prompt and Delayed Emission". In: 706.1, pp. L138–L144. DOI: 10.1088/0004-637X/706/1/L138. arXiv: 0909.2470 [astro-ph.HE].

Acciari, V. A. et al. (Feb. 2021). "MAGIC Observations of the Nearby Short Gamma-Ray Burst GRB 160821B". In: 908.1, 90, p. 90. DOI: 10.3847/1538-4357/abd249. arXiv: 2012.07193 [astro-ph.HE].

Acernese, F. et al. (Jan. 2015). "Advanced Virgo: a second-generation interferometric gravitational wave detector". In: *Classical and Quantum Gravity* 32.2, 024001, p. 024001. DOI: 10.1088/0264-9381/32/2/024001. arXiv: 1408.3978 [gr-qc].

Ackley, K. et al. (Nov. 2020). "Neutron Star Extreme Matter Observatory: A kilohertz-band gravitational-wave detector in the global network". In: 37, e047, e047. DOI: 10.1017/pasa.2020.39. arXiv: 2007.03128 [astro-ph.HE].

Aharonian, F. A. et al. (Mar. 1997). "The potential of ground based arrays of imaging atmospheric Cherenkov telescopes. I. Determination of shower parameters". In: *Astroparticle Physics* 6.3-4, pp. 343–368. DOI: 10.1016/S0927-6505(96)00069-2.

Ajello, M. et al. (June 2019). "A Decade of Gamma-Ray Bursts Observed by Fermi-LAT: The Second GRB Catalog". In: 878.1, 52, p. 52. DOI: 10.3847/1538-4357/ab1d4e. arXiv: 1906.11403 [astro-ph.HE].

Aleksić, J. et al. (Jan. 2016a). "The major upgrade of the MAGIC telescopes, Part I: The hardware improvements and the commissioning of the system". In: *Astroparticle Physics* 72, pp. 61–75. DOI: 10.1016/j.astropartphys.2015.04.004. arXiv: 1409.6073 [astro-ph.IM].

Aleksić, J. et al. (Jan. 2016b). "The major upgrade of the MAGIC telescopes, Part II: A performance study using observations of the Crab Nebula". In: *Astroparticle Physics* 72, pp. 76–94. DOI: 10.1016/j.astropartphys.2015.02.005. arXiv: 1409.5594 [astro-ph.IM].

Amati, L. et al. (July 2002). "Intrinsic spectra and energetics of BeppoSAX Gamma-Ray Bursts with known redshifts". In: 390, pp. 81–89. DOI: 10.1051/0004-6361:20020722. arXiv: astro-ph/0205230 [astro-ph].

Amati, L. et al. (July 2018). "The THESEUS space mission concept: science case, design and expected performances". In: *Advances in Space Research* 62.1, pp. 191–244. DOI: 10.1016/j.asr.2018.03.010. arXiv: 1710.04638 [astro-ph.IM].

Amati, L. et al. (Dec. 2021). "The THESEUS space mission: science goals, requirements and mission concept". In: *Experimental Astronomy* 52.3, pp. 183–218. DOI: 10.1007/s10686-021-09807-8. arXiv: 2104.09531 [astro-ph.IM].

Anand, S. (2021). "Optical follow-up of the neutron star-black hole mergers S200105ae and S200115j". In: *Nat Astron* 5.

Andreoni, Igor et al. (May 2022). "Target-of-opportunity Observations of Gravitational-wave Events with Vera C. Rubin Observatory". In: 260.1, 18, p. 18. DOI: 10.3847/1538-4365/ac617c. arXiv: 2111.01945 [astro-ph.HE].

Arnaud, K. A. (Jan. 1996). "XSPEC: The First Ten Years". In: *Astronomical Data Analysis Software and Systems V*. Ed. by George H. Jacoby and Jeannette Barnes. Vol. 101. Astronomical Society of the Pacific Conference Series, p. 17.

Artale, M. Celeste et al. (June 2020). "An astrophysically motivated ranking criterion for low-latency electromagnetic follow-up of gravitational wave events". In: 495.2, pp. 1841–1852. DOI: 10.1093/mnras/staa1252. arXiv: 2002.11214 [astro-ph.GA].

Asano, Katsuaki and Peter Mészáros (Oct. 2012). "Delayed Onset of High-energy Emissions in Leptonic and Hadronic Models of Gamma-Ray Bursts". In: 757.2, 115, p. 115. DOI: 10.1088/0004-637X/757/2/115. arXiv: 1206.0347 [astro-ph.HE].

Asano, Katsuaki and Toshio Terasawa (Nov. 2009). "Slow Heating Model of Gamma-ray Burst: Photon Spectrum and Delayed Emission". In: 705.2, pp. 1714–1720. DOI: 10.1088/0004-637X/705/2/1714. arXiv: 0905.1392 [astro-ph.HE].

— (Dec. 2015). "Stochastic acceleration model of gamma-ray burst with decaying turbulence". In: 454.2, pp. 2242–2248. DOI: 10.1093/mnras/stv2152. arXiv: 1509.04477 [astro-ph.HE].

Asano, Katsuaki et al. (July 2009). "Prompt High-Energy Emission from Proton-Dominated Gamma-Ray Bursts". In: 699.2, pp. 953–957. DOI: 10.1088/0004-637X/699/2/953. arXiv: 0807.0951 [astro-ph].

Ascenzi, S. et al. (Sept. 2020a). "High-latitude emission from the structured jet of γ-ray bursts observed off-axis". In: 641, A61, A61. DOI: 10.1051/0004-6361/202038265. arXiv: 2004.12215 [astro-ph.HE].

— (Sept. 2020b). "High-latitude emission from the structured jet of γ-ray bursts observed off-axis". In: 641, A61, A61. DOI: 10.1051/0004-6361/202038265. arXiv: 2004.12215 [astro-ph.HE].

— (Sept. 2020c). "High-latitude emission from the structured jet of γ-ray bursts observed off-axis". In: 641, A61, A61. DOI: 10.1051/0004-6361/202038265. arXiv: 2004.12215 [astro-ph.HE].

Aso, Yoichi et al. (Aug. 2013). "Interferometer design of the KAGRA gravitational wave detector". In: 88.4, 043007, p. 043007. DOI: 10.1103/PhysRevD.88.043007. arXiv: 1306.6747 [gr-qc].

Atwood, W. B. et al. (June 2009). "The Large Area Telescope on the Fermi Gamma-Ray Space Telescope Mission". In: 697.2, pp. 1071–1102. DOI: 10.1088/0004-637X/697/2/1071. arXiv: 0902.1089 [astro-ph.IM].

Bailes, M. et al. (Apr. 2021). "Gravitational-wave physics and astronomy in the 2020s and 2030s". In: *Nature Reviews Physics* 3.5, pp. 344–366. DOI: 10.1038/s42254-021-00303-8.

Band, D. (1993). "BATSE observations of gamma-ray burst spectra. I. Spectral diversity". In: *Astrophys. J.* 413. DOI: 10.1086/172995. URL: https://doi.org/10.1086/172995.

Band, D. et al. (Aug. 1993). "BATSE Observations of Gamma-Ray Burst Spectra. I. Spectral Diversity". In: 413, p. 281. DOI: 10.1086/172995.

Banerjee, Biswajit et al. (Dec. 2022). "Detecting VHE prompt emission from binary neutron-star mergers: ET and CTA synergies". In: *arXiv e-prints*, arXiv:2212.14007, arXiv:2212.14007. arXiv: 2212.14007 [astro-ph.HE].

Barniol Duran, R. and P. Kumar (2009). "Adiabatic expansion, early X-ray data and the central engine in GRBs". In: *Mon. Not. R. Astron. Soc.* 395. DOI: 10.1111/j.1365-2966.2009.14584.x. URL: https://doi.org/10.1111/j.1365-2966.2009.14584.x.

Barniol Duran, R. and P. Kumar (May 2009). "Adiabatic expansion, early X-ray data and the central engine in GRBs". In: 395.2, pp. 955–961. DOI: 10.1111/j.1365-2966.2009.14584.x. arXiv: 0806.1226 [astro-ph].

Barniol Duran, R. et al. (2016). "An anisotropic minijets model for the GRB prompt emission". In: *Mon. Not. R. Astron. Soc.* 455.

Barthelmy, Scott D. et al. (Oct. 2005). "The Burst Alert Telescope (BAT) on the SWIFT Midex Mission". In: 120.3-4, pp. 143–164. DOI: 10.1007/s11214-005-5096-3. arXiv: astro-ph/0507410 [astro-ph].

Bartos, I. et al. (June 2013). "How gravitational-wave observations can shape the gamma-ray burst paradigm". In: *Classical and Quantum Gravity* 30.12, 123001, p. 123001. DOI: 10.1088/0264-9381/30/12/123001. arXiv: 1212.2289 [astro-ph.CO].

Belgacem, Enis et al. (July 2018). "Modified gravitational-wave propagation and standard sirens". In: 98.2, 023510, p. 023510. DOI: 10.1103/PhysRevD.98.023510. arXiv: 1805.08731 [gr-qc].

Belgacem, Enis et al. (Aug. 2019). "Cosmology and dark energy from joint gravitational wave-GRB observations". In: 2019.8, 015, p. 015. DOI: 10.1088/1475-7516/2019/08/015. arXiv: 1907.01487 [astro-ph.CO].

Belli, B. M. (Apr. 1997). "Evidence for the Galactic Origin of Gamma-Ray Bursts". In: 479.1, pp. L31–L34. DOI: 10.1086/310566.

Beloborodov, Andrei M. (Aug. 2011). "Radiative Transfer in Ultrarelativistic Outflows". In: 737.2, 68, p. 68. DOI: 10.1088/0004-637X/737/2/68. arXiv: 1011.6005 [astro-ph.HE].

Beniamini, P. and T. Piran (2013). "Constraints on the synchrotron emission mechanism in gamma-ray bursts". In: *Astrophys. J.* 769. DOI: 10.1088/0004-637X/769/1/69. URL: https://doi.org/10.1088/0004-637X/769/1/69.

Beniamini, P. et al. (2018). "Marginally fast cooling synchrotron models for prompt GRBs". In: *Mon. Not. R. Astron. Soc.* 476. DOI: 10.1093/mnras/sty340. URL: https://doi.org/10.1093/mnras/sty340.

Beniamini, Paz et al. (Sept. 2016). "Natal Kicks and Time Delays in Merging Neutron Star Binaries: Implications for r-process Nucleosynthesis in Ultra-faint Dwarfs and in the Milky Way". In: 829.1, L13, p. L13. DOI: 10.3847/2041-8205/829/1/L13. arXiv: 1607.02148 [astro-ph.HE].

Beniamini, Paz et al. (Dec. 2017). "Constraints on millisecond magnetars as the engines of prompt emission in gamma-ray bursts". In: 472.3, pp. 3058–3073. DOI: 10.1093/mnras/stx2095. arXiv: 1706.05014 [astro-ph.HE].

Beniamini, Paz et al. (Feb. 2019a). "A lesson from GW170817: most neutron star mergers result in tightly collimated successful GRB jets". In: 483.1, pp. 840–851. DOI: 10.1093/mnras/sty3093. arXiv: 1808.04831 [astro-ph.HE].

— (Feb. 2019b). "A lesson from GW170817: most neutron star mergers result in tightly collimated successful GRB jets". In: 483.1, pp. 840–851. DOI: 10.1093/mnras/sty3093. arXiv: 1808.04831 [astro-ph.HE].

Beniamini, Paz et al. (Apr. 2020a). "Afterglow light curves from misaligned structured jets". In: 493.3, pp. 3521–3534. DOI: 10.1093/mnras/staa538. arXiv: 2001.02239 [astro-ph.HE].

— (Apr. 2020b). "Afterglow light curves from misaligned structured jets". In: 493.3, pp. 3521–3534. DOI: 10.1093/mnras/staa538. arXiv: 2001.02239 [astro-ph.HE].

Beniamini, Paz et al. (Feb. 2020c). "X-ray plateaus in gamma-ray bursts' light curves from jets viewed slightly off-axis". In: 492.2, pp. 2847–2857. DOI: 10.1093/mnras/staa070. arXiv: 1907.05899 [astro-ph.HE].

— (Feb. 2020d). "X-ray plateaus in gamma-ray bursts' light curves from jets viewed slightly off-axis". In: 492.2, pp. 2847–2857. DOI: 10.1093/mnras/staa070. arXiv: 1907.05899 [astro-ph.HE].

Beniamini, Paz et al. (Sept. 2022). "Robust features of off-axis gamma-ray burst afterglow light curves". In: 515.1, pp. 555–570. DOI: 10.1093/mnras/stac1821. arXiv: 2204.06008 [astro-ph.HE].

Berger, E. (Jan. 2009). "The Host Galaxies of Short-Duration Gamma-Ray Bursts: Luminosities, Metallicities, and Star-Formation Rates". In: 690.1, pp. 231–237. DOI: 10.1088/0004-637X/690/1/231. arXiv: 0805.0306 [astro-ph].

Berger, E. et al. (Sept. 2013). "An r-process Kilonova Associated with the Short-hard GRB 130603B". In: 774.2, L23, p. L23. DOI: 10.1088/2041-8205/774/2/L23. arXiv: 1306.3960 [astro-ph.HE].

Berger, Edo (Aug. 2014). "Short-Duration Gamma-Ray Bursts". In: 52, pp. 43–105. DOI: 10.1146/annurev-astro-081913-035926. arXiv: 1311.2603 [astro-ph.HE].

Bernardini, M. G. et al. (Mar. 2012). "The X-ray light curve of gamma-ray bursts: clues to the central engine". In: 539, A3, A3. DOI: 10.1051/0004-6361/201117895. arXiv: 1112.1058 [astro-ph.HE].

Biscoveanu, Sylvia et al. (Apr. 2020). "Constraining Short Gamma-Ray Burst Jet Properties with Gravitational Waves and Gamma-Rays". In: 893.1, 38, p. 38. DOI: 10.3847/1538-4357/ab7eaf. arXiv: 1911.01379 [astro-ph.HE].

Blandford, R. D. and C. F. McKee (Aug. 1976). "Fluid dynamics of relativistic blast waves". In: *Physics of Fluids* 19, pp. 1130–1138. DOI: 10.1063/1.861619.

Blandford, R. D. and R. L. Znajek (May 1977). "Electromagnetic extraction of energy from Kerr black holes." In: 179, pp. 433–456. DOI: 10.1093/mnras/179.3.433.

Bloom, J. S. et al. (Nov. 1998). "The Host Galaxy of GRB 970508". In: 507.1, pp. L25–L28. DOI: 10.1086/311682. arXiv: astro-ph/9807315 [astro-ph].

Bloom, J. S. et al. (June 2001). "The Redshift and the Ordinary Host Galaxy of GRB 970228". In: 554.2, pp. 678–683. DOI: 10.1086/321398. arXiv: astro-ph/0007244 [astro-ph].

Boella, G. et al. (Apr. 1997). "BeppoSAX, the wide band mission for X-ray astronomy". In: 122, pp. 299–307. DOI: 10.1051/aas:1997136.

Borhanian, Ssohrab and B. S. Sathyaprakash (Feb. 2022). "Listening to the Universe with Next Generation Ground-Based Gravitational-Wave Detectors". In: *arXiv e-prints*, arXiv:2202.11048, arXiv:2202.11048. arXiv: 2202.11048 [gr-qc].

Branchesi, Marica et al. (2020). "Electromagnetic Counterparts of Gravitational Waves in the Hz-kHz Range". In: *Handbook of Gravitational Wave Astronomy*. Ed. by Cosimo Bambi et al. Singapore: Springer Singapore, pp. 1–45. ISBN: 978-981-15-4702-7. DOI: 10.1007/978-981-15-4702-7_22-1. URL: https://doi.org/10.1007/978-981-15-4702-7_22-1.

Bromberg, O. et al. (Apr. 2018). "The γ-rays that accompanied GW170817 and the observational signature of a magnetic jet breaking out of NS merger ejecta". In: 475.3, pp. 2971–2977. DOI: 10.1093/mnras/stx3316. arXiv: 1710.05897 [astro-ph.HE].

Bucciantini, N. et al. (Jan. 2012). "Short gamma-ray bursts with extended emission from magnetar birth: jet formation and collimation". In: 419.2, pp. 1537–1545. DOI: 10.1111/j.1365-2966.2011.19810.x. arXiv: 1106.4668 [astro-ph.HE].

Buonanno, Alessandra et al. (Oct. 2009). "Comparison of post-Newtonian templates for compact binary inspiral signals in gravitational-wave detectors". In: 80.8, 084043, p. 084043. DOI: 10.1103/PhysRevD.80.084043. arXiv: 0907.0700 [gr-qc].

Burgay, M. et al. (Dec. 2003). "An increased estimate of the merger rate of double neutron stars from observations of a highly relativistic system". In: 426.6966, pp. 531–533. DOI: 10.1038/nature02124. arXiv: astro-ph/0312071 [astro-ph].

Burgess, J. M. (2020). "Gamma-ray bursts as cool synchrotron sources". In: *Nat. Astron.* 4. DOI: 10.1038/s41550-019-0911-z. URL: https://doi.org/10.1038/s41550-019-0911-z.

Burns, Eric (Dec. 2020). "Neutron star mergers and how to study them". In: *Living Reviews in Relativity* 23.1, 4, p. 4. DOI: 10.1007/s41114-020-00028-7. arXiv: 1909.06085 [astro-ph.HE].

Burns, Eric et al. (Feb. 2016). "Do the Fermi Gamma-Ray Burst Monitor and Swift Burst Alert Telescope see the Same Short Gamma-Ray Bursts?" In: 818.2, 110, p. 110. DOI: 10.3847/0004-637X/818/2/110. arXiv: 1512.00923 [astro-ph.HE].

Burrows, D. N. et al. (Sept. 2005). "Bright X-ray Flares in Gamma-Ray Burst Afterglows". In: *Science* 309.5742, pp. 1833–1835. DOI: 10.1126/science.1116168. arXiv: astro-ph/0506130 [astro-ph].

Butler, Nathaniel R. and Daniel Kocevski (July 2007). "X-Ray Hardness Evolution in GRB Afterglows and Flares: Late-Time GRB Activity without N_H Variations". In: 663.1, pp. 407–419. DOI: 10.1086/518023. arXiv: astro-ph/0612564 [astro-ph].

Camp, Jordan et al. (Sept. 2019). "Transient Astrophysics Probe". In: *Bulletin of the American Astronomical Society*. Vol. 51, 85, p. 85.

Chan, Man Leong et al. (June 2018). "Binary neutron star mergers and third generation detectors: Localization and early warning". In: 97.12, 123014, p. 123014. DOI: 10.1103/PhysRevD.97.123014. arXiv: 1803.09680 [astro-ph.HE].

Chen, Hsin-Yu et al. (2018). "A two per cent Hubble constant measurement from standard sirens within five years". In: *Nature* 562.7728, pp. 545–547. DOI: 10.1038/s41586-018-0606-0. URL: https://doi.org/10.1038/s41586-018-0606-0.

Chen, Hsin-Yu et al. (Feb. 2021). "A Program for Multimessenger Standard Siren Cosmology in the Era of LIGO A+, Rubin Observatory, and Beyond". In: 908.1, L4, p. L4. DOI: 10.3847/2041-8213/abdab0. arXiv: 2011.01211 [astro-ph.CO].

Chincarini, G. et al. (Dec. 2007). "The First Survey of X-Ray Flares from Gamma-Ray Bursts Observed by Swift: Temporal Properties and Morphology". In: 671.2, pp. 1903–1920. DOI: 10.1086/521591. arXiv: astro-ph/0702371 [astro-ph].

Chincarini, G. et al. (Aug. 2010). "Unveiling the origin of X-ray flares in gamma-ray bursts". In: 406.4, pp. 2113–2148. DOI: 10.1111/j.1365-2966.2010.17037.x. arXiv: 1004.0901 [astro-ph.HE].

Ciolfi, Riccardo (June 2020). "The key role of magnetic fields in binary neutron star mergers". In: *General Relativity and Gravitation* 52.6, 59, p. 59. DOI: 10.1007/s10714-020-02714-x. arXiv: 2003.07572 [astro-ph.HE].

Ciolfi, Riccardo and Jay Vijay Kalinani (Sept. 2020). "Magnetically Driven Baryon Winds from Binary Neutron Star Merger Remnants and the Blue Kilonova of 2017 August". In: 900.2, L35, p. L35. DOI: 10.3847/2041-8213/abb240. arXiv: 2004.11298 [astro-ph.HE].

Ciolfi, Riccardo et al. (Dec. 2021). "Multi-messenger astrophysics with THESEUS in the 2030s". In: *Experimental Astronomy* 52.3, pp. 245–275. DOI: 10.1007/s10686-021-09795-9. arXiv: 2104.09534 [astro-ph.IM].

Claeys, J. S. W. et al. (Mar. 2014). "Theoretical uncertainties of the Type Ia supernova rate". In: 563, A83, A83. DOI: 10.1051/0004-6361/201322714. arXiv: 1401.2895 [astro-ph.SR].

Colombo, A. et al. (Apr. 2022). "Multi-messenger observations of binary neutron star mergers in the O4 run". In: *arXiv e-prints*, arXiv:2204.07592, arXiv:2204.07592. arXiv: 2204.07592 [astro-ph.HE].

Cordier, B. et al. (Dec. 2015). "The SVOM gamma-ray burst mission". In: *arXiv e-prints*, arXiv:1512.03323, arXiv:1512.03323. arXiv: 1512.03323 [astro-ph.IM].

Corsi, Alessandra and Peter Mészáros (Sept. 2009). "Gamma-ray Burst Afterglow Plateaus and Gravitational Waves: Multi-messenger Signature of a Millisecond Magnetar?" In: 702.2, pp. 1171–1178. DOI: 10.1088/0004-637X/702/2/1171. arXiv: 0907.2290 [astro-ph.CO].

Costa, E. et al. (June 1997). "Discovery of an X-ray afterglow associated with the γ-ray burst of 28 February 1997". In: 387.6635, pp. 783–785. DOI: 10.1038/42885. arXiv: astro-ph/9706065 [astro-ph].

Coughlin, Michael and Christopher Stubbs (Oct. 2016). "Maximizing the probability of detecting an electromagnetic counterpart of gravitational-wave events". In: *Experimental Astronomy* 42.2, pp. 165–178. DOI: 10.1007/s10686-016-9503-4. arXiv: 1604.05205 [astro-ph.IM].

Coulter, D. A. et al. (Dec. 2017). "Swope Supernova Survey 2017a (SSS17a), the optical counterpart to a gravitational wave source". In: *Science*

358.6370, pp. 1556–1558. DOI: 10.1126/science.aap9811. arXiv: 1710.05452 [astro-ph.HE].

Cucchiara, A. et al. (Dec. 2011). "Constraining Gamma-Ray Burst Emission Physics with Extensive Early-time, Multiband Follow-up". In: 743.2, 154, p. 154. DOI: 10.1088/0004-637X/743/2/154. arXiv: 1107.3352 [astro-ph.HE].

Dai, Z. G. and T. Lu (Nov. 1998a). "γ-Ray Bursts and Afterglows from Rotating Strange Stars and Neutron Stars". In: 81.20, pp. 4301–4304. DOI: 10.1103/PhysRevLett.81.4301. arXiv: astro-ph/9810332 [astro-ph].

— (May 1998b). "Gamma-ray burst afterglows and evolution of postburst fireballs with energy injection from strongly magnetic millisecond pulsars". In: 333, pp. L87–L90. arXiv: astro-ph/9810402 [astro-ph].

Daigne, F. et al. (Feb. 2011). "Reconciling observed gamma-ray burst prompt spectra with synchrotron radiation?" In: 526, A110, A110. DOI: 10.1051/0004-6361/201015457. arXiv: 1009.2636 [astro-ph.HE].

Dainotti, M. G. and R. Del Vecchio (Apr. 2017). "Gamma Ray Burst afterglow and prompt-afterglow relations: An overview". In: 77, pp. 23–61. DOI: 10.1016/j.newar.2017.04.001. arXiv: 1703.06876 [astro-ph.HE].

Dainotti, M. G. et al. (July 2016). "A Fundamental Plane for Long Gamma-Ray Bursts with X-Ray Plateaus". In: 825.2, L20, p. L20. DOI: 10.3847/2041-8205/825/2/L20. arXiv: 1604.06840 [astro-ph.HE].

Dainotti, M. G. et al. (Oct. 2017). "A Study of the Gamma-Ray Burst Fundamental Plane". In: 848.2, 88, p. 88. DOI: 10.3847/1538-4357/aa8a6b. arXiv: 1704.04908 [astro-ph.HE].

Dainotti, M. G. et al. (Dec. 2020). "The Optical Luminosity-Time Correlation for More than 100 Gamma-Ray Burst Afterglows". In: 905.2, L26, p. L26. DOI: 10.3847/2041-8213/abcda9. arXiv: 2011.14493 [astro-ph.HE].

Dainotti, Maria Giovanna et al. (Oct. 2010). "Discovery of a Tight Correlation for Gamma-ray Burst Afterglows with "Canonical" Light Curves". In: 722.2, pp. L215–L219. DOI: 10.1088/2041-8205/722/2/L215. arXiv: 1009.1663 [astro-ph.HE].

Dainotti, Maria Giovanna et al. (Sept. 2013). "Determination of the Intrinsic Luminosity Time Correlation in the X-Ray Afterglows of Gamma-Ray Bursts". In: 774.2, 157, p. 157. DOI: 10.1088/0004-637X/774/2/157. arXiv: 1307.7297 [astro-ph.HE].

Dall'Osso, S. et al. (Feb. 2011). "Gamma-ray bursts afterglows with energy injection from a spinning down neutron star". In: 526, A121, A121. DOI: 10.1051/0004-6361/201014168. arXiv: 1004.2788 [astro-ph.HE].

Dall'Osso, Simone et al. (Jan. 2015). "Gravitational Waves from Massive Magnetars Formed in Binary Neutron Star Mergers". In: 798.1, 25, p. 25. DOI: 10.1088/0004-637X/798/1/25. arXiv: 1408.0013 [astro-ph.HE].

D'Avanzo, P. et al. (Sept. 2012). "A complete sample of bright Swift Gamma-ray bursts: X-ray afterglow luminosity and its correlation with the prompt emission". In: 425.1, pp. 506–513. DOI: 10.1111/j.1365-2966.2012.21489.x. arXiv: 1206.2357 [astro-ph.HE].

D'Avanzo, P. et al. (May 2018). "The evolution of the X-ray afterglow emission of GW 170817/ GRB 170817A in XMM-Newton observations". In: 613, L1, p. L1. DOI: 10.1051/0004-6361/201832664. arXiv: 1801.06164 [astro-ph.HE].

De Angelis, Alessandro et al. (June 2021). "Gamma-ray astrophysics in the MeV range". In: *Experimental Astronomy* 51.3, pp. 1225–1254. DOI: 10.1007/s10686-021-09706-y.

de Souza, Josiel Mendonça Soares et al. (Mar. 2022). "Cosmography with standard sirens from the Einstein Telescope". In: 2022.3, 025, p. 025. DOI: 10.1088/1475-7516/2022/03/025. arXiv: 2110.13316 [gr-qc].

Dereli-Bégué, Hüsne et al. (Sept. 2022). "A wind environment and Lorentz factors of tens explain gamma-ray bursts X-ray plateau". In: *Nature Communications* 13, 5611, p. 5611. DOI: 10.1038/s41467-022-32881-1. arXiv: 2207.11066 [astro-ph.HE].

Dermer, Charles D. (Oct. 2004). "Curvature Effects in Gamma-Ray Burst Colliding Shells". In: 614.1, pp. 284–292. DOI: 10.1086/426532. arXiv: astro-ph/0403508 [astro-ph].

Dessart, L. et al. (Jan. 2009). "Neutrino Signatures and the Neutrino-Driven Wind in Binary Neutron Star Mergers". In: 690.2, pp. 1681–1705. DOI: 10.1088/0004-637X/690/2/1681. arXiv: 0806.4380 [astro-ph].

Ding, Xiao-Kang et al. (June 2022). "Statistical properties of the X-ray afterglow shallow decay phase and their relationships with the prompt gamma-ray emission of gamma-ray bursts". In: 367.6, 58, p. 58. DOI: 10.1007/s10509-022-04088-9.

Domínguez, A. et al. (Feb. 2011). "Extragalactic background light inferred from AEGIS galaxy-SED-type fractions". In: 410.4, pp. 2556–2578. DOI: 10.1111/j.1365-2966.2010.17631.x. arXiv: 1007.1459 [astro-ph.CO].

Drenkhahn, G. and H. C. Spruit (Sept. 2002). "Efficient acceleration and radiation in Poynting flux powered GRB outflows". In: 391, pp. 1141–1153. DOI: 10.1051/0004-6361:20020839. arXiv: astro-ph/0202387 [astro-ph].

Dupletsa, U. et al. (2022). "gwfish: A simulation software to evaluate parameter-estimation capabilities of gravitational-wave detector networks". In: *Astronomy and Computing*, p. 100671. ISSN: 2213-1337. DOI: https://doi.org/10.1016/j.ascom.2022.100671. URL: https://www.sciencedirect.com/science/article/pii/S2213133722000853.

Eichler, David et al. (July 1989). "Nucleosynthesis, neutrino bursts and γ-rays from coalescing neutron stars". In: 340.6229, pp. 126–128. DOI: 10.1038/340126a0.

Evans, Matthew et al. (Sept. 2021a). "A Horizon Study for Cosmic Explorer: Science, Observatories, and Community". In: *arXiv e-prints*, arXiv:2109.09882, arXiv:2109.09882. arXiv: 2109.09882 [astro-ph.IM].

— (Sept. 2021b). "A Horizon Study for Cosmic Explorer: Science, Observatories, and Community". In: *arXiv e-prints*, arXiv:2109.09882, arXiv:2109.09882. arXiv: 2109.09882 [astro-ph.IM].

Evans, P. A. (2009). "Methods and results of an automatic analysis of a complete sample of Swift-XRT observations of GRBs". In: *Mon. Not. R. Astron. Soc.* 397. DOI: 10.1111/j.1365-2966.2009.14913.x. URL: https://doi.org/10.1111/j.1365-2966.2009.14913.x.

Evans, P. A. et al. (July 2007). "An online repository of Swift/XRT light curves of γ-ray bursts". In: 469.1, pp. 379–385. DOI: 10.1051/0004-6361:20077530. arXiv: 0704.0128 [astro-ph].

Evans, P. A. et al. (Aug. 2009). "Methods and results of an automatic analysis of a complete sample of Swift-XRT observations of GRBs". In: 397.3, pp. 1177–1201. DOI: 10.1111/j.1365-2966.2009.14913.x. arXiv: 0812.3662 [astro-ph].

Evans, P. A. et al. (Oct. 2016). "Swift follow-up of gravitational wave triggers: results from the first aLIGO run and optimization for the future". In: 462.2, pp. 1591–1602. DOI: 10.1093/mnras/stw1746. arXiv: 1606.05001 [astro-ph.HE].

Fan, Y. Z. and D. M. Wei (Nov. 2005). "Late internal-shock model for bright X-ray flares in gamma-ray burst afterglows and GRB 011121". In: 364.1, pp. L42–L46. DOI: 10.1111/j.1745-3933.2005.00102.x. arXiv: astro-ph/0506155 [astro-ph].

Fan, Yizhong and Tsvi Piran (June 2006). "Gamma-ray burst efficiency and possible physical processes shaping the early afterglow". In: 369.1, pp. 197–206. DOI: 10.1111/j.1365-2966.2006.10280.x. arXiv: astro-ph/0601054 [astro-ph].

Fenimore, E. E. et al. (1996). "Expanding relativistic shells and gamma-ray burst temporal structure". In: *Astrophys. J.* 473. DOI: 10.1086/178210. URL: https://doi.org/10.1086/178210.

Fenimore, Edward E. et al. (Dec. 1996). "Expanding Relativistic Shells and Gamma-Ray Burst Temporal Structure". In: 473, p. 998. DOI: 10.1086/178210. arXiv: astro-ph/9607163 [astro-ph].

Fernández, Rodrigo and Brian D. Metzger (Oct. 2013). "Delayed outflows from black hole accretion tori following neutron star binary coalescence". In: 435.1, pp. 502–517. DOI: 10.1093/mnras/stt1312. arXiv: 1304.6720 [astro-ph.HE].

Filgas, R. et al. (Feb. 2011). "The two-component jet of GRB 080413B". In: 526, A113, A113. DOI: 10.1051/0004-6361/201015320. arXiv: 1012.0328 [astro-ph.HE].

Filgas, R. et al. (Oct. 2012). "GRB 091029: at the limit of the fireball scenario". In: 546, A101, A101. DOI: 10.1051/0004-6361/201219583. arXiv: 1209.4658 [astro-ph.HE].

Fiore, F. et al. (Dec. 2020). "The HERMES-technologic and scientific pathfinder". In: *Society of Photo-Optical Instrumentation Engineers (SPIE) Conference Series*. Vol. 11444. Society of Photo-Optical Instrumentation Engineers (SPIE) Conference Series, 114441R, 114441R. DOI: 10.1117/12.2560680. arXiv: 2101.03078 [astro-ph.HE].

Fiore, Fabrizio et al. (Dec. 2021). "Distributed Architectures and Constellations for γ-ray Burst Science". In: *Galaxies* 9.4, p. 120. DOI: 10.3390/galaxies9040120. arXiv: 2112.08982 [astro-ph.HE].

Fong, W. et al. (May 2013). "Demographics of the Galaxies Hosting Short-duration Gamma-Ray Bursts". In: 769.1, 56, p. 56. DOI: 10.1088/0004-637X/769/1/56. arXiv: 1302.3221 [astro-ph.HE].

Fong, W. et al. (Jan. 2014). "Short GRB 130603B: Discovery of a Jet Break in the Optical and Radio Afterglows, and a Mysterious Late-time X-Ray Excess". In: 780.2, 118, p. 118. DOI: 10.1088/0004-637X/780/2/118. arXiv: 1309.7479 [astro-ph.HE].

Fong, W. et al. (Dec. 2015a). "A Decade of Short-duration Gamma-Ray Burst Broadband Afterglows: Energetics, Circumburst Densities, and Jet Opening Angles". In: 815.2, 102, p. 102. DOI: 10.1088/0004-637X/815/2/102. arXiv: 1509.02922 [astro-ph.HE].

— (Dec. 2015b). "A Decade of Short-duration Gamma-Ray Burst Broadband Afterglows: Energetics, Circumburst Densities, and Jet Opening Angles". In: 815.2, 102, p. 102. DOI: 10.1088/0004-637X/815/2/102. arXiv: 1509.02922 [astro-ph.HE].

Fong, Wen-fai et al. (Nov. 2022). "Short GRB Host Galaxies. I. Photometric and Spectroscopic Catalogs, Host Associations, and Galactocentric Offsets". In: 940.1, 56, p. 56. DOI: 10.3847/1538-4357/ac91d0. arXiv: 2206.01763 [astro-ph.GA].

Foreman-Mackey, D. (2013). "emcee: the MCMC hammer". In: *Publ. Astron. Soc. Pac.* 125. DOI: 10.1086/670067. URL: https://doi.org/10.1086/670067.

Foreman-Mackey, Daniel et al. (Mar. 2013). "emcee: The MCMC Hammer". In: 125.925, p. 306. DOI: 10.1086/670067. arXiv: 1202.3665 [astro-ph.IM].

Fox, D. B. et al. (Oct. 2005). "The afterglow of GRB 050709 and the nature of the short-hard γ-ray bursts". In: 437.7060, pp. 845–850. DOI: 10.1038/nature04189. arXiv: astro-ph/0510110 [astro-ph].

Frail, D. A. et al. (Nov. 2001). "Beaming in Gamma-Ray Bursts: Evidence for a Standard Energy Reservoir". In: 562.1, pp. L55–L58. DOI: 10.1086/338119. arXiv: astro-ph/0102282 [astro-ph].

Frontera, F. (2000). "Prompt and delayed emission properties of gamma-ray bursts observed with BeppoSAX". In: *Astrophys. J. Suppl. Series* 127. DOI: 10.1086/313316. URL: https://doi.org/10.1086/313316.

Frostig, Danielle et al. (Feb. 2022). "An Infrared Search for Kilonovae with the WINTER Telescope. I. Binary Neutron Star Mergers". In: 926.2, 152, p. 152. DOI: 10.3847/1538-4357/ac4508. arXiv: 2110.01622 [astro-ph.HE].

Fruchter, A. S. et al. (May 2006). "Long γ-ray bursts and core-collapse supernovae have different environments". In: 441.7092, pp. 463–468. DOI: 10.1038/nature04787. arXiv: astro-ph/0603537 [astro-ph].

Fryer, Chris L. et al. (Apr. 2012). "Compact Remnant Mass Function: Dependence on the Explosion Mechanism and Metallicity". In: 749.1, 91, p. 91. DOI: 10.1088/0004-637X/749/1/91. arXiv: 1110.1726 [astro-ph.SR].

Galama, T. J. et al. (June 1998). "The Radio-to-X-Ray Spectrum of GRB 970508 on 1997 May 21.0 UT". In: 500.2, pp. L97–L100. DOI: 10.1086/311425. arXiv: astro-ph/9804191 [astro-ph].

Gehrels, N. (2004). "The Swift gamma-ray burst mission". In: *Astrophys. J.* 611. DOI: 10.1086/422091. URL: https://doi.org/10.1086/422091.

Genet, F. and J. Granot (2009). "Realistic analytic model for the prompt and high-latitude emission in GRBs". In: *Mon. Not. R. Astron. Soc.* 399. DOI: 10.1111/j.1365-2966.2009.15355.x. URL: https://doi.org/10.1111/j.1365-2966.2009.15355.x.

Genet, F. et al. (Oct. 2007). "Can the early X-ray afterglow of gamma-ray bursts be explained by a contribution from the reverse shock?" In: 381.2, pp. 732–740. DOI: 10.1111/j.1365-2966.2007.12243.x. arXiv: astro-ph/0701204 [astro-ph].

Geng, J. . J. et al. (2017). "Steep decay of GRB X-Ray flares: the results of anisotropic synchrotron radiation". In: *Astrophys. J. Lett.* 841. DOI: 10.

3847/2041-8213/aa725a. URL: https://doi.org/10.3847/2041-8213/aa725a.

Geng, Jin-Jun et al. (June 2019). "Propagation of a Short GRB Jet in the Ejecta: Jet Launching Delay Time, Jet Structure, and GW170817/GRB 170817A". In: 877.2, L40, p. L40. DOI: 10.3847/2041-8213/ab224b. arXiv: 1904.02326 [astro-ph.HE].

Ghirlanda, G. et al. (July 2007). "Blackbody components in gamma-ray bursts spectra?" In: 379.1, pp. 73–85. DOI: 10.1111/j.1365-2966.2007.11890.x. arXiv: 0704.3438 [astro-ph].

Ghirlanda, G. et al. (Oct. 2016a). "Short gamma-ray bursts at the dawn of the gravitational wave era". In: 594, A84, A84. DOI: 10.1051/0004-6361/201628993. arXiv: 1607.07875 [astro-ph.HE].

— (Oct. 2016b). "Short gamma-ray bursts at the dawn of the gravitational wave era". In: 594, A84, A84. DOI: 10.1051/0004-6361/201628993. arXiv: 1607.07875 [astro-ph.HE].

Ghirlanda, G. et al. (Jan. 2018). "Bulk Lorentz factors of gamma-ray bursts". In: 609, A112, A112. DOI: 10.1051/0004-6361/201731598. arXiv: 1711.06257 [astro-ph.HE].

Ghirlanda, G. et al. (Mar. 2019a). "Compact radio emission indicates a structured jet was produced by a binary neutron star merger". In: *Science* 363.6430, pp. 968–971. DOI: 10.1126/science.aau8815. arXiv: 1808.00469 [astro-ph.HE].

— (Mar. 2019b). "Compact radio emission indicates a structured jet was produced by a binary neutron star merger". In: *Science* 363.6430, pp. 968–971. DOI: 10.1126/science.aau8815. arXiv: 1808.00469 [astro-ph.HE].

— (Mar. 2019c). "Compact radio emission indicates a structured jet was produced by a binary neutron star merger". In: *Science* 363.6430, pp. 968–971. DOI: 10.1126/science.aau8815. arXiv: 1808.00469 [astro-ph.HE].

Ghirlanda, G. et al. (Dec. 2021). "Gamma ray burst studies with THESEUS". In: *Experimental Astronomy* 52.3, pp. 277–308. DOI: 10.1007/s10686-021-09763-3. arXiv: 2104.10448 [astro-ph.IM].

Ghirlanda, Giancarlo and Ruben Salvaterra (June 2022). "The Cosmic History of Long Gamma-Ray Bursts". In: 932.1, 10, p. 10. DOI: 10.3847/1538-4357/ac6e43.

Ghirlanda, Giancarlo et al. (Nov. 2004). "The Collimation-corrected Gamma-Ray Burst Energies Correlate with the Peak Energy of Their νF_ν Spectrum". In: 616.1, pp. 331–338. DOI: 10.1086/424913. arXiv: astro-ph/0405602 [astro-ph].

Ghisellini, G. (2020). "Proton-synchrotron as the radiation mechanism of the prompt emission of gamma-ray bursts?" In: *Astron. Astrophys.* 636. DOI: 10.1051/0004-6361/201937244. URL: https://doi.org/10.1051/0004-6361/201937244.

Ghisellini, Gabriele et al. (Mar. 2000). "Constraints on the emission mechanisms of gamma-ray bursts". In: 313.1, pp. L1–L5. DOI: 10.1046/j.1365-8711.2000.03354.x. arXiv: astro-ph/9912461 [astro-ph].

Ghosh, Shaon et al. (Aug. 2016). "Tiling strategies for optical follow-up of gravitational-wave triggers by telescopes with a wide field of view". In: 592, A82, A82. DOI: 10.1051/0004-6361/201527712. arXiv: 1511.02673 [astro-ph.IM].

Giacobbo, Nicola and Michela Mapelli (Oct. 2018). "The progenitors of compact-object binaries: impact of metallicity, common envelope and natal kicks". In: 480.2, pp. 2011–2030. DOI: 10.1093/mnras/sty1999. arXiv: 1806.00001 [astro-ph.HE].

— (Jan. 2019). "The impact of electron-capture supernovae on merging double neutron stars". In: 482.2, pp. 2234–2243. DOI: 10.1093/mnras/sty2848. arXiv: 1805.11100 [astro-ph.SR].

— (Mar. 2020). "Revising Natal Kick Prescriptions in Population Synthesis Simulations". In: 891.2, 141, p. 141. DOI: 10.3847/1538-4357/ab7335. arXiv: 1909.06385 [astro-ph.HE].

Giacobbo, Nicola et al. (Mar. 2018). "Merging black hole binaries: the effects of progenitor's metallicity, mass-loss rate and Eddington factor". In: 474.3, pp. 2959–2974. DOI: 10.1093/mnras/stx2933. arXiv: 1711.03556 [astro-ph.SR].

Goldstein, A. et al. (Oct. 2017a). "An Ordinary Short Gamma-Ray Burst with Extraordinary Implications: Fermi-GBM Detection of GRB 170817A". In: 848, L14, p. L14. DOI: 10.3847/2041-8213/aa8f41. arXiv: 1710.05446 [astro-ph.HE].

— (Oct. 2017b). "An Ordinary Short Gamma-Ray Burst with Extraordinary Implications: Fermi-GBM Detection of GRB 170817A". In: 848.2, L14, p. L14. DOI: 10.3847/2041-8213/aa8f41. arXiv: 1710.05446 [astro-ph.HE].

Goldstein, Adam et al. (Mar. 2019). "Updates to the Fermi GBM Targeted Sub-threshold Search in Preparation for the Third Observing Run of LIGO/Virgo". In: *arXiv e-prints*, arXiv:1903.12597, arXiv:1903.12597. arXiv: 1903.12597 [astro-ph.HE].

Gompertz, B. P. et al. (Mar. 2015). "Broad-band modelling of short gamma-ray bursts with energy injection from magnetar spin-down and its implications for radio detectability". In: 448.1, pp. 629–641. DOI: 10.1093/mnras/stu2752. arXiv: 1411.5477 [astro-ph.HE].

Goodman, J. (Sept. 1986). "Are gamma-ray bursts optically thick?" In: 308, p. L47. DOI: 10.1086/184741.

Goto, Ryota and Katsuaki Asano (July 2022). "GRB Prompt Emission with Anisotropic Electron Distribution". In: 933.1, 18, p. 18. DOI: 10.3847/1538-4357/ac67d5. arXiv: 2201.13028 [astro-ph.HE].

Gottlieb, Ore et al. (Sept. 2018a). "A cocoon shock breakout as the origin of the γ-ray emission in GW170817". In: 479.1, pp. 588–600. DOI: 10.1093/mnras/sty1462. arXiv: 1710.05896 [astro-ph.HE].

— (Sept. 2018b). "A cocoon shock breakout as the origin of the γ-ray emission in GW170817". In: 479.1, pp. 588–600. DOI: 10.1093/mnras/sty1462. arXiv: 1710.05896 [astro-ph.HE].

— (Sept. 2018c). "A cocoon shock breakout as the origin of the γ-ray emission in GW170817". In: 479.1, pp. 588–600. DOI: 10.1093/mnras/sty1462. arXiv: 1710.05896 [astro-ph.HE].

Gottlieb, Ore et al. (Jan. 2018d). "The cocoon emission - an electromagnetic counterpart to gravitational waves from neutron star mergers". In: 473.1, pp. 576–584. DOI: 10.1093/mnras/stx2357. arXiv: 1705.10797 [astro-ph.HE].

— (Jan. 2018e). "The cocoon emission - an electromagnetic counterpart to gravitational waves from neutron star mergers". In: 473.1, pp. 576–584. DOI: 10.1093/mnras/stx2357. arXiv: 1705.10797 [astro-ph.HE].

Gottlieb, Ore et al. (Nov. 2020). "The structure of weakly magnetized γ-ray burst jets". In: 498.3, pp. 3320–3333. DOI: 10.1093/mnras/staa2567. arXiv: 2007.11590 [astro-ph.HE].

Gottlieb, Ore et al. (Jan. 2021). "The structure of hydrodynamic γ-ray burst jets". In: 500.3, pp. 3511–3526. DOI: 10.1093/mnras/staa3501. arXiv: 2006.02466 [astro-ph.HE].

Gottlieb, Ore et al. (July 2022a). "Black Hole to Photosphere: 3D GRMHD Simulations of Collapsars Reveal Wobbling and Hybrid Composition Jets". In: 933.1, L9, p. L9. DOI: 10.3847/2041-8213/ac7530. arXiv: 2204.12501 [astro-ph.HE].

Gottlieb, Ore et al. (July 2022b). "On the Jet-Ejecta Interaction in 3D GRMHD Simulations of a Binary Neutron Star Merger Aftermath". In: 933.1, L2, p. L2. DOI: 10.3847/2041-8213/ac7728. arXiv: 2205.01691 [astro-ph.HE].

Götz, Diego and SVOM Collaboration (Jan. 2012). "SVOM: a new mission for Gamma-Ray Bursts studies". In: *Memorie della Societa Astronomica Italiana Supplementi* 21, p. 162.

Graham, J. F. and A. S. Fruchter (Sept. 2013). "The Metal Aversion of Long-duration Gamma-Ray Bursts". In: 774.2, 119, p. 119. DOI: 10.1088/0004-637X/774/2/119. arXiv: 1211.7068 [astro-ph.HE].

Granot, Jonathan and Pawan Kumar (July 2003). "Constraining the Structure of Gamma-Ray Burst Jets through the Afterglow Light Curves". In: 591.2, pp. 1086–1096. DOI: 10.1086/375489. arXiv: astro-ph/0212540 [astro-ph].

Granot, Jonathan and Tsvi Piran (Mar. 2012). "On the lateral expansion of gamma-ray burst jets". In: 421.1, pp. 570–587. DOI: 10.1111/j.1365-2966.2011.20335.x. arXiv: 1109.6468 [astro-ph.HE].

Granot, Jonathan and Re'em Sari (Apr. 2002). "The Shape of Spectral Breaks in Gamma-Ray Burst Afterglows". In: 568.2, pp. 820–829. DOI: 10.1086/338966. arXiv: astro-ph/0108027 [astro-ph].

Granot, Jonathan et al. (Aug. 2006). "Implications of the early X-ray afterglow light curves of Swift gamma-ray bursts". In: 370.4, pp. 1946–1960. DOI: 10.1111/j.1365-2966.2006.10621.x. arXiv: astro-ph/0601056 [astro-ph].

Greiner, J. et al. (Dec. 2013a). "The unusual afterglow of the gamma-ray burst 100621A". In: 560, A70, A70. DOI: 10.1051/0004-6361/201321284. arXiv: 1304.5852 [astro-ph.HE].

Greiner, J. et al. (Dec. 2013b). "The unusual afterglow of the gamma-ray burst 100621A". In: 560, A70, A70. DOI: 10.1051/0004-6361/201321284. arXiv: 1304.5852 [astro-ph.HE].

Grimm, Stefan and Jan Harms (July 2020). "Multiband gravitational-wave parameter estimation: A study of future detectors". In: 102.2, 022007, p. 022007. DOI: 10.1103/PhysRevD.102.022007. arXiv: 2004.01434 [gr-qc].

H. E. S. S. Collaboration et al. (June 2021). "Revealing x-ray and gamma ray temporal and spectral similarities in the GRB 190829A afterglow". In: *Science* 372.6546, pp. 1081–1085. DOI: 10.1126/science.abe8560. arXiv: 2106.02510 [astro-ph.HE].

Haggard, Daryl et al. (Oct. 2017). "A Deep Chandra X-Ray Study of Neutron Star Coalescence GW170817". In: 848.2, L25, p. L25. DOI: 10.3847/2041-8213/aa8ede. arXiv: 1710.05852 [astro-ph.HE].

Hajela, A. et al. (Nov. 2019). "Two Years of Nonthermal Emission from the Binary Neutron Star Merger GW170817: Rapid Fading of the Jet Afterglow and First Constraints on the Kilonova Fastest Ejecta". In: 886.1,

L17, p. L17. DOI: 10.3847/2041-8213/ab5226. arXiv: 1909.06393 [astro-ph.HE].

Hajela, A. et al. (Mar. 2022). "Evidence for X-Ray Emission in Excess to the Jet-afterglow Decay 3.5 yr after the Binary Neutron Star Merger GW 170817: A New Emission Component". In: 927.1, L17, p. L17. DOI: 10.3847/2041-8213/ac504a. arXiv: 2104.02070 [astro-ph.HE].

Hallinan, G. et al. (Dec. 2017). "A radio counterpart to a neutron star merger". In: *Science* 358.6370, pp. 1579–1583. DOI: 10.1126/science.aap9855. arXiv: 1710.05435 [astro-ph.HE].

Harrison, F. A. et al. (Oct. 1999). "Optical and Radio Observations of the Afterglow from GRB 990510: Evidence for a Jet". In: 523.2, pp. L121–L124. DOI: 10.1086/312282. arXiv: astro-ph/9905306 [astro-ph].

Hascoët, R. et al. (June 2012). "Accounting for the XRT early steep decay in models of the prompt gamma-ray burst emission". In: 542, L29, p. L29. DOI: 10.1051/0004-6361/201219339. arXiv: 1206.6770 [astro-ph.HE].

Hayes, Fergus et al. (Mar. 2020). "Comparing Short Gamma-Ray Burst Jet Structure Models". In: 891.2, 124, p. 124. DOI: 10.3847/1538-4357/ab72fc. arXiv: 1911.04190 [astro-ph.HE].

Hild, S. et al. (May 2011). "Sensitivity studies for third-generation gravitational wave observatories". In: *Classical and Quantum Gravity* 28.9, 094013, p. 094013. DOI: 10.1088/0264-9381/28/9/094013. arXiv: 1012.0908 [gr-qc].

Hjorth, Jens et al. (June 2003). "A very energetic supernova associated with the γ-ray burst of 29 March 2003". In: 423.6942, pp. 847–850. DOI: 10.1038/nature01750. arXiv: astro-ph/0306347 [astro-ph].

Hjorth, Jens et al. (Oct. 2017). "The Distance to NGC 4993: The Host Galaxy of the Gravitational-wave Event GW170817". In: 848.2, L31, p. L31. DOI: 10.3847/2041-8213/aa9110. arXiv: 1710.05856 [astro-ph.GA].

Hobbs, G. et al. (July 2005). "A statistical study of 233 pulsar proper motions". In: 360.3, pp. 974–992. DOI: 10.1111/j.1365-2966.2005.09087.x. arXiv: astro-ph/0504584 [astro-ph].

Hotokezaka, K. et al. (July 2019). "A Hubble constant measurement from superluminal motion of the jet in GW170817". In: *Nature Astronomy* 3, pp. 940–944. DOI: 10.1038/s41550-019-0820-1. arXiv: 1806.10596 [astro-ph.CO].

Hou, Shu-Jin et al. (Dec. 2021). "Evidence of X-Ray Plateaus Driven by the Magnetar Spindown Winds in Gamma-Ray Burst Afterglows". In: 922.2, 102, p. 102. DOI: 10.3847/1538-4357/ac2c74. arXiv: 2110.00727 [astro-ph.HE].

Howell, E. J. et al. (May 2019). "Joint gravitational wave - gamma-ray burst detection rates in the aftermath of GW170817". In: 485.1, pp. 1435–1447. DOI: 10.1093/mnras/stz455. arXiv: 1811.09168 [astro-ph.HE].

Hu, You-Dong et al. (July 2014). "Internal Energy Dissipation of Gamma-Ray Bursts Observed with Swift: Precursors, Prompt Gamma-Rays, Extended Emission, and Late X-Ray Flares". In: 789.2, 145, p. 145. DOI: 10.1088/0004-637X/789/2/145. arXiv: 1405.5949 [astro-ph.HE].

Huang, Yong-Feng et al. (June 2007). "A Detailed Study on the Equal Arrival Time Surface Effect in Gamma-Ray Burst Afterglows". In: 7.3, pp. 397–404. DOI: 10.1088/1009-9271/7/3/09. arXiv: astro-ph/0701846 [astro-ph].

Hurley, Jarrod R. et al. (Feb. 2002). "Evolution of binary stars and the effect of tides on binary populations". In: 329.4, pp. 897–928. DOI: 10.1046/j.1365-8711.2002.05038.x. arXiv: astro-ph/0201220 [astro-ph].

Iacovelli, Francesco et al. (Dec. 2022). "Forecasting the Detection Capabilities of Third-generation Gravitational-wave Detectors Using GWFAST". In: 941.2, 208, p. 208. DOI: 10.3847/1538-4357/ac9cd4. arXiv: 2207.02771 [gr-qc].

Ioka, Kunihito and Takashi Nakamura (Aug. 2019). "Spectral puzzle of the off-axis gamma-ray burst in GW170817". In: 487.4, pp. 4884–4889. DOI: 10.1093/mnras/stz1650. arXiv: 1903.01484 [astro-ph.HE].

Ivezic, Z. (2008). "Large synoptic survey telescope: from science drivers to reference design". In: *Serbian Astron J* 176.

Jia, X. D. et al. (Oct. 2022). "E $_{iso}$-E$_p$ correlation of gamma-ray bursts: calibration and cosmological applications". In: 516.2, pp. 2575–2585. DOI: 10.1093/mnras/stac2356. arXiv: 2208.09272 [astro-ph.HE].

Jin, Zhi-Ping et al. (Sept. 2016). "The Macronova in GRB 050709 and the GRB-macronova connection". In: *Nature Communications* 7, 12898, p. 12898. DOI: 10.1038/ncomms12898. arXiv: 1603.07869 [astro-ph.HE].

Jin, Zhi-Ping et al. (Apr. 2018). "Short GRBs: Opening Angles, Local Neutron Star Merger Rate, and Off-axis Events for GRB/GW Association". In: 857.2, 128, p. 128. DOI: 10.3847/1538-4357/aab76d. arXiv: 1708.07008 [astro-ph.HE].

Just, O. et al. (Jan. 2016). "Neutron-star Merger Ejecta as Obstacles to Neutrino-powered Jets of Gamma-Ray Bursts". In: 816.2, L30, p. L30. DOI: 10.3847/2041-8205/816/2/L30. arXiv: 1510.04288 [astro-ph.HE].

Kalberla, P. M. W. et al. (Sept. 2005). "The Leiden/Argentine/Bonn (LAB) Survey of Galactic HI. Final data release of the combined LDS and IAR surveys with improved stray-radiation corrections". In: 440.2, pp. 775–

782. DOI: 10.1051/0004-6361:20041864. arXiv: astro-ph/0504140 [astro-ph].

Kaneko, Y. (2006). "The complete spectral catalog of bright BATSE gamma-ray bursts". In: *Astrophys. J. Suppl. Series* 166. DOI: 10.1086/505911. URL: https://doi.org/10.1086/505911.

Kann, D. A. et al. (Apr. 2006). "Signatures of Extragalactic Dust in Pre-Swift GRB Afterglows". In: 641, pp. 993–1009. DOI: 10.1086/500652. eprint: arXiv:astro-ph/0512575.

Kann, D. A. et al. (Sept. 2010). "The Afterglows of Swift-era Gamma-ray Bursts. I. Comparing pre-Swift and Swift-era Long/Soft (Type II) GRB Optical Afterglows". In: 720, pp. 1513–1558. DOI: 10.1088/0004-637X/720/2/1513. arXiv: 0712.2186.

Kann, D. A. et al. (June 2011). "The Afterglows of Swift-era Gamma-Ray Bursts. II. Type I GRB versus Type II GRB Optical Afterglows". In: 734, 96, p. 96. DOI: 10.1088/0004-637X/734/2/96. arXiv: 0804.1959.

Kasen, Daniel et al. (Nov. 2017). "Origin of the heavy elements in binary neutron-star mergers from a gravitational-wave event". In: 551.7678, pp. 80–84. DOI: 10.1038/nature24453. arXiv: 1710.05463 [astro-ph.HE].

Kasliwal, M. M. et al. (Dec. 2017). "Illuminating gravitational waves: A concordant picture of photons from a neutron star merger". In: *Science* 358.6370, pp. 1559–1565. DOI: 10.1126/science.aap9455. arXiv: 1710.05436 [astro-ph.HE].

Kimura, Shigeo S. (Feb. 2022). "Neutrinos from Gamma-ray Bursts". In: *arXiv e-prints*, arXiv:2202.06480, arXiv:2202.06480. DOI: 10.48550/arXiv.2202.06480. arXiv: 2202.06480 [astro-ph.HE].

Klingler, N. J. et al. (Nov. 2019). "Swift-XRT Follow-up of Gravitational-wave Triggers in the Second Advanced LIGO/Virgo Observing Run". In: 245.1, 15, p. 15. DOI: 10.3847/1538-4365/ab4ea2. arXiv: 1909.11586 [astro-ph.HE].

Koshut, Thomas M. et al. (Oct. 1995). "Gamma-Ray Burst Precursor Activity as Observed with BATSE". In: 452, p. 145. DOI: 10.1086/176286.

Kouveliotou, Chryssa et al. (Aug. 1993). "Identification of Two Classes of Gamma-Ray Bursts". In: 413, p. L101. DOI: 10.1086/186969.

Kroupa, Pavel (Apr. 2001). "On the variation of the initial mass function". In: 322.2, pp. 231–246. DOI: 10.1046/j.1365-8711.2001.04022.x. arXiv: astro-ph/0009005 [astro-ph].

Kulkarni, S. R. et al. (June 1998). "The gamma-ray burst of 980425 and its association with the extraordinary radio emission from a most unusual supernova". In: *arXiv e-prints*, astro-ph/9807001, astro–ph/9807001. arXiv: astro-ph/9807001 [astro-ph].

Kumar, P. and E. McMahon (2008). "A general scheme for modelling -ray burst prompt emission". In: *Mon. Not. R. Astron. Soc.* 384. DOI: 10.1111/j.1365-2966.2007.12621.x. URL: https://doi.org/10.1111/j.1365-2966.2007.12621.x.

Kumar, P. and A. Panaitescu (2000). "Afterglow emission from naked gamma-ray bursts". In: *Astrophys. J.* 541. DOI: 10.1086/312905. URL: https://doi.org/10.1086/312905.

Kumar, Pawan and Jonathan Granot (July 2003). "The Evolution of a Structured Relativistic Jet and Gamma-Ray Burst Afterglow Light Curves". In: 591.2, pp. 1075–1085. DOI: 10.1086/375186. arXiv: astro-ph/0303174 [astro-ph].

Kumar, Pawan and Alin Panaitescu (Oct. 2000). "Afterglow Emission from Naked Gamma-Ray Bursts". In: 541.2, pp. L51–L54. DOI: 10.1086/312905. arXiv: astro-ph/0006317 [astro-ph].

Kumar, Pawan et al. (July 2008). "Properties of Gamma-Ray Burst Progenitor Stars". In: *Science* 321.5887, p. 376. DOI: 10.1126/science.1159003. arXiv: 0807.0445 [astro-ph].

Lamb, G. P. et al. (Jan. 2019). "The Optical Afterglow of GW170817 at One Year Post-merger". In: 870.2, L15, p. L15. DOI: 10.3847/2041-8213/aaf96b. arXiv: 1811.11491 [astro-ph.HE].

Lamb, Gavin P. and Shiho Kobayashi (Dec. 2017a). "Electromagnetic counterparts to structured jets from gravitational wave detected mergers". In: 472.4, pp. 4953–4964. DOI: 10.1093/mnras/stx2345. arXiv: 1706.03000 [astro-ph.HE].

— (Dec. 2017b). "Electromagnetic counterparts to structured jets from gravitational wave detected mergers". In: 472.4, pp. 4953–4964. DOI: 10.1093/mnras/stx2345. arXiv: 1706.03000 [astro-ph.HE].

Lamb, Gavin P. et al. (Sept. 2021). "GRB jet structure and the jet break". In: 506.3, pp. 4163–4174. DOI: 10.1093/mnras/stab2071. arXiv: 2104.11099 [astro-ph.HE].

Lamb, Gavin P et al. (Jan. 2022a). "Inhomogeneous Jets from Neutron Star Mergers: One Jet to Rule them all". In: *arXiv e-prints*, arXiv:2201.09796, arXiv:2201.09796. arXiv: 2201.09796 [astro-ph.HE].

— (Jan. 2022b). "Inhomogeneous Jets from Neutron Star Mergers: One Jet to Rule them all". In: *arXiv e-prints*, arXiv:2201.09796, arXiv:2201.09796. arXiv: 2201.09796 [astro-ph.HE].

Lazzati, D. and M. C. Begelman (2006). "Thick fireballs and the steep decay in the early X-Ray afterglow of gamma-ray bursts". In: *Astrophys. J.* 641. DOI: 10.1086/500502. URL: https://doi.org/10.1086/500502.

Lazzati, Davide and Mitchell C. Begelman (Aug. 2005). "Universal GRB Jets from Jet-Cocoon Interaction in Massive Stars". In: 629.2, pp. 903–907. DOI: 10.1086/430877. arXiv: astro-ph/0502084 [astro-ph].

Lazzati, Davide et al. (June 2018a). "Late Time Afterglow Observations Reveal a Collimated Relativistic Jet in the Ejecta of the Binary Neutron Star Merger GW170817". In: 120.24, 241103, p. 241103. DOI: 10.1103/PhysRevLett.120.241103. arXiv: 1712.03237 [astro-ph.HE].

— (June 2018b). "Late Time Afterglow Observations Reveal a Collimated Relativistic Jet in the Ejecta of the Binary Neutron Star Merger GW170817". In: 120.24, 241103, p. 241103. DOI: 10.1103/PhysRevLett.120.241103. arXiv: 1712.03237 [astro-ph.HE].

Li, Li-Xin and Bohdan Paczyński (Nov. 1998). "Transient Events from Neutron Star Mergers". In: 507.1, pp. L59–L62. DOI: 10.1086/311680. arXiv: astro-ph/9807272 [astro-ph].

Li, Liang et al. (Oct. 2012). "A Comprehensive Study of Gamma-Ray Burst Optical Emission. I. Flares and Early Shallow-decay Component". In: 758.1, 27, p. 27. DOI: 10.1088/0004-637X/758/1/27. arXiv: 1203.2332 [astro-ph.HE].

Li, Liang et al. (May 2015). "A Correlated Study of Optical and X-Ray Afterglows of GRBs". In: 805.1, 13, p. 13. DOI: 10.1088/0004-637X/805/1/13. arXiv: 1503.00976 [astro-ph.HE].

Li, Shao-Ze et al. (July 2018). "What Powered the Optical Transient AT2017gfo Associated with GW170817?" In: 861.2, L12, p. L12. DOI: 10.3847/2041-8213/aace61. arXiv: 1804.06597 [astro-ph.HE].

Li, Yanguo et al. (Jan. 2020). "The GECAM and its payload". In: *Scientia Sinica Physica, Mechanica & Astronomica* 50.12, p. 129508. DOI: 10.1360/SSPMA-2019-0417.

Li, Yufeng et al. (Feb. 2022). "Exploring the sky localization and early warning capabilities of third generation gravitational wave detectors in three-detector network configurations". In: 105.4, 043010, p. 043010. DOI: 10.1103/PhysRevD.105.043010. arXiv: 2109.07389 [astro-ph.IM].

Liang, E. W. (2006). "Testing the curvature effect and internal origin of gamma-ray burst prompt emissions and X-Ray flares with Swift data". In: *Astrophys. J.* 646. DOI: 10.1086/504684. URL: https://doi.org/10.1086/504684.

Liang, E. W. et al. (July 2006). "Testing the Curvature Effect and Internal Origin of Gamma-Ray Burst Prompt Emissions and X-Ray Flares with

Swift Data". In: 646.1, pp. 351–357. DOI: 10.1086/504684. arXiv: astro-ph/0602142 [astro-ph].

Lien, A. (2016). "The third Swift Burst Alert Telescope gamma-ray burst catalog". In: *Astrophys. J.* 829. DOI: 10.3847/0004-637X/829/1/7. URL: https://doi.org/10.3847/0004-637X/829/1/7.

LIGO Scientific Collaboration et al. (Apr. 2015). "Advanced LIGO". In: *Classical and Quantum Gravity* 32.7, 074001, p. 074001. DOI: 10.1088/0264-9381/32/7/074001. arXiv: 1411.4547 [gr-qc].

Lin, D. . B. (2017). "Steep decay phase shaped by the curvature effect. II. Spectral evolution". In: *Astrophys. J.* 840. DOI: 10.3847/1538-4357/aa6d77. URL: https://doi.org/10.3847/1538-4357/aa6d77.

Lipunov, V. M. et al. (Mar. 2001). "Gamma-Ray Bursts as Standard-Energy Explosions". In: *Astronomy Reports* 45.3, pp. 236–240. DOI: 10.1134/1.1353364. arXiv: astro-ph/9908136 [astro-ph].

Lucarelli, Francesco et al. (Aug. 2022). "Neutrino search from {}-ray bursts during the prompt and X-ray afterglow phases using 10 years of IceCube public data". In: *arXiv e-prints*, arXiv:2208.13792, arXiv:2208.13792. arXiv: 2208.13792 [astro-ph.HE].

Lyman, J. D. et al. (July 2018). "The optical afterglow of the short gamma-ray burst associated with GW170817". In: *Nature Astronomy* 2, pp. 751–754. DOI: 10.1038/s41550-018-0511-3. arXiv: 1801.02669 [astro-ph.HE].

Lyons, N. et al. (Feb. 2010). "Can X-ray emission powered by a spinning-down magnetar explain some gamma-ray burst light-curve features?" In: 402.2, pp. 705–712. DOI: 10.1111/j.1365-2966.2009.15538.x. arXiv: 0908.3798 [astro-ph.HE].

Lyutikov, M. (2006). "Did Swift measure gamma-ray burst prompt emission radii?" In: *Mon. Not. R. Astron. Soc.* 369. DOI: 10.1111/j.1745-3933.2006.00161.x. URL: https://doi.org/10.1111/j.1745-3933.2006.00161.x.

Lyutikov, Maxim and Roger Blandford (Dec. 2003). "Gamma Ray Bursts as Electromagnetic Outflows". In: *arXiv e-prints*, astro-ph/0312347, astro–ph/0312347. arXiv: astro-ph/0312347 [astro-ph].

Lyutikov, Maxim and Vladimir V. Usov (Nov. 2000). "Precursors of Gamma-Ray Bursts: A Clue to the Burster's Nature". In: 543.2, pp. L129–L132. DOI: 10.1086/317278. arXiv: astro-ph/0007291 [astro-ph].

Madau, Piero and Tassos Fragos (May 2017). "Radiation Backgrounds at Cosmic Dawn: X-Rays from Compact Binaries". In: 840.1, 39, p. 39. DOI: 10.3847/1538-4357/aa6af9. arXiv: 1606.07887 [astro-ph.GA].

Maggiore, Michele et al. (Mar. 2020). "Science case for the Einstein telescope". In: 2020.3, 050, p. 050. DOI: 10.1088/1475-7516/2020/03/050. arXiv: 1912.02622 [astro-ph.CO].

MAGIC Collaboration et al. (Nov. 2019). "Teraelectronvolt emission from the γ-ray burst GRB 190114C". In: 575.7783, pp. 455–458. DOI: 10.1038/s41586-019-1750-x. arXiv: 2006.07249 [astro-ph.HE].

Makhathini, S. et al. (Dec. 2021). "The Panchromatic Afterglow of GW170817: The Full Uniform Data Set, Modeling, Comparison with Previous Results, and Implications". In: 922.2, 154, p. 154. DOI: 10.3847/1538-4357/ac1ffc. arXiv: 2006.02382 [astro-ph.HE].

Mancarella, Michele et al. (Mar. 2022). "Cosmology and modified gravitational wave propagation from binary black hole population models". In: 105.6, 064030, p. 064030. DOI: 10.1103/PhysRevD.105.064030. arXiv: 2112.05728 [gr-qc].

Mandel, Ilya and Floor S. Broekgaarden (July 2021). "Rates of Compact Object Coalescences". In: *arXiv e-prints*, arXiv:2107.14239, arXiv:2107.14239. arXiv: 2107.14239 [astro-ph.HE].

Mangano, V. and B. Sbarufatti (2011). "Modeling the spectral evolution in the decaying tail of gamma-ray bursts observed by Swift". In: *Adv. Space Res.* 47. DOI: 10.1016/j.asr.2010.04.038. URL: https://doi.org/10.1016/j.asr.2010.04.038.

Mapelli, Michela and Nicola Giacobbo (Oct. 2018). "The cosmic merger rate of neutron stars and black holes". In: 479.4, pp. 4391–4398. DOI: 10.1093/mnras/sty1613. arXiv: 1806.04866 [astro-ph.HE].

Mapelli, Michela et al. (Dec. 2017). "The cosmic merger rate of stellar black hole binaries from the Illustris simulation". In: 472.2, pp. 2422–2435. DOI: 10.1093/mnras/stx2123. arXiv: 1708.05722 [astro-ph.GA].

Margutti, R. et al. (Nov. 2013). "The Signature of the Central Engine in the Weakest Relativistic Explosions: GRB 100316D". In: 778.1, 18, p. 18. DOI: 10.1088/0004-637X/778/1/18. arXiv: 1308.1687 [astro-ph.HE].

Matsumoto, Tatsuya et al. (June 2019). "Generalized compactness limit from an arbitrary viewing angle". In: 486.2, pp. 1563–1573. DOI: 10.1093/mnras/stz923. arXiv: 1903.06712 [astro-ph.HE].

Meegan, C. A. et al. (Jan. 1992). "Spatial distribution of γ-ray bursts observed by BATSE". In: 355.6356, pp. 143–145. DOI: 10.1038/355143a0.

Meegan, Charles et al. (Sept. 2009a). "The Fermi Gamma-ray Burst Monitor". In: 702.1, pp. 791–804. DOI: 10.1088/0004-637X/702/1/791. arXiv: 0908.0450 [astro-ph.IM].

Meegan, Charles et al. (Sept. 2009b). "The Fermi Gamma-ray Burst Monitor". In: 702.1, pp. 791–804. DOI: 10.1088/0004-637X/702/1/791. arXiv: 0908.0450 [astro-ph.IM].

Mei, Alessio et al. (Dec. 2022a). "Constraints on the Physics of the Prompt Emission from Distant and Energetic Gamma-Ray Burst GRB 220101A". In: 941.1, 82, p. 82. DOI: 10.3847/1538-4357/aca091. arXiv: 2203.04971 [astro-ph.HE].

Mei, Alessio et al. (May 2022b). "GeV emission from a compact binary merger". In: *arXiv e-prints*, arXiv:2205.08566, arXiv:2205.08566. arXiv: 2205.08566 [astro-ph.HE].

Mei, Alessio et al. (Dec. 2022c). "Gigaelectronvolt emission from a compact binary merger". In: 612.7939, pp. 236–239. DOI: 10.1038/s41586-022-05404-7. arXiv: 2205.08566 [astro-ph.HE].

Meszaros, P. and M. J. Rees (Dec. 1993). "Gamma-Ray Bursts: Multiwaveband Spectral Predictions for Blast Wave Models". In: 418, p. L59. DOI: 10.1086/187116. arXiv: astro-ph/9309011 [astro-ph].

Mészáros, P. and M. J. Rees (1997). "Optical and long-wavelength afterglow from gamma-ray bursts". In: *Astrophys. J.* 476. DOI: 10.1086/303625. URL: https://doi.org/10.1086/303625.

Mészáros, P. and M. J. Rees (June 1997). "Poynting Jets from Black Holes and Cosmological Gamma-Ray Bursts". In: 482.1, pp. L29–L32. DOI: 10.1086/310692. arXiv: astro-ph/9609065 [astro-ph].

Mészáros, P. and M. J. Rees (1999). "GRB 990123: reverse and internal shock flashes and late afterglow behaviour". In: *Mon. Not. R. Astron. Soc.* 306. DOI: 10.1046/j.1365-8711.1999.02800.x. URL: https://doi.org/10.1046/j.1365-8711.1999.02800.x.

Metzger, B. D. et al. (May 2011). "The protomagnetar model for gamma-ray bursts". In: 413.3, pp. 2031–2056. DOI: 10.1111/j.1365-2966.2011.18280.x. arXiv: 1012.0001 [astro-ph.HE].

Metzger, Brian D. (Dec. 2019). "Kilonovae". In: *Living Reviews in Relativity* 23.1, 1, p. 1. DOI: 10.1007/s41114-019-0024-0. arXiv: 1910.01617 [astro-ph.HE].

Metzger, Brian D. and Anthony L. Piro (Apr. 2014). "Optical and X-ray emission from stable millisecond magnetars formed from the merger of binary neutron stars". In: 439.4, pp. 3916–3930. DOI: 10.1093/mnras/stu247. arXiv: 1311.1519 [astro-ph.HE].

Metzger, Brian D. et al. (Jan. 2014). "Ionization break-out from millisecond pulsar wind nebulae: an X-ray probe of the origin of superluminous supernovae". In: 437.1, pp. 703–720. DOI: 10.1093/mnras/stt1922. arXiv: 1307.8115 [astro-ph.HE].

Miceli, Davide and Lara Nava (May 2022). "Gamma-Ray Bursts Afterglow Physics and the VHE Domain". In: *Galaxies* 10.3, p. 66. DOI: 10.3390/galaxies10030066. arXiv: 2205.12146 [astro-ph.HE].

Mills, Cameron et al. (May 2018). "Localization of binary neutron star mergers with second and third generation gravitational-wave detectors". In: 97.10, 104064, p. 104064. DOI: 10.1103/PhysRevD.97.104064. arXiv: 1708.00806 [gr-qc].

Misra, K. et al. (July 2021). "Low frequency view of GRB 190114C reveals time varying shock micro-physics". In: 504.4, pp. 5685–5701. DOI: 10.1093/mnras/stab1050. arXiv: 1911.09719 [astro-ph.HE].

Mochkovitch, R. et al. (July 2021). "Prospects for kilonova signals in the gravitational-wave era". In: 651, A83, A83. DOI: 10.1051/0004-6361/202140689. arXiv: 2103.00943 [astro-ph.HE].

Mooley, K. P. et al. (Feb. 2018a). "A mildly relativistic wide-angle outflow in the neutron-star merger event GW170817". In: 554.7691, pp. 207–210. DOI: 10.1038/nature25452. arXiv: 1711.11573 [astro-ph.HE].

Mooley, K. P. et al. (Sept. 2018b). "Superluminal motion of a relativistic jet in the neutron-star merger GW170817". In: 561.7723, pp. 355–359. DOI: 10.1038/s41586-018-0486-3. arXiv: 1806.09693 [astro-ph.HE].

— (Sept. 2018c). "Superluminal motion of a relativistic jet in the neutron-star merger GW170817". In: 561.7723, pp. 355–359. DOI: 10.1038/s41586-018-0486-3. arXiv: 1806.09693 [astro-ph.HE].

Mooley, Kunal P. et al. (Oct. 2022). "Optical superluminal motion measurement in the neutron-star merger GW170817". In: 610.7931, pp. 273–276. DOI: 10.1038/s41586-022-05145-7. arXiv: 2210.06568 [astro-ph.HE].

Mu, H. . J. (2016). "The history of GRB outflows: ejection Lorentz factor and radiation location of X-Ray flares". In: *Astrophys. J.* 831. DOI: 10.3847/0004-637X/831/1/111. URL: https://doi.org/10.3847/0004-637X/831/1/111.

Mu, Hui-Jun et al. (Nov. 2016). "The History of GRB Outflows: Ejection Lorentz Factor and Radiation Location of X-Ray Flares". In: 831.1, 111, p. 111. DOI: 10.3847/0004-637X/831/1/111. arXiv: 1608.05028 [astro-ph.HE].

Murase, Kohta et al. (Feb. 2012). "The Role of Stochastic Acceleration in the Prompt Emission of Gamma-Ray Bursts: Application to Hadronic Injection". In: 746.2, 164, p. 164. DOI: 10.1088/0004-637X/746/2/164. arXiv: 1107.5575 [astro-ph.HE].

Murguia-Berthier, Ariadna et al. (June 2014). "Necessary Conditions for Short Gamma-Ray Burst Production in Binary Neutron Star Mergers".

In: 788.1, L8, p. L8. DOI: 10.1088/2041-8205/788/1/L8. arXiv: 1404.0383 [astro-ph.HE].

Nagakura, Hiroki et al. (Apr. 2014). "Jet Collimation in the Ejecta of Double Neutron Star Mergers: A New Canonical Picture of Short Gamma-Ray Bursts". In: 784.2, L28, p. L28. DOI: 10.1088/2041-8205/784/2/L28. arXiv: 1403.0956 [astro-ph.HE].

Nakar, Ehud (Nov. 2020). "The electromagnetic counterparts of compact binary mergers". In: 886, pp. 1–84. DOI: 10.1016/j.physrep.2020.08.008. arXiv: 1912.05659 [astro-ph.HE].

Nakar, Ehud and Tsvi Piran (Jan. 2017a). "The Observable Signatures of GRB Cocoons". In: 834.1, 28, p. 28. DOI: 10.3847/1538-4357/834/1/28. arXiv: 1610.05362 [astro-ph.HE].

— (Jan. 2017b). "The Observable Signatures of GRB Cocoons". In: 834.1, 28, p. 28. DOI: 10.3847/1538-4357/834/1/28. arXiv: 1610.05362 [astro-ph.HE].

— (Mar. 2021). "Afterglow Constraints on the Viewing Angle of Binary Neutron Star Mergers and Determination of the Hubble Constant". In: 909.2, 114, p. 114. DOI: 10.3847/1538-4357/abd6cd. arXiv: 2005.01754 [astro-ph.HE].

Nakar, Ehud and Re'em Sari (Mar. 2012). "Relativistic Shock Breakouts—A Variety of Gamma-Ray Flares: From Low-luminosity Gamma-Ray Bursts to Type Ia Supernovae". In: 747.2, 88, p. 88. DOI: 10.1088/0004-637X/747/2/88. arXiv: 1106.2556 [astro-ph.HE].

Nakar, Ehud et al. (Nov. 2002). "The Detectability of Orphan Afterglows". In: 579.2, pp. 699–705. DOI: 10.1086/342791. arXiv: astro-ph/0204203 [astro-ph].

Nakar, Ehud et al. (Nov. 2018). "From γ to Radio: The Electromagnetic Counterpart of GW170817". In: 867.1, 18, p. 18. DOI: 10.3847/1538-4357/aae205. arXiv: 1803.07595 [astro-ph.HE].

Nandra, Kirpal et al. (June 2013). "The Hot and Energetic Universe: A White Paper presenting the science theme motivating the Athena+ mission". In: *arXiv e-prints*, arXiv:1306.2307, arXiv:1306.2307. arXiv: 1306.2307 [astro-ph.HE].

Narayan, R. and P. Kumar (2009). "A turbulent model of gamma-ray burst variability". In: *Mon. Not. R. Astron. Soc.* 394. DOI: 10.1111/j.1745-3933.2009.00624.x. URL: https://doi.org/10.1111/j.1745-3933.2009.00624.x.

Nardini, M. et al. (Feb. 2014). "Afterglow rebrightenings as a signature of a long-lasting central engine activity?. The emblematic case of GRB

100814A". In: 562, A29, A29. DOI: 10.1051/0004-6361/201321525. arXiv: 1312.1335 [astro-ph.HE].

Nathanail, Antonios et al. (Apr. 2021). "3D magnetized jet break-out from neutron-star binary merger ejecta: afterglow emission from the jet and the ejecta". In: 502.2, pp. 1843–1855. DOI: 10.1093/mnras/stab115. arXiv: 2009.09714 [astro-ph.HE].

Nativi, L. et al. (Jan. 2022). "Are interactions with neutron star merger winds shaping the jets?" In: 509.1, pp. 903–913. DOI: 10.1093/mnras/stab2982. arXiv: 2109.00814 [astro-ph.HE].

Nava, L. et al. (2011). "Spectral properties of 438 GRBs detected by Fermi/GBM". In: *Astron. Astrophys.* 530. DOI: 10.1051/0004-6361/201016270. URL: https://doi.org/10.1051/0004-6361/201016270.

Nava, L. et al. (June 2011). "Spectral properties of 438 GRBs detected by Fermi/GBM". In: 530, A21, A21. DOI: 10.1051/0004-6361/201016270. arXiv: 1012.2863 [astro-ph.HE].

Nava, L. et al. (Apr. 2012). "A complete sample of bright Swift long gamma-ray bursts: testing the spectral-energy correlations". In: 421.2, pp. 1256–1264. DOI: 10.1111/j.1365-2966.2011.20394.x. arXiv: 1112.4470 [astro-ph.HE].

Nava, L. et al. (Aug. 2013). "Afterglow emission in gamma-ray bursts - I. Pair-enriched ambient medium and radiative blast waves". In: 433.3, pp. 2107–2121. DOI: 10.1093/mnras/stt872. arXiv: 1211.2806 [astro-ph.HE].

Nicholl, M. et al. (Oct. 2017). "The Electromagnetic Counterpart of the Binary Neutron Star Merger LIGO/Virgo GW170817. III. Optical and UV Spectra of a Blue Kilonova from Fast Polar Ejecta". In: 848.2, L18, p. L18. DOI: 10.3847/2041-8213/aa9029. arXiv: 1710.05456 [astro-ph.HE].

Nitz, Alexander H. and Tito Dal Canton (Aug. 2021). "Pre-merger Localization of Compact-binary Mergers with Third-generation Observatories". In: 917.2, L27, p. L27. DOI: 10.3847/2041-8213/ac1a75. arXiv: 2106.15259 [astro-ph.HE].

Norris, J. P. and J. T. Bonnell (May 2006). "Short Gamma-Ray Bursts with Extended Emission". In: 643.1, pp. 266–275. DOI: 10.1086/502796. arXiv: astro-ph/0601190 [astro-ph].

Norris, J. P. et al. (Mar. 1996). "Attributes of Pulses in Long Bright Gamma-Ray Bursts". In: 459, p. 393. DOI: 10.1086/176902.

Norris, J. P. et al. (July 2005). "Long-Lag, Wide-Pulse Gamma-Ray Bursts". In: 627.1, pp. 324–345. DOI: 10.1086/430294. arXiv: astro-ph/0503383 [astro-ph].

Nousek, J. A. (2006). "Evidence for a canonical gamma-ray burst afterglow light curve in the Swift XRT data". In: *Astrophys. J.* 642. DOI: 10.1086/500724. URL: https://doi.org/10.1086/500724.

Nugent, Anya E. et al. (Nov. 2022). "Short GRB Host Galaxies. II. A Legacy Sample of Redshifts, Stellar Population Properties, and Implications for Their Neutron Star Merger Origins". In: 940.1, 57, p. 57. DOI: 10.3847/1538-4357/ac91d1. arXiv: 2206.01764 [astro-ph.GA].

O'Brien, P. T. (2006). "The early X-Ray emission from GRBs". In: *Astrophys. J.* 647. DOI: 10.1086/505457. URL: https://doi.org/10.1086/505457.

O'Brien, P. T. et al. (Aug. 2006). "The Early X-Ray Emission from GRBs". In: 647.2, pp. 1213–1237. DOI: 10.1086/505457. arXiv: astro-ph/0601125 [astro-ph].

Oganesyan, G. (2017). "Detection of low-energy breaks in gamma-ray burst prompt emission spectra". In: *Astrophys. J.* 846. DOI: 10.3847/1538-4357/aa831e. URL: https://doi.org/10.3847/1538-4357/aa831e.

— (2018). "Characterization of gamma-ray burst prompt emission spectra down to soft X-rays". In: *Astron. Astrophys.* 616. DOI: 10.1051/0004-6361/201732172. URL: https://doi.org/10.1051/0004-6361/201732172.

— (2019). "Prompt optical emission as a signature of synchrotron radiation in gamma-ray bursts". In: *Astron. Astrophys.* 628. DOI: 10.1051/0004-6361/201935766. URL: https://doi.org/10.1051/0004-6361/201935766.

— (2020). "Structured jets and X-Ray plateaus in gamma-ray burst phenomena". In: *Astrophys. J.* 893. DOI: 10.3847/1538-4357/ab8221. URL: https://doi.org/10.3847/1538-4357/ab8221.

Oganesyan, Gor et al. (Apr. 2020a). "Structured Jets and X-Ray Plateaus in Gamma-Ray Burst Phenomena". In: 893.2, 88, p. 88. DOI: 10.3847/1538-4357/ab8221. arXiv: 1904.08786 [astro-ph.HE].

— (Apr. 2020b). "Structured Jets and X-Ray Plateaus in Gamma-Ray Burst Phenomena". In: 893.2, 88, p. 88. DOI: 10.3847/1538-4357/ab8221. arXiv: 1904.08786 [astro-ph.HE].

Oganesyan, Gor et al. (Aug. 2021). "Exceptionally bright optical emission from a rare and distant $\gamma-$ray burst". In: *arXiv e-prints*, arXiv:2109.00010, arXiv:2109.00010. arXiv: 2109.00010 [astro-ph.HE].

Özel, Feryal and Paulo Freire (Sept. 2016). "Masses, Radii, and the Equation of State of Neutron Stars". In: 54, pp. 401–440. DOI: 10.1146/annurev-astro-081915-023322. arXiv: 1603.02698 [astro-ph.HE].

Paczynski, B. (Sept. 1986). "Gamma-ray bursters at cosmological distances". In: 308, pp. L43–L46. DOI: 10.1086/184740.

Paczynski, B. and J. E. Rhoads (1993). "Radio transients from gamma-ray bursters". In: *Astrophys. J.* 418. DOI: 10.1086/187102. URL: https://doi.org/10.1086/187102.

Page, K. L. et al. (Dec. 2020). "Swift-XRT follow-up of gravitational wave triggers during the third aLIGO/Virgo observing run". In: 499.3, pp. 3459–3480. DOI: 10.1093/mnras/staa3032. arXiv: 2009.13804 [astro-ph.HE].

Palmerio, J. T. and F. Daigne (May 2021). "Constraining the intrinsic population of long gamma-ray bursts: Implications for spectral correlations, cosmic evolution, and their use as tracers of star formation". In: 649, A166, A166. DOI: 10.1051/0004-6361/202039929. arXiv: 2011.14745 [astro-ph.HE].

Palmerio, J. T. et al. (Mar. 2019). "Are long gamma-ray bursts biased tracers of star formation? Clues from the host galaxies of the Swift/BAT6 complete sample of bright LGRBs. III. Stellar masses, star formation rates, and metallicities at z > 1". In: 623, A26, A26. DOI: 10.1051/0004-6361/201834179. arXiv: 1901.02457 [astro-ph.HE].

Panaitescu, A. (2019). "Adiabatic and radiative cooling of relativistic electrons applied to synchrotron spectra and light curves of gamma-ray burst pulses". In: *Astrophys. J.* 886. DOI: 10.3847/1538-4357/ab4e17. URL: https://doi.org/10.3847/1538-4357/ab4e17.

Panaitescu, A. (May 2020). "X-Ray Afterglows from the Gamma-Ray Burst "Large-angle" Emission". In: 895.1, 39, p. 39. DOI: 10.3847/1538-4357/ab8bdf. arXiv: 2005.00104 [astro-ph.HE].

Panaitescu, A. et al. (July 2006). "Evidence for chromatic X-ray light-curve breaks in Swift gamma-ray burst afterglows and their theoretical implications". In: 369.4, pp. 2059–2064. DOI: 10.1111/j.1365-2966.2006.10453.x. arXiv: astro-ph/0604105 [astro-ph].

Panaitescu, A. D. and W. T. Vestrand (Oct. 2022). "The Synchrotron Low-energy Spectrum Arising from the Cooling of Electrons in Gamma-Ray Bursts". In: 938.2, 132, p. 132. DOI: 10.3847/1538-4357/ac8b75. arXiv: 2209.10014 [astro-ph.HE].

Pannarale, Francesco and Frank Ohme (Aug. 2014). "Prospects for Joint Gravitational-wave and Electromagnetic Observations of Neutron-star-Black-hole Coalescing Binaries". In: 791.1, L7, p. L7. DOI: 10.1088/2041-8205/791/1/L7. arXiv: 1406.6057 [gr-qc].

Patricelli, Barbara et al. (July 2022). "Prospects for multimessenger detection of binary neutron star mergers in the fourth LIGO-Virgo-KAGRA observing run". In: 513.3, pp. 4159–4168. DOI: 10.1093/mnras/stac1167. arXiv: 2204.12504 [astro-ph.HE].

Pavan, Andrea et al. (Sept. 2021). "Short gamma-ray burst jet propagation in binary neutron star merger environments". In: 506.3, pp. 3483–3498. DOI: 10.1093/mnras/stab1810. arXiv: 2104.12410 [astro-ph.HE].

Pavan, Andrea et al. (Nov. 2022). "Jet-environment interplay in magnetized binary neutron star mergers". In: *arXiv e-prints*, arXiv:2211.10135, arXiv:2211.10135. arXiv: 2211.10135 [astro-ph.HE].

Pe'er, A. (2008). "Temporal evolution of thermal emission from relativistically expanding plasma". In: *Astrophys. J.* 682. DOI: 10.1086/588136. URL: https://doi.org/10.1086/588136.

Pei, Y. C. (Aug. 1992). "Interstellar dust from the Milky Way to the Magellanic Clouds". In: 395, pp. 130–139. DOI: 10.1086/171637.

Perego, Albino et al. (Jan. 2022). "Production of Very Light Elements and Strontium in the Early Ejecta of Neutron Star Mergers". In: 925.1, 22, p. 22. DOI: 10.3847/1538-4357/ac3751. arXiv: 2009.08988 [astro-ph.HE].

Perna, R. and D. Lazzati (2002). "Time-dependent photoionization in a dusty medium. I. code description and general results". In: *Astrophys. J.* 580. DOI: 10.1086/343081. URL: https://doi.org/10.1086/343081.

Pescalli, A. et al. (Feb. 2015). "Luminosity function and jet structure of Gamma-Ray Burst". In: 447.2, pp. 1911–1921. DOI: 10.1093/mnras/stu2482. arXiv: 1409.1213 [astro-ph.HE].

Pescalli, A. et al. (Mar. 2016). "The rate and luminosity function of long gamma ray bursts". In: 587, A40, A40. DOI: 10.1051/0004-6361/201526760. arXiv: 1506.05463 [astro-ph.HE].

Petrov, Polina et al. (Jan. 2022). "Data-driven Expectations for Electromagnetic Counterpart Searches Based on LIGO/Virgo Public Alerts". In: 924.2, 54, p. 54. DOI: 10.3847/1538-4357/ac366d. arXiv: 2108.07277 [astro-ph.HE].

Pian, E. et al. (Nov. 2017a). "Spectroscopic identification of r-process nucleosynthesis in a double neutron-star merger". In: 551.7678, pp. 67–70. DOI: 10.1038/nature24298. arXiv: 1710.05858 [astro-ph.HE].

— (Nov. 2017b). "Spectroscopic identification of r-process nucleosynthesis in a double neutron-star merger". In: 551.7678, pp. 67–70. DOI: 10.1038/nature24298. arXiv: 1710.05858 [astro-ph.HE].

Piran, T. (June 1999). "Gamma-ray bursts and the fireball model". In: 314.6, pp. 575–667. DOI: 10.1016/S0370-1573(98)00127-6. arXiv: astro-ph/9810256 [astro-ph].

Piro, L. et al. (Oct. 2021). "Multi-messenger-Athena Synergy White Paper". In: *arXiv e-prints*, arXiv:2110.15677, arXiv:2110.15677. arXiv: 2110.15677 [astro-ph.HE].

Pozanenko, A. S. et al. (Jan. 2018). "GRB 170817A Associated with GW170817: Multi-frequency Observations and Modeling of Prompt Gamma-Ray Emission". In: 852.2, L30, p. L30. DOI: 10.3847/2041-8213/aaa2f6. arXiv: 1710.05448 [astro-ph.HE].

Preece, R. D. et al. (Jan. 2000). "The BATSE Gamma-Ray Burst Spectral Catalog. I. High Time Resolution Spectroscopy of Bright Bursts Using High Energy Resolution Data". In: 126.1, pp. 19–36. DOI: 10.1086/313289. arXiv: astro-ph/9908119 [astro-ph].

Punturo, M. et al. (2010). "The Einstein Telescope: A third-generation gravitational wave observatory". In: *Class. Quant. Grav.* 27. Ed. by Fulvio Ricci, p. 194002. DOI: 10.1088/0264-9381/27/19/194002.

Punturo, M. et al. (Oct. 2010). "The Einstein Telescope: a third-generation gravitational wave observatory". In: *Classical and Quantum Gravity* 27.19, 194002, p. 194002. DOI: 10.1088/0264-9381/27/19/194002.

Qin, Y. P. (Aug. 2008). "The Full Curvature Effect Expected in Early X-Ray Afterglow Emission from Gamma-Ray Bursts". In: 683.2, pp. 900–912. DOI: 10.1086/589277. arXiv: 0804.2175 [astro-ph].

Radice, David et al. (Dec. 2018). "Binary Neutron Star Mergers: Mass Ejection, Electromagnetic Counterparts, and Nucleosynthesis". In: 869.2, 130, p. 130. DOI: 10.3847/1538-4357/aaf054. arXiv: 1809.11161 [astro-ph.HE].

Ramirez-Ruiz, Enrico et al. (Dec. 2002). "Events in the life of a cocoon surrounding a light, collapsar jet". In: 337.4, pp. 1349–1356. DOI: 10.1046/j.1365-8711.2002.05995.x. arXiv: astro-ph/0205108 [astro-ph].

Rastinejad, J. C. et al. (Apr. 2022). "A Kilonova Following a Long-Duration Gamma-Ray Burst at 350 Mpc". In: *arXiv e-prints*, arXiv:2204.10864, arXiv:2204.10864. arXiv: 2204.10864 [astro-ph.HE].

Ravasio, M. E. (2018). "Consistency with synchrotron emission in the bright GRB 160625B observed by Fermi". In: *Astron. Astrophys.* 613. DOI: 10.1051/0004-6361/201732245. URL: https://doi.org/10.1051/0004-6361/201732245.

— (2019). "Evidence of two spectral breaks in the prompt emission of gamma-ray bursts". In: *Astron. Astrophys.* 625. DOI: 10.1051/0004-6361/201834987. URL: https://doi.org/10.1051/0004-6361/201834987.

Rees, M. J. and P. Meszaros (Aug. 1994). "Unsteady outflow models for cosmological gamma-ray bursts". In: 430, pp. L93–L96. DOI: 10.1086/187446. eprint: astro-ph/9404038.

Rees, M. J. and P. Meszaros (1994). "Unsteady outflow models for cosmological gamma-ray bursts". In: *Astrophys. J.* 430. DOI: 10.1086/187446. URL: https://doi.org/10.1086/187446.

Rees, M. J. and P. Mészáros (Mar. 1998). "Refreshed Shocks and Afterglow Longevity in Gamma-Ray Bursts". In: 496.1, pp. L1–L4. DOI: 10.1086/311244. arXiv: astro-ph/9712252 [astro-ph].

Resmi, L. et al. (Nov. 2018). "Low-frequency View of GW170817/GRB 170817A with the Giant Metrewave Radio Telescope". In: 867.1, 57, p. 57. DOI: 10.3847/1538-4357/aae1a6. arXiv: 1803.02768 [astro-ph.HE].

Rhoads, James E. (Nov. 1999). "The Dynamics and Light Curves of Beamed Gamma-Ray Burst Afterglows". In: 525.2, pp. 737–749. DOI: 10.1086/307907. arXiv: astro-ph/9903399 [astro-ph].

Ronchini, S. et al. (Sept. 2022a). "Perspectives for multimessenger astronomy with the next generation of gravitational-wave detectors and high-energy satellites". In: 665, A97, A97. DOI: 10.1051/0004-6361/202243705. arXiv: 2204.01746 [astro-ph.HE].

Ronchini, Samuele et al. (Jan. 2021). "Spectral index-flux relation for investigating the origins of steep decay in γ-ray bursts". In: *Nature Communications* 12, 4040, p. 4040. DOI: 10.1038/s41467-021-24246-x. arXiv: 2009.03913 [astro-ph.HE].

Ronchini, Samuele et al. (Nov. 2022b). "Combined X-ray and optical analysis to probe the origin of the plateau emission in γ-ray bursts afterglows". In: *arXiv e-prints*, arXiv:2211.00661, arXiv:2211.00661. arXiv: 2211.00661 [astro-ph.HE].

Rosati, P. et al. (Dec. 2021). "Synergies of THESEUS with the large facilities of the 2030s and guest observer opportunities". In: *Experimental Astronomy* 52.3, pp. 407–437. DOI: 10.1007/s10686-021-09764-2. arXiv: 2104.09535 [astro-ph.IM].

Rossi, Elena et al. (June 2002a). "Afterglow light curves, viewing angle and the jet structure of γ-ray bursts". In: 332.4, pp. 945–950. DOI: 10.1046/j.1365-8711.2002.05363.x. arXiv: astro-ph/0112083 [astro-ph].

— (June 2002b). "Afterglow light curves, viewing angle and the jet structure of γ-ray bursts". In: 332.4, pp. 945–950. DOI: 10.1046/j.1365-8711.2002.05363.x. arXiv: astro-ph/0112083 [astro-ph].

Rowlinson, A. et al. (Dec. 2010). "The unusual X-ray emission of the short Swift GRB 090515: evidence for the formation of a magnetar?" In: 409.2, pp. 531–540. DOI: 10.1111/j.1365-2966.2010.17354.x. arXiv: 1007.2185 [astro-ph.HE].

Rowlinson, A. et al. (Apr. 2013). "Signatures of magnetar central engines in short GRB light curves". In: 430.2, pp. 1061–1087. DOI: 10.1093/mnras/sts683. arXiv: 1301.0629 [astro-ph.HE].

Ryan, Geoffrey et al. (June 2020a). "Gamma-Ray Burst Afterglows in the Multimessenger Era: Numerical Models and Closure Relations". In: 896.2, 166, p. 166. DOI: 10.3847/1538-4357/ab93cf. arXiv: 1909.11691 [astro-ph.HE].

— (June 2020b). "Gamma-Ray Burst Afterglows in the Multimessenger Era: Numerical Models and Closure Relations". In: 896.2, 166, p. 166. DOI: 10.3847/1538-4357/ab93cf. arXiv: 1909.11691 [astro-ph.HE].

"Rybicki, G. B. & Lightman, A. P. Riadiative Processes in Astrophysics. Wiley-Interscience Publication (1979)." (n.d.). In: ().

Ryde, Felix and Asaf Pe'er (Sept. 2009). "Quasi-blackbody Component and Radiative Efficiency of the Prompt Emission of Gamma-ray Bursts". In: 702.2, pp. 1211–1229. DOI: 10.1088/0004-637X/702/2/1211. arXiv: 0811.4135 [astro-ph].

Salafia, O. S. et al. (July 2015a). "Structure of gamma-ray burst jets: intrinsic versus apparent properties". In: 450.4, pp. 3549–3558. DOI: 10.1093/mnras/stv766. arXiv: 1502.06608 [astro-ph.HE].

— (July 2015b). "Structure of gamma-ray burst jets: intrinsic versus apparent properties". In: 450.4, pp. 3549–3558. DOI: 10.1093/mnras/stv766. arXiv: 1502.06608 [astro-ph.HE].

— (Oct. 2016). "Light curves and spectra from off-axis gamma-ray bursts". In: 461.4, pp. 3607–3619. DOI: 10.1093/mnras/stw1549. arXiv: 1601.03735 [astro-ph.HE].

Salafia, O. S. et al. (Aug. 2019a). "On-axis view of GRB 170817A". In: 628, A18, A18. DOI: 10.1051/0004-6361/201935831. arXiv: 1905.01190 [astro-ph.HE].

— (Aug. 2019b). "On-axis view of GRB 170817A". In: 628, A18, A18. DOI: 10.1051/0004-6361/201935831. arXiv: 1905.01190 [astro-ph.HE].

Salafia, O. S. et al. (Apr. 2020a). "Gamma-ray burst jet propagation, development of angular structure, and the luminosity function". In: 636, A105, A105. DOI: 10.1051/0004-6361/201936335. arXiv: 1907.07599 [astro-ph.HE].

— (Apr. 2020b). "Gamma-ray burst jet propagation, development of angular structure, and the luminosity function". In: 636, A105, A105. DOI: 10.1051/0004-6361/201936335. arXiv: 1907.07599 [astro-ph.HE].

Salafia, O. S. et al. (Feb. 2022). "Constraints on the merging binary neutron star mass distribution and equation of state based on the fraction of

jets". In: *arXiv e-prints*, arXiv:2202.01656, arXiv:2202.01656. arXiv: 2202.01656 [astro-ph.HE].

Salafia, Om Sharan and Giancarlo Ghirlanda (Aug. 2022). "The Structure of Gamma Ray Burst Jets". In: *Galaxies* 10.5, p. 93. DOI: 10.3390/galaxies10050093.

Salafia, Om Sharan et al. (Sept. 2017). "Where and When: Optimal Scheduling of the Electromagnetic Follow-up of Gravitational-wave Events Based on Counterpart Light-curve Models". In: 846.1, 62, p. 62. DOI: 10.3847/1538-4357/aa850e. arXiv: 1704.05851 [astro-ph.HE].

Saleem, M. (Apr. 2020). "Prospects of joint detections of neutron star mergers and short GRBs with Gaussian structured jets". In: 493.2, pp. 1633–1639. DOI: 10.1093/mnras/staa303. arXiv: 1905.00314 [astro-ph.HE].

Saleem, M. et al. (Mar. 2018a). "Exploring short-GRB afterglow parameter space for observations in coincidence with gravitational waves". In: 474.4, pp. 5340–5350. DOI: 10.1093/mnras/stx3104. arXiv: 1710.06102 [astro-ph.HE].

Saleem, M. et al. (Mar. 2018b). "Rates of short-GRB afterglows in association with binary neutron star mergers". In: 475.1, pp. 699–707. DOI: 10.1093/mnras/stx3108. arXiv: 1710.06111 [astro-ph.HE].

Salvaterra, R. et al. (Apr. 2012). "A Complete Sample of Bright Swift Long Gamma-Ray Bursts. I. Sample Presentation, Luminosity Function and Evolution". In: 749.1, 68, p. 68. DOI: 10.1088/0004-637X/749/1/68. arXiv: 1112.1700 [astro-ph.CO].

Sana, H. et al. (July 2012). "Binary Interaction Dominates the Evolution of Massive Stars". In: *Science* 337.6093, p. 444. DOI: 10.1126/science.1223344. arXiv: 1207.6397 [astro-ph.SR].

Santoliquido, Filippo et al. (Aug. 2020). "The Cosmic Merger Rate Density Evolution of Compact Binaries Formed in Young Star Clusters and in Isolated Binaries". In: 898.2, 152, p. 152. DOI: 10.3847/1538-4357/ab9b78. arXiv: 2004.09533 [astro-ph.HE].

Santoliquido, Filippo et al. (Apr. 2021). "The cosmic merger rate density of compact objects: impact of star formation, metallicity, initial mass function, and binary evolution". In: 502.4, pp. 4877–4889. DOI: 10.1093/mnras/stab280. arXiv: 2009.03911 [astro-ph.HE].

Sari, R. and T. Piran (1997). "Variability in gamma-ray bursts: a clue". In: *Astrophys. J.* 485. DOI: 10.1086/304428. URL: https://doi.org/10.1086/304428.

Sari, R. et al. (Apr. 1998a). "Spectra and Light Curves of Gamma-Ray Burst Afterglows". In: 497, p. L17. DOI: 10.1086/311269. eprint: arXiv:astro-ph/9712005.

Sari, Re'em and Ann A. Esin (Feb. 2001). "On the Synchrotron Self-Compton Emission from Relativistic Shocks and Its Implications for Gamma-Ray Burst Afterglows". In: 548.2, pp. 787–799. DOI: 10.1086/31900310.48550/arXiv.astro-ph/0005253. arXiv: astro-ph/0005253 [astro-ph].

Sari, Re'em et al. (Apr. 1998b). "Spectra and Light Curves of Gamma-Ray Burst Afterglows". In: 497.1, pp. L17–L20. DOI: 10.1086/311269. arXiv: astro-ph/9712005 [astro-ph].

Sarin, Nikhil and Paul D. Lasky (Feb. 2022). "Multimessenger astronomy with a kHz-band gravitational-wave observatory". In: 39, e007, e007. DOI: 10.1017/pasa.2022.1. arXiv: 2110.10892 [astro-ph.HE].

Sarin, Nikhil et al. (Apr. 2022). "Linking the rates of neutron star binaries and short gamma-ray bursts". In: 105.8, 083004, p. 083004. DOI: 10.1103/PhysRevD.105.083004. arXiv: 2201.08491 [astro-ph.HE].

Savchenko, V. et al. (Oct. 2017). "INTEGRAL Detection of the First Prompt Gamma-Ray Signal Coincident with the Gravitational-wave Event GW170817". In: 848, L15, p. L15. DOI: 10.3847/2041-8213/aa8f94. arXiv: 1710.05449 [astro-ph.HE].

Schutz, B. F. (Sept. 1986). "Determining the Hubble constant from gravitational wave observations". In: 323.6086, pp. 310–311. DOI: 10.1038/323310a0.

Sekiguchi, Yuichiro et al. (June 2016). "Dynamical mass ejection from the merger of asymmetric binary neutron stars: Radiation-hydrodynamics study in general relativity". In: 93.12, 124046, p. 124046. DOI: 10.1103/PhysRevD.93.124046. arXiv: 1603.01918 [astro-ph.HE].

Shemi, Amotz and Tsvi Piran (Dec. 1990). "The Appearance of Cosmic Fireballs". In: 365, p. L55. DOI: 10.1086/185887.

Shen, Rongfeng and Christopher D. Matzner (Jan. 2012). "Coasting External Shock in Wind Medium: An Origin for the X-Ray Plateau Decay Component in Swift Gamma-Ray Burst Afterglows". In: 744.1, 36, p. 36. DOI: 10.1088/0004-637X/744/1/36. arXiv: 1109.3453 [astro-ph.HE].

Si, Shu-Kun et al. (Aug. 2018). "The Three-parameter Correlations About the Optical Plateaus of Gamma-Ray Bursts". In: 863.1, 50, p. 50. DOI: 10.3847/1538-4357/aad08a. arXiv: 1807.00241 [astro-ph.HE].

Singer, Leo P. et al. (Sept. 2016). "Going the Distance: Mapping Host Galaxies of LIGO and Virgo Sources in Three Dimensions Using Local Cosmography and Targeted Follow-up". In: 829.1, L15, p. L15. DOI: 10.3847/2041-8205/829/1/L15. arXiv: 1603.07333 [astro-ph.HE].

Sironi, L. et al. (Oct. 2015). "Relativistic Shocks: Particle Acceleration and Magnetization". In: 191.1-4, pp. 519–544. DOI: 10.1007/s11214-015-0181-8. arXiv: 1506.02034 [astro-ph.HE].

Smartt, S. J. (2016). "Pan-STARRS and PESSTO search for an optical counterpart to the LIGO gravitational-wave source GW150914". In: *MNRAS* 462.

Smartt, S. J. et al. (Nov. 2017). "A kilonova as the electromagnetic counterpart to a gravitational-wave source". In: 551.7678, pp. 75–79. DOI: 10.1038/nature24303. arXiv: 1710.05841 [astro-ph.HE].

Soares-Santos, M. et al. (Oct. 2017). "The Electromagnetic Counterpart of the Binary Neutron Star Merger LIGO/Virgo GW170817. I. Discovery of the Optical Counterpart Using the Dark Energy Camera". In: 848.2, L16, p. L16. DOI: 10.3847/2041-8213/aa9059. arXiv: 1710.05459 [astro-ph.HE].

Song, Hao-Ran et al. (Aug. 2019). "Viewing Angle Constraints on S190425z and S190426c and the Joint Gravitational-wave/Gamma-Ray Detection Fractions for Binary Neutron Star Mergers". In: 881.2, L40, p. L40. DOI: 10.3847/2041-8213/ab3921. arXiv: 1904.12263 [astro-ph.HE].

Stanek, K. Z. et al. (July 2003). "Spectroscopic Discovery of the Supernova 2003dh Associated with GRB 030329". In: 591.1, pp. L17–L20. DOI: 10.1086/376976. arXiv: astro-ph/0304173 [astro-ph].

Stratta, Giulia et al. (Dec. 2018). "On the Magnetar Origin of the GRBs Presenting X-Ray Afterglow Plateaus". In: 869.2, 155, p. 155. DOI: 10.3847/1538-4357/aadd8f. arXiv: 1804.08652 [astro-ph.HE].

Sutton, Patrick J. et al. (May 2010). "X-Pipeline: an analysis package for autonomous gravitational-wave burst searches". In: *New Journal of Physics* 12.5, 053034, p. 053034. DOI: 10.1088/1367-2630/12/5/053034. arXiv: 0908.3665 [gr-qc].

Tagliaferri, G. (2005). "An unexpectedly rapid decline in the X-ray afterglow emission of long -ray bursts". In: *Nature* 436. DOI: 10.1038/nature03934. URL: https://doi.org/10.1038/nature03934.

Tang, Chen-Han et al. (Nov. 2019). "Statistical Study of Gamma-Ray Bursts with a Plateau Phase in the X-Ray Afterglow". In: 245.1, 1, p. 1. DOI: 10.3847/1538-4365/ab4711. arXiv: 1905.07929 [astro-ph.HE].

Tanvir, N. R. et al. (Aug. 2013). "A 'kilonova' associated with the short-duration γ-ray burst GRB 130603B". In: 500.7464, pp. 547–549. DOI: 10.1038/nature12505. arXiv: 1306.4971 [astro-ph.HE].

The LIGO Scientific Collaboration et al. (Nov. 2021a). "GWTC-3: Compact Binary Coalescences Observed by LIGO and Virgo During the Second

Part of the Third Observing Run". In: *arXiv e-prints*, arXiv:2111.03606, arXiv:2111.03606. arXiv: 2111.03606 [gr-qc].

The LIGO Scientific Collaboration et al. (Nov. 2021b). "The population of merging compact binaries inferred using gravitational waves through GWTC-3". In: *arXiv e-prints*, arXiv:2111.03634, arXiv:2111.03634. arXiv: 2111.03634 [astro-ph.HE].

Thöne, C. C. et al. (Feb. 2013). "GRB 100219A with X-shooter - abundances in a galaxy at z =4.7". In: 428.4, pp. 3590–3606. DOI: 10.1093/mnras/sts303. arXiv: 1206.2337 [astro-ph.HE].

Troja, E. et al. (Aug. 2007). "Swift Observations of GRB 070110: An Extraordinary X-Ray Afterglow Powered by the Central Engine". In: 665.1, pp. 599–607. DOI: 10.1086/519450. arXiv: astro-ph/0702220 [astro-ph].

Troja, E. et al. (Nov. 2017). "The X-ray counterpart to the gravitational-wave event GW170817". In: 551.7678, pp. 71–74. DOI: 10.1038/nature24290. arXiv: 1710.05433 [astro-ph.HE].

Troja, E. et al. (Oct. 2019). "A year in the life of GW 170817: the rise and fall of a structured jet from a binary neutron star merger". In: 489.2, pp. 1919–1926. DOI: 10.1093/mnras/stz2248. arXiv: 1808.06617 [astro-ph.HE].

Troja, E. et al. (Feb. 2022). "Accurate flux calibration of GW170817: is the X-ray counterpart on the rise?" In: 510.2, pp. 1902–1909. DOI: 10.1093/mnras/stab3533. arXiv: 2104.13378 [astro-ph.HE].

Uhm, Z. L. and B. Zhang (2015). "On the curvature effect of a relativistic spherical shell". In: *Astrophys. J.* 808. DOI: 10.1088/0004-637X/808/1/33. URL: https://doi.org/10.1088/0004-637X/808/1/33.

Uhm, Z. Lucas and Andrei M. Beloborodov (Aug. 2007). "On the Mechanism of Gamma-Ray Burst Afterglows". In: 665.2, pp. L93–L96. DOI: 10.1086/519837. arXiv: astro-ph/0701205 [astro-ph].

Uhm, Z. Lucas and Bing Zhang (May 2014). "Fast-cooling synchrotron radiation in a decaying magnetic field and γ-ray burst emission mechanism". In: *Nature Physics* 10.5, pp. 351–356. DOI: 10.1038/nphys2932. arXiv: 1303.2704 [astro-ph.HE].

— (June 2016a). "Evidence of Bulk Acceleration of the GRB X-Ray Flare Emission Region". In: 824.1, L16, p. L16. DOI: 10.3847/2041-8205/824/1/L16. arXiv: 1509.03296 [astro-ph.HE].

— (July 2016b). "Toward an Understanding of GRB Prompt Emission Mechanism. I. The Origin of Spectral Lags". In: 825.2, 97, p. 97. DOI: 10.3847/0004-637X/825/2/97. arXiv: 1511.08807 [astro-ph.HE].

Uhm, Z. Lucas et al. (Dec. 2018). "Toward an Understanding of GRB Prompt Emission Mechanism. II. Patterns of Peak Energy Evolution and Their Connection to Spectral Lags". In: 869.2, 100, p. 100. DOI: 10.3847/1538-4357/aaeb30. arXiv: 1801.09183 [astro-ph.HE].

Urrutia, Gerardo et al. (July 2022). "Three-dimensional numerical simulations of structured GRB jets". In: *arXiv e-prints*, arXiv:2207.07925, arXiv:2207.07925. arXiv: 2207.07925 [astro-ph.HE].

van Eerten, Hendrik et al. (Apr. 2012). "Gamma-Ray Burst Afterglow Broadband Fitting Based Directly on Hydrodynamics Simulations". In: 749.1, 44, p. 44. DOI: 10.1088/0004-637X/749/1/44. arXiv: 1110.5089 [astro-ph.HE].

van Paradijs, J. et al. (Apr. 1997). "Transient optical emission from the error box of the γ-ray burst of 28 February 1997". In: 386.6626, pp. 686–689. DOI: 10.1038/386686a0.

Vanderspek, R. et al. (Dec. 2004). "HETE Observations of the Gamma-Ray Burst GRB 030329: Evidence for an Underlying Soft X-Ray Component". In: 617.2, pp. 1251–1257. DOI: 10.1086/423923. arXiv: astro-ph/0401311 [astro-ph].

Vergani, S. D. et al. (Sept. 2015). "Are long gamma-ray bursts biased tracers of star formation? Clues from the host galaxies of the Swift/BAT6 complete sample of LGRBs . I. Stellar mass at z < 1". In: 581, A102, A102. DOI: 10.1051/0004-6361/201425013. arXiv: 1409.7064 [astro-ph.HE].

Villar, V. A. et al. (Dec. 2017). "The Combined Ultraviolet, Optical, and Near-infrared Light Curves of the Kilonova Associated with the Binary Neutron Star Merger GW170817: Unified Data Set, Analytic Models, and Physical Implications". In: 851.1, L21, p. L21. DOI: 10.3847/2041-8213/aa9c84. arXiv: 1710.11576 [astro-ph.HE].

Volnova, A. A. et al. (May 2017). "Multicolour modelling of SN 2013dx associated with GRB 130702A". In: 467.3, pp. 3500–3512. DOI: 10.1093/mnras/stw3297. arXiv: 1612.07626 [astro-ph.HE].

von Kienlin, A. et al. (Apr. 2020). "The Fourth Fermi-GBM Gamma-Ray Burst Catalog: A Decade of Data". In: 893.1, 46, p. 46. DOI: 10.3847/1538-4357/ab7a18. arXiv: 2002.11460 [astro-ph.HE].

Walker, K. C. et al. (2000). "Gamma-ray bursts have millisecond variability". In: *Astrophys. J.* 537. DOI: 10.1086/308995. URL: https://doi.org/10.1086/308995.

Wanderman, David and Tsvi Piran (2010). "The luminosity function and the rate of Swift's gamma-ray bursts". In: *Monthly Notices of the Royal Astronomical Society* 406.3, pp. 1944–1958.

Wanderman, David and Tsvi Piran (Apr. 2015). "The rate, luminosity function and time delay of non-Collapsar short GRBs". In: 448.4, pp. 3026–3037. DOI: 10.1093/mnras/stv123. arXiv: 1405.5878 [astro-ph.HE].

Watson, Darach et al. (Oct. 2019). "Identification of strontium in the merger of two neutron stars". In: 574.7779, pp. 497–500. DOI: 10.1038/s41586-019-1676-3. arXiv: 1910.10510 [astro-ph.HE].

White, N. E. et al. (Aug. 2021). "The Gamow Explorer: a Gamma-Ray Burst Observatory to study the high redshift universe and enable multi-messenger astrophysics". In: *Society of Photo-Optical Instrumentation Engineers (SPIE) Conference Series*. Vol. 11821. Society of Photo-Optical Instrumentation Engineers (SPIE) Conference Series, 1182109, p. 1182109. DOI: 10.1117/12.2599293. arXiv: 2111.06497 [astro-ph.HE].

Williamson, A. R. et al. (Dec. 2014). "Improved methods for detecting gravitational waves associated with short gamma-ray bursts". In: 90.12, 122004, p. 122004. DOI: 10.1103/PhysRevD.90.122004. arXiv: 1410.6042 [gr-qc].

Wilms, J. et al. (Oct. 2000). "On the Absorption of X-Rays in the Interstellar Medium". In: 542.2, pp. 914–924. DOI: 10.1086/317016. arXiv: astro-ph/0008425 [astro-ph].

Woosley, S. E. (Mar. 1993). "Gamma-Ray Bursts from Stellar Mass Accretion Disks around Black Holes". In: 405, p. 273. DOI: 10.1086/172359.

Wu, Yiyang and Andrew MacFadyen (Dec. 2018). "Constraining the Outflow Structure of the Binary Neutron Star Merger Event GW170817/GRB170817A with a Markov Chain Monte Carlo Analysis". In: 869.1, 55, p. 55. DOI: 10.3847/1538-4357/aae9de. arXiv: 1809.06843 [astro-ph.HE].

— (Aug. 2019a). "GW170817 Afterglow Reveals that Short Gamma-Ray Bursts are Neutron Star Mergers". In: 880.2, L23, p. L23. DOI: 10.3847/2041-8213/ab2fd4. arXiv: 1905.02665 [astro-ph.HE].

— (Aug. 2019b). "GW170817 Afterglow Reveals that Short Gamma-Ray Bursts are Neutron Star Mergers". In: 880.2, L23, p. L23. DOI: 10.3847/2041-8213/ab2fd4. arXiv: 1905.02665 [astro-ph.HE].

Xu, D. et al. (May 2009). "In Search of Progenitors for Supernovaless Gamma-Ray Bursts 060505 and 060614: Re-examination of Their Afterglows". In: 696.1, pp. 971–979. DOI: 10.1088/0004-637X/696/1/971. arXiv: 0812.0979 [astro-ph].

Yang, Bin et al. (June 2015). "A possible macronova in the late afterglow of the long-short burst GRB 060614". In: *Nature Communications* 6, 7323, p. 7323. DOI: 10.1038/ncomms8323. arXiv: 1503.07761 [astro-ph.HE].

Yonetoku, D. et al. (July 2004). "Gamma-Ray Burst Formation Rate Inferred from the Spectral Peak Energy-Peak Luminosity Relation". In: 609.2, pp. 935–951. DOI: 10.1086/421285. arXiv: astro-ph/0309217 [astro-ph].

Yu, Jiming et al. (July 2021). "Multimessenger Detection Rates and Distributions of Binary Neutron Star Mergers and Their Cosmological Implications". In: 916.1, 54, p. 54. DOI: 10.3847/1538-4357/ac0628. arXiv: 2104.12374 [astro-ph.HE].

Yu, Yun-Wei et al. (July 2018). "A Long-lived Remnant Neutron Star after GW170817 Inferred from Its Associated Kilonova". In: 861.2, 114, p. 114. DOI: 10.3847/1538-4357/aac6e5. arXiv: 1711.01898 [astro-ph.HE].

Yuan, Weimin et al. (Mar. 2018). "Einstein Probe: Exploring the ever-changing X-ray Universe". In: *Scientia Sinica Physica, Mechanica & Astronomica* 48.3, p. 039502. DOI: 10.1360/SSPMA2017-00297.

Zhang, B. (2006). "Physical processes shaping gamma-ray burst X-Ray afterglow light curves: theoretical implications from the Swift X-Ray telescope observations". In: *Astrophys. J.* 642. DOI: 10.1086/500723. URL: https://doi.org/10.1086/500723.

— (2020). "Synchrotron radiation in -ray bursts prompt emission". In: *Nat. Astron.* 4. DOI: 10.1038/s41550-020-1041-3. URL: https://doi.org/10.1038/s41550-020-1041-3.

Zhang, B. and H. Yan (2011). "The internal-collision-induced magnetic reconnection and turbulence (ICMART) model of gamma-ray bursts". In: *Astrophys. J.* 726. DOI: 10.1088/0004-637X/726/2/90. URL: https://doi.org/10.1088/0004-637X/726/2/90.

Zhang, B. . B. et al. (2007). "A comprehensive analysis of Swift XRT data. I. Apparent spectral evolution of gamma-ray burst X-ray tails". In: *Astrophys. J.* 666. DOI: 10.1086/519548. URL: https://doi.org/10.1086/519548.

Zhang, B. B. et al. (July 2021). "A peculiarly short-duration gamma-ray burst from massive star core collapse". In: *Nature Astronomy* 5, pp. 911–916. DOI: 10.1038/s41550-021-01395-z. arXiv: 2105.05021 [astro-ph.HE].

Zhang, Bin-Bin et al. (Jan. 2009). "Curvature Effect of a Non-Power-Law Spectrum and Spectral Evolution of GRB X-Ray Tails". In: 690.1, pp. L10–L13. DOI: 10.1088/0004-637X/690/1/L10. arXiv: 0808.3793 [astro-ph].

Zhang, Bing and Peter Mészáros (May 2001a). "Gamma-Ray Burst Afterglow with Continuous Energy Injection: Signature of a Highly Magnetized Millisecond Pulsar". In: 552.1, pp. L35–L38. DOI: 10.1086/320255. arXiv: astro-ph/0011133 [astro-ph].

— (May 2001b). "Gamma-Ray Burst Afterglow with Continuous Energy Injection: Signature of a Highly Magnetized Millisecond Pulsar". In: 552.1, pp. L35–L38. DOI: 10.1086/320255. arXiv: astro-ph/0011133 [astro-ph].

— (June 2002). "Gamma-Ray Burst Beaming: A Universal Configuration with a Standard Energy Reservoir?" In: 571.2, pp. 876–879. DOI: 10.1086/339981. arXiv: astro-ph/0112118 [astro-ph].

Zhang, Bing et al. (May 2006a). "Physical Processes Shaping Gamma-Ray Burst X-Ray Afterglow Light Curves: Theoretical Implications from the Swift X-Ray Telescope Observations". In: 642.1, pp. 354–370. DOI: 10.1086/500723. arXiv: astro-ph/0508321 [astro-ph].

— (May 2006b). "Physical Processes Shaping Gamma-Ray Burst X-Ray Afterglow Light Curves: Theoretical Implications from the Swift X-Ray Telescope Observations". In: 642.1, pp. 354–370. DOI: 10.1086/500723. arXiv: astro-ph/0508321 [astro-ph].

Zhang, Q. et al. (Mar. 2018). "Search for the signatures of a new-born black hole from the collapse of a supra-massive millisecond magnetar in short GRB light curves". In: 475.1, pp. 266–276. DOI: 10.1093/mnras/stx3229. arXiv: 1712.04103 [astro-ph.HE].

Zhao, Wen and Linqing Wen (Mar. 2018). "Localization accuracy of compact binary coalescences detected by the third-generation gravitational-wave detectors and implication for cosmology". In: 97.6, 064031, p. 064031. DOI: 10.1103/PhysRevD.97.064031. arXiv: 1710.05325 [astro-ph.CO].